

Abstract

Title of Dissertation: From Merging Galaxies to Quasars:
The Evolution of Nuclear Activity in
Luminous and Ultraluminous Infrared Galaxies

Stacy H. Teng, Doctor of Philosophy, 2010

Dissertation directed by: Professor Sylvain Veilleux
Department of Astronomy

We present the largest X-ray survey (~ 80 objects) of luminous and ultraluminous infrared galaxies (U/LIRGs) to date. The large infrared luminosities in these objects are thought to arise from either star formation triggered by the merging of disk galaxies or by nuclear activity. U/LIRGs have been purported to be the progenitors of some quasars. In this thesis, we utilize data from *Chandra*, *XMM-Newton*, and *Suzaku* X-ray observatories to quantify the contribution to the overall power of U/LIRGs by starbursts or active galactic nuclei (AGNs). A goal of this project is to statistically examine how the starburst-to-AGN ratio evolves as a function of merger stage.

We find that a majority of U/LIRGs are X-ray faint. This may be a result of high obscuration or weak nuclear activity. The dearth of detected counts makes traditional fitting difficult. As a solution, we developed a method of using hardness ratios (HR) to estimate the spectral shapes of these weak sources. Both observational evidence and simulations show that this method is effective for sources with intrinsic column densities below $\sim 10^{22}$ cm $^{-2}$ and applicable to sources with only tens of detected counts.

Applying the HR method and traditional spectral fitting to the U/LIRG data and that of 26 PG quasars, we find a correlation of AGN dominance with dust

temperature, optical spectral type, and merger stage. The probability of having a powerful AGN increases along the merger sequence. However, the AGNs can turn on at any time, as evidenced by a large number of AGNs detected in binary U/LIRGs. Starburst dominates the total power in U/LIRGs prior to the merger. Then the black hole grows rapidly during coalescence. At this time, the AGN is likely to begin driving galactic scale winds which will quench star formation, resulting in a luminous quasar. These conclusions are in general agreement with results obtained at other wavelengths and current theoretical models.

**From Merging Galaxies to Quasars:
The Evolution of Nuclear Activity in
Luminous and Ultraluminous Infrared Galaxies**

by

Stacy H. Teng

Dissertation submitted to the Faculty of the Graduate School of the
University of Maryland at College Park in partial fulfillment
of the requirements for the degree of
Doctor of Philosophy
2010

Advisory Committee:

Professor Sylvain Veilleux, chair
Professor M. Coleman Miller
Professor Richard F. Mushotzky
Dr. Andrew Ptak
Professor Gregory Sullivan

© Stacy H. Teng 2010

Preface

Much of the work presented here has been published and presented in professional conferences. The *Chandra* pilot study presented in Chapter Two of this thesis has been published in the *Astrophysical Journal* as *A Chandra X-ray Survey of Ultraluminous Infrared Galaxies* (Teng et al. 2005). In addition, the results of the pilot study were presented as posters with the same title at the Six Years of Science with *Chandra* Conference in Boston, Massachusetts in 2005 and the 2006 Winter American Astronomical Society meeting in Washington, D.C.

An *XMM-Newton* follow-up observation on IRAS F04103–2838 presented in Chapter Three is also published in the *Astrophysical Journal* as *XMM-Newton Detection of a Compton-thick AGN in the 1-Jy ULIRG/LINER F04103–2838* (Teng et al. 2008).

Chapter Five has been published in the *Astrophysical Journal* as *Suzaku Observations of Local Ultraluminous Infrared Galaxies* (Teng et al. 2009). This work was also presented as an oral presentation in the 2009 Winter American Astronomical Society meeting in Long Beach, California.

The work presented in Chapter Six and a majority of the work presented in Chapters Two and Four were presented at the 2010 Winter American Astronomical Society meeting in Washington, D.C. as part of an oral dissertation presentation. The results from Chapter Six were also presented as a poster at the 2010 meeting

of the High Energy Astrophysics Division of the American Astronomical Society in
Waikaloa, Hawaii.

Dedicated to:

爷爷

Acknowledgements

I am indebted to all the advisors I have had along the way. First and foremost, Sylvain Veilleux for his keen scientific insights that I can only hope to aspire to have someday. He has always been encouraging, yet diplomatic even when I am wrong. I am grateful for his patience and for his allowing me to make mistakes and learn. I cannot forget Andrew Wilson who started me out on this journey with my second year project. Our meetings were always terrifying, but his insistence for quality made me better. I really appreciate Chris Reynolds and Cole Miller for always willing to answer all of my questions. Thanks are due to Richard Mushotzky, Andy Ptak, and Greg Sullivan for serving on my thesis committee and providing detailed suggestions that improved the document. I am also grateful to Jim Ulvestad, for giving me two very memorable summers in the deserts of New Mexico. He assured me that I can make it... and here I am.

Thanks to all the friends that I have made along the way – in particular, Lisa, Vanessa, Stephanie, Nicholas, Ashley, Megan, Claudia, Franziska,

Derek, and Frances. Each of them was always there when I needed help (with science or otherwise), listened when I needed to vent, and on hand when I needed fun. I also want to give a shout out to the late-night crew – Shaye, Jithin, and Alex – for entertaining me through the wee hours of the night and making these last few months bearable. Without the laughter, I would not have survived. How can I forget the Mandalay family? Thanks for keeping me well fed, even if what I wanted is not on the menu!

And of course, a special thanks is due to Matthew, the house elf, the jester, and the jedi of SuperMongo. He has stood by me through my highest highs and my lowest lows. Who else can handle my shenanigans?

Finally, I want to acknowledge my parents who moved halfway around the world and made many sacrifices so that I may succeed. This has been as much a culmination of my efforts as it has been theirs. I am grateful to my mother for her nurturing spirit and my father for giving me my very first astronomical memories.

Contents

List of Tables	x
List of Figures	xii
1 Introduction	1
1.1 Motivation	1
1.1.1 The Importance of U/LIRGs	1
1.1.2 The “Great Debate”: The Energy Source of U/LIRGs	3
1.1.3 The Evolutionary Scenario	4
1.2 X-ray Studies of U/LIRGs	5
1.2.1 X-ray Morphology	5
1.2.2 X-ray Spectra	6
1.3 An Overview of X-ray Instrumentation	12
1.3.1 <i>Chandra X-ray Observatory</i>	13
1.3.2 <i>XMM-Newton Observatory</i>	14
1.3.3 <i>Suzaku X-ray Observatory</i>	16
1.3.4 Spectral Analysis	17
1.4 The Structure of this Dissertation	19
2 <i>Chandra</i> Pilot Study	21
2.1 Introduction	21
2.2 Sample Selection	22
2.3 Observations and Data Reduction	24
2.4 Analysis and Results	26
2.4.1 Astrometry	26
2.4.2 X-Ray Structure	26
2.4.3 X-Ray Spectra	29
2.5 Discussion	38
2.5.1 The Two Bright Sources	38
2.5.2 The Twelve Faint Sources	41
2.5.3 Correlations with Infrared Color and Luminosity	43

2.5.4	Comparison with Previous Work	44
2.5.5	Emission Processes	48
2.6	Summary	52
3	<i>XMM-Newton</i> Follow-up on F04103–2838	54
3.1	Introduction	54
3.2	Observation and Data Reduction	55
3.3	Analysis	56
3.3.1	Morphology	57
3.3.2	X-Ray Variability	57
3.3.3	X-Ray Spectra	58
3.4	Discussion	66
3.4.1	The Soft Component	66
3.4.2	The Iron Feature	68
3.4.3	Energy Source of the ULIRG	71
3.5	Summary	74
4	The X-ray Properties of the <i>IRAS</i> Revised Bright Galaxy Survey Sample	76
4.1	Introduction	76
4.2	The Sample	77
4.3	Observations and Reduction on Archived Data	79
4.4	Analysis and Results on Archived Data	80
4.4.1	Imaging	80
4.4.2	Spectra	87
4.5	Discussion	89
4.5.1	X-ray Morphology of Archived Data	89
4.5.2	X-ray Spectra of Archived Data	94
4.5.3	Comparison with Previous Work	96
4.6	Summary	103
5	<i>Suzaku</i> Observations of Local U/LIRGs	105
5.1	The Need for <i>Suzaku</i>	105
5.2	Sample	106
5.3	Observations and Data Reduction	109
5.3.1	XIS Data Reduction	110
5.3.2	HXD/PIN Data Reduction	111
5.4	<i>Suzaku</i> Results	112
5.4.1	<i>IRAS</i> F05189–2524	113
5.4.2	<i>IRAS</i> F08572+3915	116
5.4.3	Mrk 273	118

5.4.4	PKS 1345+12	123
5.4.5	Arp 220	124
5.5	The Long-term Variability of <i>IRAS</i> F05189–2524 and Mrk 273	127
5.5.1	<i>IRAS</i> F05189–2524	127
5.5.2	Mrk 273	134
5.6	Summary	140
6	Quasar/ULIRG Evolution Study (QUEST): an X-ray survey of ULIRGs and PG QSOs	143
6.1	Introduction	143
6.2	Observations and Data Reduction	147
6.2.1	Data Calibration and Extraction	150
6.3	Spectral Analysis	153
6.3.1	Results: PG QSOs	153
6.3.2	Results: ULIRGs	167
6.4	PG QSOs: the Origin of the Soft Excess	177
6.4.1	Modeling PG QSOs as a Class	179
6.4.2	The Favored Model	180
6.5	The Multi-wavelength Properties of QUEST ULIRGs and PG QSOs .	189
6.5.1	AGN Contributions to Bolometric Luminosity	190
6.5.2	Trends with Merger Phase	195
6.6	Summary	198
7	Summary and Conclusions	202
7.1	Overview	202
7.2	Key Results	204
7.3	Future Work	205
A	The Reliability of the Hardness Ratio Method	207
B	Notes on Individual RBGS Sources	215
C	Ultraluminous X-ray Sources (ULXs) in the RBGS Sample	223
	Bibliography	226

List of Tables

1.1	A Comparison of X-ray Detectors	16
2.1	Some Properties of the Sample and the <i>Chandra</i> Observations ^a	24
2.2	Astrometry of Our Sample ^a	27
2.3	Spectral Models for F01572+0009 & Z11598-0112 ^a	32
2.4	Spectral Models Derived from Hardness Ratios	39
2.5	X-Ray and Infrared Fluxes and Luminosities	42
3.1	Best-fit Parameters to Models A, B, & C [†]	63
4.1	The Sample	78
4.2	Journal of Observations	79
4.3	Hardness Ratio Results for the RBGS Sample	81
4.4	Spectral Fitting Results for Bright Archive Targets	90
5.1	The <i>Suzaku</i> Sample	106
5.2	<i>Suzaku</i> Observations	109
5.3	Best-fit Parameters to <i>Suzaku</i> Spectra [†]	115
5.4	Modeling Spectra of F05189–2524 and Mrk 273 from Multiple Epochs	133
6.1	The X-ray QUEST Sample	146
6.1	The X-ray QUEST Sample	147
6.2	Journal of Observations	148
6.2	Journal of Observations	149
6.2	Journal of Observations	150
6.3	PG QSOs: PL Model Best-fit Values	154
6.4	PG QSOs: P05 Model ^a Best-fit Values	165
6.5	PG QSOs: C06 Model ^a Best-fit Values	166
6.6	Hardness Ratio Estimates of Weak ULIRGs	168
6.7	Best-fit Parameters for ULIRG Spectra with > 100 Counts	171
6.8	PG QSOs: Derived Parameters from the Global PEXRIV Model	184
A.1	Quantifying the Errors in the Hardness Ratio Method	210

C.1 Properties of ULX Candidates 225

List of Figures

1.1	The Luminosity Function of ULIRGs	2
1.2	The Spectral Energy Distribution of Quasars	6
1.3	Elements of an AGN Spectrum	7
1.4	The Unified AGN Model	8
1.5	Effects of Absorption	12
1.6	<i>Chandra</i> ACIS-S Focal Plane	14
1.7	<i>XMM-Newton</i> EPIC Focal Plane	15
2.1	The distribution of the pilot study sample in the $f(25 \mu m)/f(60 \mu m)$ versus $\log L_{IR}$ plane	23
2.2	Comparison of X-ray with optical and near-IR morphologies for two binary sources in the pilot study	29
2.3	Comparison of X-ray with optical and near-IR morphologies for the two bright sources in the pilot study	30
2.4	Comparison of model PSFs with observed radial profiles for the two bright sources in the pilot study	31
2.5	<i>Chandra</i> spectrum of F01572+0009 with best-fit model	33
2.6	<i>Chandra</i> spectrum of Z11598-0112 with best-fit model	33
2.7	Contours of constant hardness ratio in the N_H versus Γ plane	36
2.8	Contours of constant hardness ratio in the N_H versus kT plane	37
2.9	Hardness ratio derived X-ray to (far-)infrared flux relations	44
2.10	Hardness ratio derived Γ as a function of color temperatures and infrared luminosities	45
2.11	Distribution of starburst, AGN, and composite galaxies in the $\log F_{2-10 \text{ keV}}/F_{FIR}$ versus $\log f_{25\mu m}/f_{60\mu m}$	46
2.12	Comparison of photon indices between two samples for single-power-law models	47
2.13	Comparison of photon indices between two samples for two-component models	48
2.14	X-ray and far-infrared star formation rates	50
3.1	X-ray morphology of F04103-2838	58

3.2	<i>XMM-Newton</i> light curve of F04103–2838	59
3.3	EPIC PN spectrum of F04103–2838 with different binnings	62
3.4	EPIC PN spectrum of F04103–2838 and its best-fit model	65
3.5	Distribution of equivalent widths of known Fe K emissions in LINERs	70
4.1	False-color X-ray Images of the RBGS Sample	84
4.1	Cont.	85
4.2	Radial Profiles of the RBGS Sample	86
4.2	Cont.	87
4.2	Cont.	88
4.3	Spectra of the RBGS Sample	91
4.3	Cont.	92
4.3	Cont.	93
4.4	Starburst-driven Galactic Wind in UGC 08387	94
4.5	A Comparison of Photon Indices Between LIRGs and ULIRGs	97
4.6	Photon Indices of the RBGS U/LIRGs as a Function of Infrared Luminosity	98
4.7	Photon Indices of the RBGS U/LIRGs as a Function of Dust Temperature	99
4.8	Comparison of Photon Indices Between Single and Binary U/LIRGs	100
4.9	Photon Indices of the RBGS U/LIRGs as a Function of Optical Spectral Types	101
4.10	$\log(L_{2-10 \text{ keV}}/L_{FIR})$ Versus $\log(f_{25\mu\text{m}}/f_{60\mu\text{m}})$ for the RBGS U/LIRGs	102
4.11	Comparison of X-ray and Far-infrared Derived Star Formation Rates	103
5.1	<i>Suzaku</i> XIS spectra and best-fit models	117
5.2	Comparison of <i>Suzaku</i> HXD/PIN spectra with the background	120
5.3	Possible contamination of Mrk 273 in the <i>Suzaku</i> HXD/PIN field of view	122
5.4	The combined <i>Suzaku</i> XIS-HXD/PIN spectrum of Mrk 273	123
5.5	Long term variability of the X-ray flux of F05189–2524	128
5.6	Spectral variability of F05189–2524	129
5.7	Multi-epoch modeling of spectra from F05189–2524	132
5.8	Long term variability of the X-ray flux of Mrk 273	136
5.9	Spectral variability of Mrk 273	137
5.10	Multi-epoch modeling of spectra from Mrk 273	138
6.1	Spectra of QUEST PG QSOs	156
6.1	Cont.	157
6.1	Cont.	158
6.1	Cont.	159

6.1	Cont.	160
6.1	Cont.	161
6.1	Cont.	162
6.1	Cont.	163
6.2	Comparison of χ^2_ν for Three Models	164
6.3	Comparison of Γ for Three Models	167
6.4	AGN Dominance in PG QSOs and U/LIRGs	175
6.5	Comparison of 2–10 keV Luminosity with Bolometric Luminosity for PG QSOs and U/LIRGs	176
6.6	Comparison of X-ray and Mid-infrared Derived Eddington Ratios	177
6.7	Global Models for PG QSOs	182
6.8	Residuals for the Best-Fit PG QSO Global Model	183
6.9	Distribution of Inclination Angles	186
6.10	Comparison of Soft Excess with Power Law Luminosity	187
6.11	Comparison of Soft Excess with Starburst Luminosity	188
6.12	Distribution of Accretion Disc Temperature for PG QSOs	190
6.13	Comparison of X-ray and Mid-infrared AGN Diagnostic Methods	192
6.14	Distribution of AGN % in ULIRGs	194
6.15	Trends of AGN Dominance with U/LIRG Properties	196
6.16	Corrected AGN Bolometric Luminosity as a Function of Merger Stage	199
A.1	Quantifying the Errors in the Hardness Ratio Estimate of Γ	209
A.2	Comparison of the Hardness Ratio Method with Traditional Spectral Fitting	211
A.3	Quantifying the Errors in the Hardness Ratio Estimate of Flux	213

Chapter 1

Introduction

1.1 Motivation

1.1.1 The Importance of U/LIRGs

Prior to the launch of *IRAS* in 1983, only a handful of luminous ($L_{IR} = L_{8-1000\mu\text{m}} \geq 10^{11} L_{\odot}$ assuming $H_0 = 75 \text{ km s}^{-1} \text{ Mpc}^{-1}$, $q_0 = 0$) and ultraluminous ($L_{IR} = L_{8-1000\mu\text{m}} \geq 10^{12} L_{\odot}$) infrared galaxies (U/LIRGs) were known. However, the *IRAS* all sky survey changed this by detecting hundreds of these objects and U/LIRGs seem to be more commonplace in the local ($z < 0.1$) universe than previously thought. The luminosity limit of ULIRGs is equivalent to the minimum bolometric luminosity of a quasar. At luminosities above $10^{12} L_{\odot}$, the space density of ULIRGs in the local universe is greater than that of optically selected quasars with similar bolometric luminosities by a factor of ~ 1.5 (Figure 1.1). Thus ULIRGs represent the most common type of ultraluminous galaxy. Systematic ground-based optical observations have shown that U/LIRGs are almost always undergoing mergers (e.g., Sanders et al. 1988a). Sanders et al. (1988a) suggested that U/LIRGs represent phases of merging galaxies that will eventually evolve into optically-selected

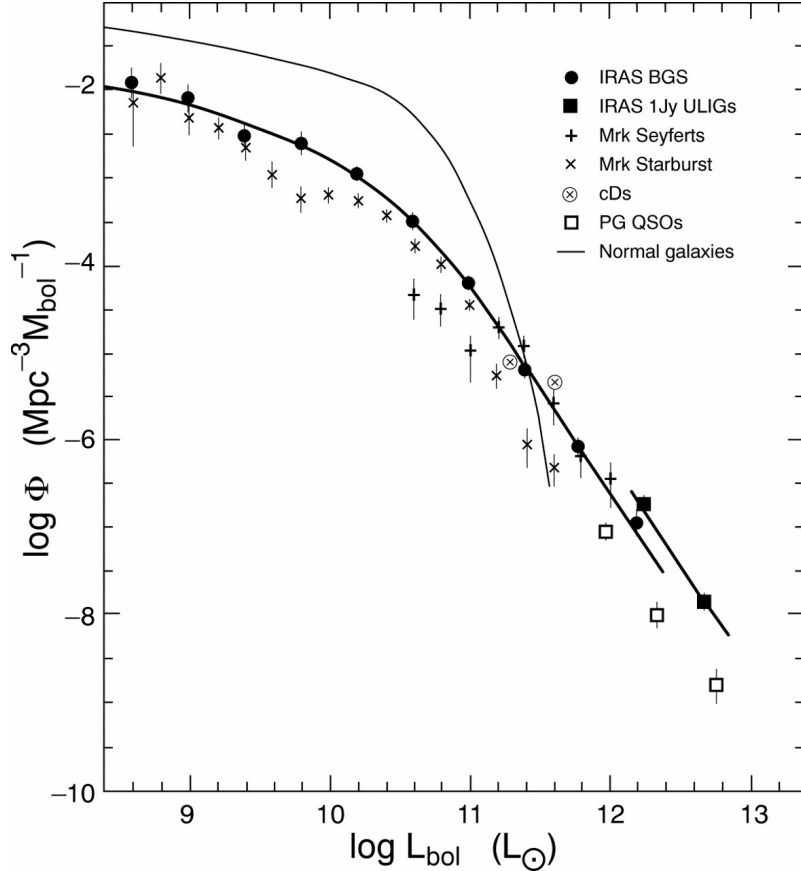


Figure 1.1: A comparison of the luminosity function of ULIRGs and other extragalactic objects from Sanders & Mirabel (1996). At bolometric luminosities above $\sim 10^{11.5} L_{\odot}$, U/LIRGs (filled squares and circles) begin to dominate the space density in the local universe.

quasars. If this is true, U/LIRGs take on a fundamental importance for the origin and evolution of quasars.

U/LIRGs are relevant to a wide range of astronomical issues, including the role played by galactic mergers in forming some or all elliptical galaxies (Genzel et al. 2001; Veilleux et al. 2002), the efficiency of transport of gas into the central regions of such mergers, the subsequent triggering of circumnuclear star formation, the resulting heating and metal enrichment of the IGM by “superwinds” (e.g., Veilleux et al. 2005), the potential growth and fueling of SMBHs, and the possible origin of quasars. These objects are also relevant to the dominant source of radiant energy

in the universe today. Star formation at $\langle z \rangle = 1.5$ could account for the observed energy density of the cosmic infrared background. On the other hand, the bolometric energy density from quasars detected in optical, radio, and X-ray surveys can only account for $\sim 5\%$ of this background. Thus while the present-day ULIRGs make a relatively small contribution to the total present-day light, their cousins at high z are fundamentally important in this regard.

1.1.2 The “Great Debate”: The Energy Source of U/LIRGs

It is clear that the high redshift cousins of U/LIRGs are fundamental to many cosmological problems. Study of these high redshift galaxies is very difficult because of their faintness, so the most useful approach is to understand first the present-day U/LIRGs. In this case, we must assume that the present-day sources and their high- z counterparts have similar basic properties such as metallicities and environments such that the physical processes that occur in local and high- z U/LIRGs are not very different. But then we immediately encounter a fundamental problem: are the large infrared luminosities of U/LIRGs, which may contribute significantly to the total infrared background, due to starbursts or accretion onto SMBHs? As noted, this problem in the local universe is fundamental to issues on cosmological scales. The power source has been the subject of a lively debate for about a decade (e.g., Ringberg’s “Great Debate”: Joseph 1999; Sanders 1999). The main arguments are as follows:

- *In Favor of Starbursts.* Optical and near infrared spectra of the 1-Jy sample (Veilleux et al. 1999a,b) show starbursts in almost all U/LIRGs, while $\sim 30\%$ show evidence for AGNs. Even in the mid-infrared, with greatly reduced extinction, only 20–30% of the U/LIRGs may be powered predominantly by an AGN (e.g., Genzel et al. 1998; Lutz et al. 1999; Veilleux et al. 2009b).

Massive central gas disks, commonly associated with starbursts, are found. Starburst models based on these data can account for most of the bolometric luminosity in most objects. The existence of a correlation between far-infrared, Brackett γ , and radio continuum luminosities favors a starburst. Radio and X-ray observations tend to show luminosities consistent with known correlations for starbursts in most cases.

- *In Favor of AGNs.* There is a clear trend of more Seyferts and AGN-like objects with increasing L_{IR} (e.g., Lutz et al. 1999; Veilleux et al. 1999a, 1995, 1999b) such that most of the objects with $L_{IR} > 10^{12.3} L_{\odot}$ and/or “warm” infrared colors ($f_{25\mu\text{m}}/f_{60\mu\text{m}} > 0.2$) are likely dominated by an AGN. For the nearest five ULIRGs (thus the best studied), the radio (high T_b core), mid-infrared (PAH line to continuum ratio), optical and near-infrared (Seyfert-like spectra, including polarized Seyfert 1 lines) and hard X-ray (similar luminosities to radio quiet QSOs) emissions suggest that three or four are dominated bolometrically by AGNs. ULIRGs, like quasars, show morphological features of strong interactions.

1.1.3 The Evolutionary Scenario

U/LIRGs are advanced mergers of gas-rich, disk galaxies sampling the entire Toomre merger sequence beyond the first peri-passage (Veilleux et al. 2002). The near-infrared light distributions in many ULIRGs fit a $R^{1/4}$ law (Scoville et al. 2000; Veilleux et al. 2006, 2002). ULIRGs also have large molecular gas concentrations in their central kpc regions (e.g., Downes & Solomon 1998) with densities comparable to stellar densities in ellipticals. Kormendy & Sanders (1992) have proposed that U/LIRGs evolve into ellipticals through merger induced dissipative collapse. In this scenario, these mergers first go through a luminous starburst phase triggered by

the encounter (pre-merger LIRG phase), followed by a dust-enshrouded AGN phase (post-merger ULIRG), and finally evolve into optically bright, “naked” QSOs once they either consume or shed their shells of gas and dust (Sanders et al. 1988a) in a powerful wind event (Hopkins et al. 2005; Rupke et al. 2005a,b,c; Veilleux et al. 2005).

1.2 X-ray Studies of U/LIRGs

The nuclei of ULIRGs may be very heavily obscured. Therefore, observations in UV, optical, near-infrared, and even the far-infrared may not penetrate through the dust to the nucleus. High resolution, high frequency radio observations can penetrate the high columns and are excellent probes of whether an AGN is present (Nagar et al. 2003). However, the bolometric luminosity in the radio band is insignificant (Figure 1.2), and thus radio observations cannot prove that accretion onto a SMBH is the dominant energy source. The remaining option is to observe U/LIRGs in hard X-rays. Below, different methods of determining AGN dominance in U/LIRGs are discussed.

1.2.1 X-ray Morphology

Pure starburst galaxies, at low redshifts, do not exhibit unresolved hard X-ray (2–10 keV) nuclei. Starbursts, such as M82, have extended hard X-ray emission from both diffuse gas and X-ray binaries (Griffiths et al. 2000). At the typical distances of the 1-Jy sample ($z \sim 0.1$), the angular extent of the diffuse, hard X-ray emission in M82 would be $\simeq 0''.05$ ($\simeq 100$ pc) and that of the X-ray binaries would be $\simeq 0''.5$ ($\simeq 1$ kpc). Starbursts in U/LIRGs also have typical extents of $\lesssim 1$ kpc (Soifer et al. 2000), so their hard X-ray emissions may be difficult to resolve with *Chandra*.

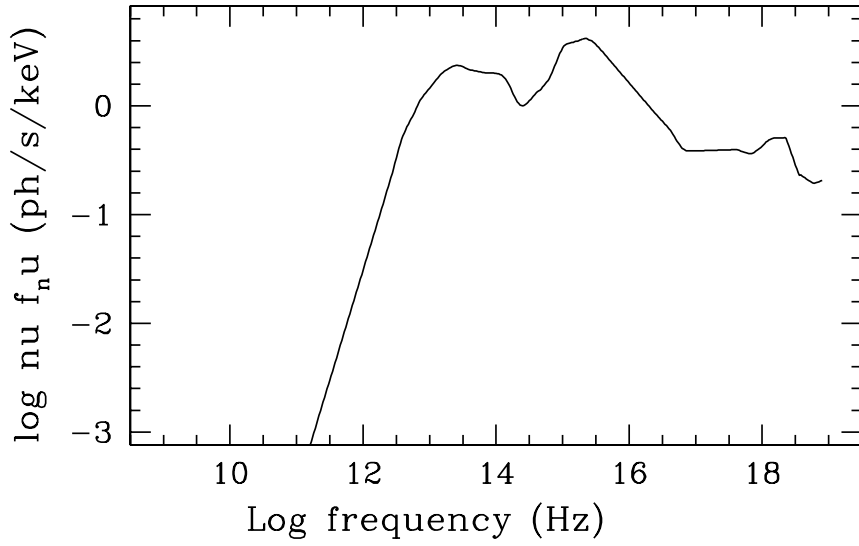


Figure 1.2: A plot of the spectral energy distribution of radio quiet quasars from Elvis et al. (1994). Clearly, the contribution of the AGN to the bolometric luminosity in the radio band ($\lesssim 10^{12}$ Hz) is negligible.

However, the absence of an unresolved hard X-ray core does not imply the lack of an AGN. If a large column of gas ($N_H \gtrsim 10^{24}$) is present, then the AGN is Compton-thick and the obscuring material can mask directly viewed X-rays from the AGN.

1.2.2 X-ray Spectra

X-ray spectroscopy of U/LIRGs can identify the presence of AGNs, but the X-ray spectrum of an AGN can be complex. Several components make up the observed spectrum (Figure 1.3), including the power law, soft excess, reflection, iron emission lines, and absorption. The physical origins of these components are shown in Figure 1.4.

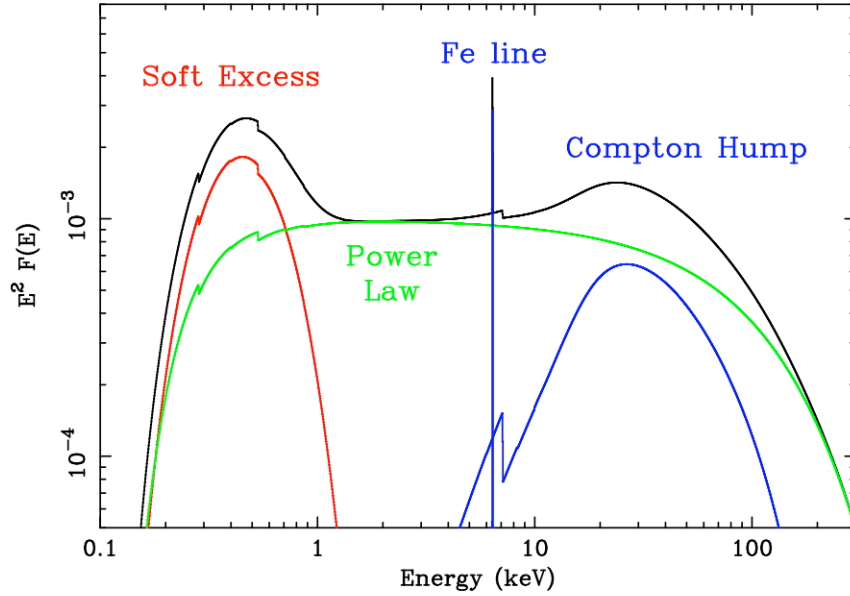


Figure 1.3: Shown are the different components of an X-ray spectrum of an AGN. These components include a power law (green), the soft excess (red), an iron line (blue delta function), and the Compton reflection hump (blue curve). The black curve is the sum of these components and what we observe in AGNs. Figure credit: Fabian (2006).

The Power Law Component

The power law component is believed to originate from the hot corona of the accretion disc. The photons from the accretion disc are up-scattered through interactions with the electrons in the corona. In general, the power law, in units of photons per unit area per unit time, is represented by the equation $N(E) \propto E^{-\Gamma}$, where Γ is the photon index. The photon index is also related to α , the spectral index, where $\Gamma = \alpha + 1$, so that the flux per unit area per unit time can be represented as $F(E) \propto E^{-\alpha}$. The canonical value for Γ observed in AGNs is $\sim 1.7 - 2.0$, but steeper spectra of Γ up to ~ 2.5 are observed in PG QSOs (e.g., Piconcelli et al. 2005; Porquet et al. 2004) and narrow line Seyfert 1 galaxies (e.g., Gallo et al. 2004; Grupe et al. 2007).

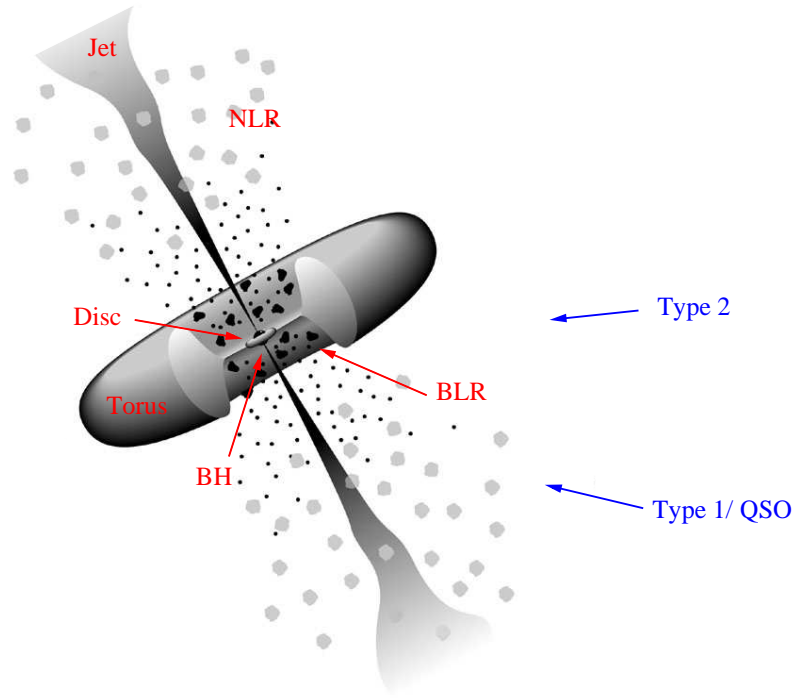


Figure 1.4: The figure is a schematic of the unified AGN model. At the center is the supermassive black hole (BH) surrounded by an accretion disc which is the origin of the power law component and possibly the soft excess. Depending on the orientation of the observer, a Type 1 (unobscured) or Type 2 (obscured) AGN is seen. The obscuration is due to the optically thick dusty torus surrounding the black hole on a parsec scale. The reflection component of the X-ray spectrum arises from the far side of the torus and the accretion disc. In the optical, the narrow and broad line regions (NLR and BLR, respectively) are the origins of the differences between Seyfert 1 and Seyfert 2 galaxies. While Seyfert 1 galaxies have both broad and narrow emission lines, Seyfert 2 galaxies do not. A subclass of Seyfert 1 galaxies called narrow line Seyfert 1 galaxies (NLS1s) also lack broad emission lines. Figure adapted from http://nedwww.ipac.caltech.edu/level5/March04/Torres/Torres2_4.html.

The Soft Excess

Another component generally seen in AGN spectra is the soft excess. As its name suggests, this is an excess of emission above the power law model at below ~ 2 keV. The soft excess is observed in both quasars and Seyfert galaxies and can be described by a blackbody with a temperature around 0.1 keV. The value for the temperature appears to be too hot to be simply due to thermal emission from the accretion disc.

The characteristic blackbody luminosity of an accretion disc is

$$L_{disc} = A_{disc} \sigma T_{disc}^4, \quad (1.1)$$

where L_{disc} is the luminosity of the disc, A_{disc} the surface area of the emitting region characterized by the inner radius of the disc, σ is the Stefan-Boltzmann constant, and T_{disc} the corresponding characteristic blackbody temperature. The temperature of the disc is radially dependent. However, since the disc radiates the gravitational energy gained from accretion as a blackbody, then $T(R) \propto R^{-3/4}$. Thus, the temperature of the disc, and therefore its luminosity, is dominated by radiation from the innermost edge of the accretion disc. Relating the disc luminosity to the Eddington luminosity (L_{Edd}) and the accretion rate of the AGN, we find that

$$T_{disc} \propto \left[\frac{L_{disc}}{L_{Edd}} \right]^{1/4} \left[\frac{M_{BH}}{M_{\odot}} \right]^{-1/4}, \quad (1.2)$$

where M_{BH} is the mass of the central black hole. Assuming accretion at the Eddington rate, the masses of the supermassive black holes at the center of these galaxies ($M_{BH} \sim 10^8 M_{\odot}$) imply that the blackbody temperature should peak at ~ 1 eV, in the ultraviolet regime of the electromagnetic spectrum.

The origin of the soft excess is still under debate. Possible origin of the soft excess include the inner accretion disc where the extreme ultraviolet photons are Compton up-scattered to form the soft excess (note that the speed and hence the Compton temperature scales as $\sqrt{M/R}$ and are largely independent of the black hole mass; Porquet et al. 2004), blurred reflection where the photoionized emission is relativistically blurred by motion in an accretion disc (Crummy et al. 2006), complex absorption (Sobolewska & Done 2007), and circumnuclear star formation. The origin of the soft excess is further discussed in Chapter 5.

The Reflection Component

A third component of an AGN spectrum can come from reflection. In this case, a portion of the direct emission may be reflected into our line of sight by obscuring material on the far side of the black hole. Iron emission lines and a Compton reflection hump due to Compton down-scattering are observed in a reflection-dominated spectrum. As shown in Figure 1.3, the Compton hump dominates at energies above 10 keV.

Typically, in the X-ray spectra of AGNs, we detect iron emission lines due to cold neutral iron (6.4 keV or Fe $K\alpha$, 7.05 keV or Fe $K\beta$), Fe XXV (6.67 keV), and Fe XXV (6.97 keV). The first set of lines is due to fluorescence in which a high energy photon is absorbed and results in the release of a lower energy photon. In the case of the iron atom, an electron in the inner most level (the K shell) is given enough energy from the absorbed photon and leaves the atom. Then an electron from the L-shell of the atom is dropped into the K-shell, releasing a $K\alpha$ photon. Similarly, a $K\beta$ photon is released if an electron from the M-shell of the atom drops two levels to the K-shell. While fluorescence can occur in any atom, we preferentially detect iron fluorescence lines due to its high fluorescence yield and relatively high cosmic abundance. The latter two lines are due to ionized iron. These lines are from reflection off ionized material.

Effects of Absorption

The interstellar medium of the host galaxies, and even our own Galaxy, can affect the observed X-ray spectrum. The effect is more prominent at softer X-ray energies because photoelectric absorption is dominated by bound-free and free-free processes which scale as ν^{-3} for individual transitions (Rybicki & Lightman 1979). Figure 1.5 explores how obscuration changes the observed power law spectrum. Assuming that

the X-ray continuum of the AGN spectrum is only a power law, increasing absorption reduces both the total flux as well as the number of counts in the soft X-ray band. The hardness ratio, defined as

$$HR = \frac{H - S}{H + S}, \quad (1.3)$$

where H is the number of counts in the hard (2–8 keV) band and S is the number of counts in the soft (0.5–2 keV) band, can be used to measure the changes in the slope of the spectrum. As demonstrated in Figure 1.5, the higher the absorption, the harder (higher hardness ratio) the spectrum becomes. Using the number of detected counts as calibration, the hardness ratio can be used to estimate the flux of sources where there are too few counts for spectral fitting. This is discussed further in Chapter 2. It is also of note that at column densities above $\sim 10^{24} \text{ cm}^{-2}$, scattering both in and out of the line of sight become important and the spectrum can no longer be modeled as a simple absorption spectrum.

The X-ray broad-band spectra of AGNs may also show absorption edges, typically near 0.7 keV (e.g., George et al. 1998; Reynolds 1997). These “warm” absorbers, mainly due to O VII and O VIII ions, are thought to be photoionized material from outflows with typical radial velocities of a few thousand km s^{-1} (McKernan et al. 2007). The absorbers can be complex, with multiple components having varying ionization states, column densities, and velocities (e.g., Holczer et al. 2010). These features are commonly found in both Seyferts and PG QSOs (e.g., Costantini et al. 2007; George et al. 1998). Absorption edges in PG QSO spectra are further discussed in Chapter 6.

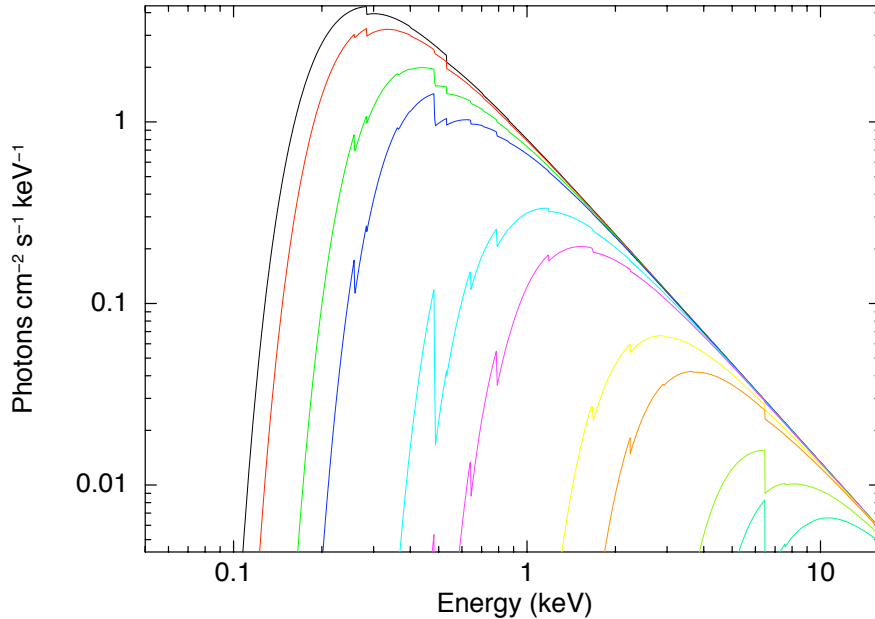


Figure 1.5: The figure shows the effects of absorption on the shape of the X-ray power law spectrum of an AGN. The power law model is a redshifted spectrum with $z = 0.1$ and $\Gamma = 1.8$. Galactic absorption is assumed to be at $2 \times 10^{20} \text{ cm}^{-2}$. From top, each curve represents intrinsic source absorption of $0, 1 \times 10^{20}, 5 \times 10^{20}, 1 \times 10^{21}, 5 \times 10^{21}, 1 \times 10^{22}, 5 \times 10^{22}, 1 \times 10^{23}, 5 \times 10^{23}, 1 \times 10^{24} \text{ cm}^{-2}$. Absorption both reduces the intensity of the source and the detected photon counts in the 0.5–2 keV band.

1.3 An Overview of X-ray Instrumentation

The data presented in this thesis are archival and new observations obtained by three X-ray observatories currently in operation. Each telescope has its unique capabilities and these are described in detail in the following sections. Table 1.1 is a comparison of some of the basic characteristics of the instruments used in this thesis.

1.3.1 *Chandra X-ray Observatory*

A majority of the observations, particularly those in Chapters 2, 3, and 5, analyzed in this thesis come from the *Chandra X-ray Observatory*. *Chandra* was launched in July of 1999 as the third mission in NASA’s Great Observatories program. Unlike optical telescopes, *Chandra* utilizes a nested mirror assembly of four paraboloid-hyperboloid grazing-incidence X-ray mirror pairs, or the High Resolution Mirror Assembly (HRMA). The largest of these iridium-coated mirror pairs has a diameter of 1.2 meters. *Chandra* has excellent spatial resolution, with the half-power diameter of the point spread function at $< 0''.5$.

There are four instruments on board *Chandra*. Two of these are focal-plane science instruments — the High Resolution Camera (HRC) and the Advanced CCD Imaging Spectrometer (ACIS). At the option of the observer, these instruments can be used in conjunction with one of the two objective transmission gratings — the High Energy Transmission Grating (HETG) and the Low Energy Transmission Grating (LETG).

Without the grating instruments, ACIS is capable of obtaining high-resolution images and moderate resolution spectra simultaneously. It consists of two different CCD arrays. ACIS-I is a 2×2 array of four CCDs and ACIS-S is a 1×6 array of six CCDs. Two of the ten CCDs are back-illuminated (BI) chips which have better quantum efficiency at lower energies than the eight front-illuminated (FI) chips. The nominal aimpoints of the ACIS instrument are located in the BI chips, I3 and S3. Figure 1.6 is an illustration of the ACIS focal plane. A build-up of contaminants on the optical blocking filters has degraded the low energy response of ACIS. This time-dependent effect is corrected for when the data is calibrated during processing. The effective energy range of ACIS is 0.1–10.0 keV. All of the *Chandra* observations

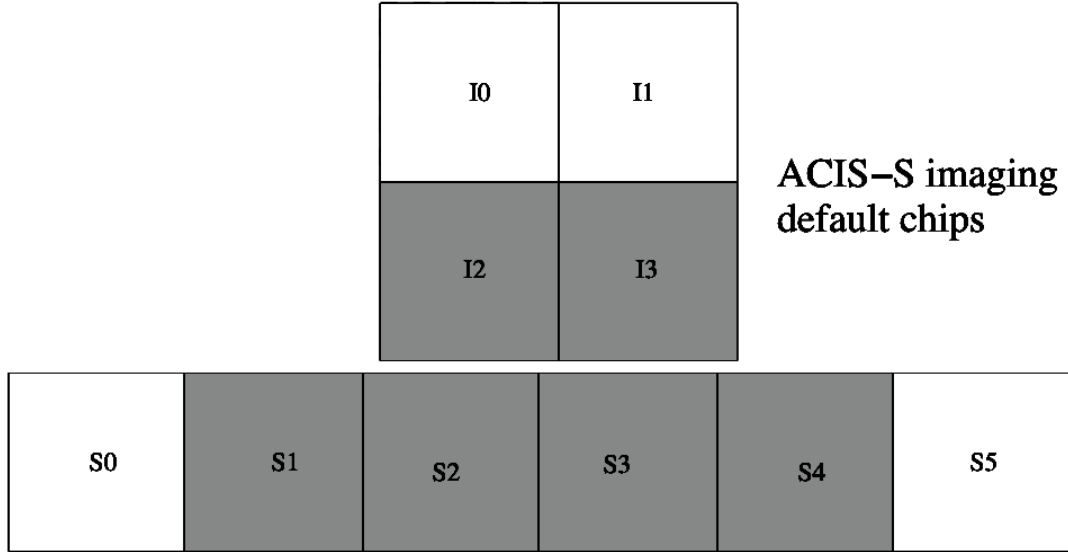


Figure 1.6: A schematic of the ACIS focal-plane. I0–I3 are the ACIS-I array and S0–S5 are the ACIS-S array. The two BI chips are I3 and S3. The nominal aimpoint of the ACIS-S array is in S3. Only six of the chips can be used at any time for observations and the shaded chips are the default configuration for ACIS-S imaging. Image credit: the *Chandra* Proposers’ Observatory Guide.

presented in this thesis were obtained using ACIS-S without grating and with the target of interest at the nominal aimpoint.

1.3.2 *XMM-Newton Observatory*

Some of the data in Chapters 2 and 4, and a large portion of the data in Chapter 5, were obtained using *XMM-Newton*, or the *X-ray Multi-Mirror Mission*. The telescope was launched in December of 1999 as part of the European Space Agency’s Horizon 2000 program. Unlike the *Chandra* mirrors, the *XMM-Newton* mirrors are coated with gold. There are three co-aligned instruments on board *XMM-Newton* — the European Photon-Imaging Camera (EPIC), the Reflection Grating Spectrometer (RGS), and the Optical Monitor (OM). We will focus on the EPIC camera here, as it is the main instrument with which the data were obtained.

The EPIC field of view is 30’ and the full-width at half maximum of the point

Comparison of focal plane organisation of EPIC MOS and pn cameras

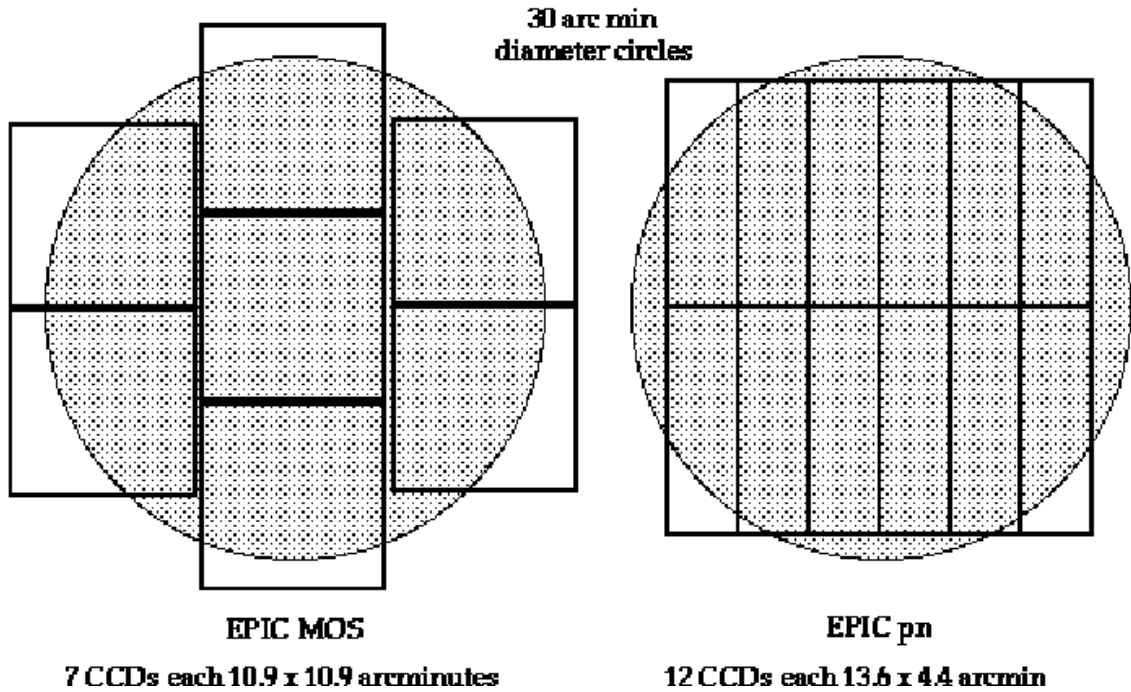


Figure 1.7: A sketch of the EPIC-MOS and -pn CCD configurations. This image was obtained from the *XMM-Newton* User's Guide.

spread function is $6''$. The effective energy range of the EPIC detectors is 0.15–15 keV. EPIC consists of three CCD arrays capable of simultaneous, moderate resolution spectroscopy and photometry. The EPIC-pn array consists of 12 CCD chips and the two EPIC-MOS arrays each has seven CCD chips. A schematic of the EPIC detectors is presented in Figure 1.7. The EPIC-pn array is located slightly off-axis so that the nominal aimpoint does not fall on a chip gap.

XMM-Newton is complementary to *Chandra* in a couple of ways. While *Chandra* has great spatial resolution, the larger collecting area of *XMM-Newton* (1550 cm^2 for EPIC over 555 cm^2 for ACIS-S at 1 keV) is advantageous when observing faint sources. However, there is a trade off where the EPIC chips also have higher background counts than the ACIS detectors. The spectral resolution of the EPIC detectors at the energy of the all-important Fe $K\alpha$ line ($\sim 6.4 \text{ keV}$) is also better than that of ACIS-S ($\sim 150 \text{ eV}$ versus $\sim 200 \text{ eV}$).

Table 1.1. A Comparison of X-ray Detectors

	<i>Chandra</i> ACIS-S	<i>XMM-Newton</i> EPIC	<i>Suzaku</i> XIS	<i>Suzaku</i> HXD
Energy Range	0.1–8 keV	0.15–10 keV	0.2–12 keV	10–600 keV
Field of View	8.3'×50.6'	30'×30'	19'×19'	0.56°×0.56° <100 keV 4.6°×4.6° >100 keV
Effective Area [cm ²]	555 at 1 keV	1550 at 1 keV	500 at 1 keV	160 at 15 keV
Spatial Resolution	0'5	6''	1.8'	...

1.3.3 *Suzaku X-ray Observatory*

Chapter 4 of this thesis uses data obtained by the *Suzaku X-ray Observatory*. Formerly known as Astro-E2, *Suzaku* was launched in July of 2005 by the Japanese Space Exploration Agency in conjunction with NASA. The effective energy range of the instruments on board is 0.2–600 keV. The telescope has two operating detectors, the X-ray Imaging Spectrometer (XIS) which is sensitive in the range of 0.2–12 keV, and the Hard X-ray Detector (HXD) which is sensitive in the 10–600 keV energy range. The telescope is able to obtain simultaneous XIS and HXD spectra.

The XIS consists of four co-aligned X-ray telescopes that focus onto four separate CCDs, each with a 19' field of view. The HXD, a non-imaging instrument, is comprised of two different types of detectors. The first is the HXD/PIN, which is made up of silicon diodes sensitive at below ~ 50 keV. The second is the HXD/GSO composed of well-type phoswich counters sensitive at above 50 keV. At below 100 keV, the HXD field of view is 0.56° and at above 100 keV, the HXD field of view is 4.6°. Therefore, source confusion is an issue for the HXD in crowded fields.

1.3.4 Spectral Analysis

As mentioned in the above section, the detectors for modern-day X-ray astronomy are mainly CCDs. At X-ray energies, the count rates are very low. Typical strong X-ray sources have count rates below one count per second. Thus, detectors can record the position, arrival time, and energy of each incident photon which means CCD observations can simultaneously image and perform spectroscopy on each object.

From the image, we select regions for both the source and the background in order to extract spectra for analysis. The spectra are raw number of counts in detector channels which are then converted into flux per detector channel by folding in the response functions of the telescope and detector. Instead of deconvolving the response from the observed spectrum to obtain the true source spectrum, the model spectrum (e.g., a power law) is folded into the response and then adjusted to match the observed spectrum. This is the method employed by the standard X-ray analysis software, XSPEC (Arnaud 1996).

The XSPEC fitting algorithm uses initial model parameters provided by the user and modifies these parameters iteratively until it finds a minimum in statistics space. Once the best fit is achieved, then a similar procedure is followed to calculate the errors for each free model parameter that corresponds to a user specified confidence range. Typically, for X-ray astronomy, this is set at the 90% confidence level, or $\Delta\chi^2 = \Delta \text{C-stat} = 2.71$ for one degree of freedom.

As has already been alluded to, there are two types of fitting statistics available in XSPEC — χ^2 and Cash (Cash 1979). Both of these statistics are used to determine the goodness of fit in this thesis. The more familiar χ^2 method is applicable for Gaussian statistics. This is used for the relatively strong sources in our samples where there are enough counts so that their spectra can be binned to at least 15

counts per bin and have enough bins for a meaningful modeling. The XSPEC implementation of χ^2 statistics is such that

$$\chi^2 = \sum_i \frac{(N_i - M_i)^2}{\sigma_i^2}, \quad (1.4)$$

where N_i is the number of observed counts in bin i , M_i is the number of model counts in bin i , and σ_i is the error associated with each bin. To determine the goodness of fit, the reduced χ^2 (χ^2_ν) is calculated by dividing the χ^2 value by the number of degrees of freedom. A best fit is indicated by $\chi^2_\nu \sim 1$. If the value is much higher than unity, then the model is a poor description of the data; however, $\chi^2_\nu \ll 1$ implies that the errors are over-estimated.

For spectra that do not have enough counts for χ^2 statistics, Cash-statistics is applied. The XSPEC implementation of this method is a slightly modified version of the original. The XSPEC definition of Cash-statistics is

$$C = 2 \sum_i [M_i - D_i + D_i(\log D_i - \log M_i)], \quad (1.5)$$

where M_i is the model of the sum of the background and source counts in each bin and D_i is the observed counts in bin i . The XSPEC implementation of this method was developed for unbinned spectra with no background subtraction. This is because in Gaussian statistics, the difference of two Gaussian distributions remains Gaussian. This is not the case for low-count, Poisson statistics for which Cash-statistics were developed. Separating the background contribution from the source spectrum requires a different approach. The background spectrum is first modeled separately; then the background model is added to the source model to fit the total observed spectrum using Cash-statistics. The XSPEC output of C-stat can be used to determine goodness of fit.

1.4 The Structure of this Dissertation

This dissertation seeks to understand the nature of U/LIRGs through X-ray observations and explore their possible evolutionary connection with quasars. Recent large surveys in other wavelengths, particularly those in the infrared (e.g., Armus et al. 2007; Farrah et al. 2007; Veilleux et al. 2009b), have demonstrated that the infrared luminosity of U/LIRGs can be attributed to both the starburst and nuclear activity. The high signal-to-noise spectra from the aforementioned papers reveal that nuclear activity contribute $\sim 40\%$ of the bolometric luminosity of U/LIRGs but to almost all of the bolometric luminosity of quasars. The infrared results suggest increasing AGN contribution with increasing infrared luminosity and merger stage. However, there is uncertainty in the measurement of the AGN contribution, depending on the method used to decompose the AGN signature from that of the starburst (Veilleux et al. 2009b). In addition, obscuration can mask AGN signatures even in the infrared. Therefore, it is crucial to perform complementary X-ray studies since X-ray is less likely to be affected by dust. The X-ray survey results could confirm those seen in the infrared.

Chapters 2, 3, and 4 are comprised of a statistical analysis of the presence of active nuclei in U/LIRGs. Snapshot X-ray surveys on U/LIRGs are performed in order to answer the question of what fraction of U/LIRGs contains X-ray selected AGNs. In Chapter 2, we develop a method for estimating the AGN contribution in low-count sources. The *XMM-Newton* follow-up observation in Chapter 3 shows that the method presented in Chapter 2 is effective in distinguishing buried AGNs. Chapter 4 is the application of the hardness ratio method on a large sample of U/LIRGs from the Revised Bright Galaxy Survey (RBGS; Sanders et al. 2003). Chapter 5 is a search for obscured AGNs in five well-studied local U/LIRGs, utilizing

the unprecedented sensitivity of *Suzaku* at above 15 keV. Chapter 6 looks at the X-ray properties of a large sample of U/LIRGs and PG QSOs in order to assess whether there is an evolutionary connection between the two classes of objects. We will compare the X-ray results with those obtained at other wavelengths in order to determine whether there is a relationship between the level of nuclear activity and the optical spectral type, infrared luminosity, color temperature, or merger stage. We will test the Sanders et al. (1988a) evolutionary scenario where the starburst-to-AGN ratio and the intrinsic column density of a U/LIRG decrease as the merger proceeds and the optical quasar emerges from its dusty cocoon. Finally, Chapter 7 summarizes the major results of this thesis and presents some possibilities for future work.

Chapter 2

Chandra Pilot Study

2.1 Introduction

Previous studies of X-ray emission from ULIRGs have been made by Ptak et al. (2003) with *Chandra* and Franceschini et al. (2003) with *XMM-Newton*. The Ptak et al. (2003) sample is a volume limited sample in which the redshifts of the galaxies do not exceed 0.045. Franceschini et al. (2003) selected their sample from the 15 ULIRGs observed by Genzel et al. (1998) which included only the brightest nearby ULIRGs and only one ULIRG with redshift greater than 0.082. Our sample encompasses ULIRGs with greater redshifts ($0.043 \leq z \leq 0.163$), and is selected to cover uniformly the *IRAS* color-luminosity plane.

The organization of this Chapter is as follows: § 2.2 discusses the sample selection, § 2.3 the observations and data reduction, § 2.4 the analysis and results concerning X-ray structure and spectra, § 2.5 a discussion of some astrophysical consequences, and § 2.6 a summary of our conclusions. We will assume $H_0 = 75 \text{ km s}^{-1} \text{ Mpc}^{-1}$, $q_0 = 0$ throughout this section.

2.2 Sample Selection

The “1-Jy sample” of ULIRGs comprises of 128 *IRAS* galaxies with the following criteria: fluxes at 60 μm exceeding 1 Jy, $L_{IR} > 10^{12} L_{\odot}$, galactic latitude $|b| > 30^{\circ}$, $f(60 \mu\text{m}) > f(12 \mu\text{m})$ (to avoid stars), *IRAS* color $\log[f(60 \mu\text{m})/f(100 \mu\text{m})] > -0.3$, and redshift $0 < z < 0.28$ (e.g., Kim & Sanders 1998; Kim et al. 2002; Veilleux et al. 1999a, 2002, 1999b). As part of our sample, we selected 13 galaxies from the 1-Jy sample. Also observed were F17208-0014 and F23365+3604 which satisfy all the criteria except the galactic latitude one (they have $|b| < 30^{\circ}$), and F15250+3609 which meets all the criteria except, marginally, the luminosity one (it has $L_{IR} = 10^{11.99} L_{\odot}$).

The galaxies were selected to cover the full range in the key parameters L_{IR} and $f(25 \mu\text{m})/f(60 \mu\text{m})$. Specifically, we have chosen galaxies that are approximately equally distributed over L_{IR} and $f(25 \mu\text{m})/f(60 \mu\text{m})$ in the following 4 bins: $\log[L_{IR}/L_{\odot}] < 12.3$, $\log[L_{IR}/L_{\odot}] > 12.3$, $f(25 \mu\text{m})/f(60 \mu\text{m}) < 0.2$ (“cool” ULIRGs), and $f(25 \mu\text{m})/f(60 \mu\text{m}) > 0.2$ (“warm” ULIRGs). The sample size of 16 galaxies is large enough to adequately sample the range of infrared luminosities and infrared colors that characterize the class of ULIRGs.

Of these 16 galaxies, only 14 were scheduled to be observed with *Chandra*. Figure 2.1 depicts the distribution of the entire 1-Jy sample in the $\log[f(25 \mu\text{m})/f(60 \mu\text{m})]$ versus $\log(L_{IR}/L_{\odot})$ plane. Also indicated are those galaxies in the 1-Jy sample which have been previously observed with *Chandra* (Ptak et al. 2003), the 14 galaxies observed by us with *Chandra*, and those observed by Franceschini et al. (2003) with *XMM-Newton*. It is notable that previous *Chandra* observations have focused preferentially on ULIRGs with low infrared luminosities [$\log(L_{IR}/L_{\odot}) < 12.3$], whereas our sample contains equal numbers of objects below and above $10^{12.3} L_{\odot}$. Fur-

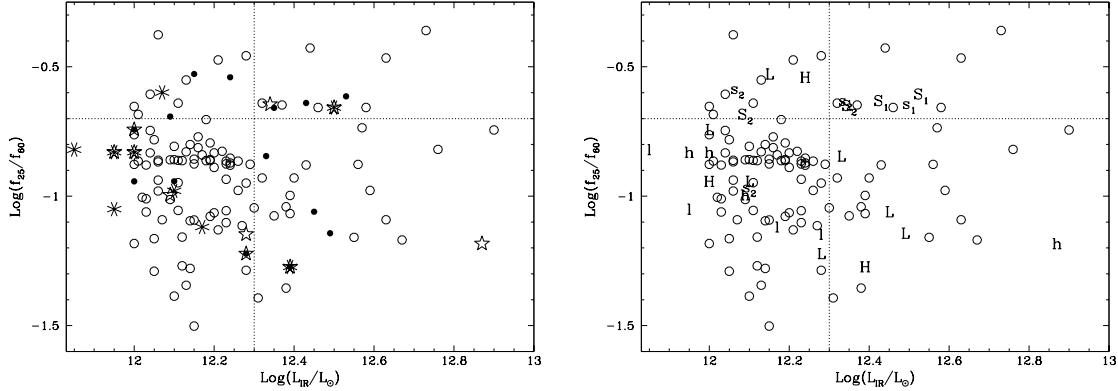


Figure 2.1: A plot of the logarithm of the *IRAS* flux ratio $f(25 \mu\text{m})/f(60 \mu\text{m})$ against the logarithm of L_{IR} for the 1-Jy sample. In the left panel, asterisks represent objects observed with *Chandra* by Ptak et al. (2003), stars represent objects observed with *XMM-Newton* by Franceschini et al. (2003), and filled circles represent objects in our sample, observed with *Chandra* and reported in this paper. Note that a few objects have been observed by two or more groups. The right panel shows the distribution of optical spectral types of ULIRGs observed by *Chandra* and *XMM-Newton*. The upper case letters represent the spectral types of our sample while the lower case letters represent the spectral types of the Ptak et al. and Franceschini et al. samples (S_1 , S_2 = type 1 and 2 Seyferts, H = H II galaxies, and L = LINERs). The four quadrants are the four parameter bins described in § 2.2. Open circles in both panels show the remaining ULIRGs in the *IRAS* 1-Jy sample.

thermore, our sample contains approximately equal numbers in each of the four quadrants of Figure 2.1. This distribution allows us to test whether objects with certain infrared colors and luminosities are powered preferentially by stars or by AGNs. It is notable that essentially all objects in our sample are classified as ongoing or old mergers based on a comparison between the optical/near-infrared images and published numerical simulations of galaxy interactions (Veilleux et al. 2002).

Table 2.1. Some Properties of the Sample and the *Chandra* Observations^a

Source Name ^b	z	$\log_{10}(\frac{L_{\text{IR}}}{L_{\odot}})$	$\log_{10}(\frac{f_{25\mu\text{m}}}{f_{60\mu\text{m}}})$	Spectral Type	In 1-Jy Sample?	Observation Date	Exposure ^c (ks)
F00188-0856	0.128	12.33	-0.85	LINER	Yes	2003 Sep 4	9.80
F01004-2237	0.118	12.24	-0.54	H II galaxy	Yes	2003 Aug 3	9.40
F01572+0009	0.163	12.53	-0.61	Seyfert 1	Yes	2003 Aug 26	10.60
Z03521+0028	0.152	12.45	-1.06	LINER	Yes	2002 Dec 25	7.20
F04103-2838	0.118	12.15	-0.53	LINER	Yes	2003 Apr 28	10.00
F10190+1322	0.077	12.00	-0.94	H II galaxy	Yes	2003 Jan 31	9.40
Z11598-0112	0.151	12.43	-0.64	Seyfert 1	Yes	2003 Apr 13	10.20
F12072-0444	0.129	12.35	-0.66	Seyfert 2	Yes	2003 Feb 1	9.20
F12112+0305	0.073	12.28	-1.22	LINER	Yes	2003 Apr 15	10.00
F15130-1958	0.109	12.09	-0.69	Seyfert 2	Yes	2003 Jun 2	9.80
F15250+3609 ^d	0.055	11.99	-0.74	LINER	No	2003 Aug 27	9.20
F16090-0139	0.134	12.49	-1.14	LINER	Yes	2003 Feb 10	9.80
F17208-0014 ^e	0.043	12.39	-1.27	H II galaxy	No	2003 May 7	8.60
F23365+3604 ^d	0.064	12.10	-0.94	LINER	No	2003 Feb 3	10.20

^aRedshift and IR luminosity are taken from Kim et al. (2002), unless otherwise noted. Spectral types are taken from Veilleux et al. (1999a) and references therein, unless otherwise noted.

^bAll source names should be preceded by IRAS.

^cTotal good time interval after dead-time corrections.

^dRedshift, IR luminosity, and spectral type are taken from Surace et al. (2000) and references therein.

^eRedshift, IR luminosity, and spectral type are taken from Veilleux et al. (1999b).

2.3 Observations and Data Reduction

The 14 galaxies were observed between December 2002 and September 2003. Each galaxy was observed in a single exposure using the ACIS S3 CCD chip with the standard frame time of 3.2 seconds. Total exposure times, actual dates of observations, and some properties of the sources are summarized in Table 2.1.

Most of the data reduction and analysis was done using CIAO v2.3 with CALDB 2.23 and XSPEC v11.2. Only a comparison of the radial profiles of two sources with models of the point spread function (PSF) was done using CIAO v3.0.2 and CALDB 2.25. The effects of the CIAO and calibration updates since v2.3 are negligible for CCD resolution observations of our sources due to the low signal-to-noise ratios. The data reduction followed the procedures outlined in the Science Analysis Threads for

ACIS data on the CIAO webpages ¹.

The position of each X-ray source was determined using the IDL routine CNTRD. The routine returns the X and Y positions of the centroid of a point source starting from user-provided initial guess positions. The R.A. and Dec were then determined using the ds9 software from SAO based on the X and Y output from CNTRD.

Nuclear spectra were extracted for the two bright X-Ray sources F01572+0009 and Z11598-0112 using the CIAO tool PSEXTRACT, which creates a source spectrum, a background spectrum, and associated response matrices. PSEXTRACT also bins output spectra to a specified minimum number of counts per bin. ACIS-ABS was then applied to correct for the degradation in the low energy response of the ACIS chips as a result of deposition of contaminants on the pre-CCD filter or the CCDs. We have ignored channels below 0.5 keV (where the instrumental calibration is uncertain) and above 8.0 keV (where there are few counts) in modeling the spectra. The data were binned to both at least 15 counts per bin and at least 3 counts per bin. The spectra were then modeled using the XSPEC package (§ 2.4.3). The 15 counts per bin spectra were modeled using χ^2 statistics, while the 3 counts per bin spectra were modeled in c-stat mode using Poissonian statistics. Although the c-stat fitting approach was devised for unbinned spectra, c-stat in XSPEC performs better if the data are binned to at least 1 count per bin. This ensures that there are no bins with zero counts or any mis-match between the source and background spectra. Therefore, the data were binned to 3 counts per bin for the c-stat mode. For the other 12 sources, hardness ratios were calculated using the counts in a soft energy band (0.5–2.0 keV) and a hard energy band (2.0–8.0 keV), using Equation 1.3. The hardness ratios were then compared with power law and MEKAL models, photoelectrically absorbed by an intervening column. This method

¹<http://cxc.harvard.edu/ciao/>.

provides estimates of the spectral parameters (§ 2.4.3). Due to the low number of counts from most of our galaxies, we cannot place meaningful constraints on more complex models.

2.4 Analysis and Results

Here, we compare the positions of the X-ray sources with the optical and near-infrared positions in § 2.4.1. Then we describe the X-ray structures in § 2.4.2. All 14 sources observed were detected with *Chandra*, but only two were bright enough for detailed spectral modeling to be performed. An analysis of the spectra of these two bright sources is presented in § 2.4.3, while those of the rest are discussed in § 2.4.3.

2.4.1 Astrometry

The positions of the X-ray peaks are offset from the infrared and optical peaks by typically $\lesssim 1''$, which is consistent with the errors of measurement in the three wavebands. Table 2.2 details the positions and offsets of each source.

2.4.2 X-Ray Structure

Two (F10190+1322 and F12112+0305) of the three sources in our sample that have double near-infrared and optical nuclei were found to have double X-ray nuclei. The X-ray separations of these nuclei agree to within $\simeq 1''$ of that of their infrared counterparts. Figure 2.2 shows X-ray grey scales of F10190+1322 and F12112+0305 with infrared and optical contours. The infrared and optical positions of the midpoints between the two nuclei were shifted to match those of the X-ray midpoints. The magnitude of the R.A. and Dec shift applied for F10190+1322 was $1''.2$ and $0''.6$,

Table 2.2. Astrometry of Our Sample^a

Source Name	RA		Dec		RA		Dec		ΔRA^b		ΔDec^b		ΔDec^b	
	X-Ray (h m s)	RA Opt. (h m s)	X-Ray ($^{\circ}$ ' '')	Dec Opt. ($^{\circ}$ ' '')	RA IR (h m s)	RA Opt. (h m s)	Dec IR ($^{\circ}$ ' '')	Dec Opt. ($^{\circ}$ ' '')	XR - Opt. ($''$)	XR - Opt. ($''$)	XR - IR ($''$)	XR - IR ($''$)	XR - IR ($''$)	ΔDec^b XR - IR ($''$)
F00188-0856	00 21 26.54	00 21 26.48	-08 39 25.9	-08 39 27.1	00 21 26.48	00 21 26.48	-08 39 27.1	-08 39 27.1	0.90	1.2	0.90	1.2	0.90	1.2
F01004-2237	01 02 49.99	01 02 49.92	-22 21 57.3	-22 21 57.0	01 02 49.94	01 02 49.94	-22 21 57.3	-22 21 57.3	1.05	-0.3	0.75	0.0	0.75	0.0
F01572+0009	01 59 50.26	01 59 50.22	+00 23 40.9	+00 23 40.6	01 59 50.23	01 59 50.23	+00 23 40.5	+00 23 40.5	0.60	0.3	0.45	0.4	0.45	0.4
Z03521+0028-E	03 54 42.22	03 54 42.23	+00 37 02.9	+00 37 02.4	03 54 42.25	03 54 42.25	+00 37 02.0	+00 37 02.0	-0.15	0.5	-0.45	0.9	-0.45	0.9
Z03521+0028-W	—	03 54 42.16	—	+00 37 02.4	03 54 42.15	03 54 42.15	+00 37 02.0	+00 37 02.0	—	—	—	—	—	—
F04103-2838	04 12 19.43	04 12 19.47	-28 30 25.0	-28 30 24.4	04 12 19.53	04 12 19.53	-28 30 24.4	-28 30 24.4	-0.60	-0.6	-1.50	-0.6	-1.50	-0.6
F10190+1322-E	10 21 42.73	10 21 42.85	+13 06 55.3	+13 06 55.3	10 21 42.81	10 21 42.81	+13 06 55.0	+13 06 55.0	-1.80	0.0	-1.20	0.3	-1.20	0.3
F10190+1322-W	10 21 42.48	10 21 42.55	+13 06 54.2	+13 06 53.1	10 21 42.56	10 21 42.56	+13 06 53.3	+13 06 53.3	-1.05	1.1	-1.20	0.9	-1.20	0.9
Z11598-0112	12 02 26.77	12 02 26.76	-01 29 15.4	-01 29 15.7	12 02 26.70	12 02 26.70	-01 29 15.8	-01 29 15.8	0.15	0.3	1.05	0.4	1.05	0.4
F12072-0444	12 09 45.15	12 09 45.12	-05 01 13.8	-05 01 13.9	12 09 45.12	12 09 45.12	-05 01 13.9	-05 01 13.9	0.45	0.1	0.45	0.1	0.45	0.1
F12112+0305-NE	12 13 46.06	12 13 46.11	+02 48 41.0	+02 48 42.4	12 13 46.07	12 13 46.07	+02 48 42.0	+02 48 42.0	-0.75	-1.4	-0.15	-1.0	-0.15	-1.0
F12112+0305-SW	12 13 45.97	12 13 45.92	+02 48 39.0	+02 48 39.4	12 13 45.97	12 13 45.97	+02 48 39.8	+02 48 39.8	0.75	-0.4	0.00	-0.8	0.00	-0.8
F15130-1958	15 15 55.20	15 15 55.16	-20 09 16.9	-20 09 17.0	15 15 55.16	15 15 55.16	-20 09 17.2	-20 09 17.2	0.60	0.1	0.60	0.3	0.60	0.3
F15250+3609 ^c	15 26 59.45	15 26 59.48	+35 58 37.1	+35 58 37.7	15 26 59.41	15 26 59.41	+35 58 37.3	+35 58 37.3	-0.45	-0.6	0.60	-0.2	0.60	-0.2
F16090-0139	16 11 40.43	16 11 40.42	-01 47 06.4	-01 47 06.5	16 11 40.42	16 11 40.42	-01 47 05.8	-01 47 05.8	0.15	0.1	0.15	-0.6	0.15	-0.6
F17208-0014 ^c	17 23 22.00	17 23 21.99	-00 16 59.8	-00 17 00.6	17 23 21.96	17 23 21.96	-00 17 00.8	-00 17 00.8	0.15	0.8	0.6	1.0	0.6	1.0
F23365+3604 ^c	23 39 01.30	23 39 01.25	+36 21 08.4	+36 21 09.1	23 39 01.27	23 39 01.27	+36 21 08.6	+36 21 08.6	0.75	-0.7	0.45	-0.2	0.45	-0.2

^aPositions are given in J2000 coordinates. X-ray positions are from this work. Unless otherwise noted, optical and IR positions are taken from Kim et al. (2002), who state that their typical positional error ($\simeq 2\sigma$) is estimated to be less than $0''.5$.

^b $\Delta\text{RA}(\lambda_1 - \lambda_2) = [\text{RA}(\lambda_1) - \text{RA}(\lambda_2)] \times [\text{Cos}[\text{Dec}(\lambda_1)] \times [15''/\text{ls}]]$. $\Delta\text{Dec}(\lambda_1 - \lambda_2) = \text{Dec}(\lambda_1) - \text{Dec}(\lambda_2)$.

^cThese sources are not part of the IRAS 1-Jy sample studied by Kim et al. (2002). Optical positions are taken from the USNO A2.0 Catalog. IR positions are taken from the 2MASS Point Source Catalog (PSC). Both catalogs are accessible through the Vizier Service at <http://vizier.u-strasbg.fr/viz-bin/VizieR>. The expected astrometric accuracy for stars in the USNO A2.0 Catalog is $0''.25$. The astrometric accuracy of the 2MASS PSC is $< 0''.2$.

respectively, in the infrared, and $1''.42$ and $0''.55$, respectively, in the optical. The R.A. and Dec shift applied for F12112+0305 was $0''.08$ and $0''.9$, respectively, in the infrared, and $0''.0$ and $0''.9$, respectively, in the optical. There is thus weak evidence that the X-ray peaks of F10190+1322 are offset from the infrared and optical peaks by a fraction of an arcsecond. The X-ray peaks of F12112+0305 are probably consistent with the locations of the infrared and optical peaks, after the small spatial shift has been applied. The linear separations of the two X-ray peaks for F10190+1322 and F12112+0305 are approximately 5.6 kpc and 3.7 kpc, respectively.

The X-ray emissions of the two bright sources F01572+0009 and Z11598-0112 are concentrated in the central regions of these galaxies. Figure 2.3 shows X-ray grey scale representations of these Seyfert 1 galaxies with infrared and optical contours superposed. The infrared and optical images have been shifted so that the infrared and optical peaks match the positions of the X-ray peaks. There is a suggestion of an E–W extension in F01572+0009 in the infrared and optical, as well as in the X-ray. The morphologies of the X-ray emission have been investigated by comparing the radial profiles of the X-ray sources with the PSF models in the standard calibration library. The X-ray spectra show that most of the observed flux from both of these bright sources is concentrated in the range of 0.5–2.0 keV. Therefore, we compared the azimuthally averaged radial profiles of these sources in this energy range with PSFs evaluated at 1.0 keV. This comparison (Figure 2.4) shows that the soft X-ray emission is unresolved or, at best, marginally resolved.

The remaining 10 sources appear to be unresolved, with the exceptions of F16090-0139 and F17208-0014. F16090-0139 appears to be extended in the NW–SE direction. Its linear extent is approximately 8.2 kpc ($3''.0$). F17208-0014 seems to be resolved with a linear diameter of approximately 5.2 kpc ($6''.2$). The upper limits to the linear sizes of the rest of the sources fall in the range of 0.5–6.3 kpc.

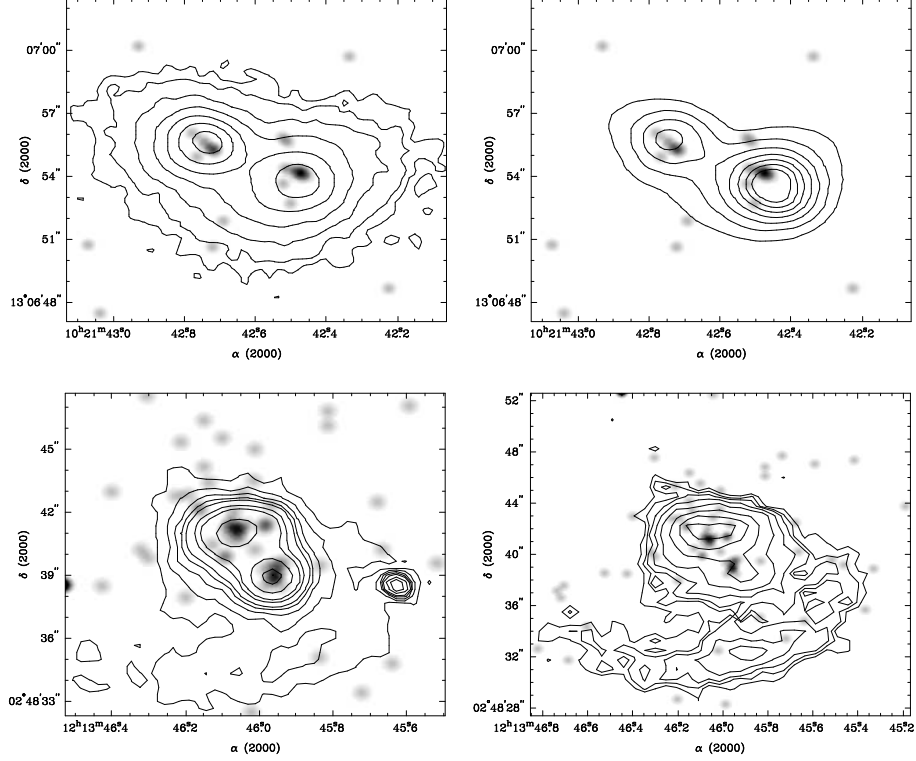


Figure 2.2: Linear grey scale representation of the X-ray emission from the double nuclei sources F10190+1322 (top) and F12112+0305 (bottom). The two left panels show X-rays as the grey scale with infrared K' band contours. The two right panels show X-rays as the grey scale with optical R band contours. The X-ray images have been smoothed to match the resolutions of the IR/optical images. The apparent “point sources” appearing on the edges of the F12112+0305 images are artifacts from the smoothing process; each of these bright “point sources” corresponds to only one count and is not a real X-ray source. The infrared and optical images are from Kim et al. (2002). The linear separations between the two X-ray peaks are 5.6 kpc for F10190+1322 and 3.7 kpc for F12112+0305.

2.4.3 X-Ray Spectra

The Bright Sources

It is not surprising that F01572+0009 and Z11598-0112 are bright X-ray sources: they are the only type 1 Seyferts in our sample. Using the 15 counts per bin data, one can use χ^2 statistics to evaluate models of the continuum emission of these sources. The spectra were first modeled with single power laws. Due to the high flux of the

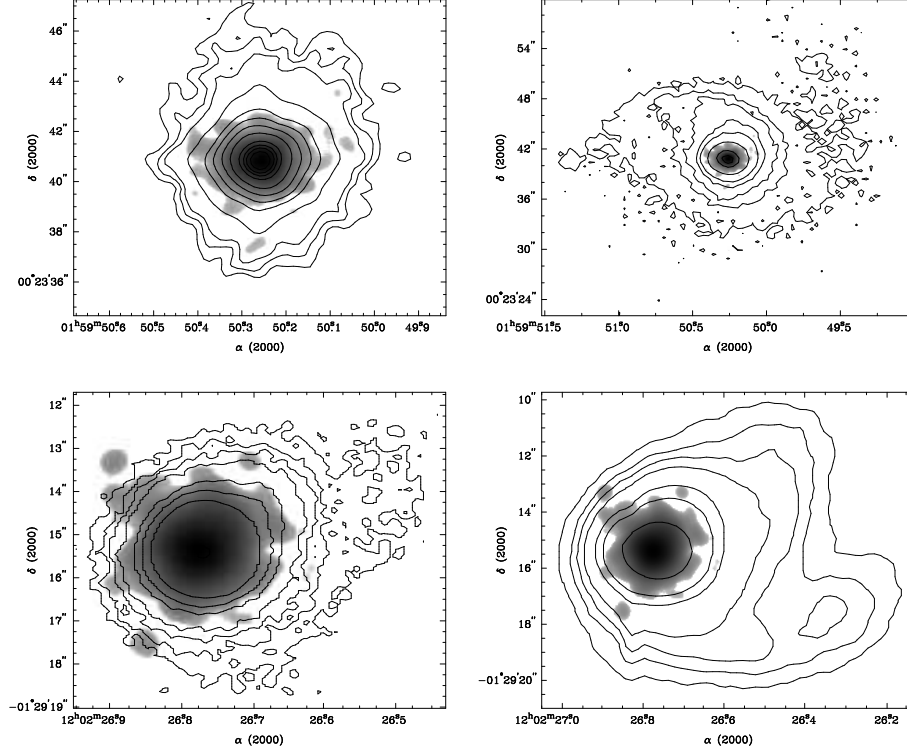


Figure 2.3: Logarithmic grey scale representations of the X-ray emission from the Seyfert 1 galaxies F01572+0009 (top) and Z11598-0112 (bottom). The left panels are X-ray grey scale with infrared K' band contours. The right panels are X-ray grey scale with optical R band contours. Note the difference in spatial scale between the left and right panels. The X-ray images have been smoothed to match the resolutions of the IR/optical images. The infrared and optical images are from Kim et al. (2002).

soft component and consequently the high signal-to-noise ratio in the soft energy bins, such single power law models underestimate the flux in the hard energy band of these bright sources. Therefore, a two component model was needed to describe the continuum spectra: a hard power law and a soft component represented by another power law or a MEKAL model were used. If most of the flux in the soft band is produced by starbursts, then the soft band flux could plausibly be represented by a MEKAL model (for a hot diffuse gas). The results of our modeling are listed in Table 2.3, and the spectrum and the double power law model of F01572+0009 are shown in Figure 2.5.

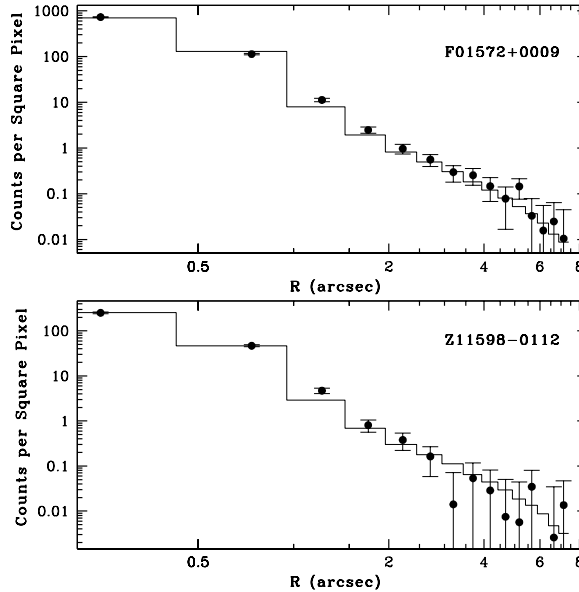


Figure 2.4: Comparison of model PSFs with observed radial profiles for the two bright sources. The x-axis is distance in arcseconds from the centroid of the emission while the y-axis is the surface brightness in counts per square pixel. The error bars are errors on the net counts per square pixel assuming Poissonian statistics. In each panel, the histogram is the model PSF obtained from the PSF library at 1.0 keV. The points are observed total counts with energy in the range of 0.5 to 2.0 keV. This diagram shows that the soft X-ray emissions from these two galaxies are unresolved or, at best, marginally resolved.

The 3 counts per bin data were used to determine if there are weak emission lines in the spectra. The continua of the data were first modeled using two power laws. The spectral indices from these fits are consistent with those obtained from binning the data to at least 15 counts per bin and using χ^2 statistics (see Table 2.3). This agreement indicates that binning the data to at least 3 counts per bin did not introduce any biases. The F01572+0009 spectrum shows an excess above the power law continuum at around 6.0 keV (Figure 2.5), but this suggestion of an emission line(s) is not significant. The spectrum of Z11598-0112 has a possible emission line at an energy consistent with redshifted Fe $K\alpha$ (Figure 2.6). We modeled the spectrum with a double power law as we had previously done with the 15 counts per

Table 2.3: Spectral Models for F01572+0009 & Z11598-0112^a

Source Name	Model	$N_H(\text{Galactic})^b$ (cm^{-2})	kT (keV)	Z^c (Z_\odot)	Γ^d	K^e	χ^2/dof
Spectra Binned to 15 Counts per Bin							
F01572+0009	PL	2.6×10^{20}	—	—	$\Gamma_1=2.4^{+0.1}_{-0.1}$	$K_{PL1}=7.3^{+0.2}_{-0.2} \times 10^{-4}$	175/132
	PL+PL	2.6×10^{20}	—	—	$\Gamma_1=2.6^{+0.1}_{-0.1}$	$K_{PL1}=6.8^{+0.3}_{-0.4} \times 10^{-4}$	142/131
	PL+MEKAL	2.6×10^{20}	$0.3^{+0.1}_{-0.1}$	1.0	$\Gamma_2=0.7^{+0.4}_{-0.5}$ $\Gamma_1=2.1^{+0.1}_{-0.1}$	$K_{PL2}=3.4^{+3.4}_{-1.9} \times 10^{-5}$ $K_{PL1}=6.2^{+0.3}_{-0.4} \times 10^{-4}$ $K_M=3.1^{+0.8}_{-0.8} \times 10^{-4}$	133/130
Z11598-0112	PL	2.3×10^{20}	—	—	$\Gamma_1=3.4^{+0.1}_{-0.1}$	$K_{PL1}=2.4^{+0.1}_{-0.1} \times 10^{-4}$	88/58
	PL+PL	2.3×10^{20}	—	—	$\Gamma_1=3.6^{+0.1}_{-0.1}$	$K_{PL1}=2.2^{+0.1}_{-0.1} \times 10^{-4}$	58/57
	PL+MEKAL	2.3×10^{20}	$0.3^{+0.1}_{-0.1}$	1.0	$\Gamma_2=0.2^{+0.3}_{-0.2}$ $\Gamma_1=2.5^{+0.3}_{-0.2}$	$K_{PL2}=7.6^{+10.4}_{-3.3} \times 10^{-6}$ $K_{PL1}=1.7^{+0.2}_{-0.2} \times 10^{-4}$ $K_M=2.7^{+0.6}_{-0.7} \times 10^{-4}$	60/56
Spectra Binned to 3 Counts per Bin							
F01572+0009	PL+PL	2.6×10^{20}	—	—	$\Gamma_1=2.6^{+0.8}_{-0.6}$	$K_{PL1}=7.1^{+2.6}_{-1.6} \times 10^{-4}$	260/252
					$\Gamma_2=0.5^{+0.3}_{-0.3}$	$K_{PL2}=3.1^{+1.8}_{-2.4} \times 10^{-5}$	
Z11598-0112	PL+PL+ZGAUSS	2.3×10^{20}	$7.0^{+0.1}_{-0.1}$	$1.0^{+1.2}_{-0.7}$	$\Gamma_1=3.5^{+0.7}_{-0.5}$	$K_{PL1}=2.3^{+0.1}_{-0.2} \times 10^{-4}$	171/129
					$\Gamma_2=1.0^{+0.5}_{-0.7}$	$K_{PL2}=1.5^{+1.5}_{-0.8} \times 10^{-5}$	
						$K_{\text{line}}=3.3^{+3.9}_{-2.4} \times 10^{-6}$	

^aAll errors are 90% confidence for each parameter. The models applied to the data are a single power law, double power law, and MEKAL plus a power law. All models assume absorption by the Galactic column. Unless otherwise mentioned, all models were applied to data in the energy range of 0.5–8.0 keV.

^bParameter fixed to the Galactic column, obtained from the CIAO observing toolkit accessible through <http://asc.harvard.edu/toolkit/colden.jsp>.

^cMetallicity fixed at solar.

^dThe photon index for the first power law (Γ_1) in the double power law model was determined using data in the soft band (0.5–2.0 keV). This value was kept fixed when fitting the double power law model to the data over the whole band (0.5–8.0 keV).

^eThe normalization of the power law models is $K_{PL} = \text{photons cm}^{-2} \text{ s}^{-1} \text{ keV}^{-1}$ at 1 keV. The normalization of the MEKAL thermal plasma model is $K_M = \frac{10^{-14}}{4\pi[D_A(1+z)]^2} \int n_e n_H dV$ where D_A is the angular size distance (cm), and n_e and n_H are the electron and hydrogen densities (cm^{-3}), respectively. The normalization of the ZGAUSS model is $K_{\text{line}} = \text{total photons cm}^{-2} \text{ s}^{-1}$ in the line.

^fThis is the energy of the line in the rest frame of the galaxy.

^gCash-statistics option in the XSPEC fitting package.

bin data. Then a narrow Gaussian feature was added to the continuum to represent the emission line. Using the c-stat statistics option in XSPEC, the best fit model suggests that the line is located at a rest energy of 7.0 keV with an equivalent width of $1.0^{+1.2}_{-0.7}$ keV (Table 2.3). Emission at 7 keV in the source frame would require the iron to be highly ionized. The photon indices for the soft and hard power laws are 3.47 and 0.99, respectively. Figure 2.6 shows the observed spectrum of Z11598-0112 together with the model components.

The significance of the line cannot be tested using the F-test because the test is only valid for Gaussian statistics. Therefore, simulated “fake” spectra, constructed in XSPEC, were used to determine the likelihood that the emission line seen in

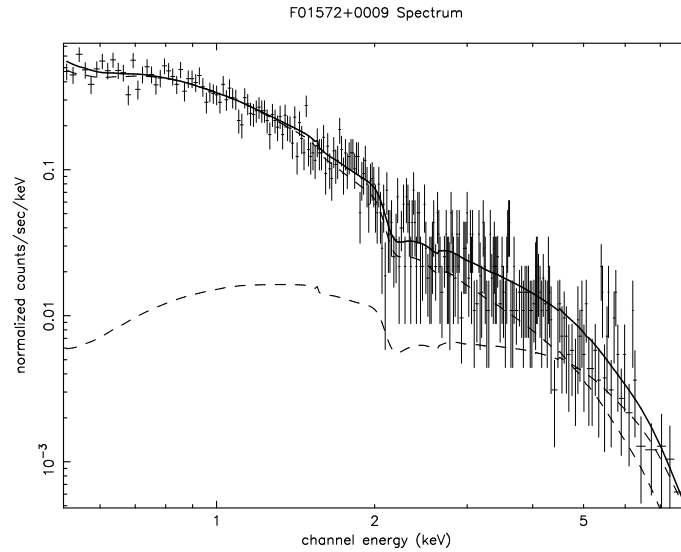


Figure 2.5: Spectrum of F01572+0009 with at least 3 counts per bin. The thick solid line is the double power law model, while the dashed lines are the two power law components of the model. There are hints of emission lines at around 6.0 keV, but the lines are not significant.

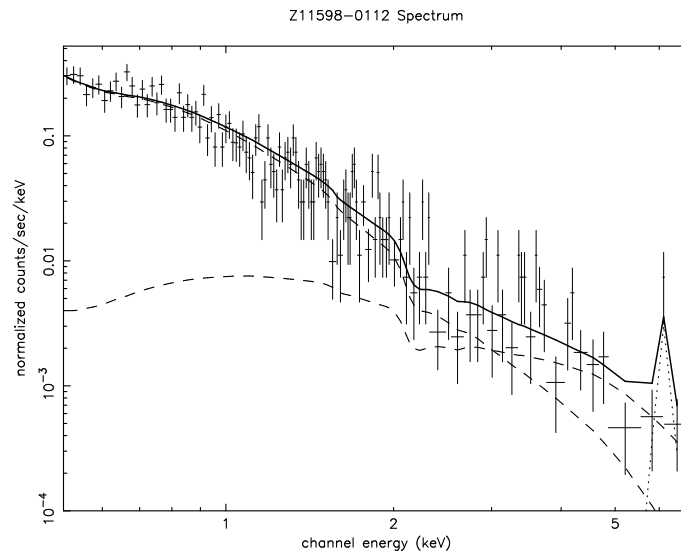


Figure 2.6: Spectrum of Z11598-0112, with at least 3 counts per bin. The thick solid line is the model, a combination of two power laws modeling the continuum (the dashed lines) and a narrow Gaussian modeling the emission feature (the dotted line).

Z11598-0112 is real. A set of 500 fake spectra were created using the FAKEIT command in XSPEC. The task uses the response matrices associated with the real spectra and the best-fit continuum model to create artificial source and background spectra. The simulated source and background spectra were also binned to at least 3 counts per bin. As a sanity check, we modeled the simulated spectra. The distribution of the photon indices in the 500 simulated spectra were consistent with the distribution of the photon indices for the observation of Z11598-0112, modeled with 3 counts per bin. Therefore, we are confident that binning the data to an arbitrary small number of counts per bin did not introduce any biases. We found that only 3 of the 500 spectra showed a flux at the energy of the line exceeding the measured line flux minus its error bar (a conservative measure of the line flux). Thus, the line is significant at above the 99% level.

It is also important to note that Z11598-0112 is considered to be a Narrow-Line Seyfert 1 (NLS1) galaxy whose $H\beta$ line width (FWHM) is 770 km s^{-1} , based on the data presented in Veilleux et al. (1999a). NLS1s tend to have steeper soft X-ray spectra than normal Seyfert 1 galaxies, as shown independently by *ASCA* observations analyzed by Leighly (1999) and Vaughan et al. (1999). Of the 24 NLS1's studied by Leighly (1999) and Vaughan et al. (1999), 79% have soft flux in excess of the power law model that fits the individual spectra at high energies; the excess flux dominates the spectra at energies $\lesssim 1.5 \text{ keV}$. The nominal power law photon indices of NLS1s over the 0.6–10 keV energy band span the range of 1.6–2.5, larger than normal Seyfert 1 galaxies (Vaughan et al. 1999). The X-ray spectral properties of Z11598-0112, in particular the steep soft X-ray spectrum and the flat hard X-ray spectrum, are consistent with a NLS1 classification.

The Faint Sources

Twelve of the fourteen galaxies that we have observed with *Chandra* do not have enough counts for the usual spectral modeling procedure. These sources have total counts in the 0.5–8.0 keV band ranging from 3 to 92. In order to determine the properties of these sources, we used hardness ratios (HR; defined in Equation 1.3) to estimate model parameters from XSPEC. The hardness ratios calculated from the data may then be compared with hardness ratios generated from models (such as a power law or a MEKAL) to determine the model parameters which describe the observations.

Two models were assumed – a single power law and a single temperature MEKAL. For a single power law, the photon index (Γ) was varied, while the temperature (kT) was varied in the MEKAL model. In both models, photoelectric absorption by cold gas was included. For each column density (N_H) and model parameter (Γ or kT) pair, XSPEC generated a model spectrum which was then multiplied by the effective area at each energy (obtained from the response matrices for the actual data) and sampled appropriately. The output was thus a model of the number of photons detected per second as a function of energy, which could be compared with the observation. These simulated data were then used to calculate the hardness ratio as a function of N_H and Γ or N_H and kT . One can then plot contours of constant hardness ratio on a diagram of N_H versus Γ (Figure 2.7) or N_H versus kT (Figure 2.8). In each panel of Figures 2.7 and 2.8, the middle curve represents the observed hardness ratio and the two other curves represent the observed hardness ratio plus and minus the error. We have made use of 1- σ values in Tables 1 and 2 of Gehrels (1986) to estimate the errors in our measurements. Numerical values of model parameters are listed in Table 2.4, and the footnotes describe how the errors in the hardness ratios, Γ , and kT were obtained.

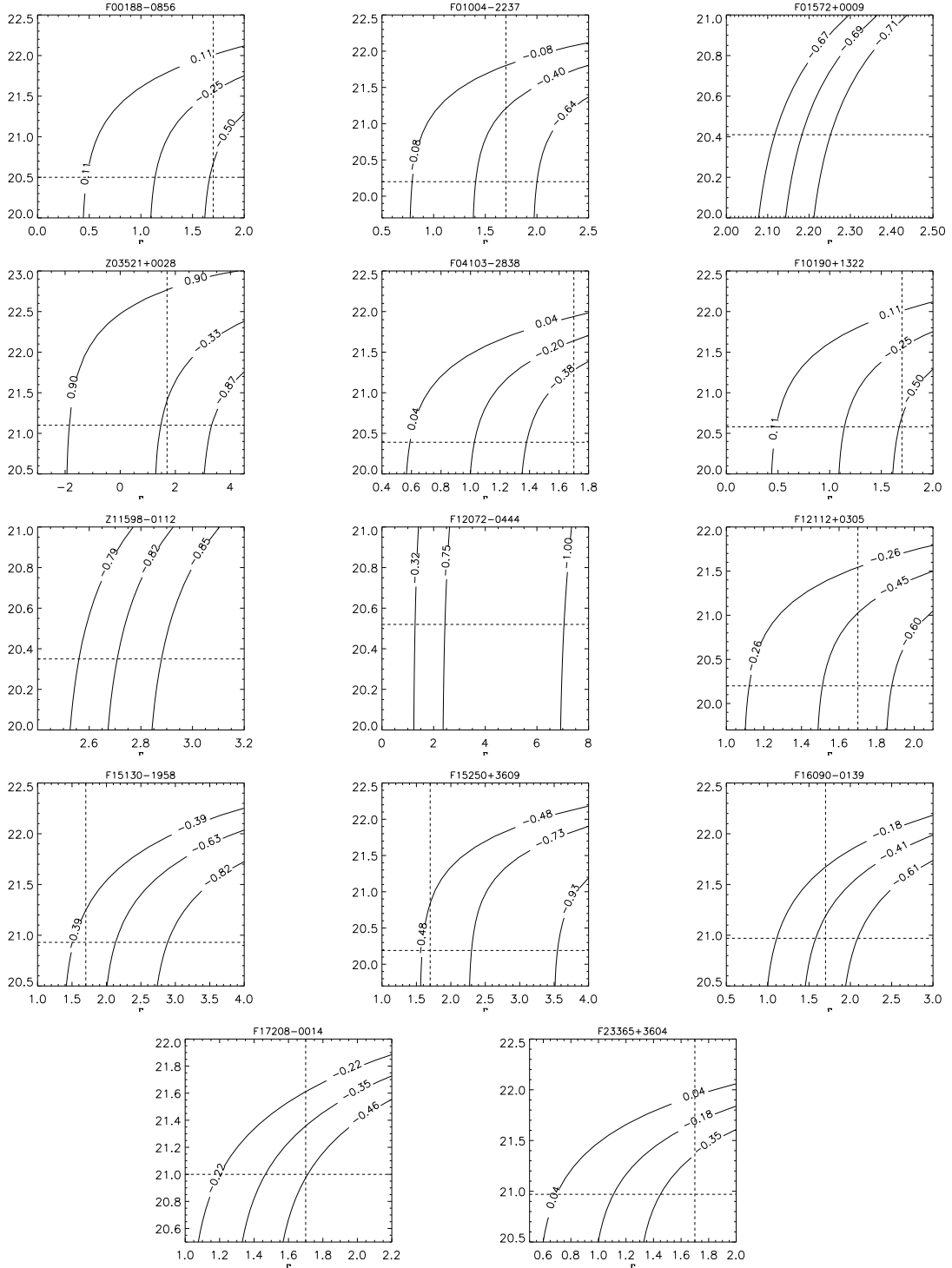


Figure 2.7: Each plot shows contours of constant hardness ratio (defined in Equation 1.3) in the N_H (y-axis) versus Γ (x-axis) plane. The middle curve represents, and is labeled with, the observed hardness ratio, while the other two curves represent the hardness ratios $1-\sigma$ away from the observed value (see Table 2.4). The horizontal dashed line represents the Galactic hydrogen column density, while the vertical dashed line represents $\Gamma = 1.7$.

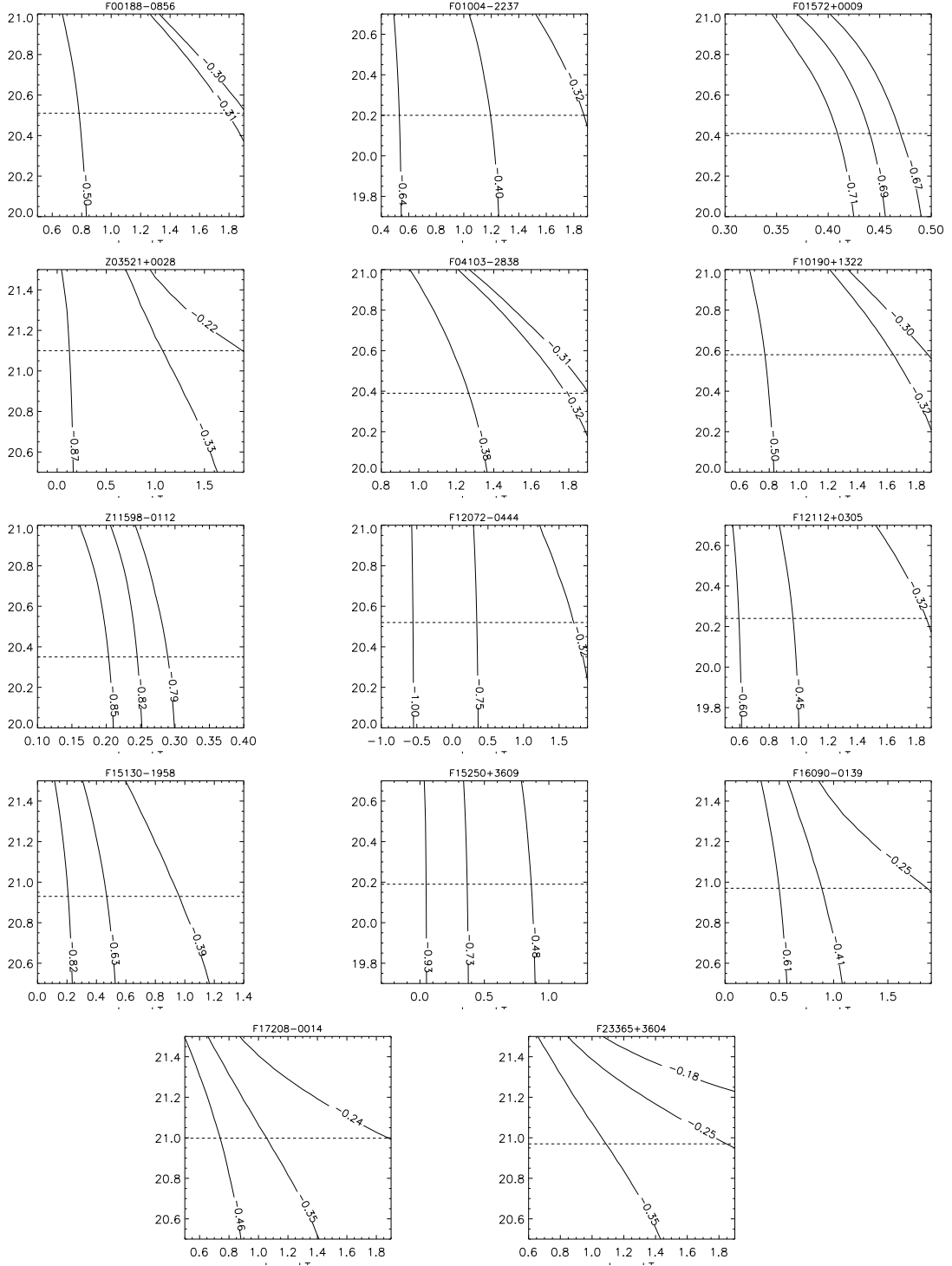


Figure 2.8: Each plot shows contours of constant hardness ratio (defined in Equation 1.3) in the N_H (y-axis) versus kT (x-axis) plane. The middle curve represents, and is label-led with, the observed hardness ratio, while the other two curves represent hardness ratios $1-\sigma$ away from the observed value (see Table 2.4). The horizontal dashed line represents the Galactic hydrogen column density.

The reliability of this hardness ratio method can be tested by comparing its results with those given by the more traditional method of fitting models to the observed spectra. For this comparison, we used the two bright sources F01572+0009 and Z11598-0112. The hardness ratio method systematically underestimated the values of the photon indices compared with spectral fitting of single power law models when the full energy band was considered (compare Tables 2.3 and 2.4). This is because, as previously mentioned in § 2.4.3, a single power law does not adequately describe the data for these two sources; their spectra are steeper at lower energies (Figures 2.5 & 2.6). Tests were made in which the two methods were compared over narrower spectral bands (within which a power law is a good representation of the spectra) and the results were found to be consistent to within the errors.

The reliability of our hardness ratio method can be further tested by comparing our results for the three galaxies that were also in the samples of Ptak et al. (2003) and Franceschini et al. (2003) with theirs. Our results for F12112+0305, F15250+3609, and F17208-0014 agree with these previous *XMM-Newton* and *Chandra* observations to within the errors.

2.5 Discussion

2.5.1 The Two Bright Sources

Based on the radial profiles of F01572+0009 and Z11598-0112 (Figure 2.4), the nuclear soft X-ray emissions are probably unresolved (F01572+0009 may be slightly extended – see § 2.4.2). This is consistent with the X-ray emission being dominated by the Seyfert 1 nuclei.

The spectra of these two sources cannot be described by a single power law. At

Table 2.4. Spectral Models Derived from Hardness Ratios

Source Name (1)	N_H (Galactic) ^a (10^{20} cm ⁻²) (2)	Total Counts (3)	Hard Counts (H) ^b (4)	Soft Counts (S) ^b (5)	Hardness Ratio (HR) ^c (6)	Γ^d (7)	N_H ($\Gamma=1.7$) ^e (10^{20} cm ⁻²) (8)	kT^f (keV) (9)
F00188-0856	3.21	16.0	6.0 ^{+3.6} _{-2.4}	10.0 ^{+4.3} _{-3.1}	-0.25 ^{+0.36} _{-0.25}	1.1 ^{+0.5} _{-0.6}	36 ⁺⁶⁴ ₋₃₁	79.9 ^{+—} ₋₇₃
F01004-2237	1.58	20.0	6.0 ^{+3.6} _{-2.4}	14.0 ^{+4.8} _{-3.7}	-0.40 ^{+0.32} _{-0.24}	1.4 ^{+0.6} _{-0.6}	16 ⁺⁴⁷ _—	15.8 ⁺⁶² ₋₁₂
F01572+0009	2.56	4386.0	674.0 ⁺²⁶ ₋₂₆	3712.0 ⁺⁶¹ ₋₆₁	-0.69 ^{+0.02} _{-0.02}	2.17 ^{+0.10} _{-0.07}	—	2.8 ^{+0.2} _{-0.2}
Z03521+0028	12.5	3.0	1.0 ^{+2.3} _{-0.8}	2.0 ^{+2.6} _{-1.3}	-0.33 ^{+1.23} _{-1.54}	1.5 ^{+1.9} _{-3.4}	25 ⁺⁵⁶⁴ _—	12.6 ⁺⁶⁵ ₋₁₁
F04103-2838	2.45	30.0	12.0 ^{+4.6} _{-3.4}	18.0 ^{+5.3} _{-4.2}	-0.20 ^{+0.24} _{-0.18}	1.05 ^{+0.35} _{-0.45}	43 ⁺⁴⁰ ₋₂₄	79.9 ^{+—} ₋₆₁
F10190+1322	3.78	16.0	6.0 ^{+3.6} _{-2.4}	10.0 ^{+4.3} _{-3.1}	-0.25 ^{+0.36} _{-0.25}	1.18 ^{+0.50} _{-0.68}	35 ⁺⁶⁵ ₋₃₀	79.9 ^{+—} ₋₇₃
Z11598-0112	2.25	1481.0	130.0 ⁺¹¹ ₋₁₁	1351.0 ⁺³⁷ ₋₃₇	-0.82 ^{+0.03} _{-0.03}	2.7 ^{+0.2} _{-0.1}	—	1.8 ^{+0.2} _{-0.2}
F12072-0444	3.32	16.0	2.0 ^{+2.6} _{-1.3}	14.0 ^{+4.8} _{-3.7}	-0.75 ^{+0.43} _{-0.25}	2.5 ^{+4.6} _{-1.1}	—	2.0 ⁺⁴⁸ ₋₁₇
F12112+0305	1.75	51.0	14.0 ^{+4.3} _{-3.7}	37.0 ^{+7.1} _{-6.1}	-0.45 ^{+0.19} _{-0.15}	1.5 ^{+0.4} _{-0.4}	11 ⁺²⁴ _—	7.9 ⁺⁷² _{-3.9}
F15130-1958	8.60	38.0	7.0 ^{+3.8} _{-2.6}	31.0 ^{+6.6} _{-5.5}	-0.63 ^{+0.24} _{-0.19}	2.15 ^{+0.75} _{-0.65}	<17	3.2 ^{+5.7} _{-1.5}
F15250+3609	1.56	37.0	5.0 ^{+3.4} _{-2.2}	32.0 ^{+6.7} _{-5.6}	-0.73 ^{+0.25} _{-0.20}	2.27 ^{+1.24} _{-0.77}	<7	2.5 ^{+5.4} _{-1.4}
F16090-0139	9.25	27.0	10.0 ^{+4.3} _{-3.1}	17.0 ^{+4.2} _{-4.1}	-0.41 ^{+0.23} _{-0.20}	1.57 ^{+0.53} _{-0.45}	15 ⁺³³ _—	7.9 ⁺⁷² _{-4.7}
F17208-0014	9.96	92.0	30.0 ^{+6.5} _{-5.5}	62.0 ^{+8.9} _{-7.9}	-0.35 ^{+0.13} _{-0.11}	1.43 ^{+0.27} _{-0.23}	23 ⁺¹⁸ _—	11.2 ⁺⁶⁹ _{-5.6}
F23365+3604	9.36	34.0	14.0 ^{+4.3} _{-3.7}	20.0 ^{+5.6} _{-4.4}	-0.18 ^{+0.32} _{-0.17}	1.10 ^{+0.35} _{-0.25}	50 ⁺³⁹ ₋₂₇	79.9 ^{+—} ₋₆₈

^aColumn densities were obtained from the CIAO observing toolkit accessible through <http://asc.harvard.edu/toolkit/colden.jsp>.

^bThe counting errors for the faint sources (< 1000 total counts) are determined assuming Poisson statistics, using Tables 1 & 2 of Gehrels (1986) and the total number of counts in each band. The counting errors for the bright sources are simply \sqrt{N} .

^cThe hardness ratio is defined in Equation ???. The errors given were determined from error propagation based on the hard and soft band counts (columns 4 and 5).

^dThe photon index for a power law model where $n(E) \propto E^{-\Gamma}$. Γ was calculated with N_H fixed at the Galactic column density. The errors in the photon indices were determined from the hardness ratio limits.

^eEstimated total column density for $\Gamma=1.7$, the photon index typical of an unobscured AGN. Listed are the column densities required to produce the observed spectra. The column densities of several sources (F01572+0009, Z11598-0112, and F12072-0444) cannot be modified to reduce Γ to 1.7, since N_H must always be greater than or equal to the Galactic value (column (2)).

^fThe temperature in a MEKAL model, assuming solar abundances. The model has an upper limit of $kT=79.9$ keV, beyond which the MEKAL model is indistinguishable from a thermal bremsstrahlung model. The errors were determined from the hardness ratio limits.

least two components are needed: a hard power law and a soft component represented by a power law or a MEKAL model. These two models describe the data equally well. We find that the best-fit MEKAL model for the soft component in both Seyfert 1 galaxies has $kT \sim 250$ eV. Ptak et al. (1999) found that similar models applied to starbursts usually have a temperature greater than 600 eV. Therefore, the low temperatures of the Seyfert 1 galaxies suggest that starburst activity may not be the dominant energy source of the soft component. The same conclusion was drawn by Boller et al. (2002) for F01572+0009.

Following the analysis done on the *XMM-Newton* observations of F01572+0009 by Boller et al. (2002), we can further support our claim that F01572+0009 and Z11598-0112 are AGN dominated through a quantitative comparison. According to

Boller & Bertoldi (1996), the ratio of soft X-ray (0.1–2.4 keV) to far-infrared (40–120 μm) fluxes is $F_{SX1}/F_{FIR} \simeq 10^{-2.5}$ for an unabsorbed starburst in equilibrium and 10^{-1} for an unabsorbed Seyfert 1 galaxy. Here we use the notation SX1 for the 0.1–2.4 keV (*ROSAT*) band, SX for the 0.5–2.0 keV (*Chandra*) band, HX1 for the 2–10 keV band, and HX for the 2–8 keV (*Chandra*) band. The far-infrared fluxes in the 40–120 μm band can be estimated using Equation 1 in Helou et al. (1985) transcribed here:

$$F_{FIR} = 1.26 \times 10^{-14} \times [2.58f_{\nu}(60\mu\text{m}) + f_{\nu}(100\mu\text{m})], \quad (2.1)$$

where f_{ν} are flux densities in Jy, and F_{FIR} is in W m^{-2} . Using the flux densities in the *IRAS* 60 and 100 μm bands, we estimate the far-infrared fluxes for F01572+0009 and Z11598-0112 to be 9.93×10^{-11} $\text{ergs cm}^{-2} \text{s}^{-1}$ and 1.13×10^{-10} $\text{ergs cm}^{-2} \text{s}^{-1}$, respectively. The *Chandra* soft X-ray fluxes are $F_{SX} = 1.54 \times 10^{-12}$ $\text{ergs cm}^{-2} \text{s}^{-1}$ for F01572+0009 and 5.79×10^{-13} $\text{ergs cm}^{-2} \text{s}^{-1}$ for Z11598-0112. The F_{SX} values can be scaled to F_{SX1} values based on the photon indices of the soft power law continuum models:

$$F_{SX1} = F_{SX} \times \left(\frac{2.4^{-(\alpha-1)} - 0.1^{-(\alpha-1)}}{2.0^{-(\alpha-1)} - 0.5^{-(\alpha-1)}} \right), \quad (2.2)$$

where the spectral index $\alpha = \Gamma - 1$ and $f_{\nu} \propto \nu^{-\alpha}$. From these estimates, we find that both F01572+0009 and Z11598-0112 have $F_{SX1}/F_{FIR} \simeq 10^{-1.2}$. These flux ratios are approximately consistent with the value ($10^{-1.4}$) found by Boller et al. (2002). The soft X-ray to far infrared flux ratios thus indicate that the two Seyfert 1 galaxies in our sample are energetically dominated by AGNs.

Given the large obscuration to the nuclei of ULIRGs, the X-ray flux in the soft band may be heavily attenuated by photoelectric absorption. Therefore, a better method of determining whether a source is starburst or AGN dominated is to compare its hard X-ray flux to its bolometric flux. Sanders & Mirabel (1996)

suggested that, on average, the bolometric flux (F_{bol}) of ULIRGs is 1.15 times the infrared flux (F_{IR}) over the 8–1000 μm band. The bolometric flux of our sources can be estimated using Equation 3 of Kim & Sanders (1998) and the *IRAS* flux densities taken directly from the *IRAS* Faint Source Catalog:

$$F_{IR} = 1.8 \times 10^{-14} \times [13.48 \times f_{\nu}(12\mu\text{m}) + 5.16 \times f_{\nu}(25\mu\text{m}) + 2.58 \times f_{\nu}(60\mu\text{m}) + f_{\nu}(100\mu\text{m})], \quad (2.3)$$

where f_{ν} are flux densities in Jy, and F_{FIR} is in W m^{-2} .

A study of 109 quasars from the Palomar-Green survey by Sanders et al. (1989) suggests that the hard X-ray (HX1, 2–10 keV) to bolometric luminosity ratio $\gtrsim 10^{-4}$ for these quasars. Equations “0” and 1 of Franceschini et al. (2003) suggest $F_{HX1}/F_{bol} < 10^{-4}$ for starbursts. Therefore, a F_{HX1}/F_{bol} value $\gtrsim 10^{-4}$ implies AGN dominance. F_{HX1}/F_{bol} for F01572+0009 and Z11598-0112 are $10^{-2.2}$ and $10^{-3.1}$, respectively. This result further emphasizes that the two Seyfert 1 galaxies in our sample are AGN dominated. This is consistent with what Veilleux et al. (1999a,b) concluded based on the broad line region (BLR) luminosity to bolometric luminosity ratio. It appears that detection of an optical/near-infrared BLR in a ULIRG is a sufficient condition to predict AGN dominance in a ULIRG.

2.5.2 The Twelve Faint Sources

Applying the nominal photon index derived from the hardness ratio, we estimated the 0.5–2.0 keV soft X-ray fluxes of the weak sources. Using Equations 2.1 and 2.2, we calculated the soft X-ray to far-infrared flux ratio (F_{SX1}/F_{FIR}) for each galaxy in our sample, and found $F_{SX1}/F_{FIR} \lesssim 10^{-3.5}$ for all sources, well below the values quoted above for both an unabsorbed starburst and an unabsorbed Seyfert 1 galaxy. Furthermore, all of the weak sources have $F_{HX1}/F_{bol} < 10^{-4.0}$ and are thus not AGN dominated. The results are provided in Table 2.5. The large error bars in the flux ratios result from uncertainties in our estimation of the photon index.

Table 2.5. X-Ray and Infrared Fluxes and Luminosities

Source Name	F_{FIR} (ergs cm ⁻² s ⁻¹)	$F_{\text{SX1}}^{\text{a}}$ (ergs cm ⁻² s ⁻¹)	$F_{\text{HX1}}^{\text{b}}$ (ergs cm ⁻² s ⁻¹)	$\log_{10}(\frac{F_{\text{SX1}}}{F_{\text{FIR}}})$	$\log_{10}(\frac{F_{\text{HX1}}}{F_{\text{bol}}})$	$L_{\text{SX1}}^{\text{c}}$ (ergs s ⁻¹)	$L_{\text{HX1}}^{\text{c}}$ (ergs s ⁻¹)	$L_{\text{bol}}^{\text{c}}$ (ergs s ⁻¹)
F00188-0856	$1.3 \pm 0.1 \times 10^{-10}$	$7.2^{+6.5}_{-6.0} \times 10^{-15}$	$2.3^{+2.4}_{-1.8} \times 10^{-14}$	$-4.2^{+0.4}_{-0.4}$	$-4.1^{+0.5}_{-0.5}$	$2.5^{+2.3}_{-2.1} \times 10^{41}$	$8.0^{+8.4}_{-6.3} \times 10^{41}$	$1.0 \pm 0.7 \times 10^{46}$
F01004-2237	$9.7 \pm 0.6 \times 10^{-11}$	$1.1^{+8.8}_{-1.1} \times 10^{-14}$	$2.0^{+1.7}_{-1.4} \times 10^{-14}$	$-3.9^{+3.4}_{-0.4}$	$-4.2^{+0.4}_{-0.3}$	$3.4^{+4.9}_{-3.4} \times 10^{41}$	$6.0^{+4.9}_{-4.2} \times 10^{41}$	$8.8 \pm 0.7 \times 10^{45}$
F01572+0009	$9.9 \pm 0.7 \times 10^{-11}$	$5.8^{+6.1}_{-9.3} \times 10^{-12}$	$1.5^{+0.1}_{-0.6} \times 10^{-12}$	$-1.2^{+0.001}_{-0.001}$	$-2.2^{+0.05}_{-0.05}$	$3.5^{+0.1}_{-0.7} \times 10^{44}$	$9.0^{+0.7}_{-0.6} \times 10^{43}$	$1.5 \pm 0.1 \times 10^{46}$
Z03521+0028	$6.6 \pm 0.5 \times 10^{-11}$	$2.0^{+5.7}_{-7.1} \times 10^{-15}$	$3.7^{+3.2}_{-2.5} \times 10^{-15}$	$-4.5^{+1.1}_{-0.4}$	$-4.8^{+0.4}_{-0.3}$	$1.0^{+0.9}_{-0.7} \times 10^{41}$	$1.9^{+1.6}_{-0.7} \times 10^{41}$	$1.2 \pm 0.1 \times 10^{46}$
F04103-2838	$8.1 \pm 0.4 \times 10^{-11}$	$1.1^{+7.1}_{-1.1} \times 10^{-14}$	$3.8^{+2.2}_{-2.2} \times 10^{-14}$	$-3.9^{+0.4}_{-0.4}$	$-4.1^{+0.3}_{-0.3}$	$3.3^{+2.1}_{-3.3} \times 10^{41}$	$1.1^{+0.7}_{-0.7} \times 10^{42}$	$1.2 \pm 0.2 \times 10^{46}$
F10190+1322	$1.8 \pm 0.1 \times 10^{-10}$	$6.4^{+5.7}_{-4.9} \times 10^{-15}$	$1.8^{+1.7}_{-1.4} \times 10^{-14}$	$-4.4^{+0.4}_{-0.3}$	$-4.3^{+0.3}_{-0.3}$	$7.9^{+6.9}_{-6.0} \times 10^{40}$	$2.2^{+2.1}_{-1.7} \times 10^{41}$	$4.4 \pm 0.2 \times 10^{45}$
Z11598-0112	$1.1 \pm 0.1 \times 10^{-10}$	$7.0^{+0.6}_{-0.6} \times 10^{-12}$	$2.6^{+0.1}_{-0.1} \times 10^{-13}$	$-1.2^{+0.05}_{-0.05}$	$-3.1^{+0.03}_{-0.03}$	$3.5^{+0.3}_{-0.3} \times 10^{44}$	$1.3^{+0.1}_{-0.1} \times 10^{43}$	$1.7 \pm 0.1 \times 10^{46}$
F12072-0444	$1.1 \pm 0.1 \times 10^{-10}$	$2.3^{+1.6}_{-2.3} \times 10^{-14}$	$4.0^{+3.6}_{-3.7} \times 10^{-15}$	$-3.7^{+3.3}_{-0.4}$	$-4.8^{+0.4}_{-0.3}$	$8.2^{+5.3}_{-5.2} \times 10^{41}$	$1.4^{+1.3}_{-1.0} \times 10^{41}$	$9.9 \pm 0.6 \times 10^{45}$
F12112+0305	$4.0 \pm 0.2 \times 10^{-10}$	$2.3^{+1.1}_{-1.3} \times 10^{-14}$	$3.5^{+1.7}_{-1.7} \times 10^{-14}$	$-4.2^{+0.2}_{-0.2}$	$-4.3^{+0.2}_{-0.2}$	$2.6^{+1.2}_{-1.2} \times 10^{41}$	$3.8^{+1.9}_{-1.9} \times 10^{41}$	$8.2 \pm 0.4 \times 10^{45}$
F15130-1958	$9.1 \pm 0.7 \times 10^{-11}$	$3.0^{+1.3}_{-1.7} \times 10^{-14}$	$1.4^{+0.8}_{-0.7} \times 10^{-14}$	$-3.5^{+0.2}_{-0.3}$	$-4.2^{+0.2}_{-0.2}$	$7.7^{+4.0}_{-4.0} \times 10^{41}$	$3.6^{+1.9}_{-1.8} \times 10^{41}$	$5.8 \pm 0.4 \times 10^{45}$
F15250+3609	$3.1 \pm 0.1 \times 10^{-10}$	$2.2^{+2.2}_{-1.2} \times 10^{-14}$	$6.2^{+5.8}_{-4.9} \times 10^{-15}$	$-4.2^{+3.5}_{-0.4}$	$-5.1^{+0.4}_{-0.4}$	$1.3^{+6.5}_{-1.3} \times 10^{41}$	$3.8^{+3.5}_{-3.0} \times 10^{40}$	$4.3 \pm 0.2 \times 10^{45}$
F16090-0139	$1.8 \pm 0.1 \times 10^{-10}$	$1.2^{+1.2}_{-1.5} \times 10^{-14}$	$1.9^{+1.6}_{-1.5} \times 10^{-14}$	$-4.2^{+0.4}_{-0.4}$	$-4.3^{+0.4}_{-0.4}$	$4.8^{+6.0}_{-4.8} \times 10^{41}$	$7.4^{+6.1}_{-5.8} \times 10^{41}$	$1.4 \pm 0.1 \times 10^{46}$
F17208-0014	$1.5 \pm 0.1 \times 10^{-9}$	$4.4^{+1.6}_{-1.5} \times 10^{-14}$	$9.0^{+3.7}_{-3.4} \times 10^{-14}$	$-4.5^{+0.2}_{-0.1}$	$-5.5^{+0.2}_{-0.2}$	$1.6^{+2.6}_{-2.6} \times 10^{41}$	$3.3^{+1.4}_{-1.3} \times 10^{41}$	$9.7 \pm 0.4 \times 10^{46}$
F23365+3604	$3.4 \pm 0.2 \times 10^{-10}$	$1.1^{+1.1}_{-1.1} \times 10^{-14}$	$3.9^{+2.4}_{-2.4} \times 10^{-14}$	$-4.5^{+2.3}_{-0.4}$	$-4.2^{+0.3}_{-0.3}$	$9.2^{+9.2}_{-9.2} \times 10^{40}$	$3.3^{+2.0}_{-2.0} \times 10^{41}$	$5.6 \pm 0.3 \times 10^{45}$

^aSoft X-ray flux in the range of 0.1–2.4 keV scaled from the 0.5–2.0 keV flux using Equation 2.2. The 0.5–2.0 keV flux of the 12 weak sources is based on the power law model derived from the hardness ratio.

^bHard X-ray flux in the range of 2.0–10.0 keV scaled from the 2.0–8.0 keV flux calculated using an equation similar to Equation 2.2. The 2.0–8.0 keV flux of the 12 weak sources is based on the power law model derived from the hardness ratio.

^cLuminosity distance calculated from Equation 2 of Kim & Sanders (1998).

2.5.3 Correlations with Infrared Color and Luminosity

In Figure 2.9 we plot the values of F_{SX1}/F_{FIR} and F_{HX1}/F_{FIR} for our sample of galaxies as a function of the infrared luminosities and the log of the *IRAS* 25-to-60 μm flux ratio. It appears that both Seyfert 1's have “warm” colors, high infrared luminosity, and high X-ray to far-infrared flux ratios, as expected. If having “warm” colors and high infrared luminosity is a pre-requisite for AGN dominance, then the other source (F12072-0444) in our sample in this quadrant of Figure 2.1, which has a low X-ray to far-infrared flux ratio, could be a Compton-thick AGN.

Figure 2.10 shows the distribution of photon index *assuming the Galactic column* as a function of infrared color and luminosity. With the exception of one LINER, all the non-Seyfert galaxies have photon indices less than 2. There is no obvious correlation between Γ and infrared color or luminosity. It is evident that the Seyferts have larger Γ s than the rest of the sample.

If an intrinsic spectral shape is assumed, we can calculate N_H from the observed spectra. By fixing Γ at 1.7, we used the hardness ratio curves in Figure 2.7 to estimate N_H . The results are tabulated in column (8) of Table 2.4. None of the sources appears to be Compton-thick. In fact, they have relatively low column densities of $\sim 10^{21} \text{ cm}^{-2}$. This implies that the power source for the non-Seyfert 1 galaxies could simply be intrinsically weak AGNs. However, we cannot rule out the possibility that Compton-thick AGNs are present. If the flux of a Compton-thick AGN is dominated by scattering from highly ionized gas, then the gas would scatter elastically and the spectrum would appear similar to that of a Seyfert 1. In this case, the HR result would be that of an unobscured source.

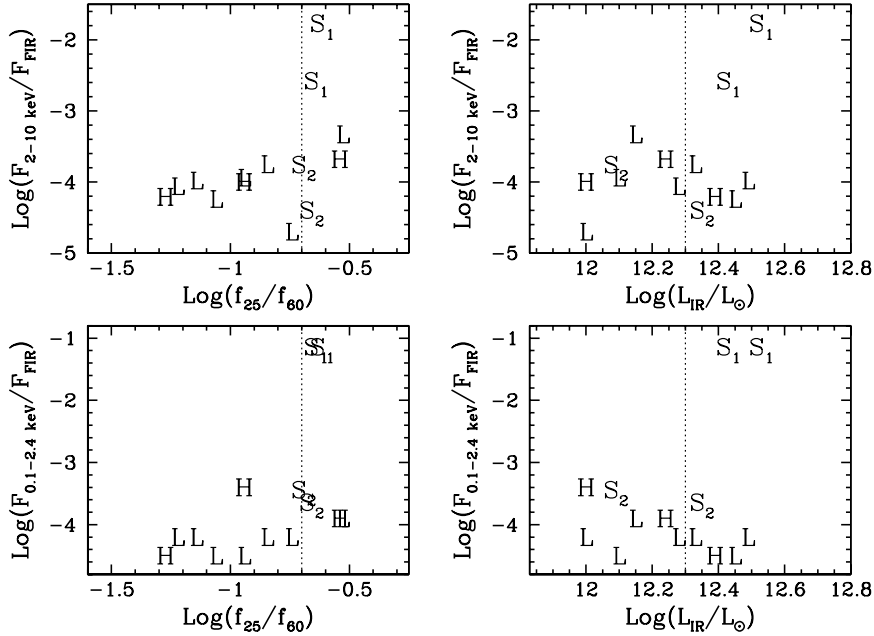


Figure 2.9: Plots of the log of the ratio of hard X-ray (2.0–10 keV) to far-infrared flux (calculated from Equation 2.1) and the log of the ratio of soft X-ray (0.1–2.4 keV) flux to far-infrared flux versus the log of the 25 μ m to 60 μ m flux ratio and the log of the infrared luminosity between 8 and 1000 μ m (the last two being the axes of Figure 2.1). The symbols represent the optical spectral classifications. S₁ represents type 1 Seyfert galaxies, S₂ type 2 Seyfert galaxies, L LINERs, and H H II regions. There is a clear segregation between the two bright Seyfert 1 ULIRGs and the rest of our sample. The Seyfert 1’s have high X-ray luminosity, high infrared luminosity, high X-ray to infrared flux ratios, and “warm” colors. The 2–10 keV flux was calculated from F_{HX} in a similar manner to the way in which F_{SX1} was calculated from F_{SX} (see text, Equation 2.2). The dotted lines represent the divisions of the infrared colors and luminosity bins that were used in the selection of the sample for observation with *Chandra* (§ 2.2 and Figure 2.1).

2.5.4 Comparison with Previous Work

Following Figure 5 of Ptak et al. (2003), we have plotted the ratio of hard X-ray to far-infrared flux as a function of the *IRAS* 25-to-60 μ m flux ratio. We reproduced the Ptak et al. (2003) plot and added our results to their figure (Figure 2.11). The two type 1 Seyferts in our sample lie within the region occupied by other Seyferts and composites. The dotted line in Figure 2.11 represents the average $F_{2-10 \text{ keV}}/F_{\text{FIR}}$ of

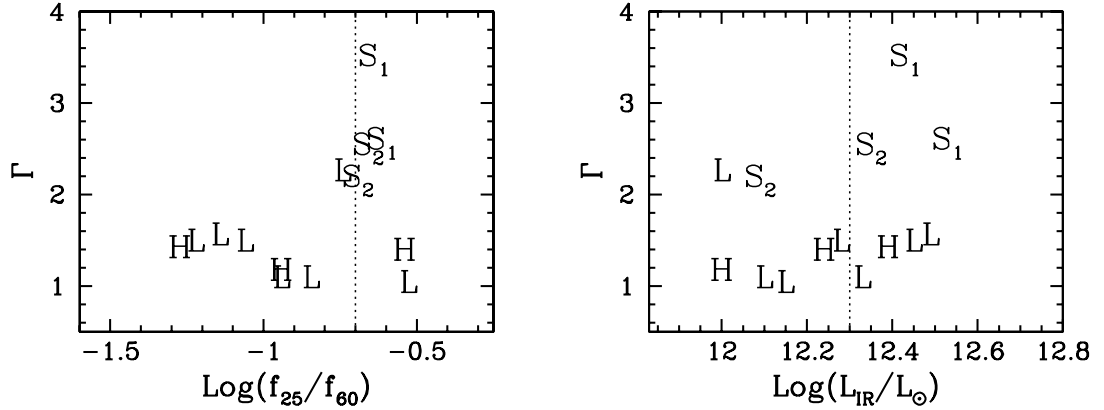


Figure 2.10: Plot of the photon index (Γ), assuming the Galactic column, as a function of *IRAS* 25–60 μm colors and infrared luminosities. With the exception of one LINER, all the non-Seyfert galaxies have photon indices below 2. There is no clear correlation between the photon index and the infrared flux ratio, or between the photon index and the infrared luminosity. The plot key is the same as Figure 2.9 and the dotted lines represent the same divisions of the infrared colors and luminosity bins that were used in the selection of the sample for observation with *Chandra* (§ 2.2 and Figure 2.1).

the pure starbursts. Our data agree with Ptak et al. (2003) in that the ratios of the hard X-ray to FIR fluxes of ULIRGs are usually similar to those of pure starbursts, suggesting that most ULIRGs are powered by starbursts.

Figure 2.12 compares the photon indices of a single-power-law fit to our galaxy spectra with those from the Ptak et al. (2003) sample. This histogram shows that our spectra tend to have higher photon indices. The Ptak et al. (2003) single power law fits are very poor models of the data based on the statistical values they reported. Therefore, we have also compared our estimated photon indices with the photon indices from their two component (plasma + power law) fits (Figure 2.13). The histograms in Figure 2.13 peak at $\Gamma \sim 1.0\text{--}1.5$ for both samples.

The far-infrared luminosity is a good measure of the star formation rate (SFR) in dusty systems like ULIRGs. Comparison of the SFR from X-ray measurements with the SFR from the FIR measurements will indicate if there is any energy contribution

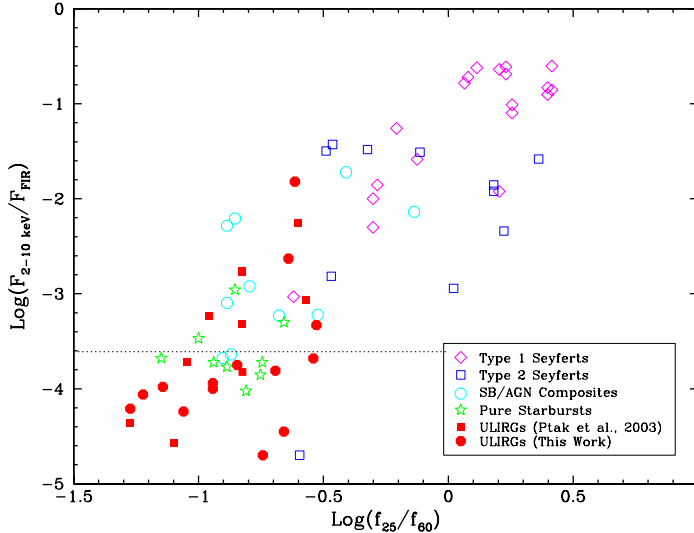


Figure 2.11: Plot of $\log(F_{2-10 \text{ keV}}/F_{FIR})$ vs. $\log f_{25\mu\text{m}}/f_{60\mu\text{m}}$. The type 1 Seyferts in our sample are distributed near the Seyferts, while the others are located among the starbursts and composites. All members of the 1-Jy sample have $\log(f_{25\mu\text{m}}/f_{60\mu\text{m}}) \lesssim -0.35$ (see Figure 2.1). Here we have only included the values for the Ptak et al. (2003) ULIRGs derived from their global spectra. The dotted line represents the average $\log(F_{2-10 \text{ keV}}/F_{FIR})$ values for the pure starbursts.

from sources other than the starburst (e.g., an AGN). If the galaxy is powered purely by a starburst, then one would expect its “SFR in X-rays” to equal its “SFR in FIR”. There are many references in the literature that relate the 2–10 keV hard X-ray luminosity to $\text{SFR}_{2-10 \text{ keV}}$. We have chosen to adopt the Ranalli et al. (2003) and Persic et al. (2004) relations because they appear to be the best-fits to pure starbursts (Hornschemeier et al. 2005, Figure 6b). The two $\text{SFR}_{2-10 \text{ keV}}$ values will give approximate upper and lower limits as a function of SFR_{FIR} ². Figure 2.14 relates the SFR from the Ranalli et al. (2003) and Persic et al. (2004) relations to

²It should be noted here that both the Ranalli et al. (2003) and Persic et al. (2004) relations are calibrated based on the Kennicutt (1998) relation for FIR. Kennicutt (1998) defined the FIR band to be 8–1000 μm , which is our definition of the IR band. However, since subsequent SFR relations are calibrated assuming the Kennicutt (1998) relation is for the wavelength range of 40–120 μm , we will use our FIR values to determine SFR_{FIR} to be consistent with the literature.

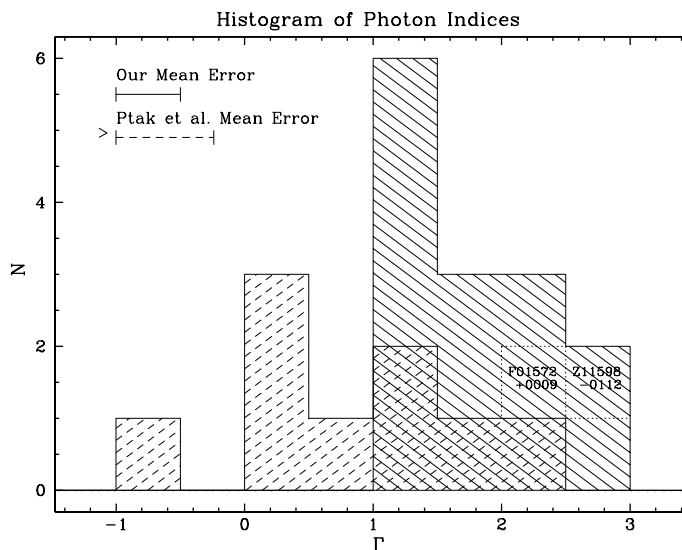


Figure 2.12: A comparison of the photon indices of a single-power-law model between our sample (solid hashes) and the Ptak et al. (2003) sample (dashed hashes). The boxes corresponding to the two Seyfert 1 nuclei in our sample (F01572+0009 and Z11598-0112) are indicated; their photon indices were calculated from the “hardness ratio” method (Table 2.4) as for the rest of the sample. The histogram indicates that the spectra from our sample are softer than those from Ptak et al. (2003). Note that Ptak et al. (2003) quoted error bars only for models with $\chi^2/dof < 1.5$. Therefore, the mean error for their sample was calculated from models for two of the ten galaxies in their sample.

the SFR from the FIR luminosity. We have included the Ptak et al. (2003) sample in the plot. From the figure, it is evident that our two Seyfert 1 galaxies have X-ray luminosities in excess of that expected from a starburst (as discussed above). The only other source from our sample located above the line of equality is the LINER F04103-2838. The four galaxies Ptak et al. (2003) determined to have AGN contributions in their spectra (Mrk 231, Mrk 273, IRAS 05189-2524, and NGC 6240) are also located far above the line of equality. The rest of the ULIRGs are most likely powered by starbursts.

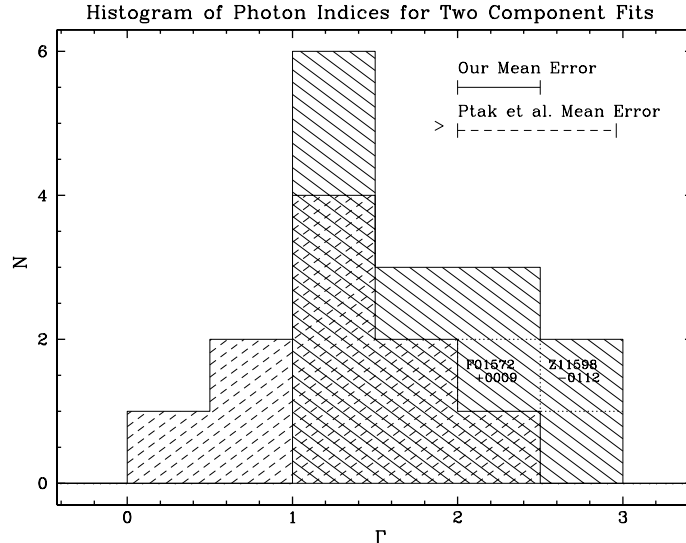


Figure 2.13: A comparison between the power-law photon indices of our sample (solid hashes) and the Ptak et al. (2003) sample (dashed hashes). The boxes corresponding to the two Seyfert 1 nuclei in our sample (F01572+0009 and Z11598-0112) are indicated; their single power law photon indices were calculated from the “hardness ratio” method (Table 2.4) as for the rest of the sample. The Γ ’s for the Ptak et al. (2003) data are their 2–10 keV results from the plasma plus power law models. The histogram indicates that the spectra from our sample are softer than those from Ptak et al. (2003). Ptak et al. (2003) quoted error bars only for models with $\chi^2/dof < 1.5$. Therefore, the mean error for their sample was calculated from models for seven of the ten galaxies in their sample.

2.5.5 Emission Processes

In this section, we explore the possible emission processes that may be responsible for the detected X-ray emission.

X-ray Binaries

Persic & Rephaeli (2002) suggested that X-ray binaries dominate the 2–15 keV luminosity in the absence of an AGN. There are two types of X-ray binaries. The high mass type (HMXB) produces X-ray emission from the accretion of wind material of an OB star onto its neutron star or black hole companion whereas the low mass type (LMXB) produces X-ray emission from accretion onto a neutron star or black

hole via Roche lobe overflow from a low mass companion (Persic & Rephaeli 2002). Assuming the lifetime of a single burst of star formation is approximately 10^8 years, the X-ray emission from HMXBs are expected to dominate the hard spectra because the low mass stars have not had time to evolve away from the main sequence and to come into Roche lobe contact (Persic et al. 2004). As a result, the spectra of the galaxies should reflect the properties of HMXBs with average $\Gamma \simeq 1.0\text{--}1.4$ (Persic et al. 2004, and references therein).

However, in mergers, multiple events of starbursts may occur due to recurrent tidal interactions (Persic et al. 2004). In this scenario, the low mass companions in binaries formed in the earlier starburst events have had time to evolve and, therefore, the X-ray emission from LMXBs may also contribute to the hard X-ray spectra. To determine the significance of this contribution, mass estimates from Veilleux et al. (2002) were used in conjunction with Equation 7 of Colbert et al. (2004) to approximate the SFR based on the global hard X-ray luminosity. The LMXB-subtracted SFRs are within $\sim 3\%$ of the SFRs found without subtraction of the contribution of LMXBs. Therefore, the LMXBs do not contribute significantly to the X-ray luminosity. This is expected for systems with young starburst systems.

Based on the peaks of the histograms in Figure 2.13 and the above discussion, the spectra of our sources may well be dominated by contributions from HMXBs. This implies that the weak sources are starburst dominated, as suggested by their values of $\log(F_{2-10 \text{ keV}}/F_{FIR})$ (Figures 2.11 and 2.14). If we assume that the luminosity in the hard X-ray band is solely due to X-ray binaries with luminosities $\gtrsim 10^{37}$ ergs s^{-1} , then the galaxies in our sample contain $10^3\text{--}10^5$ binaries that contribute to the X-ray emission. Assuming a universal stellar initial mass function and star formation rate, these values are 4–170 times the number of X-ray binaries in the nearby starburst galaxies M82 and NGC 253 which in turn have 4–16 times the

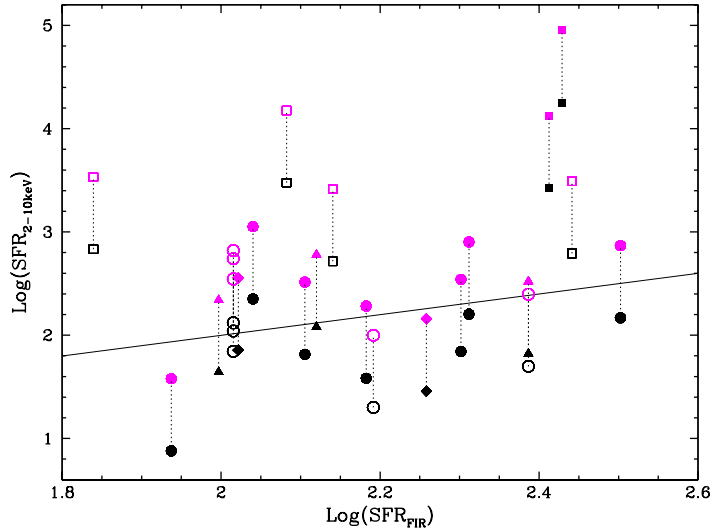


Figure 2.14: A plot of $\text{SFR}_{2-10 \text{ keV}}$ as a function of SFR_{FIR} . The star formation rates are in solar masses per year. For each galaxy, two values of $\text{SFR}_{2-10 \text{ keV}}$ (connected by dotted lines) are plotted based on the relations from Ranalli et al. (2003) and Persic et al. (2004). The top value is from the Persic et al. (2004) relation, while the bottom value is from the Ranalli et al. (2003) relation. The solid line, represents the line of equality: $\text{SFR}_{2-10 \text{ keV}} = \text{SFR}_{FIR}$. It should be noted here that NGC 6240 (the leftmost pair of open squares) is a luminous infrared galaxy (LIRG) and is used by Ptak et al. (2003) only for comparison purposes because of its high hard X-ray luminosity compared to starburst ULIRGs. Plot key: filled squares – optically classified Seyfert 1 ULIRGs from this work, filled diamonds – Seyfert 2 ULIRGs from this work, filled triangles – H II ULIRGs from this work, filled circles – LINER ULIRGs from this work, open squares – Ptak et al. (2003) AGN ULIRGs and open circles – Ptak et al. (2003) starburst ULIRGs.

number of binaries in the Milky Way (Persic & Rephaeli 2002). If ultraluminous X-ray sources (ULXs) contribute to the emission, then a smaller number of X-ray binaries would be required.

Thermal Bremsstrahlung

On the other hand, the hard X-ray emission may result from thermal bremsstrahlung from a hot wind driven by either a starburst or an AGN. For low abundances, the dominant emission process of a thermal gas is, of course, bremsstrahlung. Rupke et al. (2002) and Rupke et al. (2005a,b,c) have shown evidence for galactic winds in the 1-Jy sample. The spectrum of thermal bremsstrahlung is almost “flat” with $\Gamma \sim 1.2$ for $E \lesssim kT$. This value of Γ coincides with the peak of the histograms of observed photon indices in Figures 2.12 and 2.13. For a given luminosity, a relationship between the size of the emitting region and electron density can be determined. Assuming the emitting region is spherical, the ion density equals that of the electrons, and a gas temperature of $10^7 - 10^8$ K, the radius of the emitting region based on Equation 5.14b and Figure 5.3 of Rybicki & Lightman (1979) is

$$R \approx 1.5 \times 10^7 L_{ff}^{\frac{1}{3}} f^{-\frac{1}{3}} n_e^{-\frac{2}{3}} \text{ cm}, \quad (2.4)$$

where f is the filling factor for the hot gas ($L \propto R^3 f \epsilon_{ff}$). If the luminosity of these sources in the 0.5–8.0 keV band is completely due to thermal bremsstrahlung, assuming an electron density of $n_e = 1 \text{ cm}^{-3}$ and $f = 1$, the size of the emitting regions ranges from 0.21 to 0.50 kpc. These sizes of the X-ray emitting regions, deduced assuming dominance of bremsstrahlung emission, are consistent with our finding that most of our faint sources are unresolved by *Chandra*. Conversely, we can derive a lower limit to the gas density if we assume the upper limit of the size of the emitting region is $0''.5$, the spatial resolution of ACIS. In this case, n_e is in the range of 0.8–7.4 cm^{-3} if the filling factor is assumed to be unity. These densities are consistent with the cold neutral phase of the interstellar medium.

Absorbed Active Galactic Nuclei

As discussed in Section 2.5.3, if we assume $\Gamma \simeq 1.7$ (the photon index of a typical unabsorbed AGN), the column density can be estimated from the hardness ratios. For many of the galaxies in our sample, the total column density estimated in this way exceeds the Galactic value (see Table 2.4). This suggests that many of the galaxies in our sample may be absorbed AGNs with total N_H about 2–16 times the Galactic value – i.e. up to $N_H \simeq 5 \times 10^{22} \text{ cm}^{-2}$. These column density estimates could be inaccurate if absorption is patchy or if scattering from an ionized medium is significant, as in the cases of NGC 1068 (Matt et al. 2004) and NGC 6240 (Ptak et al. 2003). Nevertheless, Compton-thick AGNs have been detected in several ULIRGs – e.g., IRAS 19254-7245 (Braitto et al. 2003), Mrk 231 (Braitto et al. 2004; Ptak et al. 2003). If the intervening column density is ~ 1000 or more times the Galactic value, then Compton scattering will become important. The quality of our data does not allow us to rule out this possibility.

2.6 Summary

We have obtained and analyzed X-ray observations of 14 ULIRGs with the *Chandra X-Ray Observatory*. Although all 14 galaxies were detected in the 0.5–8.0 keV energy range, only two were bright enough for traditional spectral fitting to be applicable. Spectral analysis of these two galaxies (F01572+0009 and Z11598-0112) with Seyfert 1 type optical spectra shows that their soft X-ray emissions are unresolved. There is a suggestion of an emission line at 7.0 keV in the rest frame of Z11598-0112. Monte Carlo simulations of the spectrum showed that this line is significant at more than the 99% confidence level. The soft X-ray to far-infrared flux ratios and the hard X-ray to bolometric flux ratios of F01572+0009 and Z11598-0112 indicate that

these two galaxies are energetically dominated by AGNs. This result is consistent with the statement by Veilleux et al. (1999a,b) that detection of an optical/near-infrared BLR in a ULIRG is a sufficient condition to predict AGN dominance in a ULIRG.

Unfortunately, the rest (and majority) of our sample is too faint for conventional spectral fitting. Instead, we used hardness ratios to estimate their spectral parameters. The soft X-ray to far-infrared flux ratios and the hard X-ray to bolometric flux ratios suggest that these galaxies are not energetically dominated by AGNs. A comparison between star formation rates derived from hard X-ray and far-infrared luminosities seems to support the idea that these objects are powered by starbursts, although the large uncertainties on the empirical relation between hard X-ray luminosities and star formation rates prevent us from making a definitive statement. A histogram of the photon indices of the X-ray spectra peaks at $\Gamma = 1.0\text{--}1.5$, consistent with the spectrum expected from high mass X-ray binaries or bremsstrahlung from a hot, starburst- (or AGN-) driven wind. However, we cannot rule out the possibility that these very hard X-ray spectra and the very low hard X-ray to far-infrared flux ratios are produced by absorbed AGNs.

Chapter 3

XMM-Newton Follow-up on

F04103–2838

3.1 Introduction

In our pilot study (§2.1), all 14 ULIRGs were detected by *Chandra*, though most (11/14) had less than 40 counts. The analysis showed that the two brightest galaxies in the sample have optical and X-ray spectral characteristics of Seyfert 1 nuclei. Most others have X-ray photon indices (estimated using hardness ratios) and hard X-ray to far-infrared flux ratios which are similar to those of starbursts.

One exception, F04103–2838, had a hardness ratio (deduced from only 30 counts) that suggested the presence of a starburst coexisting with an AGN. The low signal-to-noise data could not distinguish between a Compton-thick AGN or an intrinsically faint nuclear source. This object is optically classified as a LINER (Veilleux et al. 1999a). F04103–2838 has one of the largest 25-to-60 μm flux ratios of all 1 Jy ULIRGs ($f_{25}/f_{60} = 0.30$). In fact, this is the warmest of all *IRAS* 1 Jy ULIRGs with optical LINER or H II classification. This source is even warmer than some of

the Seyfert galaxies in the 1 Jy sample (see Fig. 1 of §2.1). Recent *Spitzer* detection of [Ne V] and [O IV] lines from this source has confirmed the existence of an AGN in this system (Veilleux et al. 2009b), making it a rare example of a ULIRG optically classified as a LINER that is not classified as a starburst on the basis of mid-infrared spectroscopy (Lutz et al. 1999; Taniguchi et al. 1999). In this paper, we present an *XMM-Newton* observation of F04103–2838 which delves deeper into the nature of this AGN.

F04103–2838 is an interacting galaxy system in the late stages of a merger as indicated by the presence of a single nucleus with distinct tidal tails (Dasyra et al. 2006a; Veilleux et al. 2002). This object has an infrared (8–1000 μm) luminosity of $10^{12.15}L_{\odot}$ and a cosmological redshift of 0.118. Assuming $H_0 = 75 \text{ km s}^{-1} \text{ Mpc}^{-1}$ and $q_0 = 0$ (used throughout this paper), the luminosity distance of this object is 497 Mpc. At this distance, $1''$ corresponds to ~ 2.4 kpc. In § 3.2 of this paper, we describe our new *XMM-Newton* observation of F04103–2838 and the methods we used to reduce these data. In § 3.3, we present the analysis of these data, emphasizing the results on the X-ray morphology, the lack of flux variability, and the spectral decomposition of the X-ray emission. The implications of these results are discussed in § 3.4. The main conclusions are summarized in § 3.5.

3.2 Observation and Data Reduction

F04103–2838 was observed with *XMM-Newton* during orbit #1132 on 13 February, 2006 (ObsID: 0301330401; PI: Wilson) with the EPIC instrument. The EPIC cameras were operating in full-frame mode. Each of the detectors used the medium filter.

The data were processed using the standard procedures of the *XMM-Newton*

Science Analysis System (SAS) version 6.5.0 released on 17 August, 2005. The processing procedures outlined in §4.11 of the *XMM-Newton* SAS User’s Guide were followed. The event lists were calibrated with the latest available calibration files as of June, 2006. Times of high background flares were flagged. The total good time interval on source for each camera was 17.5 ksec for PN, 21.8 ksec for MOS1, and 21.5 ksec for MOS2.

Source and background counts were extracted from circular regions with radii of 24". Because the source is near a gap in the CCD and a nearby X-ray luminous source, the background was extracted from a circular region with the same area as the source extraction region in a neighboring piece of the sky in which no obvious X-ray sources reside. The total 0.2–10 keV counts extracted from the source region are 224 for PN, 52 for MOS1, and 48 from MOS2. The expected background counts in the source region are 45 for PN and 50 for MOS1/2 based on the expected background count rates quoted in the *XMM* User’s Handbook. Since the extracted source counts are approximately the same as the expected background counts for the MOS detectors, we will exclude the MOS spectra in our spectral analysis of the source.

3.3 Analysis

In §3.3.1, we describe the distribution of the X-ray emission from F04103–2838. In §3.3.2 we point out the lack of variability of this object. A detailed analysis of the X-ray spectrum and iron complex is presented in §3.3.3.

3.3.1 Morphology

To improve the signal-to-noise ratio of the images, the PN and MOS1/2 events were combined using the SAS task *emosaic* and then smoothed with a 5'' Gaussian using *asmooth* to match the spatial resolution of *XMM*. The resultant image is displayed in the left panel of Figure 3.1. A comparison of the 0.2–2 keV (unsmoothed) radial profile with the *XMM-Newton* point spread function (PSF) at 1 keV indicates that the source is unresolved (see Fig. 1, right panel). Only the EPIC PN data were used for the radial profile calculations because of the small number of counts detected by the MOS1/2 cameras. The PSF of the PN camera is well described by a King profile¹ and was normalized so that the total number of counts per square pixel under the curve match the total number of detected counts per square pixel. The *Chandra* data from §2.1 verifies that the source is unresolved.

3.3.2 X-Ray Variability

The time interval covered by our observation was divided into four equal bins of 5234 seconds to search for significant X-ray variability, another potential indicator of dominant AGN activity. The 0.2–10 keV and 2–10 keV EPIC PN count rates were calculated for both source and background. Figure 3.2 shows the 0.2–10 and 2–10 keV light curves of the source and background. To within the errors, the source is not significantly variable on the 5-6 hour time scale of our observations.

¹PSF = $A[1 + (\frac{r}{r_0})^2]^{-\alpha}$, where $A \sim 4.756$, $r_0 \sim 5.5$ pixels, and $\alpha \sim 1.6$. See: <http://xmm.vilspa.esa.es/docs/documents/CAL-TN-0018.pdf>.

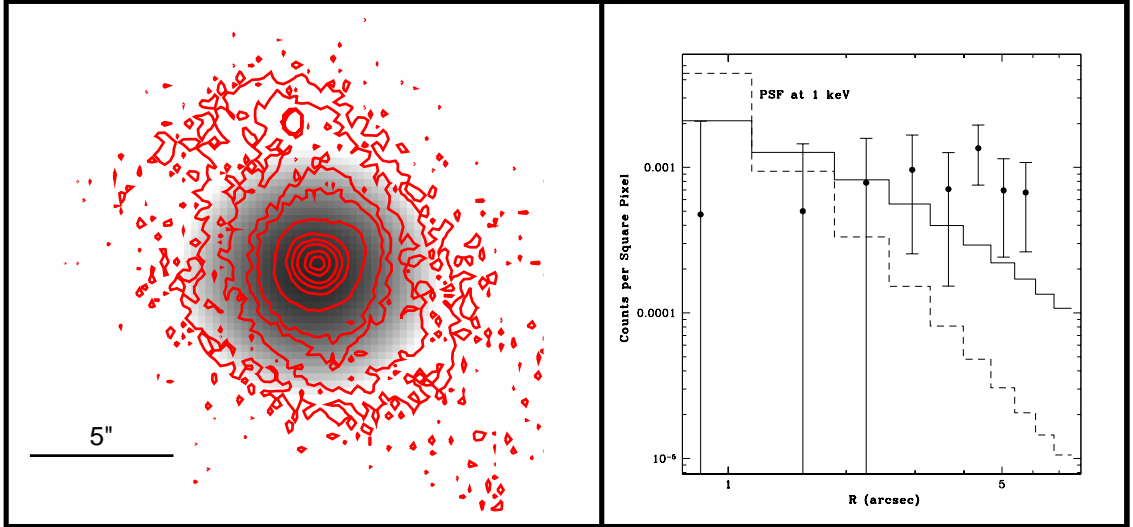


Figure 3.1: *Left*: EPIC mosaic image of F04103–2838 smoothed with a Gaussian (FWHM \sim 5'') and displayed on a linear grey scale. The contours are optical R-band data from Kim et al. (2002). *Right*: Comparison of unsmoothed EPIC PN PSF at 1 keV with observed 0.2–2 keV radial profile of F04103–2838. The dashed line represents the theoretical PSF while the solid line represents the PSF broadened due to uncertainties in the correction for pointing drift of the telescope. The absolute pointing drift (APD) error is conservatively assumed to be 3'', the upper limit (see *XMM-Newton* Observer's Handbook). The error bars were calculated using Gehrels (1986). The source is unresolved within the uncertainty of the measurements.

3.3.3 X-Ray Spectra

The extracted source and background spectra from each detector were binned using the FTOOLS *grppha* to at least 3, 5, and 15 counts bin^{-1} . The binned and unbinned spectra were then analyzed using XSPEC version 11.3.2t. The quoted errors on the derived best-fitting model parameters correspond to a 90% confidence level ($\Delta\chi^2/\Delta\text{c-stat} = 2.706$). The χ^2 goodness-of-fit test was used to judge the fits to the spectrum binned to at least 15 counts bin^{-1} . The Cash statistics (c-stat) option in XSPEC was used for spectra binned to at least 3 and 5 counts bin^{-1} and the unbinned data. The spectral model was applied to the EPIC PN data only (see §3.2). All models were corrected for Galactic absorption using

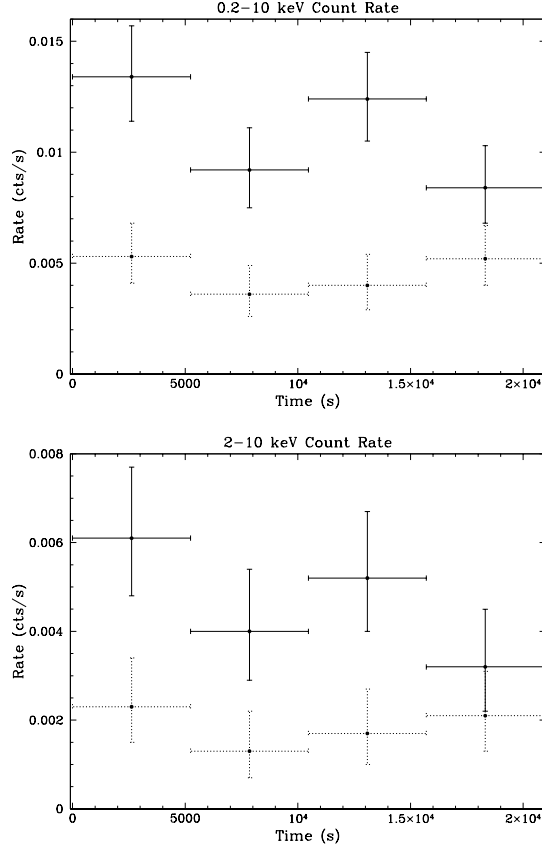


Figure 3.2: The 0.2–10 keV and 2–10 keV light curves for F04103–2838. The solid crosses denote the source count rate, while the dotted crosses denote the background count rate. Background-subtraction was not applied to the source spectrum. The time bins are each 5234 seconds. The error bars are Poissonian counting errors calculated following Gehrels (1986) at the 84% significance level. Within the errors, the source is not variable on the ~ 20 ksec time scale of our observation. The lack of short timescale variations is expected of sources where most of the primary X-ray flux is reprocessed.

$$N_{\text{H,Galactic}} = 2.45 \times 10^{20} \text{ atoms cm}^{-2} \text{ (Dickey \& Lockman 1990).}$$

Effects of Binning

By definition, spectra binned to at least 15 counts bin^{-1} have the highest signal-to-noise ratios while the spectra binned to at least 3 counts bin^{-1} show the most spectral details. The first task is to determine whether the mode of binning af-

fects the spectral parameters derived from the best-fit model². Since Cash-statistics were developed for the modeling of unbinned data, we also modeled the unbinned spectrum for comparison.

Two simple models were applied to the spectra. Model A is an absorbed power-law distribution. Model B is the same as A, except for the inclusion of a Gaussian component to model the Fe K emission at 6–7 keV (rest frame). Table 3.1 lists the best-fit parameters of each model and Figure 3.3 shows each set of spectra with the best-fit models. The significant improvement in fitting statistics of model B over model A suggests that there is indeed an emission line at an energy consistent with Fe K α emission. However, since the number of counts is relatively low (especially when the data is binned to only 3 or 5 counts bin⁻¹), the F-test cannot be used to determine whether the addition of the Gaussian component to model A is significant. The likelihood of the line being a result of statistical variations was tested using

²Gaussian statistics apply to data binned to at least 15 counts bin⁻¹ while Poisson statistics apply to the data binned to at least 3 or 5 counts bin⁻¹ and unbinned data. Since the difference of two Gaussian distributions remains a Gaussian distribution, a background-subtracted spectrum binned to at least 15 counts bin⁻¹ retains the properties of a Gaussian distribution and can be modeled normally. However, the same is not true for a Poisson distribution. Therefore, the background cannot be simply subtracted for data binned to at least 3 or 5 counts bin⁻¹ and unbinned data and then modeled. One way of treating the background is to model the background spectrum separately and then add the background model to the continuum model when fitting the source spectrum. For this paper, the background is modeled using a simple, relatively flat power law ($\Gamma \sim 1.0$). This treatment of the background is applied to all modeling of data binned to at least 3 and 5 counts bin⁻¹ and the unbinned spectrum. A representation of the background spectrum and model is shown in the bottom panel of Figure 3.4. A more vigorous treatment of the background in C-statistics is to model the background using advanced statistical techniques such as Markov chain Monte Carlo (MCMC). These modeling methods are able to include the likelihood of the observed counts in the background to derived a best-fit for the spectrum.

simulations. To this end, 10000 spectra were created using the *fakeit* command in XSPEC for each set of binned or unbinned data. The simulated spectra were created using model A. Then these spectra were fitted by both models A and B. If the line is a result of statistical variations, then one would expect a large fraction of the simulated spectra to be well described by model B. The fitting statistics were used to calculate $\Delta c\text{-stat}(A-B)$ [or $\Delta\chi^2(A-B)$ for the 15 counts bin^{-1} data] which was then compared with the values presented in Table 3.1. For the 15 counts bin^{-1} data, 1000 of 10000 (10.0%) had $\Delta\chi^2$ greater than 3.76. This implies that model B (the inclusion of the emission line) is significant at the 90.0% level (a 1.6σ detection). Similarly, the simulations show that the line is significant at the 96.87% level (313 out of 10000; 2.2σ) for the 5 counts bin^{-1} data, at the 93.5% level (507 out of 10000; 1.8σ) for the 3 counts bin^{-1} data, and at the 94.0% level (608 out of 10000; 1.9σ) for the unbinned data. From these simulations, the line is significant to at least the 90.0% level.

The 3 counts bin^{-1} data also suggest that the iron line can be decomposed into two narrower emission lines with centroid energies at 6.3 (EW ~ 0.6 keV) and 6.7 keV (EW ~ 0.4 keV) in the rest frame. These energies are consistent with emission arising from neutral iron and Fe XXV, respectively. The fitting statistics of the double-line model to the unbinned data is only slightly better than that of the single-line model. The detection of these narrow lines in the Fe K complex is significant at only the $\sim 60\%$ level based on 10000 simulations of the unbinned data. Therefore, the detection of the doublet needs to be confirmed with data of higher spectral resolution and signal-to-noise ratio.

Our modeling and simulations show that Cash-statistics give consistent results for the unbinned spectrum and the spectra binned to at least 3 and 5 counts bin^{-1} . Since Cash statistics were designed for unbinned spectra, we will use only the un-

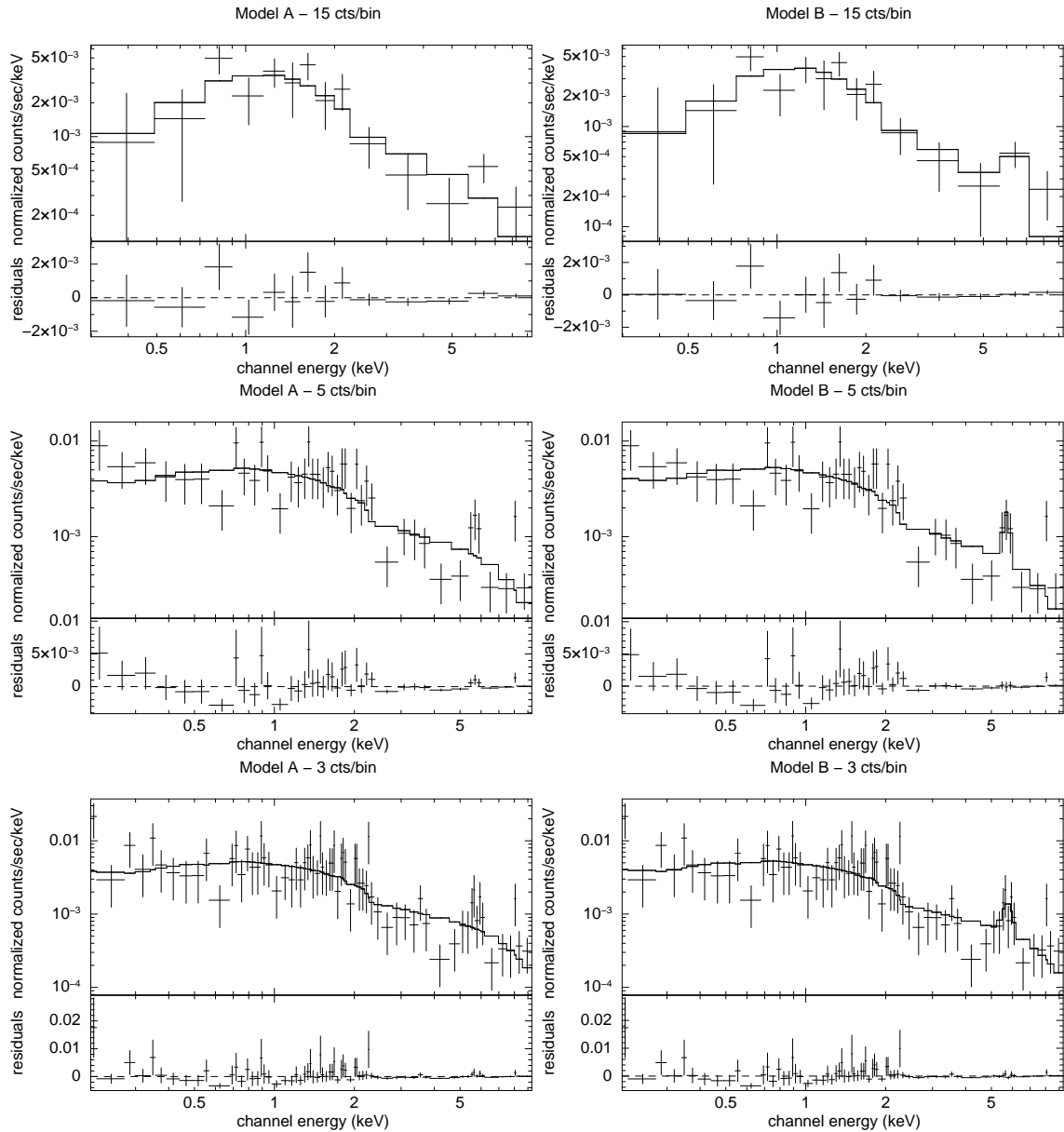


Figure 3.3: EPIC PN spectrum and best-fit models to F04103–2838 with different binnings: ≥ 15 counts bin^{-1} (top panels), ≥ 5 counts bin^{-1} (middle), and ≥ 3 counts bin^{-1} (bottom). The unbinned spectrum was modeled but is not shown here. Model A (left panels) is a simple absorbed power-law distribution; model B (right) is the same as A, but includes a Gaussian component to model the Fe K emission. The best-fit model parameters are listed in Table 3.1. The iron line is most prominent in the data binned to 5 counts bin^{-1} and the Fe K doublet may be present in the 3 counts bin^{-1} data. X-axis of the figures represents energy in the observer’s frame.

Table 3.1. Best-fit Parameters to Models A, B, & C[†]

Model	A	A	A	A	A	B	B	B	B	B	B	C
Parameters	15 cts bin ⁻¹	5 cts bin ⁻¹	3 cts bin ⁻¹	unbinned	15 cts bin ⁻¹	5 cts bin ⁻¹	3 cts bin ⁻¹	unbinned	unbinned	unbinned	unbinned	unbinned
N _H ^a	0.20 ^{+0.28} _{-0.16}	0.00 ^{+0.04} _{-0.00}	0.00 ^{+0.04} _{-0.00}	0.00 ^{+0.04} _{-0.00}	0.30 ^{+0.36} _{-0.22}	0.00 ^{+0.06} _{-0.00}	0.00 ^{+0.06} _{-0.00}	0.00 ^{+0.06} _{-0.00}	0.00 ^{+0.06} _{-0.00}	0.19 ^{+0.33} _{-0.19}		
Γ	1.42 ^{+0.61} _{-0.41}	1.01 ^{+0.21} _{-0.20}	1.00 ^{+0.21} _{-0.20}	1.00 ^{+0.21} _{-0.20}	1.80 ^{+0.90} _{-0.60}	1.12 ^{+0.25} _{-0.22}	1.11 ^{+0.26} _{-0.22}	1.09 ^{+0.27} _{-0.22}	1.09 ^{+0.27} _{-0.22}	1.36 ^{+0.97} _{-0.44}		
E _{line} ^b	—	—	—	—	6.57 ^{+1.46} _{-1.20}	6.37 ^{+0.18} _{-0.17}	6.42 ^{+0.26} _{-0.29}	6.43 ^{+0.27} _{-0.28}	6.43 ^{+0.27} _{-0.28}	6.43 ^{+0.26} _{-0.26}		
σ ^b	—	—	—	—	0.00 ^{+1.20} _{-1.20}	0.14 ^{+0.20} _{-0.17}	0.23 ^{+0.28} _{-0.28}	0.25 ^{+0.25} _{-0.25}	0.25 ^{+0.25} _{-0.25}	0.26 ^{+0.24} _{-0.24}		
EW ^b	—	—	—	—	1.96 ^{+1.90} _{-1.95}	1.33 ^{+0.24} _{-0.24}	1.37 ^{+0.33} _{-1.01}	1.39 ^{+0.32} _{-1.02}	1.39 ^{+0.32} _{-1.02}	1.62 ^{+1.12} _{-1.12}		
kT ^b	—	—	—	—	—	—	—	—	—	0.10 ^{+0.03} _{-0.03}		
Stat./dof ^c	12.4/11	66.5/40	83.0/67	858.2/1958	8.6/8	58.8/37	77.1/64	852.1/1955	852.1/1955	848.1/1953		
F _{0.2–2keV} (total) ^d	0.96 ^{+0.42} _{-0.71}	1.07 ^{+0.29} _{-0.21}	1.07 ^{+0.29} _{-0.21}	1.05 ^{+0.30} _{-0.20}	2.93 ^{+0.68} _{-0.46}	1.08 ^{+0.17} _{-0.17}	1.08 ^{+0.21} _{-0.19}	1.06 ^{+0.19} _{-0.21}	1.06 ^{+0.19} _{-0.21}	2.17 ^{+0.87} _{-0.86}		
(AGN) ^d	—	—	—	—	2.93 ^{+1.40} _{-1.64}	1.08 ^{+0.22} _{-0.22}	1.08 ^{+0.19} _{-0.19}	1.06 ^{+0.21} _{-0.21}	1.06 ^{+0.21} _{-0.21}	1.64 ^{+0.50} _{-0.50}		
F _{2–10keV} (total) ^d	3.96 ^{+1.37} _{-2.57}	4.70 ^{+3.58} _{-2.04}	4.73 ^{+3.62} _{-2.12}	4.85 ^{+3.75} _{-2.10}	3.65 ^{+1.64} _{-1.64}	4.57 ^{+2.27} _{-3.05}	4.60 ^{+1.54} _{-3.27}	4.76 ^{+3.35} _{-2.75}	4.76 ^{+3.35} _{-2.75}	4.56 ^{+2.04} _{-0.98}		
(AGN) ^d	—	—	—	—	3.65 ^{+1.64} _{-1.64}	4.57 ^{+2.27} _{-3.05}	4.60 ^{+1.54} _{-3.27}	4.76 ^{+3.35} _{-2.75}	4.76 ^{+3.35} _{-2.75}	4.56 ^{+1.92} _{-1.01}		
L _{0.2–2keV} (total) ^e	0.29 ^{+0.12} _{-0.21}	0.31 ^{+0.09} _{-0.06}	0.31 ^{+0.09} _{-0.06}	0.31 ^{+0.09} _{-0.06}	0.86 ^{+0.20} _{-0.41}	0.31 ^{+0.05} _{-0.05}	0.31 ^{+0.06} _{-0.05}	0.31 ^{+0.05} _{-0.05}	0.31 ^{+0.05} _{-0.05}	0.64 ^{+0.26} _{-0.26}		
(AGN) ^e	—	—	—	—	0.86 ^{+0.20} _{-0.41}	0.31 ^{+0.05} _{-0.05}	0.31 ^{+0.06} _{-0.05}	0.31 ^{+0.05} _{-0.05}	0.31 ^{+0.05} _{-0.05}	0.48 ^{+0.26} _{-0.26}		
L _{2–10keV} (total) ^e	1.16 ^{+0.40} _{-0.76}	1.39 ^{+1.06} _{-0.60}	1.40 ^{+1.06} _{-0.62}	1.44 ^{+1.11} _{-0.62}	1.07 ^{+0.43} _{-0.30}	1.35 ^{+0.67} _{-0.90}	1.36 ^{+0.45} _{-0.45}	1.40 ^{+0.96} _{-0.81}	1.40 ^{+0.96} _{-0.81}	1.35 ^{+0.45} _{-0.29}		
(AGN) ^e	—	—	—	—	1.07 ^{+0.43} _{-0.30}	1.35 ^{+0.67} _{-0.90}	1.36 ^{+0.45} _{-0.45}	1.40 ^{+0.96} _{-0.81}	1.40 ^{+0.96} _{-0.81}	1.35 ^{+0.57} _{-0.30}		

[†]Model A: Absorption_{Galactic} × Absorption_{source} × PL. Model B: Absorption_{Galactic} × Absorption_{source} × (PL + Line). Model C: Absorption_{Galactic} × [MEKAL + Absorption_{source} × (PL + Line)], where MEKAL is the Mewe, Kaastra, & Liedahl thermal plasma model (see the XSPEC manual for details), PL is a power-law model representing the AGN, Line is the Fe K emission line with a Gaussian profile, Absorption_{Galactic} is the absorption from N_{H,Galactic} = 2.45 × 10²⁰ atoms cm⁻², and Absorption_{source} is the intrinsic absorption within the source.

^aIntrinsic (i.e. within the galaxy) column density in units of 10²² atoms cm⁻².

^bFe K line energy (rest frame), width, equivalent width, and thermal gas temperature all in keV.

^cFitting statistics per degrees of freedom. Cash statistics are used for unbinned spectra and spectra binned to at least 3 and 5 counts bin⁻¹, while χ² statistics are used for spectra binned to at least 15 counts bin⁻¹.

^dAbsorption-corrected flux in units of 10⁻¹⁴ ergs cm⁻² s⁻¹. The AGN value includes the flux from both the power-law component and the iron line.

^eAbsorption-corrected luminosity in units of 10⁴² ergs s⁻¹. The AGN value includes the flux from both the power-law component and the iron line.

binned spectrum in subsequent modeling. The iron line is most prominent in the data binned to at least 5 counts bin^{-1} , we will use the spectrum binned to at least 5 counts bin^{-1} as a visual and qualitative check for the model of the unbinned data.

AGN + Starburst Continuum Models

Aside from models A and B mentioned above, we modeled the unbinned spectrum with slightly more complex models to account for the possibility that a starburst may coexist with the AGN in F04103–2838. Cautioning against over-interpreting data with only modest signal-to-noise ratios, even these more “complex” models were kept as simple as possible.

The first model (model C) is a combination of absorbed power-law and MEKAL spectra (with metallicity fixed at solar) representing the emission from the AGN and starburst, respectively. The second model (model D) is a combination of two absorbed power laws, with one power law representing the AGN and the other representing the high mass X-ray binaries (HMXBs) associated with the possible starburst in this object. Finally, a third model (model E) was a combination of the two above mentioned models: a power law for the AGN, a power law for the HMXBs, and a MEKAL model for the hot gas. For all of these models, a Gaussian with centroid energy between 6 and 7 keV was included to model the iron line.

While all of these models give better fitting statistics than the simpler power law models, only model C is a realistic fit to the data. Models D and E are rejected on the grounds that the best-fit power law values are physically unrealistic descriptions of AGNs. Therefore, we adopt model C as the “best-fit model” (Figure 3.4) and list the fitting parameters in Table 3.1. This is perhaps not surprising given that ULIRGs are known from observations at optical and infrared wavelengths to show the presence of both an AGN and a starburst (e.g., Genzel et al. 1998; Kim, Veilleux,

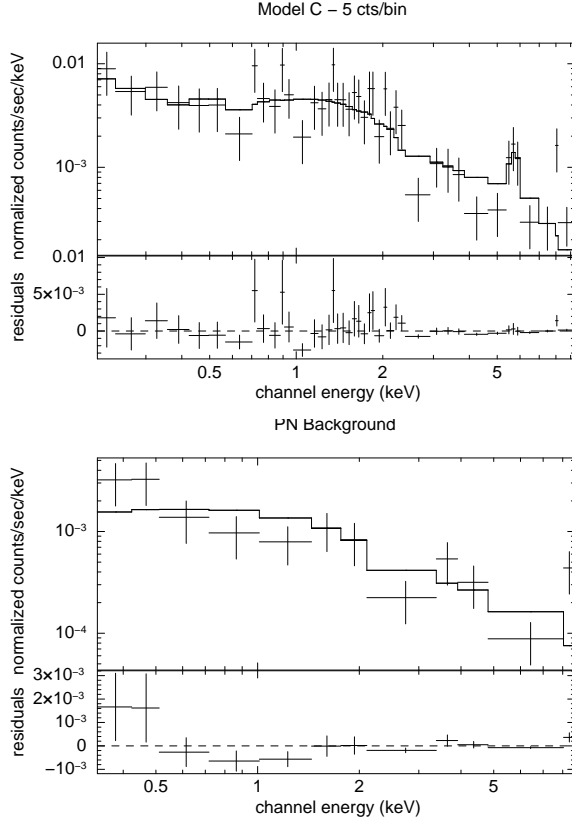


Figure 3.4: EPIC PN source and background spectra of F04103–2838 binned to at least 5 counts bin^{-1} with the best-fit *unbinned* model (C) applied. The X-axis of the figures represents energy in the observer’s frame. *Top*: The source model includes a MEKAL component for the thermal emission, a power-law component to represent the AGN component, a Gaussian component to model the Fe K emission, and a relatively flat power-law ($\Gamma \sim 1.0$) for the background. The model parameters are listed in Table 3.1. *Bottom*: A binned background spectrum with the background model used in the modeling of the unbinned spectrum and spectra binned to at least 5 and 3 counts bin^{-1} . No significant features are seen in the background spectrum.

& Sanders 1998); F04103–2838 does not appear to be an exception.

3.4 Discussion

3.4.1 The Soft Component

The results from the spectral fitting suggest that the soft X-ray (0.2–2 keV) flux is best described as thermal emission from hot gas with $kT \sim 0.1$ keV ($T \sim 1.2 \times 10^6$ K). This is somewhat lower than the range of gas temperatures (0.6–0.8 keV) found in LINERs (González-Martín et al. 2006). The results for F04103–2838 is also somewhat lower than the results from Grimes et al. (2005) who performed a *Chandra* archival study of the soft X-ray emission from starburst galaxies ranging in luminosity from dwarf galaxies to ULIRGs. The authors found that the soft X-ray thermal emission of these starburst galaxies tends to fall in the temperature range $kT \sim 0.25$ –0.8 keV with ULIRGs occupying the upper end of this temperature range. These large temperatures can all be attributed to powerful starbursts.

The soft X-ray emission in F04103–2838 is likely the result of thermal bremsstrahlung from a hot gas produced by the merger-induced starburst or by intrinsically extended soft X-ray emission heated by the AGN. If the ion density equals that of the electrons, the relationship between the electron density (n_e) and luminosity of an emitting region of a given volume (V) is

$$L_{ff} \approx 1.7 \times 10^{-25} n_e^2 f V \text{ ergs s}^{-1}, \quad (3.1)$$

where f is the filling factor for the hot gas³. The non-AGN contribution of the nominal 0.2–2 keV luminosity from the best-fit model (model C) for F04103–2838 is 1.6×10^{41} ergs s⁻¹. Assuming the emitting region is spherical with a diameter of

³Equation 3.1 is based on equation (5.14b) and Figure 5.2 of Rybicki & Lightman (1979) for $T = 10^6$ K in the energy range of 0.2–2 keV.

$\leq 5''^4$, the average electron density has a lower limit of $\sim 0.19 f^{-1/2} \text{ cm}^{-3}$. This value is consistent with simulation results for the warm ($10^{5.5} \lesssim T \lesssim 10^{6.5} \text{ K}$) component in the wind models of Strickland & Stevens (2000). Conversely, if we assume that the electron density and the filling factor are both unity, then the above equation implies that the emitting region is $\sim 0.3 \text{ kpc}$, consistent with the source being unresolved by *Chandra* (Teng et al. 2005).

Observationally, this hot gas component is difficult to probe because of its low density and emissivity. Strickland & Stevens (2000) performed hydrodynamic simulations of starburst-driven galactic winds with various ISM models. The authors found that, in general, the soft X-ray emission comes from gas with low filling factors ($10^{-3} < f < 10^{-1}$; see also Cecil, Bland-Hawthorn, & Veilleux 2002; and Strickland et al. 2004a, 2004b for observational constraints). Using these values for f , the electron density of the hot gas in F04103–2838 is $\sim 0.6\text{--}5.9 \text{ cm}^{-3}$, consistent with values derived by Netzer et al. (2005) in a better studied U/LIRG, NGC 6240.

The soft X-ray emission detected in F04103–2838 may be thus the result of superwinds from the starburst. X-ray superbubbles have been observed in Arp 220 (Iwasawa et al. 2005) and NGC 6240 (Netzer et al. 2005). Furthermore, powerful outflow events are now thought to take place in most ULIRGs (e.g., Rupke et al. 2002, 2005a, b, c, though their sample did not include F04103–2838).

⁴While the selection of a $\leq 5''$ emitting region is based on the spatial resolution of the telescope, it should be noted that the linear diameter of $5''$ at the distance of F04103–2838 is less than a factor of two larger than the soft X-ray (0.5–2.5 keV) emitting region of NGC 6240 (Komossa et al. 2003). Therefore, the assumption of a $\leq 5''$ diameter is reasonable, even though it was chosen based on the instrument PSF.

3.4.2 The Iron Feature

F04103–2838 joins the growing list of ULIRGs with Fe K detections [e.g., Arp 220 (Iwasawa et al. 2005), Z11598-0112 (§2.1), F19254-7245 (Braitto et al. 2003; Franceschini et al. 2003), Mrk 231 (Braitto et al. 2004; Maloney & Reynolds 2000; Ptak et al. 2003), F05189-2524 (Ptak et al. 2003), Mrk 273 (Ptak et al. 2003), and UGC 05101 (Imanishi et al. 2003; Ptak et al. 2003)], supporting the view that an obscured AGN exists in many of these objects. The presence of an AGN in F04103–2838 was first suggested by §2.1 based on the large hard X-ray to far-infrared flux ratio; the *XMM* detection of Fe K now indicates that the luminosity of this AGN has probably been underestimated.

Few LINERs have detected Fe $K\alpha$ lines. Terashima et al. (2002) studied a sample of 53 LINERs and low-luminosity Seyfert galaxies using *ASCA*. Of the 21 LINERs in their sample, Fe emission lines were detected in only five galaxies (NGC 1052, NGC 3998, NGC 4261, NGC 4579, and NGC 4736). Of these five objects, four (i.e. those excluding NGC 4261) have centroid line energies consistent within the uncertainties of the measurements with Fe $K\alpha$ emission due to neutral iron ($E \sim 6.4$ keV).

Three other LINERs have known Fe K detections; all three are powerful luminous or ultraluminous infrared galaxies. These galaxies are Arp 220 (Iwasawa et al. 2005), NGC 6240 (Komossa et al. 2003; Ptak et al. 2003), and UGC 5101 (Imanishi et al. 2003; Ptak et al. 2003). *Chandra* observations of Arp 220, the archetypal ULIRG, show an iron line at 6.7 ± 0.1 keV. This is consistent with emission due to Fe XX up to Fe XXVI, but not neutral iron at 6.4 keV (Iwasawa et al. 2005). Komossa et al. (2003) detected Fe K emission from each of the two nuclei in NGC 6240. Their analysis showed that the iron lines in each nucleus are consistent with Fe $K\alpha$ and

Fe $K\beta$ emissions.

In Figure 3.5 we show the distribution of published Fe K equivalent widths of all LINERs and ULIRGs known to have line emission. Arp 220, NGC 6240, and F04103–2838 appear to have iron emission with the greatest EW measurements of all the LINERs and ULIRGs. These large Fe K features could be results of the blending of multiple narrower lines. Komossa et al. (2003) did not publish the EWs of the lines from each of the nuclei in NGC 6240. The result quoted here is from Ptak et al. (2003). The authors did not distinguish Fe $K\alpha$ emission from Fe $K\beta$ emission and the EW measurement is likely dominated by the brighter southern nucleus alone. The large equivalent widths of the ULIRGs are telltale signs of obscured AGNs where line-of-sight columns of material exceeding 10^{24} cm^{-2} prevent a direct view of the AGN; the 2 – 10 keV flux is dominated by light scattered off electrons (e.g., Ghisellini et al. 1994; Krolik et al. 1994). The large amount of molecular gas ($\sim 10^4 M_{\odot} \text{ pc}^{-2}$) within 400 pc from the nuclei of NGC 6240 (e.g., Bryant & Scoville 1999) is sufficient to cause this obscuration. A similar explanation likely applies to F04103–2838, although we are not aware of any CO measurements in this system.

Interestingly, the Fe K complex in NGC 6240 breaks up into a number of narrow lines. Both Netzer et al. (2005) and Boller et al. (2003) detected Fe K lines due to neutral iron ($6.41 \pm 0.2 \text{ keV}$), Fe XXV ($6.68 \pm 0.02 \text{ keV}$), and Fe XXVI ($7.01 \pm 0.04 \text{ keV}$) in NGC 6240. Komossa et al. (2003) also detected lines at 6.4 and 6.95 keV. The centroid energies of the lines due to neutral iron and Fe XXV in NGC 6240 are consistent with the respective centroid energies suggested by the doublet in the F04103–2838 3 counts bin^{-1} data. Although simulations suggest the two line model is only significant at the $\sim 60\%$ level, a FWHM of $\sim 30000 \text{ km s}^{-1}$ ($\sigma \sim 0.3 \text{ keV}$) seems too broad and the two component interpretation may be more likely. The Fe XXVI line in NGC 6240 is much fainter than the other lines so it is not

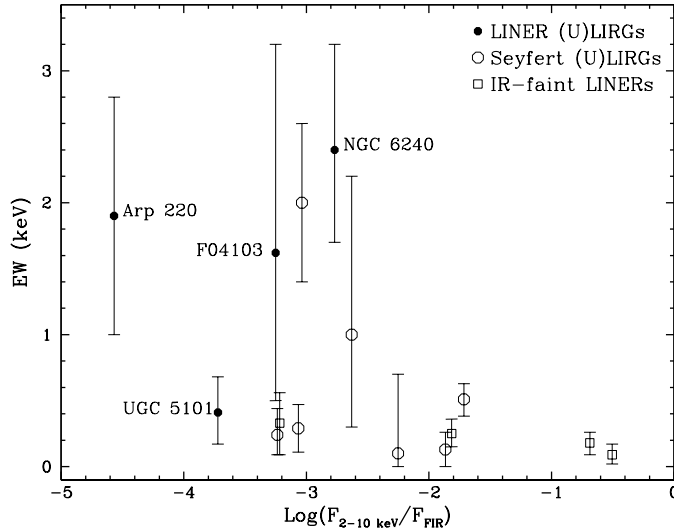


Figure 3.5: Distribution of equivalent widths of Fe K emission features in LINERs and U/LIRGs versus absorption-corrected 2–10 keV to far-infrared flux ratio. In general, the U/LIRGs have higher EWs than IR-faint LINERs. Of these, F19254–7245 (EW \sim 2 keV) was determined to be Compton-thick by Braito et al. (2003). The values included in this figure are drawn from Terashima et al. (2002), Braito et al. (2003), Imanishi et al. (2003), Ptak et al. (2003), Braito et al. (2004), Imanishi & Terashima (2004), Iwasawa et al. (2005), §2.1, and this work. The equivalent widths for the four LINER U/LIRGs included in this sample are labeled. The F04103–2838 value plotted is derived from our best-fit model (C). Note that Komossa et al. (2003) detected Fe K emission from each of the two nuclei in NGC 6240. Therefore, the single value quoted by Ptak et al. (2003) is a sum of the Fe K α and Fe K β emission due to neutral iron, likely dominated by the brighter southern nucleus. The value quoted for Arp 220 may also be due to a blend of emission lines arising from ionized iron (Fe XX up to Fe XXVI). The value (\sim 0.5 keV) quoted for the ULIRG Mrk 463 is a sum of the emission due to neutral iron and Fe XXV.

surprising that we were unable to detect this feature in the modest signal-to-noise ratio data of F04103–2838.

Despite their X-ray similarities, F04103–2838 is \sim 2.5 times more infrared luminous than NGC 6240. These objects also differ in terms of *IRAS* f_{25}/f_{60} ratios (0.15 for NGC 6240 and 0.30 for F04103–2838) and merger state (NGC 6240 is in a pre-merger phase with a nuclear separation of \sim 1.3 kpc while F04103–2838 is in the post-merger stage with a single coalesced nucleus). There is growing observational

evidence (e.g., Dasyra et al. 2006a, 2007, 2006b; Ishida 2004; Veilleux et al. 2006, 2002) and theoretical motivation (e.g., Hopkins et al. 2005) that mergers of gas-rich galaxies often produce “cool” ($f_{25}/f_{60} < 0.2$) luminous infrared galaxies that evolve into “warm” ($f_{25}/f_{60} \geq 0.2$) ULIRGs before becoming optical quasars. If this evolutionary sequence applies to NGC 6240 and F04103–2838, the first object may actually be the precursor to the latter.

3.4.3 Energy Source of the ULIRG

The lack of short timescale variability (see §3.3.2) is to be expected if most of the primary X-ray flux is being absorbed or reprocessed. As discussed in §4.2, the large equivalent width of the iron line in F04103–2838 implies the presence of a highly obscured AGN. It is very difficult in such cases to estimate the intrinsic luminosity of the AGN without measurements of the > 10 keV flux from the buried AGN (e.g., Mrk 231; Braitto et al. 2004). Here we follow the method of Maloney & Reynolds (2000) to estimate the intrinsic luminosity of F04103–2838.

In their analysis of an *ASCA* observation of Mrk 231, they discussed two ways of estimating the intrinsic AGN flux. The observed X-ray flux is due to a combination of two effects: reflection and scattering. Maloney & Reynolds (2000) estimated the intrinsic AGN flux from the reflection and the scattering components separately. In their geometry, the observer has an obstructed view of the nucleus so the observed flux must be either scattered or reflected into the line of sight along which there is some amount of absorbing material. The reflected component is light from the central engine reflected off of the circumnuclear torus; the amount of reflection depends on the size of the reflecting surface, the composition of the torus, and geometry. On the other hand, the scattered component is light from the central engine (unobstructed by the torus) scattered into the line of sight. Based on their

spectral fitting of the *ASCA* data, Maloney & Reynolds (2000) found that the X-ray flux of Mrk 231 is scattering-dominated with 75% scattered and 25% reflected light.

Due to the low signal-to-noise ratio of our data on F04103–2838, the same spectral fitting as performed by Maloney & Reynolds (2000) could not be done. The large equivalent width of the Fe K α line (~ 1.6 keV) above 1 keV suggests a reflection-dominated spectrum. However, the width of the line implies it could be a blend of narrower Fe K α and ionized iron emission lines (as suggested by the 3 counts bin $^{-1}$ data). If this were the case, the Fe K α EW may be more consistent with a scattering dominated spectrum. Therefore, we will consider two cases: (1) the majority of the observed flux is due to reflection and (2) the majority of the observed flux is due to scattering to estimate the intrinsic X-ray luminosity of the AGN.

After correction for absorption, the nominal 0.2–10 keV flux of the buried AGN in F04103–2838 derived from our best-fit model (model C) is 1.83×10^{42} ergs s $^{-1}$. In the first scenario, we will assume the reflection component is 75% and the scattering component is 25% of the total observed flux. This implies that $L_{\text{scattered}} = 0.45 \times 10^{42}$ ergs s $^{-1}$ and $L_{\text{reflected}} = 1.38 \times 10^{42}$ ergs s $^{-1}$ for the AGN in F04103–2838. In Maloney & Reynolds (2000), the luminosity from the reflected portion is scaled up by a factor of 25 in their modeling of the reflection process. The reflection process differs for different galaxies; it depends on the ionization state of the mirror and the steepness of the photon index of the central black hole. Maloney & Reynolds (2000) assumed reflection from neutral material, a reflecting fraction of 10%, and the canonical value of the photon index due to an AGN ($\Gamma = 1.8$). The scaling factor used by Maloney & Reynolds (2000) corrects for the flattening of a spectrum with $\Gamma = 1.8$ to $\Gamma \sim 1.1$ (based on a single absorbed power-law model) for Mrk 231 due to reflection. The correction factor of 25, therefore, is a maximum correction factor. The minimum scaling factor is 10 to simply correct for a reflecting surface

fraction of 10%. We will conservatively assume this minimum scaling factor of 10 for the reflection component. For the scattering component, we will assume the same scattering fraction as Maloney & Reynolds (2000) (i.e. 1% for electron scattering). After the corrections, the intrinsic 0.2–10 keV luminosity of the AGN in this scenario, where reflection dominates the observed flux, is 1.4×10^{43} ergs s⁻¹ (from reflection) and 4.5×10^{43} ergs s⁻¹ (from scattering). Therefore, the total reflection- and scattering-corrected luminosity in the 0.2–10 keV band is 5.9×10^{43} ergs s⁻¹ if we assume reflected light dominates the observed spectrum.

Similarly, for the second scenario where the majority of the observed flux was scattered into the line of sight, we will assume the reflection component is 25% and the scattering component is 75% of the total observed flux. This implies that the intrinsic 0.2–10 keV luminosity of the AGN is 4.5×10^{42} ergs s⁻¹ (from reflection) and 1.4×10^{44} ergs s⁻¹ (from scattering). Hence, the corrected 0.2–10 keV luminosity is 1.4×10^{44} ergs s⁻¹. It should be noted that in both cases we considered, the luminosity from the scattering portion dominated the total after the corrections.

Thus, with the assumptions made above, the intrinsic 0.2–10 keV luminosity of the AGN ranges from 0.6 to 1.4×10^{44} ergs s⁻¹. This range in luminosity overlaps with that of quasars ($\sim 10^{44}$ ergs s⁻¹; e.g., Elvis et al. 1994; Piconcelli et al. 2005) and is similar to that of NGC 6240 ($\sim 0.7 - 2 \times 10^{44}$ ergs s⁻¹, after correction for an HI column density of $1 - 2 \times 10^{24}$ cm⁻²; Vignati et al. 1999). The ratio $\log(L_{2-10 \text{ keV}}/L_{\text{IR}})$ for F04103–2838 corrected for scattering and reflection is -2.2 to -1.7. These values fall precisely within the range found in radio-quiet PG quasars (-3 to -1; Sanders et al. 1989). Assuming F04103–2838 has the same X-ray to bolometric luminosity ratio as radio-quiet QSOs (Elvis et al. 1994, $L_x/L_{\text{bol}} \sim 3\%$), the AGN contribution to the bolometric luminosity of F04103–2838 is $\sim 15\text{--}38\%$. Therefore, within the large uncertainties, the AGN in F04103–2838, while not dominating the

total energy output, is an important contributor to the overall energetics of the galaxy.

3.5 Summary

The results from our analysis of the *XMM-Newton* spectrum of the 1-Jy ULIRG/LINER F04103–2838 can be summarized as follows:

1. The soft (0.2–2 keV) X-ray flux of F04103–2838 is attributed to hot gas with $kT \sim 0.1$ keV. This temperature is similar to that derived in other starburst galaxies and LINERs. The electron density in F04103–2838 is $\sim 0.6\text{--}5.9$ cm^{-3} , consistent with theoretical predictions and observational estimates in wind systems.
2. An Fe $K\alpha$ line located at ~ 6.4 keV with an equivalent width of ~ 1.6 keV is detected in F04103–2838. The line could be intrinsically broad or could be made up of two narrow lines located at rest frame energies of ~ 6.3 and 6.7 keV but this decomposition is only significant at the $\sim 60\%$ level, so it needs to be verified with higher resolution spectra.
3. The large equivalent width of the Fe $K\alpha$ line suggests that the AGN is Compton-thick. Using simple assumptions, we estimate that the intrinsic 0.2–10 keV luminosity of this AGN is $0.6 - 1.4 \times 10^{44}$ ergs s^{-1} . If these assumptions are correct and the galaxy has a QSO-like X-ray to bolometric luminosity ratio, the AGN detected by our observations does not dominate the bolometric luminosity of F04103–2838.
4. The X-ray spectral characteristics of F04103–2838 are strikingly similar to those of the local luminous infrared galaxy NGC 6240. Given the similar-

ties in X-ray properties but differences in merger state and in infrared color and luminosity, objects like NGC 6240 could conceivably be the precursors of ULIRGs like F04103–2838.

Chapter 4

The X-ray Properties of the *IRAS* Revised Bright Galaxy Survey Sample

4.1 Introduction

Franceschini et al. (2003); Ptak et al. (2003); Teng et al. (2005) only focused on the upper end of the infrared luminosity function, *i.e.* mostly objects after the first peri-passage (Veilleux et al. 2002). To get a complete picture of the merger process, LIRGs also need to be studied in a similar fashion. The present study extends previous surveys to a lower luminosity range (down to $L_{IR} \simeq 10^{11.3} L_{\odot}$) with objects chosen from the *IRAS* RBGS (Sanders et al. 2003). The RBGS objects are the brightest 60 μm extragalactic sources in the sky. With 629 galaxies, the sample is large enough to provide a temporal account of the merging process. The objects contained in the RBGS are in various stages of merging: disk galaxies in small groups prior to the first peri-passage, interacting pairs with tidal tails, close binaries, and

merged galaxies. Observations of these objects would provide an unbiased picture of the X-ray properties of U/LIRGs along the merger sequence.

The organization of this chapter is as follows. The sample is discussed in §4.2. The observation and reduction method of the archived data are described in §4.3. The results from the analysis of the archived data are presented in §4.4. They are then combined with those from the literature in §4.5 to look for trends with global optical and infrared properties. Finally, the results are summarized in §4.6. Appendix B includes information on each individual source in the sample. Appendix C discusses the properties of some ultraluminous X-ray source (ULX) candidates found in our sample of sources. In this paper, we adopt $H_0=75 \text{ km s}^{-1} \text{ Mpc}^{-1}$, $\Omega_M=0.3$, and $\Omega_\Lambda=0.7$. All luminosities presented in this chapter are based on this cosmology.

4.2 The Sample

Our sample consists of two subsets. The first subset consists of 34 galaxies from the *Chandra* archive that are in the RBGS with $L_{IR} > 10^{11.3} L_\odot$. This subset is composed of data from two different surveys: a survey of eight binary “NGC 6240-like” galaxies (PI: Komossa, AO7; see Komossa et al. 2003) and a survey of 26 RBGS galaxies with $L_{IR} > 10^{11.5} L_\odot$ (PI: Sanders, AO8). Together, these two surveys cover the range in infrared luminosities from $10^{11.3-12.6} L_\odot$. Table 4.1 lists the basic properties of this subset. The second subset consists of the 22 galaxies observed by Ptak et al. (2003) and Teng et al. (2005) with *Chandra*. The results from these papers will be combined with those from the first subset in § 4.5.3.

Table 4.1. The Sample

Object	z	$\log(\frac{L_{\text{IR}}}{L_{\odot}})$	$\log(\frac{f_{25\mu\text{m}}}{f_{60\mu\text{m}}})$	Spectral Type	Nuclei #	Nuclear Separation	$N_{\text{H,Galactic}}$ [10^{20} cm^{-2}]	Scale [kpc/'']	D_{L} [Mpc]
(1)	(2)	(3)	(4)	(5)	(6)	(7)	(8)	(9)	(10)
IRAS F01364-1042	0.048	11.94	-1.19	L ¹	1:1	...	2.5	0.88	198.9
III Zw 035	0.027	11.56	-1.12	L (N)/H II (S) ¹	2:2	6.6	5.1	0.51	110.2
IRAS 03359+1523	0.035	11.51	-1.02	H II ¹	1:2	10.6	14.8	0.65	143.7
ESO 203-IG001	0.053	11.99	-1.11	...	1:2	6.6	1.8	0.96	220.4
VII Zw 031	0.054	12.12	-0.98	H II ²	1:1	...	8.0	0.98	224.7
ESO 255-IG007	0.039	12.00	-0.78	...	1:3	13.7; 30.5 ^b	5.0	0.72	160.5
IRAS 07251-0248	0.088	12.57	-1.01	...	1:1	...	16.1	1.54	375.0
ESO 60-IG016	0.046	11.89	-0.90	...	1:2	13.2	8.2	0.84	190.3
IRAS F08572+3915	0.058	12.09	-0.64	L ¹	1:2	3.9	2.6	1.05	242.0
IRAS 09022-3615	0.060	12.43	-0.99	...	1:1	...	29.3	1.08	250.7
IRAS F09111-1007	0.054	12.17	-1.18	H II/S 2 ²	1:1	...	4.8	0.98	224.7
UGC 04881	0.039	11.75	-0.94	H II (NE)/H II (SW) ¹	2:2	11.5	1.5	0.72	160.5
IRAS F10038-3338 ^a	0.034	11.83	-0.91	...	2:2	...	8.8	0.63	139.4
IRAS F10173+0828	0.049	11.99	-0.96	...	1:1	...	3.0	0.90	203.2
IRAS 13120-5453	0.031	12.39	-1.15	S 2 ²	1:1	...	26.1	0.58	126.9
VV 250B ^a	0.031	11.88	-0.74	L/H II ²	1:2	34.5	1.9	0.58	126.9
UGC 08387	0.023	11.76	-1.05	L ¹	1:1	...	1.0	0.43	93.6
IRAS 14348-1447	0.083	12.31	-1.14	L (NE)/L (SW) ¹	2:2	4.0	7.8	1.46	352.5
IRAS F14378-3651	0.068	12.27	-1.07	L/S 2 ²	1:1	...	6.1	1.22	258.8
VV 340A	0.033	11.79	-1.17	L/H II ²	1:2	36.9	3.2	0.61	135.2
I Zw 107	0.041	11.86	-0.82	H II (N)/L (S) ¹	2:2	6.5	1.9	0.76	169.0
NGC 6090	0.029	11.45	-0.78	H II (NE)/H II (SW) ¹	1:2	4.2	1.6	0.54	118.5
ESO 069-IG006	0.046	12.06	-1.00	...	2:2	70.5	8.6	0.84	190.3
IRAS F17132+5313	0.051	12.07	-1.07	H II (NE) ¹	2:2	5.8	2.7	0.93	211.8
IRAS F18293-3413	0.018	11.92	-0.95	H II ¹	1:1	...	12.7	0.34	72.9
ESO 593-IG008 ^a	0.049	12.06	-1.08	H II (N)/L (S) ¹	2:2	...	10.8	0.90	203.2
IRAS F19297-0406	0.086	12.33	-1.08	H II ¹	1:1	...	19.4	1.50	366.0
IRAS 19542+1110	0.065	12.09	-1.03	...	1:1	...	15.1	1.17	272.6
CGCG 448-020	0.036	12.06	-0.75	H II ²	2:2	10.6	11.0	0.67	147.9
IRAS 21101+5810	0.039	11.71	-1.02	...	1:1	...	44.8	0.72	160.5
ESO 239-IG002	0.043	11.96	-0.78	...	1:1	...	1.4	0.79	177.5
IRAS F22491-1808	0.077	12.36	-0.99	H II ¹	1:1	...	2.7	1.36	325.7
NGC 7592	0.024	11.32	-0.94	H II (E)/S 2 (W) ¹	2:2	12.9	4.0	0.45	97.7
ESO 077-IG014	0.042	11.90	-1.11	H II ²	2:2	16.8	3.0	0.71	173.3

Note. — Col. (1): Object name. Col (2): redshift. Col. (3): logarithm of infrared (8–1000 μm) luminosity relative to solar. Col. (4): logarithm of the 25-to-60 μm *IRAS* flux ratio, a measure of the dust temperature. Col. (5): optical galaxy spectral type: S = Seyfert, L = LINER (¹ Veilleux et al. [1995] classification; ² NED classification, which is more uncertain). Col. (6): the right number is the number of optical nuclei in the interacting system and the left number is the number of optical nuclei in the DSS image that lies within the *IRAS* 3- σ error ellipse (see Sanders et al. 2003). Col. (7): Nuclear separation in arcseconds for objects with multiple nuclei determined from the DSS images. Col. (8): Galactic hydrogen column density (Dickey & Lockman 1990). Col. (9): physical size corresponding to 1''. Col. (10): luminosity distance.

^aSee note on this source in Appendix B.

^bNuclear separation of nuclei B and C relative to nucleus A, respectively.

Table 4.2. Journal of Observations

Object	PI	Observation	Date	Exposure
(1)	Name	ID	[UT]	[ksec]
(1)	(2)	(3)	(4)	(5)
IRAS F01364-1042	Sanders	7081	10 September 2007	14.6
III Zw 035	Komossa	6855	24 February 2006	14.8
IRAS 03359+1523	Komossa	6856	17 December 2005	14.8
ESO 203-IG001	Sanders	7802	17 January 2008	14.8
VII Zw 031	Sanders	7887	27 May 2007	15.0
ESO 255-IG007	Sanders	7803	27 May 2007	13.6
IRAS 07251-0248	Sanders	7804	01 December 2006	15.6
ESO 60-IG016	Sanders	7888	31 May 2007	14.8
IRAS F08572+3915	Komossa	6862	26 January 2006	14.6
IRAS 09022-3615	Sanders	7805	04 September 2007	14.8
IRAS F09111-1007	Sanders	7806	20 March 2007	14.8
UGC 4881	Komossa	6857	12 January 2006	14.8
IRAS F10038-3338	Sanders	7807	07 March 2007	14.4
IRAS F10173+0828	Sanders	7808	18 January 2008	15.0
IRAS 13120-5453	Sanders	7809	01 December 2006	14.8
VV 250B	Sanders	7010	22 August 2007	14.6
UGC 08387	Sanders	7811	12 February 2007	14.2
IRAS 14348-1447	Komossa	6861	12 March 2006	14.8
IRAS F14378-3651	Sanders	7889	25 June 2007	14.0
VV 340A	Sanders	7812	17 December 2006	15.2
I ZW 107	Komossa	6858	11 September 2006	14.6
NGC 6090	Komossa	6859	14 May 2006	14.8
ESO 069-IG006	Sanders	7813	21 June 2007	14.6
IRAS F17132+5313	Sanders	7814	03 April 2007	14.8
IRAS F18293-3413	Sanders	7815	25 February 2007	13.8
ESO 593-IG008	Sanders	7816	09 June 2007	15.0
IRAS F19297-0406	Sanders	7890	18 June 2007	16.6
IRAS 19542+1110	Sanders	7817	10 September 2007	15.0
CGCG 448-020	Sanders	7818	10 September 2007	14.6
IRAS 21101+5810	Sanders	7819	01 July 2007	15.0
ESO 239-IG002	Sanders	7820	10 September 2007	14.6
IRAS F22491-1808	Sanders	7821	13 July 2007	14.4
NGC 7592	Komossa	6860	15 October 2006	13.6
ESO 077-IG014	Sanders	7822	26 January 2008	15.0

Note. — Col. (1): Object name. Col (2)–(3): *Chandra* principal investigator of the proposal and observation identification number. Col. (4): beginning date in UT. Col. (5): net exposure time in kiloseconds after screening for good time intervals.

4.3 Observations and Reduction on Archived Data

Galaxies in the first subset were observed by *Chandra* between December, 2005 and January, 2008. Each galaxy was observed in a single exposure using the ACIS S3 CCD chip for ~ 15 ks. The actual dates and exposure times of the observations are listed in Table 4.2.

The data reduction was done using CIAO version 3.4.1 and CALDB version 3.4.2. The effects of the calibration updates since version 3.4.2 are negligible for CCD resolution observations of our sources due to the low signal-to-noise ratios. The data reduction followed the procedures outline in the Science Analysis Threads for ACIS data at the CIAO Web site¹.

4.4 Analysis and Results on Archived Data

4.4.1 Imaging

For the imaging analysis portion of this paper, the optical positions of the galaxies were determined using the IDL `cntrd` routine from the Palomar Digitized Sky Survey (DSS) images. The routine returns the X and Y positions of the centroid starting from user-provided initial guess positions. The sky coordinates of the centroid were then found using the DS9 software from SAO based on the centroid position on the image. The DSS centroid coordinates are listed in Table 4.3. Determination of more accurate coordinates from archived *HST* data is postponed until Evans et al.(2010, in prep.).

¹<http://cxc.harvard.edu/ciao3.4/index.html>

Table 4.3: Results on Detected RBGS Sources

Object	Nucleus ID	DSS Centroid RA	DSS Centroid Dec	Extended?	Total Counts	Hard Counts	Soft Counts	Hardness Ratio	Estimated Γ	Estimated $F_{0.5-2 \text{ keV}}$	Estimated $F_{2-10 \text{ keV}}$
(1)	(2)	(3)	(4)	(5)	(6)	(7)	(8)	(9)	(10)	(11)	(12)
IRAS F01364-1042		01 38 52.84	-10 27 11.4	no	26	15 ^{+4.96} _{-3.83}	11 ^{+4.42} _{-3.27}	0.15 ^{+0.25} _{-0.19}	0.45 ^{+0.41} _{-0.71}	0.282 ^{+0.0004} _{-0.0028}	3.64 ^{+1.49} _{-0.64}
III Zw 035	NE	01 44 30.61	+17 06 08.4	no	43	12 ^{+4.56} _{-3.42}	31 ^{+6.63} _{-5.54}	-0.44 ^{+0.18} _{-0.27}	1.62 ^{+0.43} _{-0.45}	0.84 ^{+0.01} _{-0.01}	1.72 ^{+0.25} _{-0.25}
	SW	01 44 30.39	+17 06 02.6	no	23	9 ^{+4.11} _{-2.94}	14 ^{+4.83} _{-3.70}	-0.22 ^{+0.20} _{-0.20}	1.16 ^{+0.50} _{-0.65}	0.37 ^{+0.06} _{-0.04}	1.56 ^{+0.54} _{-0.29}
IRAS 03359+1523	E ^a	03 38 47.08	+15 32 54.9	yes	90	16 ^{+5.08} _{-3.96}	74 ^{+9.60} _{-7.95}	-0.64 ^{+0.10} _{-0.08}	2.36 ^{+0.36} _{-0.35}	2.74 ^{+0.12} _{-0.14}	1.79 ^{+0.22} _{-0.17}
	W	03 38 46.35	+15 32 55.8	no	2	1 ^{+0.83} _{-0.83}	1 ^{+0.83} _{-0.83}	0.00 ^{+0.59} _{-0.59}	0.90 ^{+1.45} _{-0.90} b	0.03 ^{+0.01} _{-0.01}	0.20 ^{+0.08} _{-0.08}
ESO 203-IG001	NE ^a	04 46 49.50	-48 33 30.1	no	2	0 ^{+0.00} _{-0.00}	2 ^{+1.29} _{-1.29}	-1.00 ^{+0.00} _{-0.00}
VII Zw 031		05 16 46.41	+79 40 13.2	yes	177	31 ^{+6.63} _{-5.54}	146 ^{+12.08} _{-12.08}	-0.65 ^{+0.07} _{-0.28}	2.25 ^{+0.24} _{-0.28}	4.39 ^{+0.09} _{-0.09}	3.52 ^{+0.35} _{-0.25}
ESO 255-IG007	A ^a	06 27 21.70	-47 10 35.9	yes	217	37 ^{+7.14} _{-6.06}	180 ^{+13.42} _{-13.42}	-0.66 ^{+0.06} _{-0.05}	2.20 ^{+0.21} _{-0.24}	5.45 ^{+0.07} _{-0.07}	4.68 ^{+0.40} _{-0.30}
	B	06 27 22.57	-47 10 46.3	yes	88	22 ^{+5.65} _{-4.50}	66 ^{+8.00} _{-8.00}	-0.50 ^{+0.01} _{-0.01}	1.77 ^{+0.33} _{-0.33}	1.96 ^{+0.03} _{-0.03}	3.24 ^{+0.35} _{-0.35}
	C	06 27 23.12	-47 11 02.7	no	20	10 ^{+3.11} _{-3.11}	10 ^{+3.11} _{-3.11}	0.00 ^{+0.30} _{-0.30}	0.75 ^{+0.53} _{-0.53}	0.29 ^{+0.003} _{-0.003}	2.26 ^{+0.95} _{-0.46}
IRAS 07251-0248		07 27 37.66	-02 54 56.7	no	5	0 ^{+1.84} _{-0.00}	5 ^{+3.38} _{-2.16}	-1.00 ^{+0.74} _{-0.00}
ESO 60-IG016	E ^a	08 52 31.97	-69 01 56.5	yes	114	73 ^{+9.05} _{-9.05}	41 ^{+7.46} _{-6.38}	0.28 ^{+0.10} _{-0.09}	0.28 ^{+0.20} _{-0.28}	1.14 ^{+0.004} _{-0.003}	19.04 ^{+2.78} _{-1.75}
IRAS F08572+3915	NW ^a	09 00 25.43	+39 03 53.1	no	9	7 ^{+3.75} _{-3.75}	2 ^{+2.54} _{-2.54}	0.56 ^{+0.49} _{-0.49}	-0.43 ^{+0.67} _{-0.67} b	0.05 ^{+0.01} _{-0.01}	26.08 ^{+7.84} _{-7.84}
IRAS 09022-3615		09 04 12.67	-36 27 01.0	yes	252	109 ^{+10.44} _{-10.44}	143 ^{+11.96} _{-11.96}	-0.13 ^{+0.06} _{-0.06}	1.38 ^{+0.19} _{-0.15}	6.15 ^{+0.14} _{-0.14}	17.81 ^{+1.13} _{-1.30}
IRAS F09111-1007		09 13 38.77	-10 19 20.6	yes	95	15 ^{+4.96} _{-3.83}	80 ^{+9.98} _{-8.93}	-0.68 ^{+0.09} _{-0.07}	2.26 ^{+0.39} _{-0.35}	2.23 ^{+0.04} _{-0.04}	1.70 ^{+0.22} _{-0.19}
UGC 04881	NE	09 15 55.60	+44 19 58.5	no	35	6 ^{+3.58} _{-2.38}	29 ^{+6.45} _{-5.35}	-0.66 ^{+0.18} _{-0.12}	2.11 ^{+0.59} _{-0.58}	0.73 ^{+0.02} _{-0.02}	0.71 ^{+0.17} _{-0.17}
	SW	09 15 54.70	+44 19 52.2	no	25	2 ^{+2.64} _{-1.58}	23 ^{+5.87} _{-4.74}	-0.84 ^{+0.20} _{-0.13}	2.84 ^{+1.02} _{-0.84}	0.05 ^{+0.003} _{-0.003}	0.19 ^{+0.06} _{-0.06}
IRAS F10038-3338	E+W	10 06 04.50	-33 53 06.5	yes	66	16 ^{+3.96} _{-3.96}	50 ^{+7.05} _{-7.05}	-0.52 ^{+0.10} _{-0.10}	1.89 ^{+0.39} _{-0.39}	1.56 ^{+0.04} _{-0.04}	2.14 ^{+0.23} _{-0.23}
IRAS F10173+0828		10 20 00.37	+08 13 30.1	no	11	2 ^{+2.64} _{-1.29}	9 ^{+4.11} _{-2.94}	-0.64 ^{+0.42} _{-0.22}	2.10 ^{+1.08} _{-1.18}	0.23 ^{+0.01} _{-0.01}	0.24 ^{+0.14} _{-0.06}
IRAS 13120-5453		13 15 06.33	-55 09 23.2	yes	293	119 ^{+10.91} _{-10.91}	174 ^{+13.19} _{-13.19}	-0.19 ^{+0.06} _{-0.06}	1.46 ^{+0.15} _{-0.17}	7.21 ^{+0.19} _{-0.15}	18.75 ^{+1.17} _{-1.21}
VV250	B(SE) ^a	13 15 34.93	+62 07 28.1	yes	339	96 ^{+9.75} _{-9.75}	243 ^{+15.59} _{-15.59}	-0.43 ^{+0.05} _{-0.05}	1.53 ^{+0.19} _{-0.15}	6.15 ^{+0.02} _{-0.01}	14.37 ^{+0.78} _{-0.85}
UGC 08387		13 20 35.34	+34 08 22.7	yes	285	70 ^{+8.35} _{-8.35}	215 ^{+14.66} _{-14.66}	-0.51 ^{+0.05} _{-0.05}	1.69 ^{+0.16} _{-0.16}	5.47 ^{+0.03} _{-0.01}	10.10 ^{+0.56} _{-0.56}
IRAS 14348-1447	NE	14 37 38.43	-15 00 20.5	yes	34	6 ^{+3.58} _{-2.38}	18 ^{+5.32} _{-4.20}	-0.50 ^{+0.25} _{-0.17}	1.80 ^{+0.62} _{-0.69}	0.53 ^{+0.03} _{-0.02}	0.80 ^{+0.25} _{-0.15}
	SW	14 37 38.26	-15 00 23.6	no	23	13 ^{+4.7} _{-3.56}	20 ^{+5.55} _{-4.43}	-0.21 ^{+0.22} _{-0.17}	1.20 ^{+0.43} _{-0.52}	0.57 ^{+0.01} _{-0.01}	2.22 ^{+0.58} _{-0.36}
IRAS F14378-3651		14 40 58.92	-37 04 31.9	no	41	25 ^{+6.07} _{-4.97}	16 ^{+5.08} _{-3.96}	0.22 ^{+0.19} _{-0.15}	0.35 ^{+0.36} _{-0.42}	0.45 ^{+0.002} _{-0.001}	6.67 ^{+1.52} _{-1.05}
VV 340	A(N) ^a	14 57 00.65	+24 37 01.6	yes	261	47 ^{+6.83} _{-6.83}	214 ^{+14.63} _{-14.63}	-0.64 ^{+0.05} _{-0.05}	2.10 ^{+1.26} _{-1.26}	5.50 ^{+0.04} _{-0.04}	5.48 ^{+0.47} _{-0.47}
I Zw 107	A(N)	15 18 06.08	+42 44 45.2	yes	147	22 ^{+5.76} _{-4.65}	125 ^{+11.18} _{-11.18}	-0.70 ^{+0.07} _{-0.06}	2.26 ^{+0.27} _{-0.20}	3.23 ^{+0.03} _{-0.03}	2.53 ^{+0.26} _{-0.20}
	B(S)	15 18 06.23	+42 44 38.9	no	16	1 ^{+0.23} _{-0.23}	15 ^{+4.96} _{-3.83}	-0.88 ^{+0.27} _{-0.10}	3.15 ^{+2.10} _{-2.10}	0.40 ^{+0.05} _{-0.02}	0.09 ^{+0.05} _{-0.02}
NGC 6090	NE [†]	16 11 40.48	+52 27 27.5	yes	252	28 ^{+6.35} _{-5.26}	224 ^{+14.97} _{-14.97}	-0.78 ^{+0.05} _{-0.04}	2.55 ^{+0.26} _{-0.23}	5.70 ^{+0.06} _{-0.11}	2.90 ^{+0.21} _{-0.20}
	SW	16 11 40.33	+52 27 23.5	yes	72	9 ^{+2.94} _{-2.94}	63 ^{+8.35} _{-8.35}	-0.75 ^{+0.08} _{-0.08}	2.43 ^{+0.44} _{-0.44}	1.60 ^{+0.05} _{-0.02}	0.97 ^{+0.15} _{-0.11}

Continued on Next Page...

Table 4.3 – Continued

Object	Nucleus ID (2)	DSS Centroid RA (3)	DSS Centroid Dec (4)	Extended? (5)	Total Counts (6)	Hard Counts (7)	Soft Counts (8)	Hardness Ratio (9)	Estimated Γ (10)	Estimated $F_{0.5-2}$ keV (11)	Estimated F_{2-10} keV (12)
ESO 069-IG006	N	16 38 11.81	-68 26 06.7	yes	147	$24^{+5.97}_{-3.96}$	$123^{+11.09}_{-10.09}$	$-0.67^{+0.07}_{-0.07}$	$2.35^{+0.27}_{-0.16}$	$3.90^{+0.10}_{-0.10}$	$2.71^{+0.28}_{-0.25}$
	S	16 38 13.62	-68 27 16.5	no	178	$141^{+11.87}_{-11.87}$	$37^{+7.14}_{-6.06}$	$0.58^{+0.07}_{-0.06}$	$-0.40^{+0.16}_{-0.29}$	$1.05^{+0.001}_{-0.001}$	$52.10^{+8.02}_{-8.96}$
IRAS F17132+5313	NE	17 14 20.35	+53 10 30.6	yes	67	$11^{+4.42}_{-3.27}$	$56^{+7.46}_{-7.39}$	$-0.67^{+0.12}_{-0.09}$	$2.18^{+0.41}_{-0.43}$	$1.46^{+0.03}_{-0.02}$	$1.28^{+0.21}_{-0.15}$
	SW	17 14 19.75	+53 10 28.5	no	4	$0^{+1.84}_{-0.00}$	$4^{+3.16}_{-1.91}$	$-1.00^{+0.92}_{-0.00}$
IRAS F18293-3413		18 32 41.16	-34 11 25.8	yes	434	$119^{+10.91}_{-10.91}$	$315^{+17.75}_{-17.75}$	$-0.45^{+0.04}_{-0.04}$	$1.81^{+0.14}_{-0.14}$	$11.14^{+0.15}_{-0.15}$	$17.20^{+1.00}_{-0.83}$
ESO 593-IG008	N+S	19 14 31.18	-21 19 05.2	yes	80	$16^{+3.96}_{-3.96}$	$64^{+9.10}_{-9.10}$	$-0.60^{+0.11}_{-0.11}$	$2.17^{+0.39}_{-0.39}$	$2.06^{+0.07}_{-0.07}$	$1.88^{+0.28}_{-0.20}$
CGCG 448-020	SE ^a	20 57 24.07	+17 07 35.9	yes	135	$19^{+5.44}_{-4.32}$	$116^{+10.77}_{-10.77}$	$-0.72^{+0.07}_{-0.06}$	$2.57^{+0.30}_{-0.32}$	$4.03^{+0.14}_{-0.14}$	$2.02^{+0.20}_{-0.15}$
	NW	20 57 23.70	+17 07 45.1	no	5	$0^{+1.84}_{-0.00}$	$5^{+3.38}_{-2.16}$	$-1.00^{+0.74}_{-0.00}$
ESO 239-IG002		22 49 39.86	-48 58 58.5	yes	114	$16^{+5.08}_{-3.96}$	$98^{+10.38}_{-10.38}$	$-0.72^{+0.08}_{-0.06}$	$2.32^{+0.33}_{-0.33}$	$2.50^{+0.03}_{-0.02}$	$1.81^{+0.21}_{-0.17}$
IRAS F22491-1808		22 51 49.24	-17 52 24.0	yes	41	$5^{+3.36}_{-2.16}$	$36^{+5.97}_{-5.97}$	$-0.76^{+0.10}_{-0.10}$	$2.50^{+0.60}_{-0.60}$	$0.98^{+0.02}_{-0.02}$	$0.54^{+0.08}_{-0.08}$
NGC 7592	E	23 18 22.55	-04 24 58.9	yes	109	$19^{+5.44}_{-4.32}$	$90^{+10.50}_{-9.47}$	$-0.65^{+0.09}_{-0.07}$	$2.19^{+0.54}_{-0.35}$	$2.65^{+0.08}_{-0.04}$	$2.41^{+0.31}_{-0.31}$
	W	23 18 21.70	-04 24 56.5	yes	156	$26^{+6.16}_{-5.07}$	$130^{+11.40}_{-12.49}$	$-0.67^{+0.07}_{-0.06}$	$2.20^{+0.26}_{-0.26}$	$3.83^{+0.05}_{-0.05}$	$3.28^{+0.31}_{-0.26}$
ESO 077-IG014	NE	23 21 05.43	-69 12 47.4	yes	51	$14^{+4.83}_{-3.70}$	$37^{+7.14}_{-6.06}$	$-0.45^{+0.16}_{-0.12}$	$1.60^{+0.31}_{-0.41}$	$0.94^{+0.01}_{-0.01}$	$1.99^{+0.37}_{-0.26}$
	SW	23 21 03.57	-69 13 01.0	yes	31	$4^{+3.16}_{-1.91}$	$27^{+5.26}_{-5.16}$	$-0.74^{+0.12}_{-0.12}$	$2.47^{+0.71}_{-0.72}$	$0.71^{+0.03}_{-0.02}$	$0.42^{+0.02}_{-0.02}$

Note. — Col. (1): Object name. Col (2): the designation of each optical nucleus that is detected by *Chandra*. Col (3): the right ascension of the optical centroid derived from DSS images in J2000.0 coordinates. Col (4): the declination of the optical centroid derived from DSS images in J2000.0 coordinates. Col (5): morphology of the soft (<2 keV) X-ray emission relative to the telescope PSF at 1 keV. Col. (6): number of detected counts in the full band (0.5–8 keV). Col. (7)–(8): number of detected counts in the hard band (2–8 keV) and in the soft band (0.5–2 keV), respectively. The errors are at 90% confidence level, calculated using methods outlined in Gehrels (1986). Col. (9): the hardness ratio. Col. (10): the nominal Γ value to the best-fit power-law model based on the hardness ratio and assuming only Galactic absorption. Col. (11–12): estimated 0.5–2 keV and 2–10 keV fluxes calculated from the 0.5–2 keV and 2–8 keV count rates based on the estimated power law index. The fluxes are presented in units of 10^{-14} ergs s^{-1} cm^{-2} .

^aThe nucleus in the merger system that is within the *IRAS* 3- σ position error ellipse if resolved (see Sanders et al. 2003).

^bThe upper limit to the hardness ratio exceeds +1, which is undefined by the definition of hardness ratio. Therefore, it is impossible to determine the lower limit of the power law.

False-color X-ray images were created for sources with high enough signal-to-noise ratio (*i.e.* source detected at > 20 counts) by dividing the original full-band (0.5–8 keV) raw images into three bands: 0.5–2 keV (red), 2–6 keV (green), and 6–8 keV (blue). Then all these and the original full-band images were smoothed with a $0.''5$ Gaussian, the FWHM of the point-spread function (PSF) of the detector. The color images were then combined to create false-color images for each galaxy in DS9. Contours of the full-band emission were also created in DS9 and then overlaid above the false-color images. The optical centroid positions were also included in the images to juxtapose the optical nucleus with the X-ray emission. Figure 4.1 displays these false-color images.

The morphologies of the X-ray emission are investigated by comparing the radial profiles of the X-ray sources with the PSF models in the standard calibration library. The radial profiles in Figure 4.2 were created with the unsmoothed 0.5–2 keV band image and compared with the standard model PSF at 1 keV, the energy near which the full-band emission peaks. Unfortunately, these sources do not have enough counts in the 2–6 keV band to produce radial profiles at higher energies to check for extended emission from hot gas.

Of the 47 individual nuclei considered in the archive subset, 43 were detected by *Chandra*. Of these, only 35 had high enough detected counts for the false-color images to be created. As the false-color images in Figure 4.1 show, the peak 0.5–8 keV X-ray emission coincide with the optical centroid to within the DSS image resolution and the astrometric uncertainty of *Chandra* in all but four of the nuclei (NGC 6090NE, ESO 069–IG006N, F17132+5313NE, and F22491–1808).

In addition to extended 0.5–2 keV emission, 10 of the 35 nuclei with false-color images exhibit unresolved core emission above 2 keV. These are III Zw 035NE, ESO060-IG016E, IRAS 09111–1007, IRAS 13120–5453, IRAS 14348–1447SW, VV 340A,

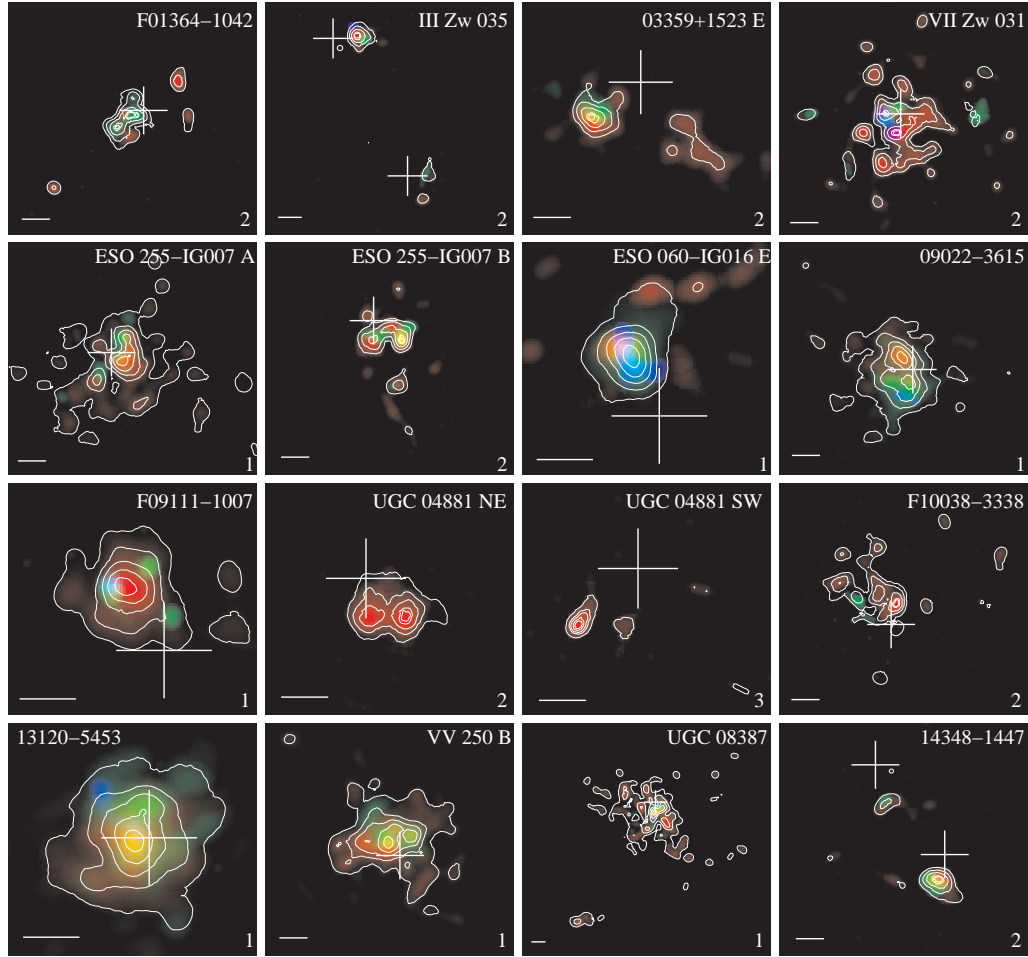


Figure 4.1: False-color images of the nuclei with more than 20 counts in the archive subset. Red band represents the 0.5–2 keV emission where thermal emission from starbursts would dominate, green the 2–6 keV emission, and blue the 6–8 keV emission which is the energy range of Fe K emission lines. The contours represent emission from the full *Chandra* band of 0.5–8 keV. Since the range of signal-to-noise ratio is so great in this large sample of objects, the sample was divided into three groups with different contour levels to best show the features. The contour levels are 10, 30, 50, 70, 90% of maximum for group 1, 30, 50, 70, 90, 95% of maximum for group 2, and 50, 70, 80, 90, 95% of maximum for group 3. The group numbers are indicated at the bottom right corner of each image. The horizontal bar at the bottom left of each image denotes 1'' with the corresponding linear size for each galaxy listed in Table 4.1. In each image, North is up and East is to the left. The crosses mark the DSS centroid positions while the width of the crosses represent the DSS image resolution (1.''7). Note that the current 90% astrometric uncertainty of *Chandra* is $\sim 0.''6$. Several objects show extended soft X-ray emission.

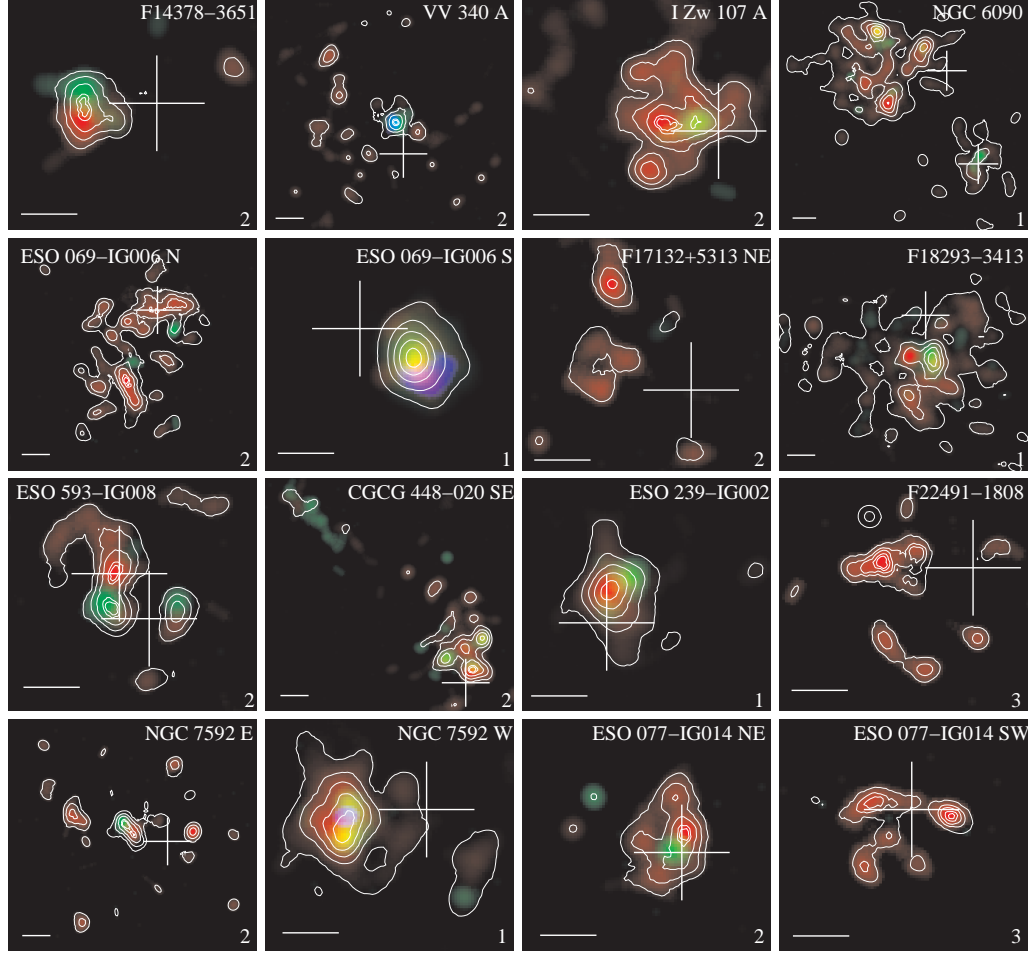


Figure 4.1: Cont.

ESO 069-IG006S, NGC 6090NE, ESO 239-IG002, and NGC 7592W. Of the seven nuclei with unresolved emission above 2 keV and known optical spectral type, all except NGC 6090 NE are either Seyfert galaxies (IRAS 09111-1007, IRAS 13120-5453, NGC 7592W) or LINERs (III Zw 035NE, IRAS 14348-1447SW, VV 340A), suggesting that some infrared selected LINERs host an AGN.

Several galaxies in the archive sample contain discrete, point-like X-ray sources with luminosities $\gtrsim 10^{39}$ ergs s $^{-1}$. The properties of these candidate ultraluminous X-ray sources (ULXs) are described in Appendix C.

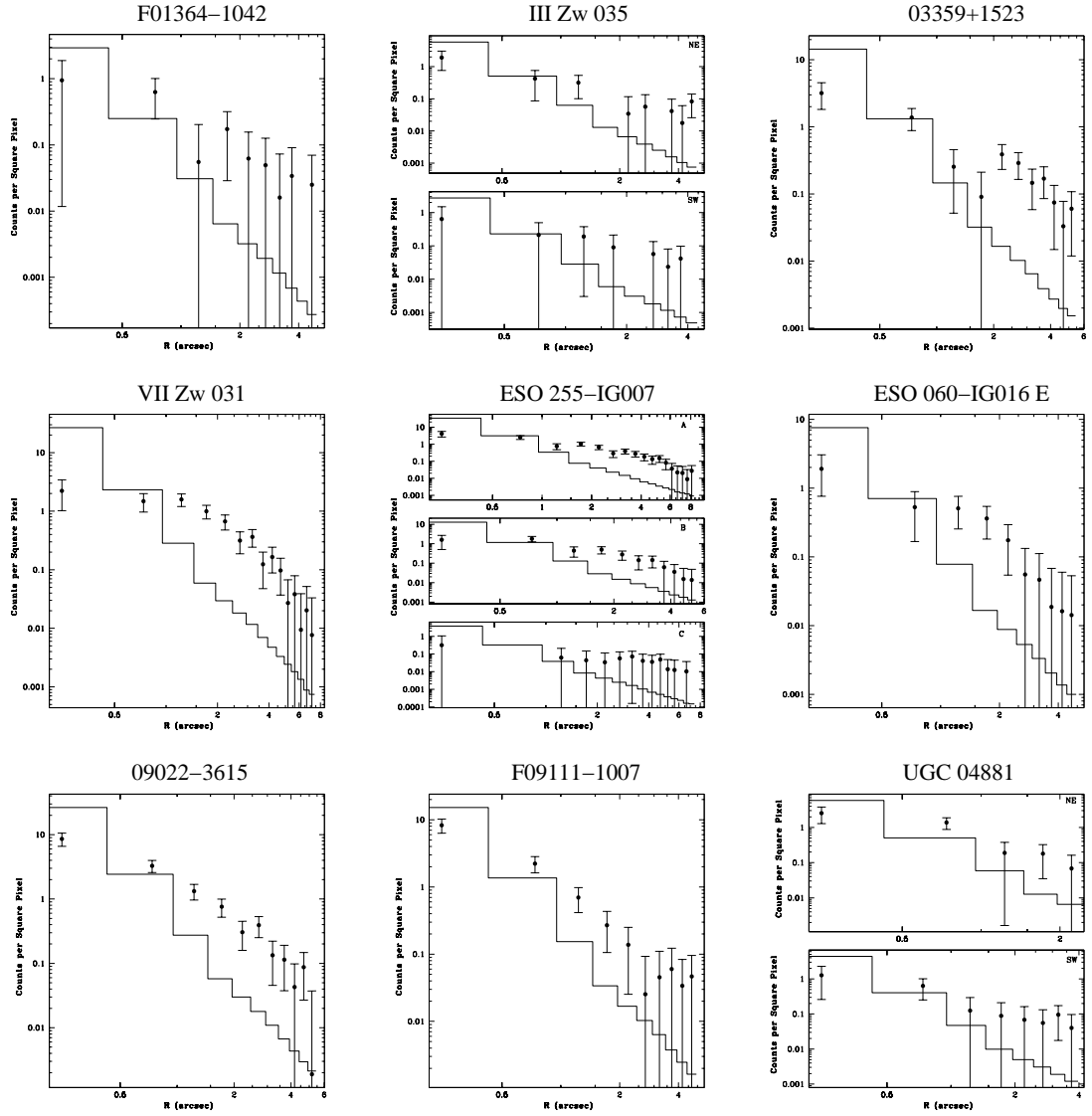


Figure 4.2: Radial profiles for all detected nuclei with more than 15 counts compared with model PSFs. The x-axis is distance in arcseconds from the centroid of the X-ray emission, while the y-axis is the surface brightness in counts per square pixel. The error bars are errors on the net counts per square pixel assuming Poisson statistics. In each panel, the histogram is the model PSF obtained from the PSF library at 1 keV. The points are observed total counts with energy in the range of 0.5–2 keV. These diagrams show that most of the soft X-ray emission from these galaxies are extended, in contrast to the radial profiles of the Seyfert 1 ULIRGs in Teng et al. (2005) and the LINER/ULIRG IRAS F04103–2838 in Teng et al. (2008). Note that the nuclei of F10038–3338, NGC 6090, and ESO 593-IG008 are so close together that their radial profile is of the two nuclei combined.

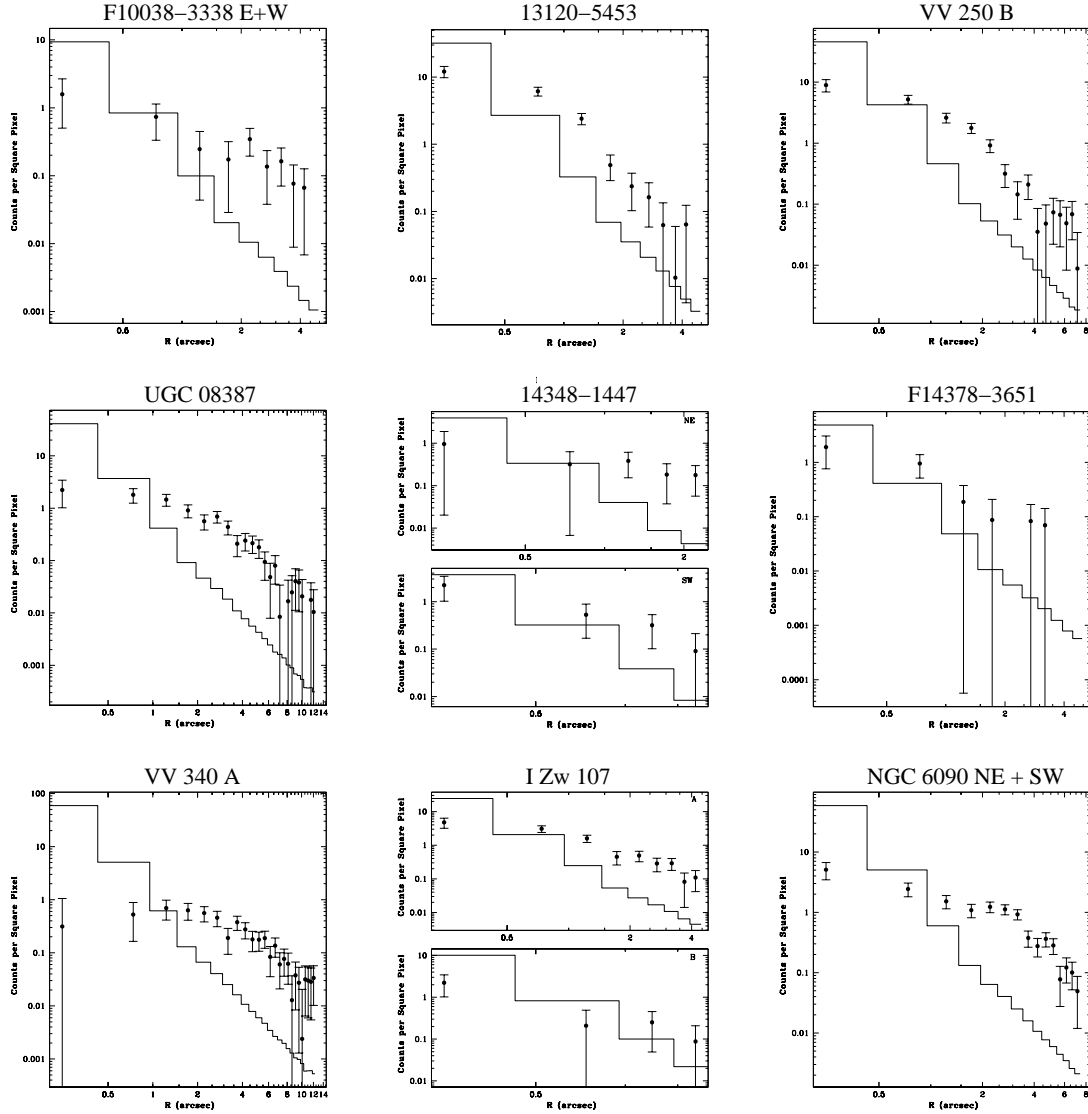


Figure 4.2: Cont.

4.4.2 Spectra

For the 17 nuclei with more than 100 counts, it is possible to use the traditional spectral fitting method to determine the spectral properties of these sources. Unbinned spectra of these nuclei were extracted and then fitted. The spectral analysis was performed using `HEASoft` version 6.4 with `XSPEC` version 11.3.2ag. The channels below 0.5 keV where the instrumental calibration is uncertain and above 8.0 keV

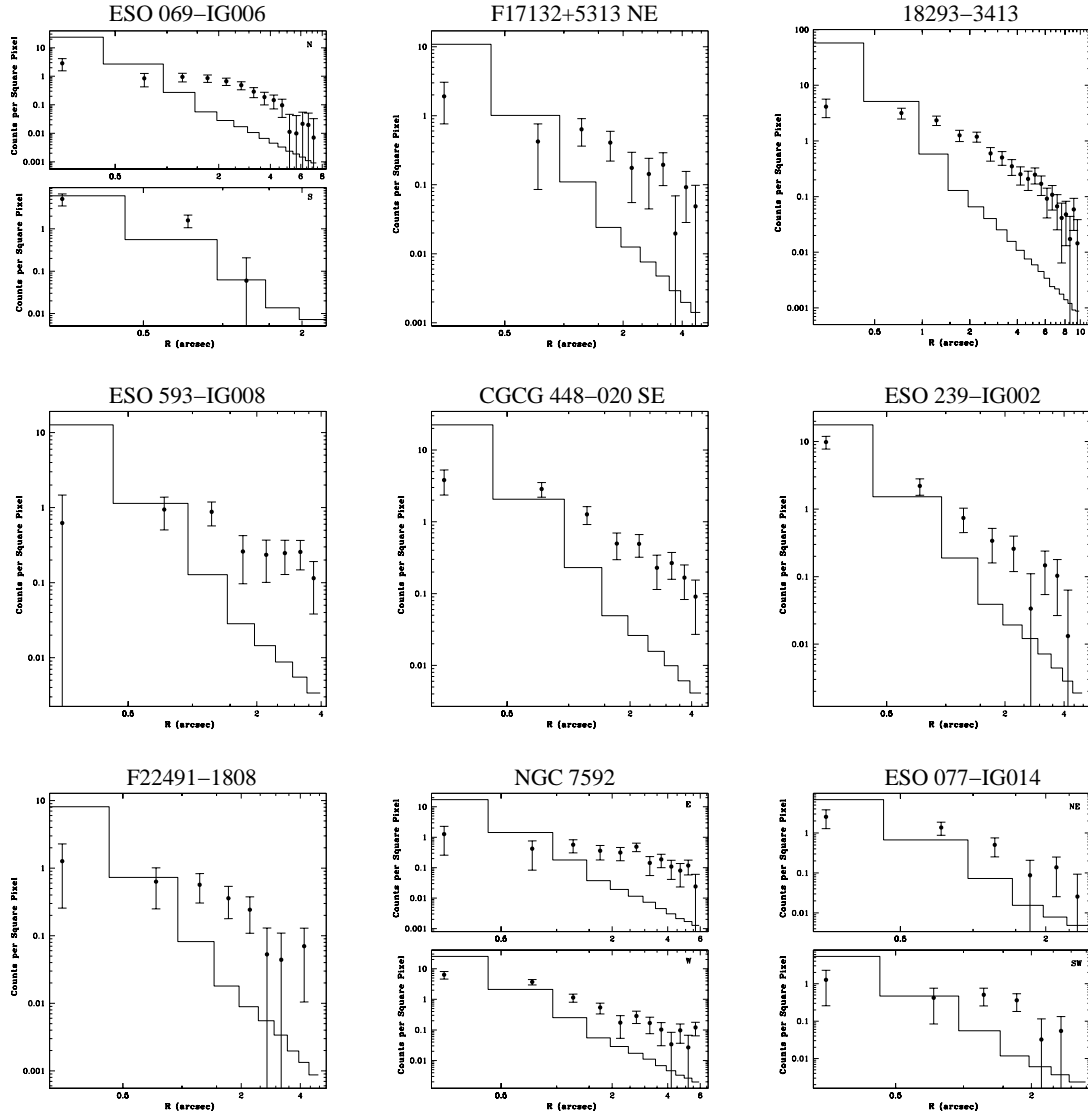


Figure 4.2: Cont.

where there are few counts are ignored in the modeling of the spectra. The Cash statistics option in XSPEC was used for the spectral fitting of the unbinned spectra. All the errors in the model parameters are at the 90% level for one parameter of interest ($\Delta c\text{-stat}=2.7$).

Unlike Gaussian statistics, low count spectra like these cannot be background subtracted and then modeled. Therefore, the background spectra were first modeled and then the background models are incorporated into the models of the source

spectra. To prevent over-interpretation of the data, only simple models were considered: single power law, absorbed power law, single MEKAL model, a scattering model², and various combinations of these. For several sources, emission lines were also included in the model. The `goodness` task in XSPEC was used to determine the best-fit model for each object. The spectral fitting results are in Table 4.4 and the spectra are displayed in Figure 4.3.

We also wish to include the fainter objects (< 100 counts) in our spectral analysis. For these, we apply the HR method of Teng et al. (2005). In this method, the HRs calculated from the data are compared with the HRs generated from two simple models, a single power law and a single MEKAL model, to determine the model parameters that describe the observations (see Teng et al. 2005, for details). The reliability of the HR method is discussed in Appendix A. Three detected nuclei (ESO 203-IG001NE, IRAS 07251-0248, and IRAS F17132+5313SW) are excluded from the HR analysis because they do not have any counts in the hard band. Table 4.3 lists the detected counts and the HR analysis results. The X-ray fluxes of the detected nuclei are estimated assuming the power-law index derived from HRs and Galactic absorption only. The discussion of the spectral properties of these objects is postponed until § 4.5.2.

4.5 Discussion

4.5.1 X-ray Morphology of Archived Data

As Figures 4.1 and 4.2 show, most of the sources have extended soft X-ray (0.5–2 keV) emission. These emissions are likely galactic winds or circumnuclear star

²The scattering model is represented by an absorbed power law for the directly transmitted component and an unabsorbed power law with the same photon index for the scattered component.

Table 4.4. Spectral Fitting Results for Bright Archive Targets

Object (1)	Best Model (2)	$N_{\text{H, source}}$ [10^{22} cm^{-2}] (3)	kT_1 [keV] (4)	kT_2 keV (5)	Γ (6)	E_{line} [keV] (7)	EW [keV] (8)	Line ID (9)	c-stat (10)	d.o.f. (11)	Unabsorbed $F_{0.5-2 \text{ keV}}$ (12)	Unabsorbed $F_{2-8 \text{ keV}}$ (13)	$\frac{F_{\text{MEKAL}}}{F_{0.5-8 \text{ keV}}}$ (14)
VII Zw 031	A	—	$1.37^{+0.29}_{-0.15}$	—	$1.62^{+1.95}_{-0.94}$	0.83	$0.33^{+0.33}_{-0.32}$	Fe XVII	253.0	506	$0.36^{+1.71}_{-0.10}$	$0.10^{+0.27}_{-0.09}$	0.71
ESO 255-IG007	A	—	$0.68^{+0.46}_{-0.38}$	$2.72^{+1.03}_{-0.59}$	—	—	—	—	263.5	508	$0.47^{+0.13}_{-0.10}$	$0.33^{+0.18}_{-0.17}$	1.00
ESO 60-IG016	E	$17.22^{+7.05}_{-4.96}$	—	—	$2.27^{+0.67}_{-0.69}$	—	—	—	323.6	508	$4.92^{+1.50}_{-4.77}$	$3.40^{+1.04}_{-2.19}$	0.00
IRAS 09022-3615	D	—	—	—	$1.03^{+0.23}_{-0.24}$	1.06	$0.25^{+0.07}_{-0.06}$	Fe XVIII-XXII	389.1	509	$0.47^{+0.17}_{-0.17}$	$1.55^{+0.42}_{-0.59}$	0.00
IRAS 13120-5453	E	$0.20^{+0.22}_{-0.18}$	—	—	$1.47^{+0.35}_{-0.33}$	1.83	$0.10^{+0.10}_{-0.08}$	Si XIII	396.2	508	$0.77^{+0.21}_{-0.66}$	$1.52^{+0.42}_{-0.41}$	0.00
VV250	F	$1.40^{+1.74}_{-0.69}$	$0.67^{+0.17}_{-0.07}$	—	$2.70^{+1.01}_{-0.59}$	3.86	$0.13^{+0.07}_{-0.04}$	Ca XIX	330.0	506	$2.85^{+0.27}_{-0.12}$	$1.08^{+0.46}_{-0.46}$	0.08
UGC 08387	A	—	$0.98^{+0.21}_{-0.22}$	—	$1.48^{+0.32}_{-0.19}$	1.86	$0.20^{+0.14}_{-0.09}$	Si XIII	311.4	507	$0.46^{+0.12}_{-0.13}$	$0.53^{+0.20}_{-0.33}$	0.19
VV 340	A(N)	—	$0.77^{+0.11}_{-0.17}$	—	$2.56^{+0.48}_{-0.45}$	1.86	$0.28^{+0.03}_{-0.04}$	Si XIII	353.9	506	$0.61^{+0.15}_{-0.12}$	$0.45^{+0.43}_{-0.31}$	0.27
I ZW 107	A(N)	$0.31^{+0.70}_{-0.16}$	$0.88^{+0.20}_{-0.19}$	—	$2.51^{+0.59}_{-0.37}$	—	—	Fe K α	208.6	507	$0.50^{+0.29}_{-0.16}$	$0.20^{+0.60}_{-0.17}$	0.83
NGC 6090	NE	—	$0.79^{+0.05}_{-0.12}$	$3.08^{+3.62}_{-1.22}$	—	1.38	$0.10^{+0.20}_{-0.09}$	Mg XI	237.5	506	$0.51^{+0.19}_{-0.09}$	$0.22^{+0.16}_{-0.15}$	1.00
ESO 069-IG006	N	—	$0.64^{+0.15}_{-0.15}$	$1.76^{+1.29}_{-0.48}$	—	1.80	$0.51^{+0.57}_{-0.50}$	Fe XXIII-XXV	216.4	507	$0.38^{+0.14}_{-0.12}$	$0.07^{+0.07}_{-0.05}$	1.00
	S	$3.41^{+1.81}_{-1.39}$	—	—	$1.60^{+0.82}_{-0.72}$	—	—	—	382.4	509	$1.39^{+0.15}_{-1.04}$	$2.43^{+0.78}_{-0.85}$	0.00
IRAS F18293-3413	F	$0.39^{+0.57}_{-0.26}$	$0.85^{+0.12}_{-0.09}$	—	$1.41^{+0.45}_{-0.46}$	1.36	$0.35^{+0.28}_{-0.06}$	Mg XI	440.9	505	$1.05^{+0.53}_{-0.36}$	$1.23^{+2.80}_{-0.86}$	0.24
CGCG 448-020	SE	$0.10^{+0.15}_{-0.10}$	$1.04^{+0.37}_{-0.36}$	—	$2.24^{+0.44}_{-0.42}$	—	—	Si XIII	214.5	507	$0.44^{+0.14}_{-0.11}$	$0.24^{+0.12}_{-0.10}$	0.19
ESO 239-IG002	A	—	$0.64^{+0.23}_{-0.23}$	—	$1.67^{+0.47}_{-0.51}$	—	—	—	230.1	508	$0.22^{+0.08}_{-0.09}$	$0.23^{+0.12}_{-0.16}$	0.18
NGC 7592	E	—	$0.56^{+0.14}_{-0.13}$	$4.10^{+24.01}_{-0.19}$	—	—	—	—	221.2	508	$0.23^{+0.14}_{-0.07}$	$0.15^{+0.16}_{-0.14}$	1.00
	W	—	$0.64^{+0.41}_{-0.32}$	—	$2.21^{+0.74}_{-0.51}$	—	—	—	231.9	508	$0.35^{+0.11}_{-0.11}$	$0.17^{+0.10}_{-0.12}$	0.26

Note. — Col. (1): Object name. Col. (2): best-fit continuum model modified by Galactic absorption — A=MEKAL plus single power law, B=double MEKAL, C=scattering model, D=single power law, E=absorbed power law, F=MEKAL plus single absorbed power law. Col. (3): equivalent hydrogen column density within the source. Col. (4)–(5): temperature of the MEKAL model. Col. (6): spectral index of the power-law component. Col. (7): rest frame energy of the emission line; value fixed. The width (σ) of the lines are fixed at 0 keV. Col. (8): equivalent width of the emission line. Col. (9): identification of the emission line. Col. (10): XSPEC c-statistics value. Col. (11): degrees of freedom of the model. Col. (12)–(13): absorption corrected flux in $10^{-13} \text{ ergs s}^{-1} \text{ cm}^{-2}$. Col. (14): the percentage of thermal emission relative to the 0.5–8 keV flux.

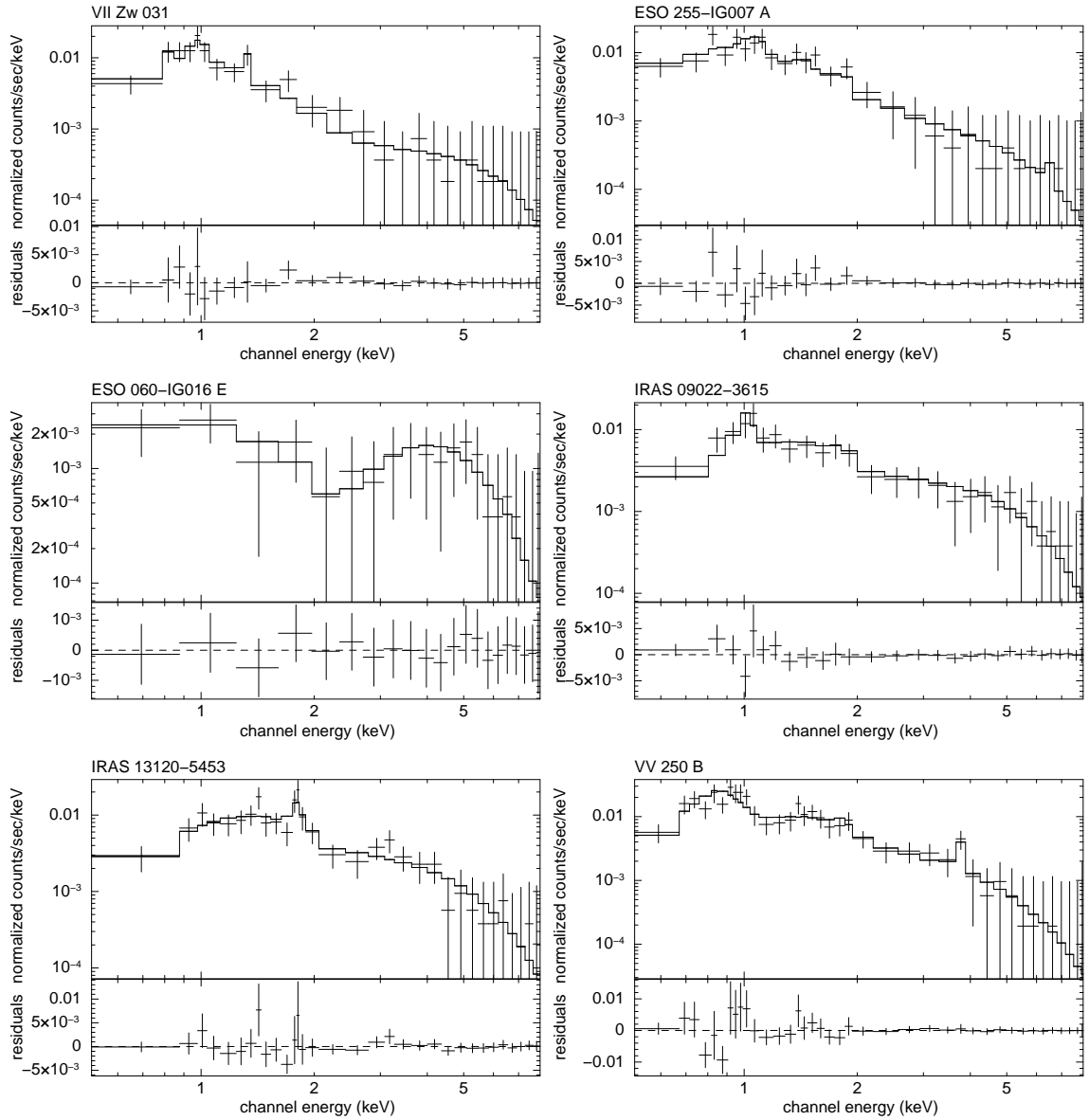


Figure 4.3: Spectra of sources with more than 100 counts and their best-fit models. While the unbinned, un-background-subtracted spectra were used for modeling with the c-stat option in XSPEC, they are displayed as unbinned data grouped to $3\text{-}\sigma$ or in sets of 25 bins. The background spectra are modeled separately and are accounted for in the best-fit models of the sources. The x-axis of the figures represents energy in the observer’s frame. The parameter values of the best-fit models are listed in Table 4.4.

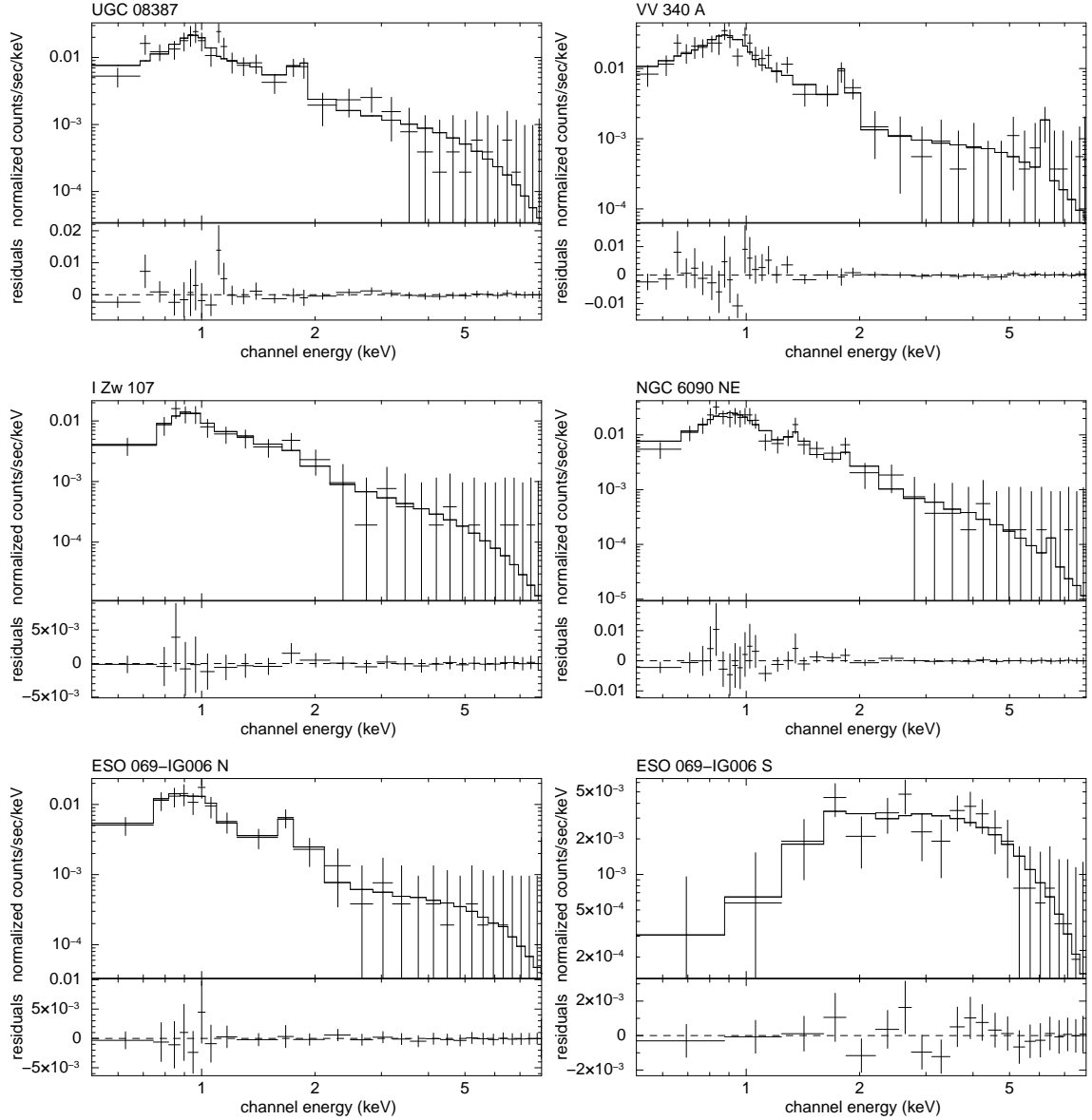


Figure 4.3: Cont.

formation due to merger-induced starbursts. The X-ray data and complementary radio observations show that this is clearly the case in one source in particular — UGC 08387. Figure 4.4 compares the VLA 3.6 cm observation of this source from Condon et al. (1991) with the *Chandra* full band emission. The radio emission is from the disk of the galaxy, consistent with CARMA CO observations which show rotation of the disk along the same position angle (B.A. Zauderer, private

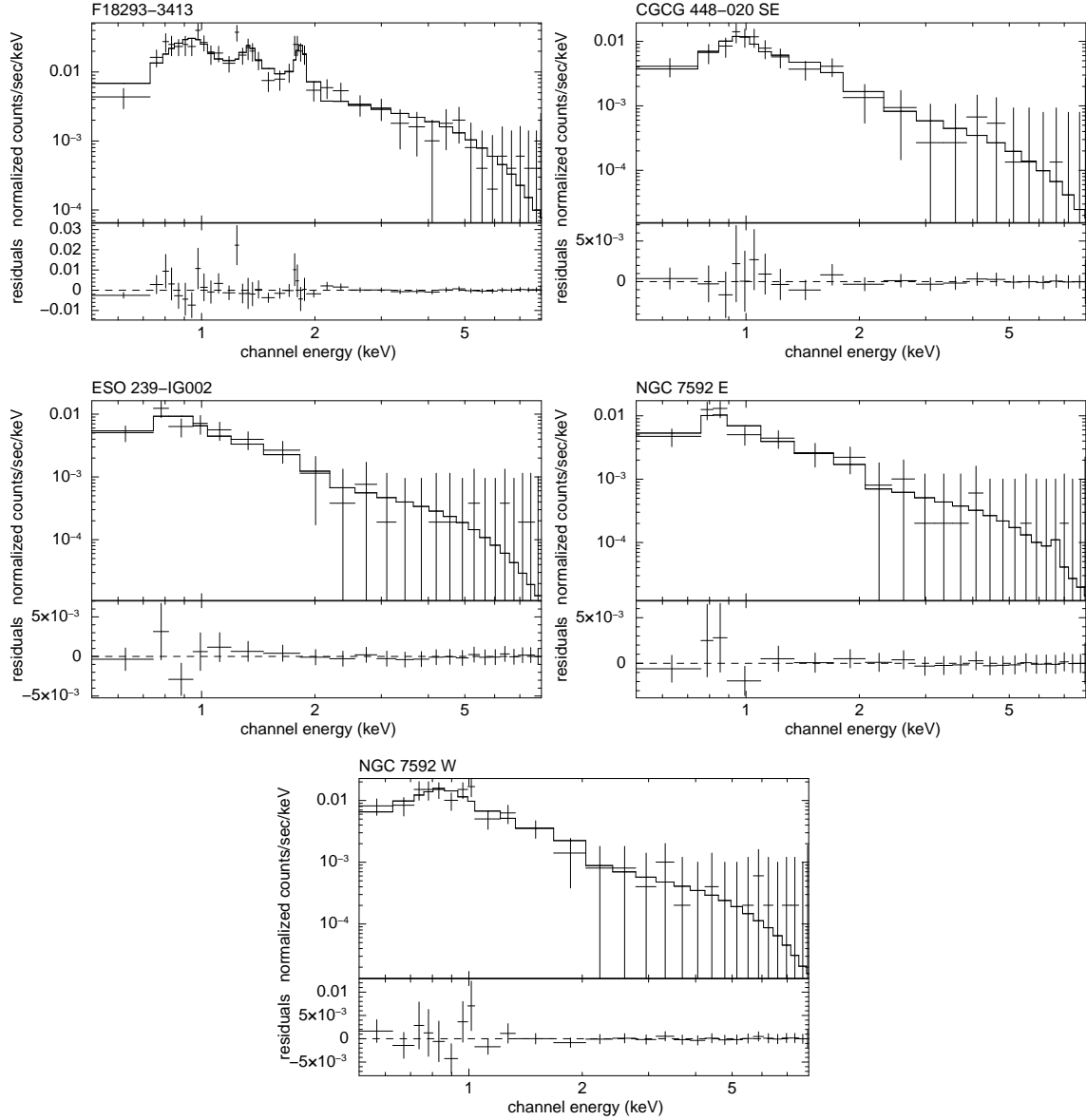


Figure 4.3: Cont.

communication). There is soft X-ray emission perpendicular to the disk extending ~ 1 kpc above and below the disk. The X-ray emission is likely due to hot clumps of material expelled by a starburst- or AGN-driven galactic wind (Veilleux et al. 2005). Detailed discussion of the X-ray morphology of the other sources is postponed until Iwasawa et al.(2009, in prep.).

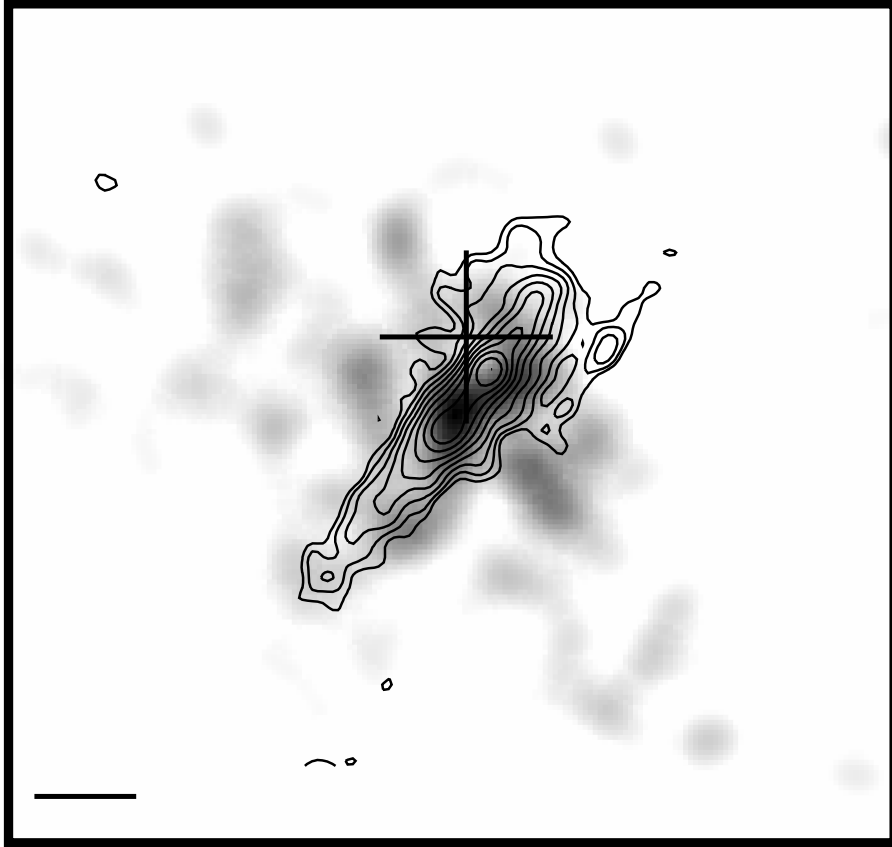


Figure 4.4: VLA 3.6 cm contours of UGC 08387 overlaid on top of the X-ray 0.5–8 keV grey scale. The cross marks the location of the optical centroid from DSS images as in Figure 4.1. The radio contours have a position angle of $\sim 140^\circ$, consistent with that of CO disk rotation in this galaxy. The unresolved hard X-ray (6–8 keV) emission coincides with the center of the radio contours. The soft (0.5–2 keV) X-ray emission extends ~ 1 kpc, above and below the disk, suggestive of a galactic wind.

4.5.2 X-ray Spectra of Archived Data

Of the 17 nuclei that have enough counts for spectral fitting, 13 have a thermal component in their spectra. All 13 of these galaxies have a thermal component with a temperature ~ 0.6 – 1.4 keV, consistent with those seen in U/LIRGs (Grimes et al. 2005; Teng et al. 2009, 2005). Four of these galaxies show no power-law component but have a second thermal component with a slightly higher temperature of ~ 2.0 – 4.0 keV. This temperature range is consistent with that of the older low-mass X-ray

binary (LMXB) population. The power law components in the other 13 galaxies are also consistent with those observed in U/LIRGs. With the exception of IRAS 09022–3615, the power laws have indices in the range of ~ 1.4 – 2.7 , comparable to the values of ~ 1.1 – 2.7 measured by Teng et al. (2005).

The spectra of some of these 17 bright nuclei also exhibit emission lines arising from Si, Mg, Ca, and Fe. These emission lines are found in nine of the 17 objects, though only three have multiple emission features. These α -elements are direct products of massive-star nucleosynthesis and often found in X-ray observations of supernova remnants (e.g., Hughes et al. 2000; Kinugasa & Tsunemi 1999; Warren et al. 2005). The detection of these lines in actively star-forming galaxies is therefore not surprising.

Appendix A shows that the HR method is a good estimator of the photon index of a single power-law model if the column density is $\lesssim 10^{22}$ cm $^{-2}$. Five of the detected nuclei (IRAS F01364–1042, ESO 060–IG016E, IRAS F08572+3915NW, IRAS F14378–3651, and ESO 069–IG006S) have photon index upper limits below unity. A likely explanation for the inverted power law is heavy absorption. The softer photons are more readily affected by absorption and thus the observed AGN spectrum appears harder if there is no secondary source of soft X-ray photons from thermal processes. IRAS F14378–3651 is optically classified as a Seyfert 2 source, consistent with this view. Infrared observations of IRAS F08572+3915 have found that it has strong absorption features characteristic of deeply buried AGNs (Armus et al. 2007; Imanishi et al. 2006; Veilleux et al. 2009b). Modeling of the unbinned spectra of ESO 060-IG016E and ESO069-IG006S found these objects to be moderately obscured. The optical spectral types of these two objects are unknown.

4.5.3 Comparison with Previous Work

In this section, we combine the results from our analysis of archive data presented in § 4.4 and discussed in § 4.5 with those from Ptak et al. (2003) and Teng et al. (2005).

The Distribution of Estimated Photon Indices

One of the goals of this study is to determine whether there is a difference in the X-ray properties of various categories of objects: LIRGs *vs.* ULIRGs, “warm” *vs.* “cool” objects based on the 25-to-60 μm flux ratios, binary *vs.* single sources, and sources of different optical spectral types. The combined sample includes 36 detected nuclei (excluding those that fall outside of the *IRAS* $3\text{-}\sigma$ error ellipse) from the archive data, the 14 objects from Teng et al. (2005), and eight more objects from Ptak et al. (2003). While Ptak et al. (2003) did not use the HR method presented in this paper and in Teng et al. (2005), they performed spectral fits to their sample with a single power-law model. Since this estimate is very similar to the hardness ratio method, the addition of these eight objects brings our working sample to a total of 58 detected nuclei with spectral shapes estimated in similar manners. The spectral indices of these 58 nuclei range from -0.55 to 3.15 and cover infrared luminosity in the range of $10^{11.32-12.53} L_{\odot}$.

Figure 4.5 is a histogram of the distribution of the estimated X-ray spectral index for LIRGs and ULIRGs. LIRGs have slightly softer X-ray spectra (median $\Gamma = 2.1$) than ULIRGs (median $\Gamma = 1.5$) on average, but this difference is not statistically significant based on a two-tailed Kolmogorov-Smirnov (K-S) test ($P_{null} = 10\%$). Figure 4.6 suggests that objects in the lowest infrared luminosity bin may have softer spectra than the other objects, perhaps indicating that starburst

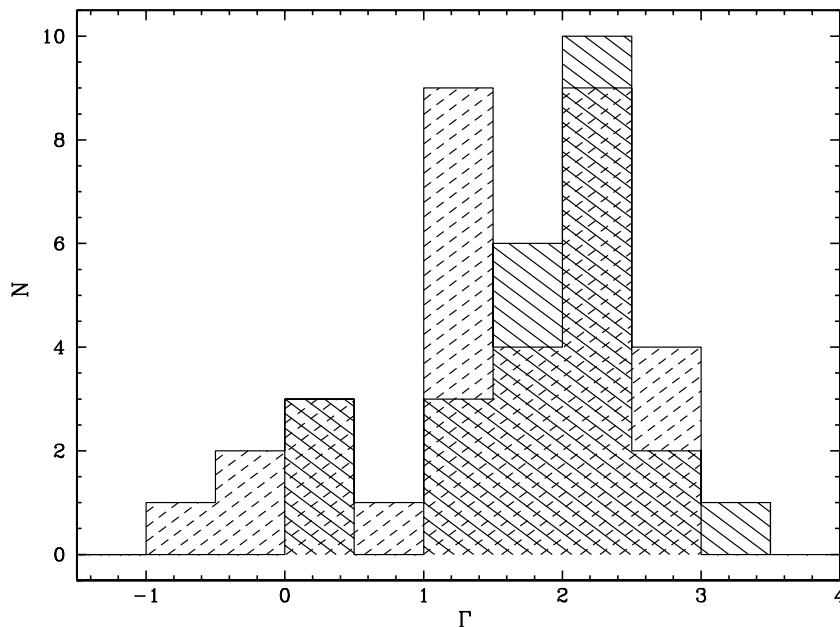


Figure 4.5: A comparison of the photon indices of LIRGs (solid hashes) and ULIRGs (dashed hashes) in the Ptak et al. (2003), Teng et al. (2005), and the archive samples as estimated by the hardness ratio method (or the single power law fits in Ptak et al. 2003). On average, the LIRGs have slightly softer spectra (median $\Gamma = 2.1$) than the ULIRGs (median $\Gamma = 1.5$), but this distinction is not statistically significant based on a two-tailed K-S test. The average error in the Γ measurements is ~ 0.5 , the width of a single bin.

activity (synonymous with the soft thermal emission) is more dominant in these objects relative to their higher luminosity counterparts. However, this difference is not significant due the wide range of Γ in each bin.

While there are not enough “warm” objects observed in the combined sample with $\log(f_{25 \mu m}/f_{60 \mu m}) > -0.7$ to create a histogram of photon index distribution for the “warm” and “cool” objects, Figure 4.7 plots the binned average Γ as a function of the *IRAS* 25-to-60 μm flux ratio. There does not seem to be any dependence of Γ on the infrared flux ratio. Similarly, a K-S test of the Γ distribution between single and binary objects shows that both groups have the same distribution (Figure 4.8).

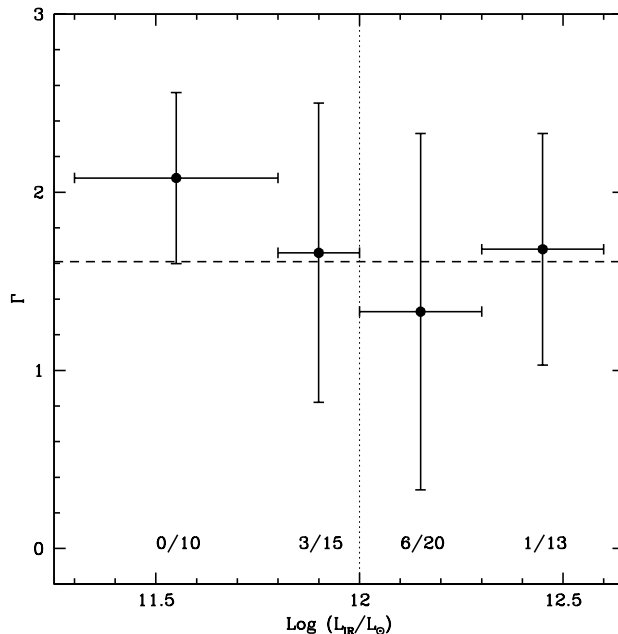


Figure 4.6: The photon indices of U/LIRGs in the Ptak et al. (2003), Teng et al. (2005), and the archive samples as estimated by the hardness ratio method (or the single power law fits in Ptak et al. 2003) as a function of L_{IR} . The vertical error bars are the standard deviation in each bin. The horizontal dashed line is the average Γ of the whole sample and the vertical dotted line divides the LIRGs from the ULIRGs. The numbers below each bin represent the number of sources with an inverted X-ray spectrum ($\Gamma < 1$) out of the total number of sources in that bin. The lower luminosity LIRGs (first bin in L_{IR}) seems to have slightly softer spectra than the other objects, but this difference is not statistically significant.

In Figure 4.9, the sample of 48/58 nuclei with optical spectral type classifications are separated into four different spectral types³ so that their average spectral properties can be compared. There is no statistically significant difference between each of the spectral types. However, the average Γ for the Seyfert 1's agrees with the canonical value of an AGN spectrum ($\Gamma \sim 1.8$). The average Γ of ~ 1.2 for Seyfert 2's is lower, perhaps due to additional obscuration. In this group, $\sim 44\%$ of

³For objects with borderline spectral identification, we used the more AGN-like classification. LINER/HII objects are considered LINERs, and HII/Seyfert and LINER/Seyfert objects are considered Seyferts.

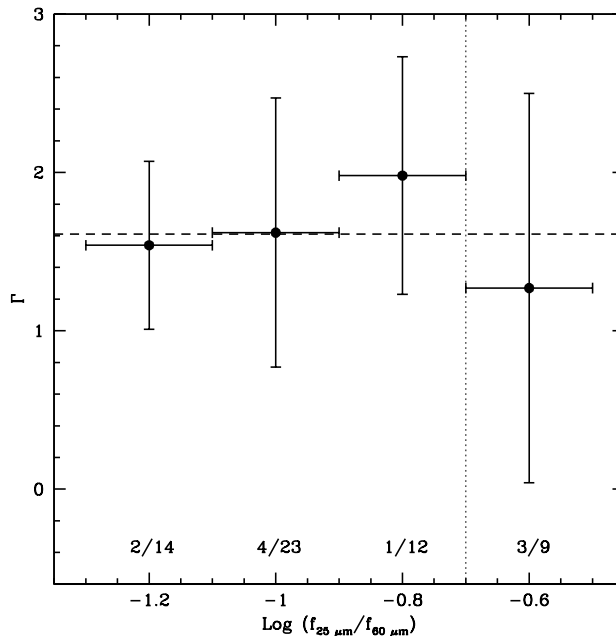


Figure 4.7: The photon indices of U/LIRGs in the Ptak et al. (2003), Teng et al. (2005), and the archive samples as estimated by the hardness ratio method (or the single power law fits in Ptak et al. 2003) as a function of color temperature. The color temperatures are represented in equal bins of 0.2 and the vertical error bars are the standard deviation in each bin. The horizontal dashed line is the average Γ of the whole sample and the vertical dotted line separates the “cool” objects to the left from the “warm” objects to the right. The numbers below each bin have the same meaning as those in Figure 4.6. There is no statistically significant correlation between color temperature and photon index.

the Seyfert 2’s have inverted spectra. The pure HII-like objects have the highest average Γ , perhaps indicative of dominant star formation.

AGN Signatures in RBGS U/LIRGs

Teng et al. (2005) followed Figure 5 in Ptak et al. (2003) and plotted the ratio of hard X-ray to far-infrared flux as a function of the *IRAS* 25-to-60 μm flux ratio. We have added the archive results to this plot, displayed in Figure 4.10. The dotted line in Figure 4.10 represents the average $F_{2-10 \text{ keV}}/F_{FIR}$ of pure starbursts. The results of the archive U/LIRGs agree with those of Ptak et al. (2003) and Teng et al.

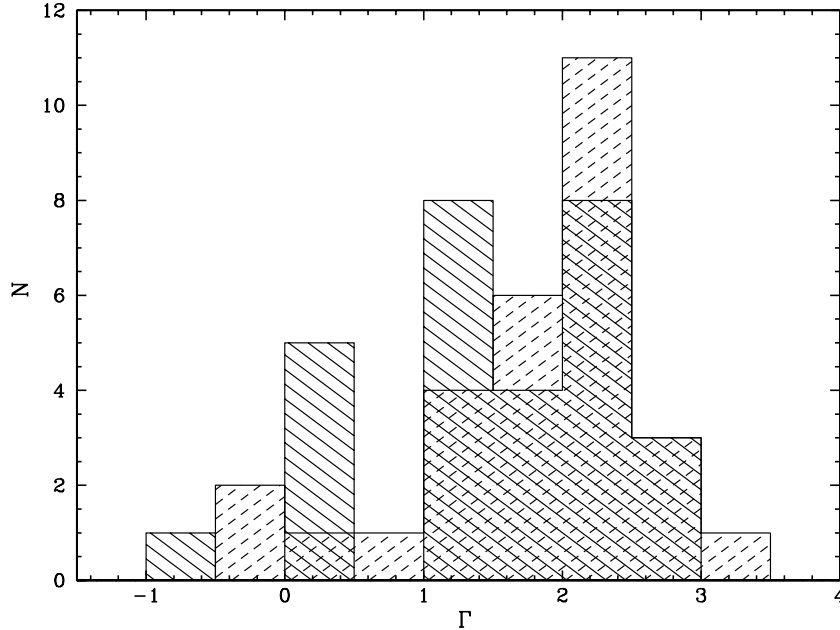


Figure 4.8: A comparison of the photon indices of single (solid hashes) and double (dashed hashes) nucleus sources in the Ptak et al. (2003), Teng et al. (2005), and the archive samples as estimated by the hardness ratio method (or the single power law fits in Ptak et al. 2003). The distributions of the two samples are nearly identical. The two-tailed K-S test confirms that the two samples are drawn from the same population. The average error of the Γ measurements is ~ 0.5 , the width of a single bin.

(2005). The ratios of hard X-ray to FIR fluxes of U/LIRGs are usually similar to those of pure starbursts, suggesting that most U/LIRGs are powered by starbursts. Seven U/LIRGs lie above the dotted line in the region populated by starburst/AGN composites and other AGNs. These objects likely contain AGNs since most of them have unresolved X-ray nuclei, display Fe K emission lines, or are optically classified as Seyfert galaxies. Interestingly, seven of these 12 sources are part of binary systems. This suggests that some AGNs do turn on prior to the final stages of merger. Another possibility is that these AGNs pre-date the interaction.

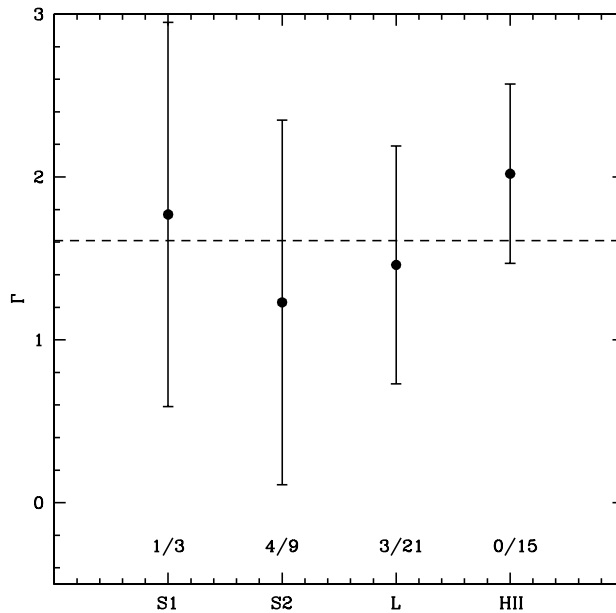


Figure 4.9: A comparison of the average photon indices of Seyfert 1, Seyfert 2, LINER, and HII-like sources in the Ptak et al. (2003), Teng et al. (2005), and the archive samples as estimated by the hardness ratio method (or the single power law fits in Ptak et al. 2003). This figure only includes the 48 nuclei in the sample with optical spectral type classifications. The values below each bin are the same as those in Figure 4.6. The dashed line represents the average Γ of those sources and the vertical error bars in each bin represents the standard deviation within the bin. There are no statistically significant difference between the types. However, the average Γ of ~ 1.8 in the Seyfert 1's is the same as the canonical value for AGNs. The average Γ of ~ 1.2 in the Seyfert 2's imply that many have inverted spectra and thus possibly significant obscuration. The pure HII-like objects have average Γ of ~ 2.0 which is steeper than that of the other types, consistent with the idea of star formation is more important in these systems.

X-ray SFR

The far-infrared luminosity is a good measure of the star formation rate (SFR) in dusty systems like U/LIRGs. Comparison of the SFR from X-ray and FIR measurements may show whether there is any energy contribution from sources other than the starburst (e.g., an AGN). Figure 4.11 plots the FIR SFR against the X-ray SFR relation from Ranalli et al. (2003) for objects in the sample. Seyfert-like objects

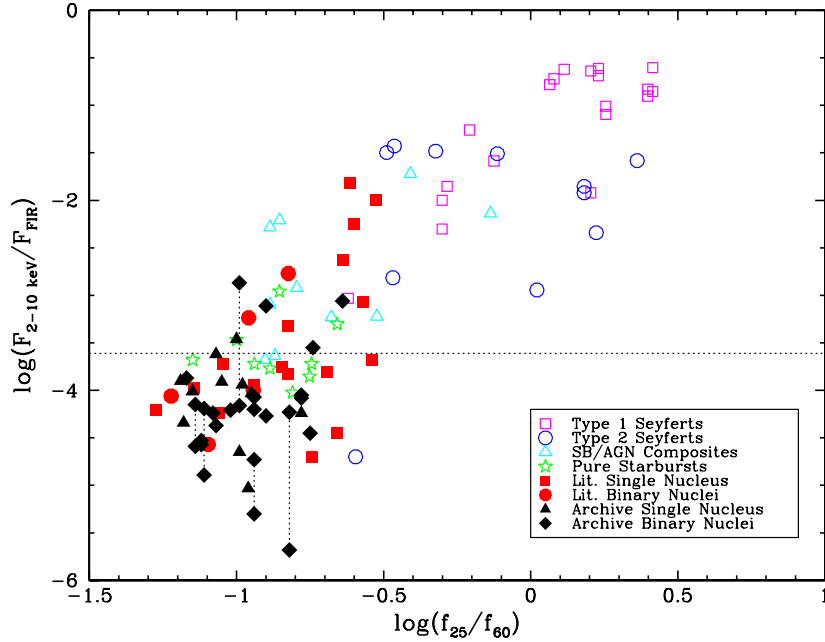


Figure 4.10: Plot of $\log(L_{2-10 \text{ keV}}/L_{FIR})$ vs. $\log(f_{25\mu m}/f_{60\mu m})$. This is the same plot as the one presented in Teng et al. (2005) with values from the RBGS sample added. The properties of the archive objects are consistent with U/LIRGs shown in Teng et al. (2005) and Ptak et al. (2003). The dotted line represents the average $\log(L_{2-10 \text{ keV}}/L_{FIR})$ values for the pure starbursts. Multiple nuclei in the same system are linked with a vertical dotted line. The archive objects shown here are nuclei that are within the *IRAS* $3\text{-}\sigma$ position error ellipse. There are 12 U/LIRGs that lie above the dotted line, seven of which are part of binary systems. This may suggest that, at least in some sources, the AGNs turn on prior to final coalescence or are pre-date the interaction.

and sources with AGN signatures in the X-ray tend to have excess 2–10 keV emission relative to their FIR emission. No object with L_{IR} below $\sim 10^{11.9} L_{\odot}$ exhibits excess 2–10 keV emission. There is therefore a trend of increasing AGN fraction with increasing infrared luminosity, confirming results seen in the optical (Veilleux et al. 1999a, 1995, 1999b) and mid-infrared (Desai et al. 2007; Farrah et al. 2007; Genzel et al. 1998; Lutz et al. 1999; Spoon et al. 2007; Tran et al. 2001; Veilleux et al. 2009b).

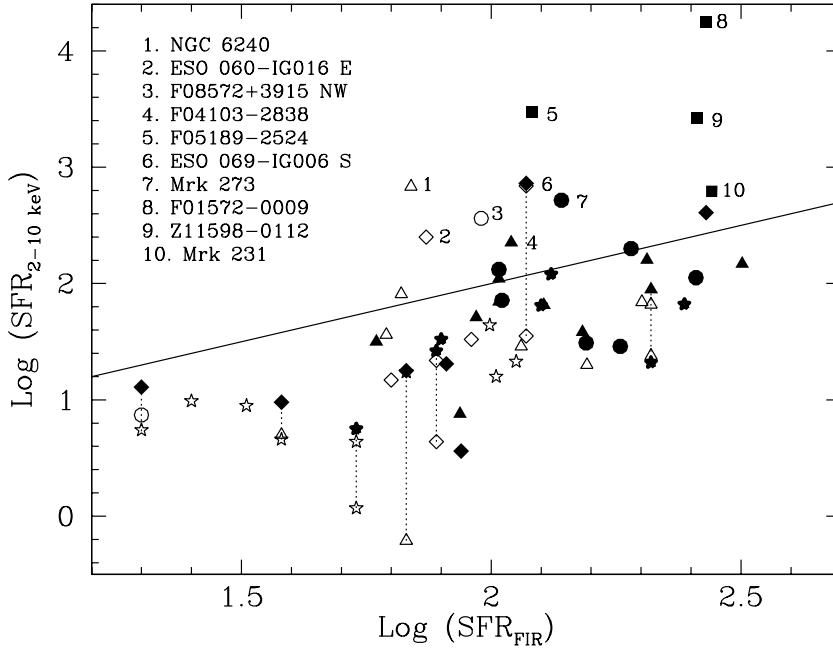


Figure 4.11: FIR-based star formation rates versus star formation rates derived from the 2–10 keV flux and the Ranalli et al. (2003) relation between hard X-ray luminosity and star formation rate among star-forming galaxies, in solar masses per year. ULIRGs have FIR-based star formation rates above $\sim 100 M_{\odot} \text{ yr}^{-1}$. Objects included are drawn from Ptak et al. (2003), Teng et al. (2005), and objects in the current sample that are within the *IRAS* $3\text{-}\sigma$ position error ellipse. Seyfert 1, Seyfert 2, LINER, and HII-like U/LIRGs are represented as squares, circles, triangles, and stars, respectively. Diamonds are objects with no known spectral type. Open symbols represent individual sources in multiple-nuclei systems, while the filled symbols represent either the sum of these binary systems or single-nucleus sources. Multiple nuclei in the same system are linked with a vertical dotted line. The fraction of objects that lie above the line of equality (solid line) increases with increasing FIR-based star formation rates, suggesting an increasing AGN contribution with increasing infrared luminosity.

4.6 Summary

Our analysis of the *Chandra* survey of 56 galaxies in the RBGS indicates that the X-ray properties of LIRGs are similar to those of ULIRGs. The main results are summarized as follows:

1. The soft X-ray morphology of most U/LIRGs is extended. The emission likely

arises from merger-induced star formation and/or galactic winds. Several sources also show unresolved hard X-ray nuclei which suggest the presence of AGNs. Discrete, super-soft X-ray sources are also observed in a few galaxies and have luminosities in the range of $\sim 10^{40}$ ergs s $^{-1}$, typical of ultraluminous X-ray sources.

2. There appears to be little difference in spectral slope between LIRGs and ULIRGs except perhaps that the former tend to have softer spectra than the latter.
3. Twelve of the RBGS sources seem to host AGNs and seven of these are in binary systems. This differs from the simple form of the merger-to-quasar evolutionary scenario where the AGNs turn on during the final stage of merging. However, the AGNs may also pre-date the interaction.
4. The trend of increasing $F_{2-10 \text{ keV}}/F_{FIR}$ with increasing infrared luminosity brings further support for an increasing AGN fraction with increasing infrared luminosity as seen at optical and mid-infrared wavelengths.

Chapter 5

Suzaku Observations of Local U/LIRGs

5.1 The Need for *Suzaku*

Recent surveys with *XMM-Newton* and *Chandra* (e.g., Franceschini et al. 2003; Ptak et al. 2003; Teng et al. 2005) have found that $\sim 40\%$ of observed ULIRGs show signatures of AGNs. The observed 2–10 keV luminosity of the surveyed sample is $\sim 10^{40}$ – 10^{43} ergs s $^{-1}$, with a majority of the sources having luminosities below 10^{42} ergs s $^{-1}$. While the ratio $\log(L_{2-10 \text{ keV}}/L_{IR})$ is small in nearby ULIRGs (from -4 to -1 ; e.g., Teng et al. 2005), this is not much smaller than that found in radio-quiet QSOs (from -3 to -1). Moreover, absorption may be a factor even at these energies. If the absorbing column exceeds $\sim 10^{24}$ cm $^{-2}$, the primary continuum emission is suppressed significantly by absorption and Compton down-scattering. Thus observations at $\gtrsim 10$ keV are best to detect Compton-thick AGNs. The sensitivity of *Suzaku* at these high energies is well suited for the study of highly obscured sources like ULIRGs.

Table 5.1. The *Suzaku* Sample

Object	z	$\log F_{\text{IR}}$ [ergs/s/cm ²]	$f_{25\ \mu\text{m}}/f_{60\ \mu\text{m}}$	Spectral Type	$N_{\text{H,Galactic}}$ [10 ²⁰ cm ⁻²]	Scale [kpc/'']	D_{L} [Mpc]
(1)	(2)	(3)	(4)	(5)	(6)	(7)	(8)
F05189–2524	0.042	–8.87	0.25	S2/S1	1.92	0.71	173.3
F08572+3915	0.058	–9.18	0.23	LINER/S2	2.60	1.05	242.0
Mrk 273	0.038	–8.78	0.10	S2	1.10	0.70	156.3
PKS 1345+12	0.122	–9.65	0.35	S2/S1	1.90	2.05	531.8
Arp 220	0.018	–8.11	0.08	LINER	4.27	0.34	72.9

Note. — Col. (1): Object name. Col (2): redshift. Col. (3): logarithm of infrared (8–1000 μm) flux. Col. (4): the 25-to-60 μm *IRAS* flux ratio, a measure of the dust temperature. Col. (5): galaxy spectral type. Col. (6): Galactic hydrogen column density (Dickey & Lockman 1990). Col. (7): Physical size corresponding to 1''. Col. (8): Luminosity distance.

In this chapter, we present *Suzaku* XIS (0.5–10 keV) and HXD/PIN (15–40 keV) observations of five well-known local ULIRGs. In §5.2, we discuss our sample. In §5.3, we report the observations and describe the methods we used to reduce the data. In §5.4, the results from our spectral analysis of the *Suzaku* data are discussed. In §5.5, we combine the *Suzaku* data with earlier published and unpublished *XMM-Newton* and *Chandra* data to fine tune our spectral models. The results of this study are summarized in §5.6. Throughout this chapter, we adopt the cosmology of $H_0=75\ \text{km s}^{-1}\ \text{Mpc}^{-1}$, $\Omega_{\text{M}}=0.3$, and $\Omega_{\Lambda}=0.7$.

5.2 Sample

The five ULIRGs in the present study are F05189–2524, F08572+3915, Mrk 273, PKS 1345+12, and Arp 220. They were selected because they have readily available *Suzaku* data, either from our own program (PI: Veilleux) or from the public archive. They are among the nearest, brightest, and best-studied ULIRGs in the *IRAS* Bright Galaxy Survey (Sanders et al. 2003). Table 5.1 lists the basic properties of these sources. Here we briefly review the relevant literature on each source.

F05189–2524 is an unresolved late stage merger surrounded by tidal debris (Veilleux et al. 2002, 2006) with “warm” infrared colors. It is optically classified as a Seyfert 2, but near-infrared spectroscopy of this source reveals the presence of an obscured broad line region (BLR) at Pa α (Veilleux et al. 1999a,b). Spectra from previous *ASCA* (Risaliti et al. 2000; Severgnini et al. 2001), *XMM-Newton* (Imanishi & Terashima 2004), and *Chandra* (Ptak et al. 2003) observations flatten out above 2 keV and are best fit by an absorbed power law with $N_{\text{H}} \sim 0.5 - 1 \times 10^{23}$ cm $^{-2}$, $\Gamma \sim 1.0-1.9$, and a thermal component with $kT \sim 0.1-0.9$ keV. The absorption-corrected 2–10 keV luminosity derived from the published *XMM-Newton* and *Chandra* data is $\sim 10^{43}$ ergs s $^{-1}$.

F08572+3915 is another “warm” ULIRG, consisting of a pair of interacting galaxies with nuclear separation of ~ 6 kpc (Veilleux et al. 2002, and references therein). The northwestern nucleus is classified as a LINER. A 2-cm radio core coincides with the northwestern nucleus (Nagar et al. 2003). However, only an upper limit on its 2–10 keV flux exists in the literature – 7.6×10^{-12} ergs cm $^{-2}$ s $^{-1}$ – from the *HEAO* satellite (Polletta et al. 1996).

Mrk 273 is in the early phase of a merger where the nuclei are separated by 680 pc (Veilleux et al. 2002) and is optically classified as a Seyfert 2 (Veilleux et al. 1999a). A [Si VI] 1.96 μm feature, a strong indicator of AGN activity, is detected in this “cool” ULIRG (Veilleux et al. 1999b). Its radio flux falls above the radio-to-FIR correlation of starbursts and a bright AGN-like radio core is detected on VLBA scale in this object (Lonsdale et al. 1993). The *Chandra* 0.5–2 keV X-ray spectrum of Mrk 273 is best explained with a MEKAL plasma with $kT \sim 1.3$ keV and its 2–10 keV spectrum is best fit by an absorbed power law with $\Gamma \sim 1.0$ and $N_{\text{H}} \sim 10^{23}$ cm $^{-2}$ (Ptak et al. 2003). The flat slope of the 2–10 keV continuum may be a result of reflection, but the *Chandra* observation of Ptak et al. (2003) shows a very

weak Fe K α emission line with an equivalent width of $\sim 0.09\text{--}0.44$ keV. Comparisons of observations by *ASCA*, *BeppoSAX*, and *Chandra* show that this source exhibits possible long term flux variability (Xia et al. 2002).

PKS 1345+12 is yet another “warm” ULIRG. It is in the early stage of a merger with two nuclei separated by 4.0 kpc (Veilleux et al. 2002). Optically classified as a Seyfert 2 galaxy (Kim & Sanders 1998; Sanders et al. 1988b), infrared observations by Veilleux et al. (1997) suggest a buried BLR at Pa α . Observations by Evans et al. (1999) have shown that the eastern nucleus has colors consistent with reddened starlight while the the western nucleus has extremely red colors indicative of an optical quasar. The western nucleus is also coincident with peak CO emission (Evans et al. 1999), a radio core (Nagar et al. 2003), and 0.5–8 keV X-ray emission (Imanishi & Terashima 2004). According to Imanishi & Terashima (2004), the *Chandra* continuum is consistent with that of an absorbed AGN (power law $\Gamma=1.8$ with $N_{\text{H}} \sim 4.5 \times 10^{22}$ cm $^{-2}$). The *Chandra* data also showed a narrow Fe K α emission line with an equivalent width of ~ 0.13 keV.

Finally, Arp 220 is by far the best-studied ULIRG due to its vicinity. Optically classified as a LINER, this “cool” ULIRG is also an early merger with nuclei separated by ~ 0.4 kpc (Veilleux et al. 2002). Multi-wavelength data suggest the presence of a black hole in the western nucleus (Downes & Eckart 2007, and references therein). Previous *Chandra* observations detected both nuclei as well as extended soft X-ray emission from lobes and plumes that extend beyond the optical galaxy (Clements et al. 2002; McDowell et al. 2003). The full *Chandra* band nuclear spectrum is best fit by a thermal MEKAL component with $kT \sim 0.8$ keV and a flat power law with $\Gamma \sim 1.1$ absorbed by a column of $\sim 10^{21}$ cm $^{-2}$ (Ptak et al. 2003). Analysis of *XMM-Newton* data by Iwasawa et al. (2005) suggests the presence of an Fe K emission line with equivalent width of ~ 1.9 keV emanating from the western

Table 5.2. *Suzaku* Observations

Object	Observation ID	PI Name	Date [UT]	XIS Net Exposure [ksec]	HXD Net Exposure [ksec]
(1)	(2)	(3)	(4)	(5)	(6)
F05189–2524	701097010	Veilleux; Anabuki	2006 April 10	78.2	48.0
F08572+3915	701053010	Gallagher	2006 April 14	77.2	58.1
Mrk 273	701050010	Veilleux	2006 July 7	79.9	76.3
PKS 1345+12	702053010	Veilleux	2008 January 7	53.0	41.4
Arp 220	700006010	<i>Suzaku</i> SWG	2006 January 7	98.6	86.9

Note. — Col. (1): Object name. Col (2)–(3): *Suzaku* proposal number and principal investigator of archived data. Col. (4): beginning observing date in UT. Col. (5)–(6): net exposure time in kiloseconds after screening and HXD deadtime corrections.

nucleus.

5.3 Observations and Data Reduction

The details of the *Suzaku* observations are listed in Table 5.2. Three of the sources (F05189–2524, Mrk 273, and PKS 1345+12) were of our own program (PI: Veilleux, Anabuki was co-PI for F05189–2524) and the other two, F08572 + 3915 (PI: Gallagher) and Arp 220 (PI: the *Suzaku* Science Working Group, or SWG), were downloaded from the public archive. All of the observations were performed at the HXD aim point to increase the sensitivity of the HXD. The analysis of the data on F05189–2524, F08572+3915, Mrk 273, and Arp 220 was performed with version 6.3.1 of HEASoft and CALDB version 20071016. PKS 1345+12 was observed at the end of Cycle 2 and after the completion of the data analysis on the other objects in the sample. Thus, the analysis of the data on PKS 1345+12 was performed with the more up-to-date version 6.4 of HEASoft and CALDB version 20080401.

5.3.1 XIS Data Reduction

The XIS data reduction followed the guidelines provided in the *Suzaku* Data Reduction Guide¹. The data were screened following the version 2 data screening criteria. Due to nearby field sources, cleaned events for all objects except PKS 1345+12 were then extracted in circular regions with 1' radii (the minimum recommended region size) centered on the targets wherever possible. The PKS 1345+12 field is rather empty, so the extraction region has a radius of $\sim 3.1'$. Since the extraction regions are so large, *Chandra* ACIS data were used as a check to ensure no other X-ray sources were included in the extraction regions. Background events were extracted in same-sized nearby source-free regions. The source spectra were binned to at least 50 counts bin^{-1} for PKS 1345+12 and at least 15 counts bin^{-1} for the others so that χ^2 statistics can be used when modeling the spectra.

The response (RMF) and auxiliary (ARF) files were produced using `xisrmfgen` and `xissimarfgen`. The ARF files were generated assuming 400,000 incident photons and the default grid spacing.

In the modeling of the XIS data, the XIS1, XIS2, and XIS3 detectors are assumed to have the data processing version 2.0 cross-normalization factors of 1.065, 1.035, and 1.067 with respect to the XIS0 detector, respectively².

¹See <http://heasarc.gsfc.nasa.gov/docs/suzaku/analysis/abc/>.

²See: <ftp://legacy.gsfc.nasa.gov/suzaku/doc/xrt/suzakumemo-2007-11.pdf>.

5.3.2 HXD/PIN Data Reduction

The HXD/PIN data were reduced following the guidelines provided by the *Suzaku* team. The HXD/PIN spectra for both sources were extracted after the selection of good time intervals (the “ANDed GTI” from both the data and the non-X-ray background provided by the *Suzaku* HXD team). Dead-time corrections (on the order of about 5%) were applied to the extracted source spectra. The extracted spectra were binned using `grppha`³.

The response files were provided by the HXD team. Due to changes in the bias voltages and the threshold over time, we used the first-epoch response file for observations of F05189–2524, F08572+3915, and Arp 220, second-epoch for Mrk 273, and fourth-epoch for PKS 1345+12.

As its name implies, the non-X-ray backgrounds (NXB) from charged particles modeled by the HXD team do not include the cosmic X-ray background (CXB) which peaks within the energy range of the HXD/PIN. The CXB for each galaxy was modeled following a recipe⁴ provided by the HXD team. The simulated CXB is approximately 5% of the NXB. The NXB and CXB were added together using `mathpha` to provide total backgrounds for the HXD/PIN data.

At the time of this writing, the accuracy of the processing version 2.0 HXD/PIN background model is 3.8%⁵. However, a $\sim 10\%$ offset in the version 2.0 background model was discovered for data taken between March and May of 2006 due to changes

³We binned the data using group 0 31 2 32 63 4 64 95 8 96 127 32 128 255 64. Each set of three numbers represent the channel range grouped and the number of channel bins in each group. This choice of grouping was used so that each bin contains approximately the same number of photons.

⁴See: http://heasarc.gsfc.nasa.gov/docs/suzaku/analysis/pin_cxb.html.

⁵This is the $1\text{-}\sigma$ statistical plus systematic error in the 15–40 keV band for a net integration time of 10 ksec. See: <ftp://legacy.gsfc.nasa.gov/suzaku/doc/hxd/suzakumemo-2007-09.pdf>.

in the PIN observing mode. For the affected data (F05189–2524 and F08572+3915), processing version 1.2 HXD/PIN background were used as recommended by the *Suzaku* team. Dead time corrections were also performed on the backgrounds for the affected data⁶. The reproducibility of the version 1.2 background is between 5 and 10%⁷. For the modeling of the data, the cross-normalization of the PIN with respect to XIS0 is 1.16 and 1.13 for the version 1.2 and 2.0 backgrounds, respectively⁸.

5.4 *Suzaku* Results

The spectra were analyzed using the XSPEC package (version 11.3.2ag). The energy range of the detectors were limited to 0.5–10 keV for the XIS detectors and 15–40 keV for the PIN detector to avoid calibration problems. All the errors in the parameters are at the 90% level for one parameter of interest ($\Delta\chi^2 = 2.7$).

In the modeling of the spectra, a simple power-law distribution absorbed only by the Galactic column is first assumed. If the model is not a satisfactory fit to the data, then more components are added on to the model until a satisfactory fit is achieved. The continuum model components considered in this paper are: (1) an absorbed power-law model which represents emission from an AGN (model parameters fitted include a column density, N_{H} , a power law index, Γ , and a normalization factor), (2) a thermal MEKAL model representing emission from stars or galactic winds (with a gas temperature, kT , and a normalization factor), (3) a partial-covering fraction model where some fraction, f_{cover} , of the intrinsic nuclear radiation is absorbed and the rest goes through unimpeded. The other parameters fitted are the equivalent

⁶See: <http://www.astro.isas.ac.jp/suzaku/analysis/hxd/v1/pinnxb/>

⁷See: <ftp://legacy.gsfc.nasa.gov/suzaku/doc/hxd/suzakumemo-2006-43.pdf>.

⁸See: <ftp://legacy.gsfc.nasa.gov/suzaku/doc/xrt/suzakumemo-2006-40.pdf> for version 1.2 backgrounds and [suzakumemo-2007-11.pdf](ftp://legacy.gsfc.nasa.gov/suzaku/doc/xrt/suzakumemo-2007-11.pdf) for version 2.0 backgrounds.

column density, N_{H} , Γ , and a normalization factor. (4) a scattering model where an absorbed power law represents the direct transmitted component and an unabsorbed power law of the same photon index represents a scattered component (N_{H} , Γ , and a normalization factor for each of the direct and scattered components), (5) a neutral reflection model⁹ with an unabsorbed power law representing the direct component and a reflection component with the same photon index as the direct component (Γ and a normalization factor for each of the reflected and transmitted components), and finally, (6) a pure ionized reflection model as proposed by Ross & Fabian (2005) without any direct transmitted component (Γ and a normalization factor).

5.4.1 *IRAS F05189–2524*

XIS Spectrum

The XIS spectrum of F05189–2524 is shown in Figure 5.1. First, we find that it is well-modeled by a simple power-law model plus a MEKAL component with abundances fixed at solar all modified by Galactic absorption ($\chi^2_{\nu} = 1.57$ for 124 degrees of freedom). An additional Gaussian component is needed ($\Delta\chi^2=22.8$ for a change in d.o.f. of 3) to reproduce the emission line at ~ 6.4 keV (*i.e.* the Fe K α line; equivalent width, or EW, ~ 1.84 keV). While the spectrum shows excess emission at around 1.3 and 1.9 keV (Si XIII emission features), the addition of a second and a third Gaussian component to the model does not significantly improve the fit ($\Delta\chi^2=0.05$ for a change in d.o.f. of 3). The excess emission at 1.9 keV may be a calibration feature associated with absorption edges from the mirror. The relatively

⁹The reflection component is represented by the PEXRAV model in XSPEC. For the spectral fitting, the metal abundance, iron abundance, and inclination angle are fixed at the default value. The relative reflection parameter is fixed at -1 , thus modeling only the reflection component. No energy cut off is assumed. Therefore, only Γ and the normalization factor are free parameters.

flat spectral index and the large equivalent width of the iron line suggest that the spectrum may be reflection dominated. The addition of a reflection component to the continuum model results in a better fit ($\chi^2_\nu = 1.49$ for 123 d.o.f.). The F-test probability for the addition of one parameter (the normalization of the reflected component) is relatively small, at 1.6×10^{-2} , implying that it is reasonable to add the extra component. While the spectral index required for this fit, $\Gamma = 2.68^{+0.30}_{-0.13}$, is unusually steep for an AGN where the canonical value for Γ is ~ 1.8 , it is not too different from the range seen in PG quasars (1.3–2.48; Piconcelli et al. 2005). The best-fit reflection model parameters to the XIS spectrum are listed in Table 5.3 and the best-fit model is shown with the spectrum in Figure 5.1.

HXD/PIN Data

F05189–2524 is undetected by the HXD/PIN. As mentioned in § 5.3.2, the documentation provided by the *Suzaku* team state that the reproducibility of the version 1.2 HXD/PIN backgrounds are on average ~ 5 –10%. Here we estimate the systematic and statistical error of the HXD/PIN data for our specific observation. The standard deviation of the histogram of the 15–40 keV residuals from the 1-day (40 ksec) observations in the documentation imply that the systematic error of the NXB is $\sim 2.4\%$. Considering the net HXD/PIN integration time and the 15–40 keV total background count rate for observations with integration times longer than 40 ksec, the statistical error of the F05189-2524 observation is $\sim 0.9\%$. Thus, the total $1\text{-}\sigma$ error (systematic and statistical errors added in quadrature) for the HXD/PIN observation of F05189-2524 is $\sim 2.6\%$. Therefore, the 15–40 keV $3\text{-}\sigma$ detection limit for this observation is ~ 0.020 counts per second (cps).

Table 5.3: Best-fit Parameters to *Suzaku* Spectra[†]

Object	Best-fit Model	kT [keV]	Γ	$N_{\text{H, source}}$ [10^{23} cm $^{-2}$]	f	E_{line} [keV]	σ [keV]	EW [keV]	K	$\chi^2/\text{d.o.f.}$	Observed $F_{0.5-2}$ keV (12)	Unabsorbed $F_{0.5-2}$ keV (13)	Observed F_{2-10} keV (14)	Unabsorbed F_{2-10} keV (15)	Observed F_{12-40} keV (16)	Unabsorbed F_{12-40} keV (17)
(1)	(2)	(3)	(4)	(5)	(6)	(7)	(8)	(9)	(10)	(11)	(12)	(13)	(14)	(15)	(16)	(17)
XIS Only																
F05189-2524	A	$0.71^{+0.13}_{-0.04}$	$2.68^{+0.13}_{-0.15}$...	$82.73^{+0.14}_{-0.15}$	$6.40^{+0.82}_{-0.87}$	$0.00^{+0.00}_{-0.00}$	$0.47^{+0.75}_{-0.10}$	$2.20^{+0.48}_{-1.84} \times 10^{-5}$	$185/123$	$0.66^{+0.10}_{-0.10}$	$0.70^{+0.14}_{-0.10}$	$1.03^{+0.39}_{-0.38}$	$1.03^{+0.40}_{-0.40}$
Mrk 273	B	$0.64^{+0.04}_{-0.04}$	$1.56^{+0.09}_{-0.09}$	$8.64^{+1.71}_{-1.20}$	$0.09^{+0.03}_{-0.03}$	$6.39^{+0.03}_{-0.03}$	$0.00^{+0.10}_{-0.10}$	$0.56^{+0.15}_{-0.11}$	$3.65^{+1.84}_{-0.90} \times 10^{-4}$	$233/187$	$1.17^{+0.13}_{-0.13}$	$8.95^{+4.10}_{-2.05}$	$4.29^{+0.33}_{-1.97}$	$20.44^{+9.48}_{-4.84}$
PKS 1345+12	B	...	$1.64^{+0.09}_{-0.04}$	$0.43^{+0.03}_{-0.02}$	0.02	$3.13^{+0.52}_{-0.54} \times 10^{-4}$	$164/156$	$0.37^{+0.09}_{-0.10}$	$5.93^{+2.47}_{-0.73}$	$9.53^{+3.17}_{-0.29}$	$11.91^{+3.12}_{-0.74}$
Arp 220	C	$0.67^{+0.07}_{-0.04}$	$1.93^{+0.07}_{-0.07}$	$0.07^{+0.02}_{-0.02}$...	$6.70^{+0.13}_{-0.08}$	$0.05^{+0.27}_{-0.05}$	$0.42^{+0.54}_{-0.32}$	$1.80^{+0.78}_{-0.40} \times 10^{-9}$	$181/176$	$0.66^{+0.10}_{-0.11}$	$1.85^{+0.73}_{-0.40}$	$0.98^{+0.29}_{-0.42}$	$1.04^{+0.74}_{-0.35}$
Combined XIS+HXD/PIN Spectra																
Mrk 273	B	$0.64^{+0.04}_{-0.04}$	$1.40^{+0.10}_{-0.11}$	$14.09^{+1.63}_{-1.53}$	$0.05^{+0.03}_{-0.03}$	$6.38^{+0.03}_{-0.04}$	$0.03^{+0.08}_{-0.15}$	$0.68^{+0.18}_{-0.15}$	$6.14^{+2.39}_{-1.77} \times 10^{-4}$	$268/199$	$1.15^{+0.12}_{-0.10}$	$14.50^{+5.32}_{-3.98}$	$4.68^{+0.75}_{-1.53}$	$43.19^{+16.03}_{-12.09}$	$66.59^{+22.33}_{-35.53}$	$76.27^{+28.79}_{-21.45}$

Note. — [†] F08572+3915 is undetected by the XIS and is thus not included in this table. [‡] Since the spectrum is pure reflection, the normalization factor is of the reflection component. Col. (1): Object name. Col. (2): favored model – (A) reflection plus power law model, (B) scattering model, (C) ionized reflection model. Col (3): temperature of the thermal starburst component from the MEKAL model. Col. (4): slope to the power-law model. Col. (5): absorption within the source. Col. (6): the ratio of the normalization parameter between the reflected (or scattered) component to the direct component. Col. (7): rest energy of the emission line. Col. (8): line width of the emission line. Col. (9): equivalent width of the emission line. Col. (10): normalization factor of the direct component in photons cm $^{-2}$ s $^{-1}$ at 1 keV. Col. (11): χ^2 fitting statistics per degree of freedom. Col. (12)–(17): flux in units of 10^{-13} ergs s $^{-1}$ cm $^{-2}$.

5.4.2 *IRAS F08572+3915*

XIS Non-Detection and *XMM-Newton* and *Chandra* Data

As mentioned previously in § 5.2, there has never been a published X-ray detection of F08572+3915 in the X-ray energy range. It is also undetected by the XIS. A constraint on the limiting flux of F08572+3915 can be derived from the background. The average background count rate from the XIS front illuminated detectors (XIS0, 2, 3) is $\sim 1.3 \times 10^{-3}$ cps. Assuming an ideal, flat background ($\Gamma \sim 1$), the *WebPIMMS*¹⁰ application was used to estimate the observed flux of the background spectrum. The application yields a flux of $\sim 4 \times 10^{-14}$ ergs s⁻¹ cm⁻², more than two orders of magnitude better than the upper limit placed on this object by *HEAO*.

F08572+3915 was observed with both *XMM-Newton* and *Chandra*, but the results of the analysis were never published. F08572+3915 is undetected in the archived *XMM-Newton* data (ObsID: 0200630101, PI: Imanishi, $t_{\text{effective}}=13$ ksec). But the lower background and better spatial resolution of the *Chandra* ACIS-S archival data (ObsID: 6862, PI: Komossa, $t_{\text{effective}}=15$ ksec) provide a conclusive detection of nine counts in the 0.5–8 keV band. The *Chandra* detection coincides with the optical northwestern nucleus (*i.e.* the LINER/Seyfert 2 nucleus). Assuming a canonical AGN power law spectrum ($\Gamma=1.8$) modified by Galactic absorption for the Seyfert 2 nucleus, the detected count rate of F08572+3915 in the *Chandra* band corresponds to an observed 0.5–10 keV flux of $\sim 5 \times 10^{-15}$ ergs s⁻¹ cm⁻², consistent with the upper limit derived from the XIS observations. This limit is also lower than the sensitivity limit of *Suzaku*.

The *Chandra* detection implies that the Seyfert nucleus may be a weak X-ray source or a heavily obscured AGN. If we assume no intrinsic absorption, the 0.5–

¹⁰<http://heasarc.gsfc.nasa.gov/Tools/w3pimms.html>

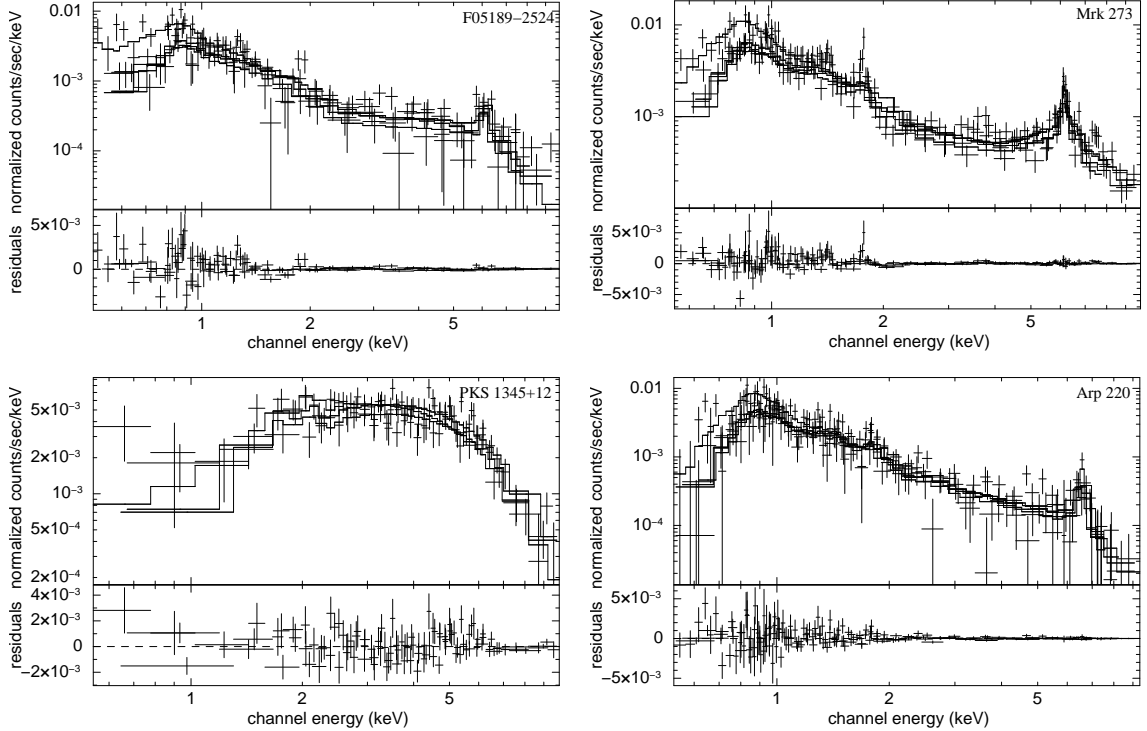


Figure 5.1: Spectra of F05189–2524 (top left), Mrk 273 (top right), PKS 1345+12 (bottom left) and Arp 220 (bottom right) with their respective best-fit models for all four XIS detectors. *F08572 + 3915* is not detected by the XIS. The data are binned to at least 50 counts bin^{-1} for PKS 1345+12 and at least 15 counts bin^{-1} for the others. The horizontal axis is energy in the observer’s frame. In F05189–2524, Mrk 273, and Arp 220, an emission line is detected near 6.4–6.7 keV, consistent with emission arising from neutral or ionized iron. The same emission line also appears to be present in PKS 1345+12, but the detection is not statistically significant ($\Delta\chi^2=2.0$ for $\Delta\text{d.o.f}=2$). Other than PKS 1345+12, the 0.5–2 keV spectrum for each object has a thermal component with temperatures of $\sim 0.7\text{--}0.8$ keV, consistent with earlier results on ULIRGs. The best-fit parameters are listed in Table 5.3.

10 keV flux from the *Chandra* observation of this object implies an intrinsic luminosity of $\sim 5 \times 10^{40}$ ergs s^{-1} . This luminosity falls within the range of X-ray luminosities of LINERs as measured by Terashima & Wilson (2003) and is consistent with LINERs being powered by low-luminosity AGNs.

However, like many other LINER 2s (Terashima & Wilson 2003), F08572+3915 is likely to be affected by absorption. Infrared observations of this object do show strong absorption features and weak PAH emission characteristic of deeply buried

AGNs with a line-of-sight extinction of $A_V \geq 78$ mag. (Imanishi et al. 2006; Armus et al. 2007; Veilleux et al. 2008). A CO-based estimate of the column density by Evans et al. (2002) is in the range of $\sim 3\text{--}10 \times 10^{24}$ cm $^{-2}$. The hardness ratio of the F08572+3915 detection is 0.56. Following the hardness ratio method presented in Teng et al. (2005), a single power law with an estimated photon index of ~ -0.43 would fit the data. The inverted power law spectrum may be an indication of a large column density since the softer 0.5–2 keV photons are more readily affected by absorption. The estimated 0.5–10 keV flux from the hardness ratio method, which assumes Galactic absorption only, is 3×10^{-14} ergs s $^{-1}$ cm $^{-2}$, corresponding to a luminosity of $\sim 2 \times 10^{41}$ ergs s $^{-1}$.

HXD/PIN Data

F08572+3915 is not detected by the HXD/PIN above the total background. Following the procedure outlined in § 5.4.1, the HXD/PIN 3- σ detection limit was used to approximate the limiting count rate and observed flux in the 15–40 keV band. The 3- σ upper limit on the count rate for F08572+3915 in the HXD/PIN band is ~ 0.020 cps.

5.4.3 Mrk 273

XIS Spectrum

Mrk 273 is detected by the XIS. We first tried to model the XIS spectrum with a MEKAL component describing the starburst and a heavily absorbed power-law distribution which does not fit the 2–10 keV spectrum properly. Rather, the XIS spectrum is well modeled by the scattering model plus a MEKAL component with abundances fixed at solar and all components modified by Galactic absorption. Approximately 9% of the intrinsic AGN emission is scattered. An additional Gaussian

component is needed to model the emission line at ~ 6.4 keV ($EW \sim 0.56$ keV). While the spectrum shows excess emission at around 1.9 keV (Si XIII emission), the addition of a second Gaussian component to the model does not significantly improve the fit ($\Delta\chi^2=1$ with $\Delta d.o.f.=3$). Again, the feature at 1.9 keV may be a calibration feature associated with absorption edges from the mirror. A reflection model was also tested on the XIS spectrum, but this results in a worse fit ($\chi^2_\nu = 1.52$ for 187 d.o.f.) than the scattering model ($\chi^2_\nu = 1.25$ for 187 d.o.f.). The best-fit parameters to the XIS spectrum are listed in Table 5.3 and the XIS spectrum with the best-fit model is shown in Figure 5.1.

HXD/PIN Data & Contaminants

Mrk 273 is marginally detected by the HXD/PIN. The net (observed minus background) HXD/PIN spectrum of Mrk 273 is $\sim 5.4\%$ of the total (NXB+CXB) background. Figure 5.2 is a comparison of the spectrum, total background, and net spectrum. The current best estimate for the error in the version 2.0 NXB background is 3.8% for observations with net integration time of 10 ksec. We estimate the error on our Mrk 273 observation following the steps outlined in §5.4.1. The total systematic plus statistical error for the Mrk 273 observation is $\sim 3.0\%$, implying the HXD/PIN detection of Mrk 273 is at $\sim 1.8\text{-}\sigma$ (or with $\sim 93\%$ confidence).

Because the PIN is not an imaging detector and has a very large field of view ($34' \times 34'$, ~ 3.5 times the area of the XIS field of view), there may be sources of contamination in the HXD/PIN signal. While hard X-ray and soft gamma ray catalogs (e.g., the INTEGRAL reference catalog; Ebisawa et al. 2003) do not list any sources of comparable flux within the PIN field of view and energy range, most of these flux values are based on modeling of previous observations at lower energies. There remains a possibility that the signal may come from a previously unobserved

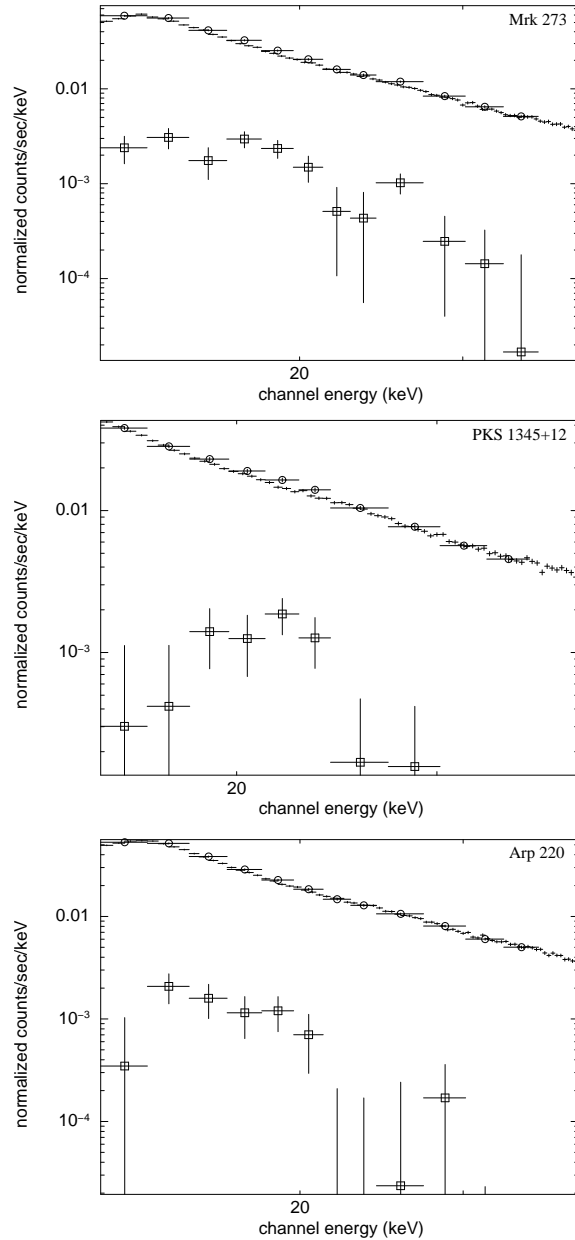


Figure 5.2: HXD/PIN spectrum (open circles), together with the background spectrum (NXB+CXB; small crosses) and the net spectrum (open squares) of Mrk 273, PKS 1345+12, and Arp 220. The net spectrum for Mrk 273, PKS 1345+12, and Arp 220 is 5.4%, 3.4%, and 2.2% above the background, respectively. Mrk 273 is the only source that is detected above the background beyond the uncertainties of the background modeling (at the $1.8\text{-}\sigma$ level). The spectra of F05189–2524 and F08572+3915 do not lie above the background, so they are not shown here.

nearby source. Three likely candidates are detected within the field of view of the XIS. Mrk 273x is an unabsorbed Seyfert 2 galaxy at a redshift of 0.458 located approximately $1.2'$ northeast of Mrk 273. The XIS spectrum of Mrk 273x is well fit by a power-law component modified only by Galactic absorption ($\Gamma \sim 1.69_{-0.12}^{+0.11}$; $\chi^2_{\nu} \sim 1.21$ for 77 d.o.f.). The observed 0.5–10 keV flux of Mrk 273 is approximately 2.9 times that of Mrk 273x. SBS 1342+560 is a background QSO at a redshift of 0.937 located approximately $6.3'$ south of Mrk 273. The XIS spectrum of this source is also well fit by a power-law component modified only by Galactic absorption ($\Gamma \sim 2.03 \pm 0.05$; $\chi^2_{\nu} \sim 1.28$ for 242 d.o.f.). The observed 0.5–10 keV flux of Mrk 273 is approximately 1.5 times that of this source. Lastly, SDSS J1342512.06+554759.6 is a background QSO at a redshift of 1.17 located approximately $7'$ southeast of Mrk 273. Its XIS spectrum is also well fit by a power-law component modified only by Galactic absorption ($\Gamma \sim 1.62 \pm 0.07$; $\chi^2_{\nu} \sim 1.29$ for 139 d.o.f.). The observed 0.5–10 keV flux of Mrk 273 is approximately 1.9 times that of this source.

Thus, none of the objects within the XIS field of view shows evidence of being highly obscured. One would therefore expect their spectral energy distributions at higher energies to follow the power law seen at low energies. If that is indeed the case, their contributions to the overall PIN signal of Mrk 273 are negligible; this is explained in the next section.

Combined XIS-HXD/PIN Spectral Modeling

We modeled the combined XIS and PIN spectrum of Mrk 273 with the scattering model. All of the best-fit parameters are consistent with the values obtained from the fit of the XIS spectrum alone with the exception of the column density which increased by a factor of ~ 2 . The HXD/PIN contributions from the neighboring sources have been taken into account by adding the best-fit XIS model of the

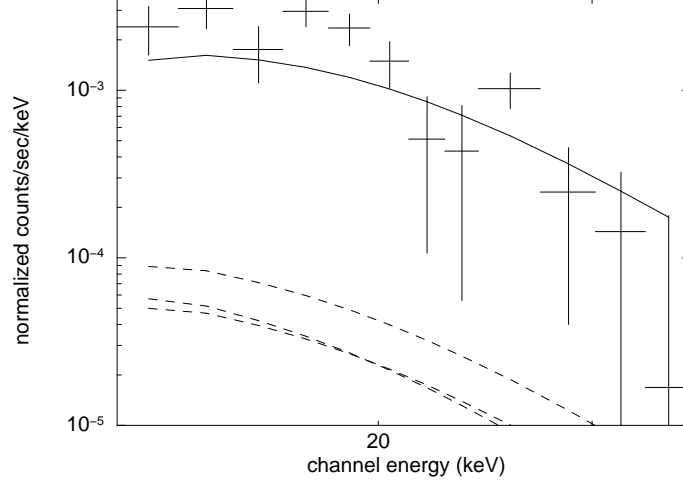


Figure 5.3: The net background-subtracted 15–40 keV HXD/PIN spectrum of Mrk 273 compared with the spectral models of possible contaminants in the PIN field of view. The solid line represents the best-fit model from the XIS-HXD/PIN spectral fitting and is a sum of the flux from Mrk 273 and the contaminants. The dashed lines represent the best-fit XIS models of the contaminants extrapolated to the HXD/PIN energy range. The contributions from these contaminants to the overall PIN signals are negligible.

contaminants to the HXD/PIN component of the Mrk 273 model (see Figure 5.3). The best-fit model to the full-band Mrk 273 spectrum in this case has parameter values listed in Table 5.3 and the spectrum is shown in Figure 5.4 with the XIS-HXD/PIN spectrum. While the photon index value of ~ 1.4 may suggest flattening of the spectrum due to reflection, the addition of a reflection component resulted in a statistically worse fit ($\chi^2_\nu = 1.66$ for 197 d.o.f.) relative to that obtained from the scattering model ($\chi^2_\nu = 1.35$ for 199 d.o.f.). Approximately 5% of the intrinsic AGN flux is scattered. The gas temperature of ~ 0.7 keV is consistent with the range found in ULIRGs (Grimes et al. 2005). Overall, the best-fit model of Mrk 273 agrees well with X-ray observations of other ULIRGs (e.g., Franceschini et al. 2003; Ptak et al. 2003; Teng et al. 2008, 2005). The comparison of the XIS data with published results is postponed until § 5.5.2.

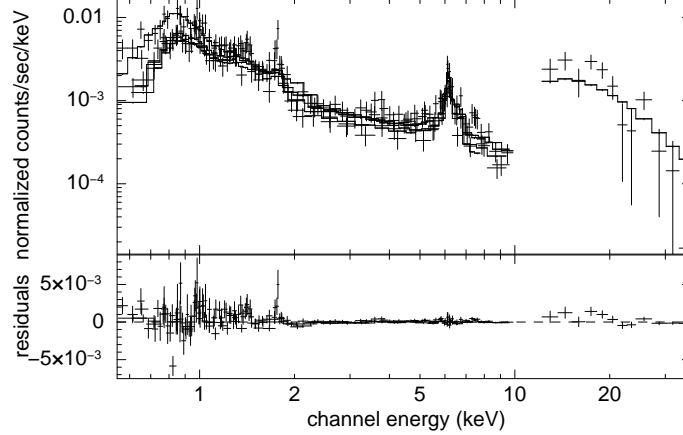


Figure 5.4: The combined XIS-HXD/PIN spectrum of Mrk 273 with the best-fit scattering model. The horizontal axis is energy in the observer’s frame. The directly transmitted AGN flux is $\sim 5\%$ of the intrinsic flux. The iron line at ~ 6.4 keV is detected and a MEKAL model with gas temperature ~ 0.7 keV is needed to reproduce the soft X-rays. The cross-normalization of the HXD/PIN with respect to XIS0 is assumed to be 1.13. The best-fit parameters for the full band (XIS+HXD/PIN) modeling are listed in Table 5.3.

5.4.4 PKS 1345+12

XIS Spectrum

The XIS spectrum of PKS 1345+12 is shown in Figure 5.1. It is best modeled by a scattering continuum model (§ 5.4) modified by Galactic absorption. The transmitted AGN flux is $\sim 2\%$ of the intrinsic AGN flux. Unlike other ULIRGs, the 0.5–2 keV spectrum does not require a MEKAL thermal component. The best-fit parameters are listed in Table 5.3. These best-fit values and the model of the 0.5–10 keV continuum are consistent with *Chandra* measurements reported by Imanishi & Terashima (2004). The Imanishi & Terashima (2004) model for the *Chandra* data includes a narrow Fe line at 6.4 keV. This emission line also appears in the XIS spectrum, but is statistically insignificant ($\Delta\chi^2=2.0$ for a change in d.o.f. of 2). This is also consistent with the fact that the lower limit to the equivalent width of the Fe line in the Imanishi & Terashima (2004) model is 0 keV. No flux or spectral

variation were detected over the 0.5–10 keV energy range between the *Chandra* and *Suzaku* observations.

The unabsorbed 0.5–10 keV flux for PKS 1345+12 is $\sim 6.0 \times 10^{43}$ ergs s⁻¹ and the absorption corrected ratio $\log(L_{2-10 \text{ keV}}/L_{IR})$ is ~ -2.3 , consistent with the range found in PG quasars. This and the lack of a thermal component in the 0.5–2 keV spectrum suggest that the X-ray spectrum is dominated by an AGN.

HXD/PIN Data

The net HXD/PIN spectrum of PKS 1345+12 lies $\sim 3.4\%$ above the total background (Figure 5.2). Accounting for the uncertainties in the PIN background of $\sim 3.1\%$ (see § 5.4.1 on how this was calculated), the detection is at only 1.1σ . There are not enough net counts for a meaningful spectral fitting of the full-band (XIS+HXD/PIN) spectrum. However, assuming no contamination from nearby sources, the net observed 15–40 keV count rate for PKS 1345+12 is $9.9 \pm 2.8 \times 10^{-3}$ cps. Using the XIS best-fit model, given the lack of an obvious reflection component, the 15–40 keV count rate translates to a flux of $\sim 4.4_{-1.3}^{+1.1} \times 10^{-12}$ ergs s⁻¹ cm⁻².

5.4.5 Arp 220

XIS Spectrum

Arp 220 is detected by the XIS. At first, the XIS spectrum was modeled by a simple power-law model plus a MEKAL component for the thermal contribution from the starburst. An additional Gaussian component is needed to reproduce the emission line at ~ 6.7 keV (EW ~ 1.98 keV), which is consistent with emission from Fe XX–Fe XXVI. This model with only Galactic absorption is a satisfactory fit to the XIS data ($\chi^2_{\nu} \sim 1.03$ for 174 d.o.f.). The XIS extraction window encompasses the two nuclei of Arp 220 and a significant fraction of the extended soft X-ray emission

(McDowell et al. 2003). Nevertheless, the power-law plus MEKAL model to the XIS-only data are consistent with the results from the *Chandra* observation of the nuclear binary source (Clements et al. 2002). There is, therefore, no obvious sign of spectral or flux variability in Arp 220.

The *Suzaku* data on Arp 220 can be interpreted in several ways: (1) an AGN is not present, (2) there is a low-luminosity, unobscured AGN, or (3) there is a heavily obscured AGN.

In the first case where an AGN is not present, the detected Fe line at ~ 6.7 keV would originate from hot gas heated by the heavy starburst activity. However, the measured equivalent width for the line of $1.98_{-0.57}^{+0.99}$ keV seems too large for an Fe emission line arising from a pure starburst. Iwasawa et al. (2005) fitted the 2.5–10 keV continuum of the *XMM-Newton* data with a collisionally ionized plasma model. The model requires a gas temperature of ~ 7 keV and a metallicity of ~ 2 times solar in order to reproduce the 6.7 keV Fe feature (EW ~ 2 keV). This temperature is inconsistent with the detected Ca XIX line in the *XMM-Newton* data. The XIS data do suggest the presence of an emission feature at ~ 3.9 keV consistent with Ca XIX, but this detection is not statistically significant.

The weak but unobscured AGN case is unlikely based on CO observations by Downes & Eckart (2007). Their observations with IRAM imply a column density of $\sim 1.3 \times 10^{25} \text{ cm}^{-2}$ for the western nucleus of Arp 220. Unless the covering fraction of the absorber is much less than unity, the unobscured AGN interpretation of the data is inconsistent with the CO observations.

In contrast, the third scenario of a heavily obscured AGN is consistent with the Fe line detection and the CO observation of a large column density. The ionized reflection model as proposed by Ross & Fabian (2005, and references therein) can reconcile the large equivalent width of the highly ionized iron line as well as the large

absorbing column. Since the absorbing column is so large, the observed spectrum is purely reflected. The XIS data is best fit by a MEKAL plus an ionized reflection model with the ionization parameter (ξ) fixed at 10^3 ergs cm s⁻¹ ($\chi^2_\nu = 1.03$ for 176 d.o.f.; see Table 5.3 and Figure 5.1). Thus the third scenario for explaining the *Suzaku* data on Arp 220 is favored.

Based solely on the XIS data, the unabsorbed 0.5–10 keV luminosity of Arp 220 is only $\sim 1.8 \times 10^{41}$ ergs s⁻¹ cm⁻², much lower than that found in quasars. The absorption-corrected ratio $\log(L_{2-10 \text{ keV}}/L_{IR})$ is ~ -4.9 , consistent with those found in some nearby ULIRGs (Teng et al. 2005), but lower than those of radio-quiet quasars. Of course, if Arp220 is highly absorbed then the intrinsic $\log(L_{2-10 \text{ keV}}/L_{IR})$ is higher and may be within the range for PG quasars. The thermal component of the spectrum has a 0.5–2 keV luminosity of $\sim 3 \times 10^{40}$ ergs s⁻¹. If this luminosity is completely due to thermal bremsstrahlung, then applying this to Equation (1) of Teng et al. (2008), the spatial extent of the emitting region is $\sim 2 - 11$ kpc, depending on the choice of filling factor ($10^{-3} < f_{gas} < 10^{-1}$) and assuming an electron density of 1 cm⁻³.

HXD/PIN Data

As shown in Figure 5.2, the net HXD/PIN spectrum of Arp 220 is only $\sim 2.2\%$ above the (NXB+CXB) background, so it is within the uncertainties of the PIN background modeling ($\sim 3.0\%$, calculated following procedures in § 5.4.1). Thus, the estimated 15–40 keV count rate for Arp 220 is ~ 0.025 cps.

5.5 The Long-term Variability of *IRAS* F05189–2524 and Mrk 273

Within the span of the *Suzaku* observations (~ 80 ksec each), no significant variability is detected in the XIS data for both F05189–2524 and Mrk 273. However, there is evidence for long-term variability in both sources when the *Suzaku* data are compared with previous *ASCA*, *BeppoSax*, *Chandra*, and *XMM-Newton* data. In this section, we discuss the results of these comparisons and their implications for the spectral models.

5.5.1 *IRAS* F05189–2524

F05189–2524 was observed by *XMM-Newton* in March 2001 and then by *Chandra* in October 2001 and January 2002. We extracted the spectra from the *XMM-Newton* and *Chandra* archives. There do not appear to be significant variations in the 0.5–2 keV flux of F05189–2524. The 2006 *Suzaku* measurement is within a standard deviation of the weighted average of the previous measurements. In contrast, the *Suzaku* 2–10 keV flux is a factor of ~ 30 lower than the measurements made by other observatories, ~ 4 standard deviations away from the weighted average of the previous measurements (see Figure 5.5 and 5.6).

None of the *XMM-Newton* and *Chandra* data shows a significant iron feature near 6.4 keV, in contrast to our more recent *Suzaku* data, so we did not consider reflection models for these archived data. The scattering model (§ 5.4) with a thermal MEKAL component gave adequate fits to the spectra. In the modeling of these data, we allowed the internal column density and the parameters for the power-law component describing the AGN within the source to vary freely. The models suggest that the

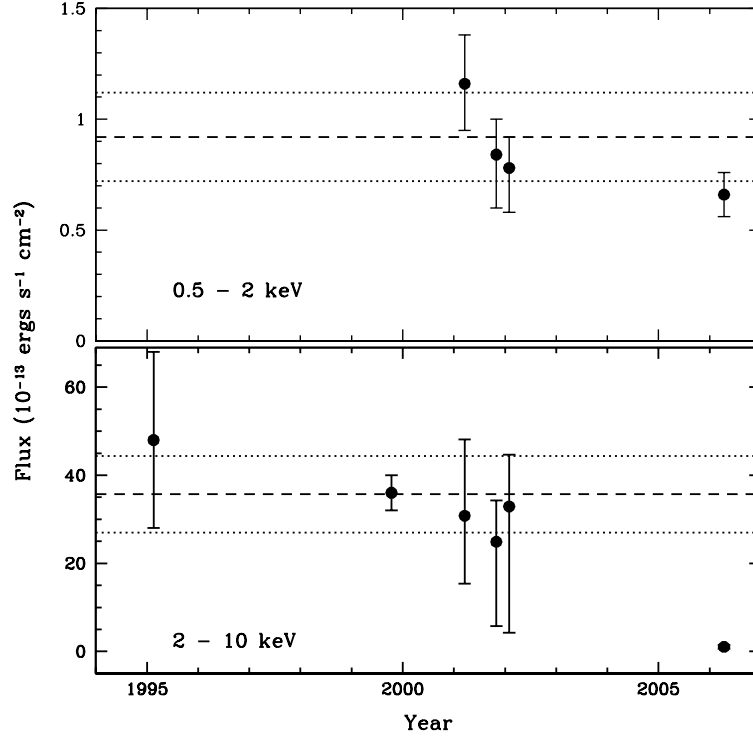


Figure 5.5: Observed 0.5–2 keV (top) and 2–10 keV (bottom) fluxes of F05189–2524 from 1995 to 2006 as determined from *ASCA*, *BeppoSAX*, *XMM-Newton*, *Chandra*, and *Suzaku* data. While there has been little change in the 0.5–2 keV flux, the nominal 2–10 keV flux of F05189–2524 has decreased by a factor of ~ 30 since previous observations. The dashed line represents the average “high” state flux (measurements made prior to *Suzaku*) as weighted by the measurement errors while the dotted lines denote one standard deviation away from the mean. The 2–10 keV flux value as measured by *Suzaku* is ~ 4 standard deviations away from the weighted mean. The *ASCA* (1995) and *BeppoSAX* (1999) values are drawn from Severgnini et al. (2001); the *XMM-Newton* (2001) and *Chandra* (2002) values are drawn from our modeling of the archived spectra with the scattering model in this work (see §5.5.1). The error bars for the 2006 value are within the data point.

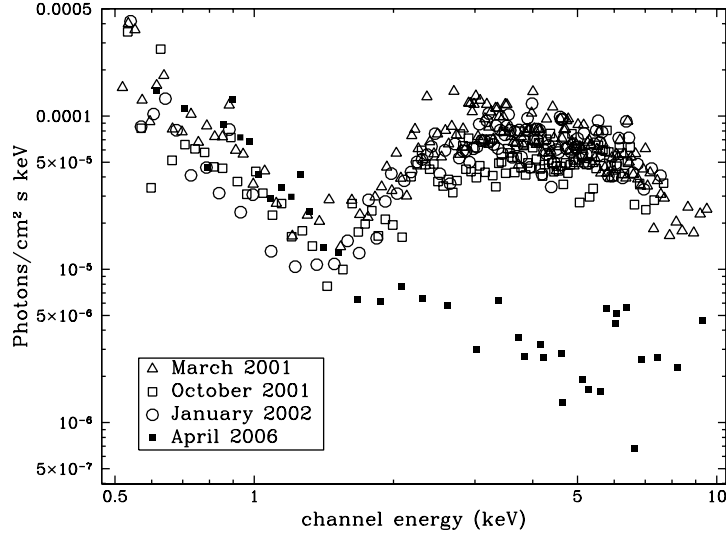


Figure 5.6: Comparison of the unfolded spectra of F05189–2524 from the 2001 March *XMM-Newton* (open triangles), 2001 October *Chandra* (open squares), 2002 January *Chandra* (open circles), and 2006 April *Suzaku* (closed squares) observations. The unfolded spectra were created using the best-fit models to each individual spectrum. Below ~ 1.3 keV, there appears to have been negligible change in flux or spectral shape between the different observations. However, above ~ 1.3 keV, the spectral change is obvious. The iron line is prominent in the *Suzaku* data, but is not noticeable in the other observations. The best-fit models to the spectrum changed from a scattering-dominated scenario in 2001 and 2002 to a reflection-dominated scenario in 2006. This may be an indication that the central source has faded prior to 2006 or variations in the column density.

archived *XMM-Newton* and the two sets of *Chandra* spectra are absorbed by a column density of 7.6×10^{22} , 6.8×10^{22} , and 6.1×10^{22} cm^{-2} , respectively. We also deduce that the observed 2–10 keV flux of the AGN has decreased from 3×10^{-12} $\text{ergs s}^{-1} \text{cm}^{-2}$ in the 2001 *XMM-Newton* data to 1×10^{-13} $\text{ergs s}^{-1} \text{cm}^{-2}$ in the 2006 *Suzaku* data *i.e.* a reduction of a factor of ~ 30 .

The decrease in flux and the change in spectral shape may be due to a number of reasons. Here, we test three scenarios by modeling the multiple epoch data simultaneously with a single model. The three scenarios considered are: (1) a change in the column density while the properties of the AGN remain the same, (2) a change in the covering fraction of the absorber while the properties of the

AGN remain the same, and (3) the column density and covering fraction remain the same while the intrinsic AGN luminosity is changed. In this scenario, a reflection component is visible in the “low-state” AGN.

The first scenario is tested by modeling all four data sets simultaneously by a single scattering model plus a MEKAL component modified only by Galactic absorption and a Gaussian describing the iron line. All of the model parameters are set to be the same for each of the data groups, except for the column density parameter which is allowed to vary independently. This results in a satisfactory fit to the data ($\chi^2_\nu = 1.26$ for 503 d.o.f.). This model and the multi-epoch data are shown in Figure 5.7 and the best-fit parameters are listed in Table 5.4.

For the second scenario, the multi-epoch data are simultaneously fit by a single partial covering fraction model. All of the model parameters are set to be the same between epochs, except for the covering fraction. The modeling of this scenario results in an unacceptable fit with $\chi^2_\nu \sim 8$. The addition of another partial-covering absorber to this model results in a still unsatisfactory fit with $\chi^2_\nu = 2.2$ for 498 degrees of freedom. Thus the partial-covering model is not a good description of the data.

Lastly, the third scenario is examined. In this scenario, the active nucleus has switched off prior to the final set of observations, leaving behind a residual reflection component visible in the “low” state. This has been observed previously in NGC 4051 (Guainazzi et al. 1998) and NGC 1365 (Risaliti et al. 2005). The model for this scenario is a combination of a MEKAL component, plus a reflection component on top of a scattering model. A Gaussian is also added to model the Fe line seen in the *Suzaku* data. For the *Suzaku*-epoch, the scattered component normalization is held fixed at zero. Similarly, for the non-*Suzaku*-epochs, the reflected component normalization is fixed at zero. Additionally, the absorption parameter in each of

the non-*Suzaku*-epochs is allowed to vary independently while the *Suzaku*-epoch absorption parameter is held fixed at zero. Since the intrinsic AGN luminosity has changed, the normalization factors for the direct component are different for the *Suzaku*- and non-*Suzaku*-epochs. The modeling of the data with this scenario is more successful with $\chi^2_\nu = 1.30$ for 502 degrees of freedom. The best-fit parameters to this model are listed in Table 5.4 and the model shown in Figure 5.7.

Both the increase in column density and the decrease in intrinsic luminosity of the AGN appear to be equally good descriptions of the data. The change in column density model implies that the structure of the absorber is complex. This has been previously observed in NGC 1365 (Risaliti et al. 2005), NGC 4151 (Puccetti et al. 2007), and in a group of Seyfert 2 galaxies (Risaliti et al. 2002). However, in the modeling of the first scenario, the N_{H} value required to explain the data is $> 2 \times 10^{24}$ cm^{-2} . At this limit, we can no longer model it as a pure absorption spectrum since scattering both in and out of the line of sight are becoming important.

The thermal 0.5–2 keV luminosity is $\sim 1 \times 10^{41}$ ergs s^{-1} . Following the methods presented in § 5.4.5, the physical extent of the emitting region is ~ 4 –17 kpc. The absorption-corrected 0.5–10 keV luminosity of the AGN detected in F05189–2524 at its “high” state (2000–2002 observations) is $\sim 3 \times 10^{43}$ ergs s^{-1} , almost as luminous as some quasars (Elvis et al. 1994). The absorption-corrected ratio $\log(L_{2-10 \text{ keV}}/L_{\text{IR}})$ is ~ -2.5 , consistent with that found in radio-quiet PG quasars. The corresponding numbers for the “low” state as observed by *Suzaku* are $\sim 8 \times 10^{41}$ ergs s^{-1} and -4.1 , respectively, well below that of radio-quiet PG quasars.

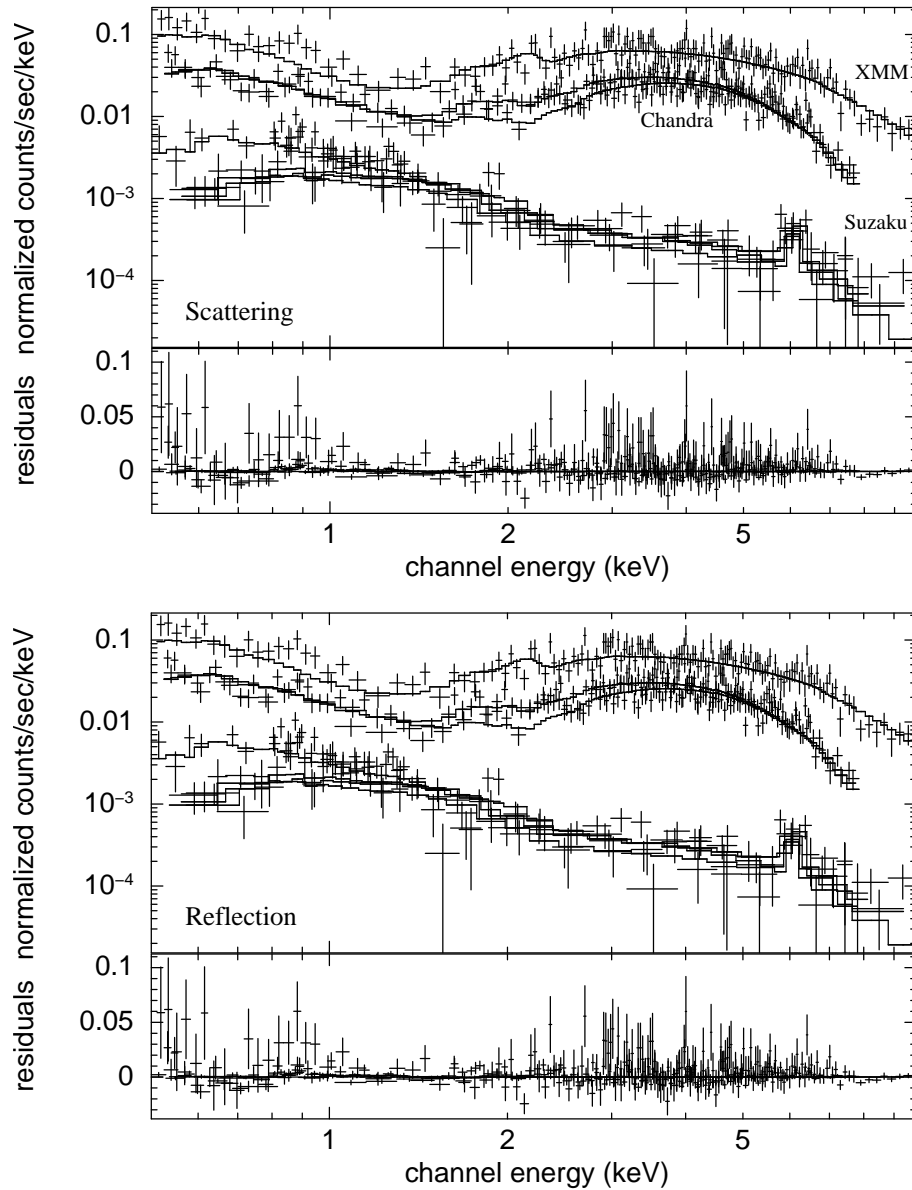


Figure 5.7: The two models to the *Chandra*-ACIS, *XMM-Newton*-EPIC pn, and *Suzaku*-XIS/PIN data used to explain the change in the 2–10 keV spectral shape of F05189–2524: (top) change in the absorbing column alters the spectral shape of the source, and (bottom) the AGN has switched off and has left behind a residual reflection component (see §5.5.1 for details). The response from each detector is folded in with the data. The horizontal axis is energy in the observer’s frame. The cross-normalization factor is assumed to be unity for *XMM-Newton* and *Chandra* with respect to *Suzaku*-XIS0. Both models have comparable reduced χ^2 values (1.27 for 503 d.o.f. versus 1.30 for 502 d.o.f.) and appear to fit the overall 0.5–10 keV spectrum well. Neither model can be ruled out by the data. Table 5.4 lists the results from this modeling.

Table 5.4: Modeling Spectra of F05189–2524 and Mrk 273 from Multiple Epochs

Telescope	kT [keV]	Γ	f	$N_{\text{H, source 1}}$ [10^{23} cm^{-2}]	$f_{\text{cover 1}}$	$N_{\text{H, source 2}}$ [10^{23} cm^{-2}]	$f_{\text{cover 2}}$	E_{line} [keV]	σ [keV]	EW [keV]	K	Observed $F_{0.5-2}$ keV (13)	Unabsorbed $F_{0.5-2}$ keV (14)	Observed F_{2-10} keV (15)	Unabsorbed F_{2-10} keV (16)	Observed F_{15-40} keV (17)	Unabsorbed F_{15-40} keV (18)
(1)	(2)	(3)	(4)	(5)	(6)	(7)	(8)	(9)	(10)	(11)	(12)	(13)	(14)	(15)	(16)	(17)	(18)
F05189–2524: scattering model, change in column density ($\chi^2/\text{d.o.f.} = 640/503$)																	
XMM (2001)	$0.23^{+0.02}_{-0.03}$	$1.91^{+0.08}_{-0.05}$	0.02	$0.58^{+0.03}_{-0.03}$	$6.37^{+0.27}_{-0.25}$	0.73	$0.64^{+0.31}_{-0.16}$	$1.42^{+0.98}_{-0.12} \times 10^{-3}$	$1.02^{+0.10}_{-0.11}$	$30.00^{+1.29}_{-17.53}$	$29.38^{+5.42}_{-4.35}$	$42.03^{+6.58}_{-1.79}$
Chandra (2001)	0.23	1.91	0.02	$0.90^{+0.05}_{-0.05}$	6.37	0.73	0.64	1.42×10^{-3}	$0.77^{+0.08}_{-0.08}$	30.00	$25.67^{+3.33}_{-5.79}$	42.03
Chandra (2002)	0.23	1.91	0.02	$0.71^{+0.04}_{-0.04}$	6.37	0.73	0.64	1.42×10^{-3}	$0.87^{+0.09}_{-0.10}$	30.00	$27.69^{+7.66}_{-6.00}$	42.03
Suzaku (2006)	0.23	1.91	0.02	$21.55^{+2.18}_{-1.71}$	6.37	0.73	0.64	1.42×10^{-3}	$0.70^{+0.10}_{-0.08}$	30.00	$1.45^{+0.28}_{-0.25}$	42.03
F05189–2524: reflection dominated, change in AGN luminosity ($\chi^2/\text{d.o.f.} = 659/502$)																	
XMM (2001)	$0.24^{+0.02}_{-0.01}$	$1.79^{+0.07}_{-0.13}$	0.02	$0.59^{+0.05}_{-0.05}$	$1.27^{+0.24}_{-0.21} \times 10^{-3}$	$1.02^{+0.12}_{-0.10}$	$27.02^{+1.55}_{-18.21}$	$29.92^{+3.15}_{-4.03}$	$42.80^{+6.03}_{-0.50}$
Chandra (2001)	0.24	1.79	0.02	$0.93^{+0.09}_{-0.09}$	1.27×10^{-3}	$0.77^{+0.10}_{-0.10}$	27.02	$25.90^{+2.72}_{-3.03}$	42.80
Chandra (2002)	0.24	1.79	0.02	$0.72^{+0.02}_{-0.06}$	1.27×10^{-3}	$0.87^{+0.10}_{-0.10}$	27.02	$28.16^{+3.82}_{-3.03}$	42.80
Suzaku (2006)	0.24	1.79	6.82	$6.32^{+0.17}_{-0.22}$	$0.00^{+0.46}_{-0.00}$	$1.95^{+3.64}_{-1.00}$	$2.18^{+0.30}_{-0.36} \times 10^{-5}$	$0.69^{+0.09}_{-0.10}$	$0.75^{+0.10}_{-0.10}$	$1.06^{+0.33}_{-0.14}$	$1.06^{+0.36}_{-0.11}$
Mrk 273: change in covering fraction ($\chi^2/\text{d.o.f.} = 521/376$)																	
Chandra (2000)	$0.79^{+0.03}_{-0.03}$	$1.73^{+0.04}_{-0.02}$...	$15.91^{+0.86}_{-0.73}$	$3.00^{+0.23}_{-0.20}$	$0.96^{+0.01}_{-0.02}$	$6.40^{+0.06}_{-0.13}$	$0.00^{+0.06}_{-0.07}$	$2.24^{+0.20}_{-0.11} \times 10^{-3}$	$0.25^{+0.04}_{-0.00}$	$0.75^{+2.92}_{-0.15}$	$0.73^{+2.92}_{-0.15}$	$47.29^{+4.25}_{-2.26}$	$7.49^{+3.06}_{-2.36}$	$84.10^{+7.89}_{-4.48}$
XMM(2002)	0.79	1.73	...	15.91	3.00	$0.81^{+0.02}_{-0.02}$	6.40	0.00	0.25	0.25	2.24×10^{-3}	$0.85^{+0.27}_{-0.03}$	47.29	$4.09^{+0.87}_{-0.87}$	84.10
Suzaku(2006)	0.79	1.73	...	15.91	3.00	$0.69^{+0.02}_{-0.02}$	6.40	0.00	0.25	0.25	2.24×10^{-3}	$1.11^{+0.03}_{-0.42}$	47.29	$4.36^{+0.30}_{-1.96}$	84.10	$67.35^{+22.51}_{-40.50}$	$78.48^{+8.40}_{-4.45}$

Note. — Col. (1): Spacecraft used and year of the observation. Col (2): temperature of the thermal starburst component from the MEKAL model. Col. (3): slope to the power-law model. Col. (4): the ratio of the normalization parameters between the reflected (or scattered) component to the direct component. Col. (5)–(8): absorption within the source and corresponding covering fraction for the covering fraction absorber model. Col. (9): rest energy of the emission line. Col. (10): line width of the emission line. Col. (11): equivalent width of the emission line. Col. (12): normalization factor of the direct component in photons $\text{cm}^{-2} \text{ s}^{-1}$. Col. (13)–(18): flux in units of $10^{-13} \text{ ergs s}^{-1} \text{ cm}^{-2}$.

5.5.2 Mrk 273

Xia et al. (2002) compiled a list of observed fluxes of Mrk 273 and Mrk 273x from *ASCA*, *BeppoSax*, and *Chandra* dating from 1994 to 2000¹¹. We add to this list the *XMM-Newton* observation from 2002 analyzed by Balestra et al. (2005) and our *Suzaku* observation from 2006. Figure 5.8 shows the observed fluxes of Mrk 273 and Mrk 273x over the 12-year period. Since *ASCA* and *BeppoSax* did not have the spatial resolution to separate Mrk 273 from Mrk 273x, the flux points from 1994 and 1998 represent the sum of the two galaxies. As the figure shows, the total flux between Mrk 273 and Mrk 273x appears to have increased in 2006 in the 0.5–2 keV band and appears to be in a “high” flux state in 2000 relative to all the other measurements.

Although Mrk 273x was once thought to be a BL Lacertae object because of its high X-ray to optical B-band flux ratio (Xia et al. 1998), its 2–10 keV flux has never shown dramatic variability. The *Suzaku* data support the assessment of Xia et al. (2002) that Mrk 273x is unlikely to be a BL Lac object. As discussed in §4.3.2, its spectrum is well fit by a simple power law modified only by Galactic absorption, in agreement with the findings in Balestra et al. (2005).

Assuming a constant flux for Mrk 273x implies that the nominal observed 2–10 keV flux from Mrk 273 dropped by about a factor of two from 1994 to 1998, then increased by a factor of ~ 2.5 from 1998 to 2000, and then again dropped by a factor of more than two from 2000 to 2002. It appears to have remained roughly the same from 2002 to 2006. This variability in flux is not very significant when considering the uncertainties of the measurements. However, the spectral variability is clearly

¹¹Although the authors tabulated the fluxes from 1996 to 2000, the *ASCA* observation date was mis-identified and the data set was actually taken in December of 1994 (see Iwasawa 1999).

seen when comparing the spectra of Mrk 273 from *Chandra*, *XMM-Newton*, and *Suzaku* (Figure 5.9). The higher 0.5–2 keV flux in 2006 and the higher 2–10 keV flux in 2000 as shown in Figure 5.8 correlate with the difference in the spectral shapes of the source in each of these epochs.

Modeling the Multiple Epoch Data

As with the multiple data sets of F05189–2524, we first modeled the archived *Chandra* and *XMM-Newton* spectra of Mrk 273 individually. These data sets were each best fit by the scattering model. The fits to the *Chandra* (*XMM-Newton*) data imply an intrinsic column density of 4.1 (6.8) $\times 10^{23}$ cm $^{-2}$ and an intrinsic 2–10 keV flux of 2.5 (2.0) $\times 10^{-12}$ ergs s $^{-2}$ cm $^{-2}$. A comparison of the *Chandra* (*XMM-Newton*) data with the fits to the 2006 *Suzaku* XIS data in Table 5.3 suggests that the intrinsic column density has increased by $\sim 110\%$ ($\sim 27\%$) while the intrinsic 2–10 keV luminosity has decreased by $\sim 80\%$ (0%) if we were to compare data only over the 0.5–10 keV range. However, the addition of the HXD/PIN data (Table 5.3) implies that the column density has increased by a factor of ~ 4 (~ 2) and the intrinsic 2–10 keV luminosity has increased by a factor of ~ 3 (~ 4).

Next, all three data sets are modeled with a single model simultaneously to determine whether the change in the spectral shape is due to the change in column density or the intrinsic AGN luminosity. Three scenarios are considered: the change in spectral shape is due to (1) a change in the absorbing column and the intrinsic AGN flux remains the same, (2) a change in the intrinsic AGN luminosity with the absorbing column remaining constant, and (3) a change in the covering fraction of the absorber with the column density and intrinsic luminosity remaining constant.

To evaluate the first scenario, all three data sets are simultaneously modeled by a scattering plus MEKAL model modified only by Galactic absorption and a

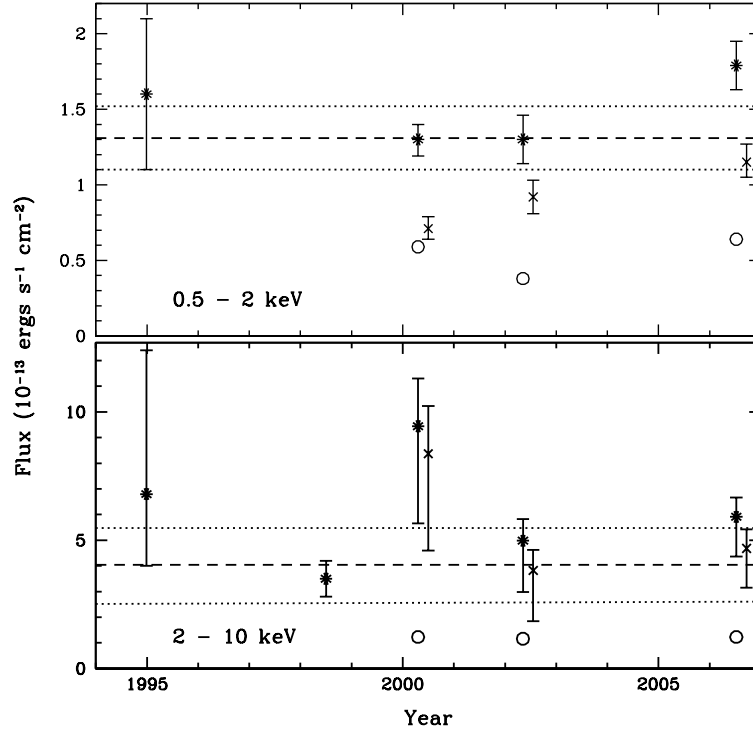


Figure 5.8: Observed 0.5–2 keV (top) and 2–10 keV (bottom) fluxes of Mrk 273 (crosses) and Mrk 273x (open circles) from 1994 to 2006 as determined from *ASCA*, *BeppoSAX*, *XMM-Newton*, *Chandra*, and *Suzaku* data. Each asterisk represents the sum of the fluxes from Mrk 273 and Mrk 273x. In the top panel, the dashed line represents the weighted average of the data points for Mrk 273 and Mrk 273x from 1994, 2000, and 2002 and the dotted lines represent a single standard deviation away from that mean. In the bottom panel, the dashed line represents the weighted average of the data points for Mrk 273 and Mrk 273x from 1994, 1998, 2002, and 2006 and the dotted lines denote one standard deviation away from the mean. Small flux increases in Mrk 273 may be observed in 2006 in the 0.5–2 keV band and in 2000 in the 2–10 keV band. The *ASCA* (1994) and *BeppoSAX* (1998) values are drawn from Iwasawa (1999) and Risaliti et al. (2000), respectively. The *Chandra* (2000) and *XMM-Newton* (2002) values are derived from our modeling of the archived spectra with the scattering model (see §5.5.2). The error bars to the total flux are the sums of the errors in the measured fluxes of Mrk 273 and Mrk 273x added in quadrature. A small horizontal offset was applied to the Mrk 273 data points to better display the measurement errors. Since the errors on the *BeppoSAX* measurements are not published, they are assumed to be $\pm 20\%$ based on the results on *F05189 – 2524* by Severgnini et al. (2001).

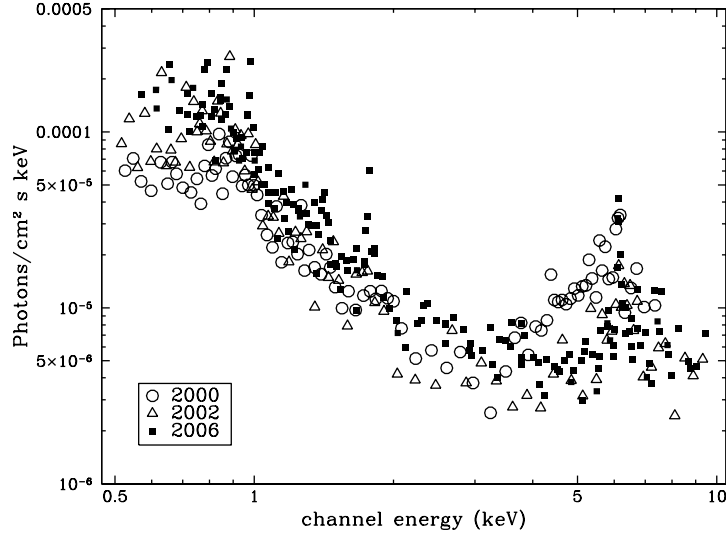


Figure 5.9: Comparison of the unfolded spectra of Mrk 273 from the 2000 *Chandra* (open circles), 2002 *XMM-Newton* (open triangles), and 2006 *Suzaku* (closed squares) observations. The unfolded spectra were created using the best-fit models to each individual spectrum. The shapes of the spectra appear consistent between 1 and 2 keV. The flux of the *Suzaku* spectrum is higher than that of the others below 1 keV, while the *Chandra* spectrum appears to be higher than the others between 4 and 6 keV. These differences are correlated with the flux variability as shown in Figure 5.8. This comparison also shows that the iron line at 6.4 keV is detected in all three observations. While the 2–10 keV flux variability is not very significant, the spectral shape of the source has changed between 2000 and 2006. This change may be due to the variations in the column density.

Gaussian describing the iron line. All of the model parameters are set to be the same for all of the data groups, but the column density for data sets from each epoch is allowed to vary (assuming the intrinsic luminosity remains the same). As before, the contaminants in the HXD/PIN field of view are taken into account in the modeling. This interpretation of the data results in a poor fit ($\chi^2_\nu = 1.76$ for 380 d.o.f.), much worse than the modeling to each data set alone and underestimates the flux of the HXD/PIN data (see Figure 5.10).

The second scenario is explored by again modeling the multi-epoch data simultaneously with a single model. The model is the same as that used in the first scenario. However, in this case, the model parameters for each epoch are set to be

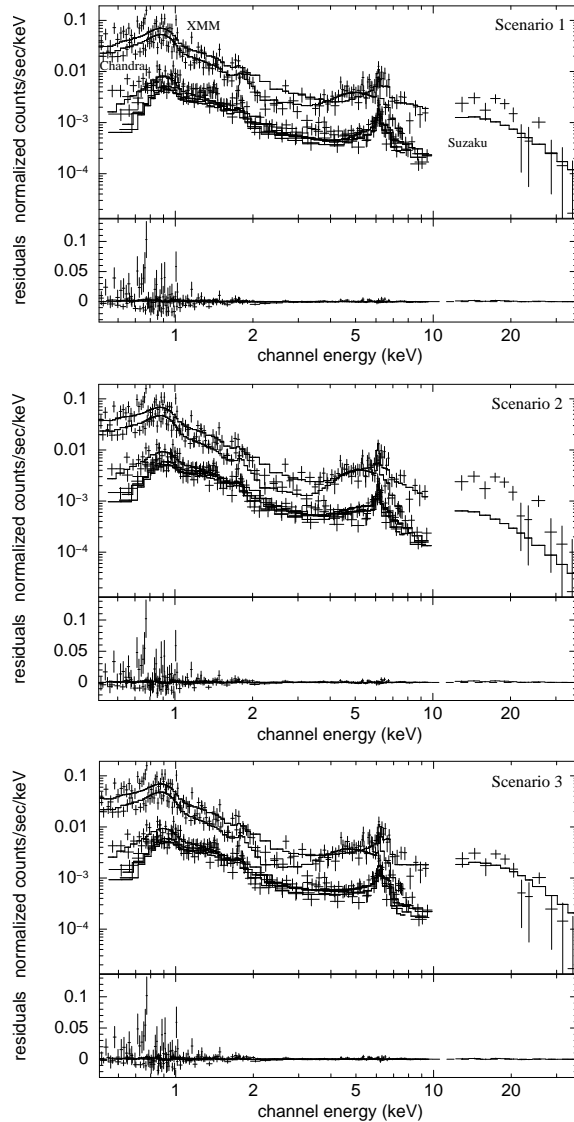


Figure 5.10: The three models to the *Chandra*-ACIS, *XMM*-Newton-EPIC pn, and *Suzaku*-XIS/PIN data used to explain the changes in the 2–10 keV spectral shape of Mrk 273: scenario 1 (top) tests only a change in the absorbing column, scenario 2 (middle) tests only a change in the intrinsic luminosity of the AGN, and scenario 3 (bottom) tests the change in the covering fraction of the absorber (see §5.5.2 for details). The response from each detector is folded in with the data. The horizontal axis is energy in the observer’s frame. The cross-normalization factor is assumed to be unity for *XMM*-Newton and *Chandra* with respect to *Suzaku*-XIS0. While all three models have similar reduced χ^2 values (1.76, 1.53, and 1.39 respectively), the third model provides the best-fit to the overall 0.5–40 keV spectrum. Thus, we favor the third scenario (change in the covering fraction of the absorbers) as the best explanation for the change in the 2–10 keV spectral shape of Mrk 273. Table 5.4 lists the results from this modeling.

the same except for the normalization of the power law. In this case, we are testing whether the change in the intensity of the power-law component can describe the observations. The best-fit model for this scenario takes into account the contributions from the nearby contaminants. While the model describes the 0.5–10 keV data for each epoch well ($\chi^2_\nu = 1.53$ for 378 d.o.f.), it fits the HXD/PIN data very poorly, severely under-estimating the HXD/PIN flux (see Figure 5.10).

To test the third scenario, the *Chandra*, *XMM-Newton*, and *Suzaku* spectra are modeled using two absorbers with the same column densities for data from each epoch but with covering fractions that are allowed to vary freely. The contributions to the HXD/PIN flux from the neighboring XIS sources are taken into account in the fitting of the *Suzaku* data. The best-fit model ($\chi^2_\nu = 1.39$ for 376 d.o.f.) is shown in Figure 5.10 and the best-fit parameter values are listed in Table 5.4. Based on Figure 5.10, the third scenario is the preferred model for the multiple epoch data.

Using the parameters derived for this third scenario, the absorption-corrected luminosity from the AGN is 4.0×10^{43} ergs s⁻¹ in the 0.5–10 keV band and 2.3×10^{43} ergs s⁻¹ in the 15–40 keV band. The ratio $\log(L_{2-10 \text{ keV}}/L_{IR})$ is ~ -2.3 , within the range found in radio-quiet PG quasars. The thermal 0.5–2 keV luminosity is $\sim 1 \times 10^{40}$ ergs s⁻¹. Following the methods discussed in § 5.4.5, the emission region is ~ 4 –17 kpc in size.

Given the lack of knowledge of the detailed geometry of the nuclear region, it is difficult to derive a quantitative measure of the distance from the central source to the absorber. However, the year-to-year time variability suggests that the absorber is close (~ 1 pc) to the nucleus.

Comparison with OSSE Data

Dermer et al. (1997) observed Mrk 273 with the OSSE instrument on-board the *Compton Gamma Ray Observatory*. Though their observations resulted in a non-detection, they placed upper limits on the 50–100 keV band flux and the column density. Possible explanations suggested by Dermer et al. (1997) for the non-detection include the possibility that this ULIRG is gamma-ray weak or the AGN source is highly variable in gamma-rays and they happened to have observed the object in the low-flux state.

Another explanation for the non-detection is that the AGN in Mrk 273 is hidden behind a large and patchy column of gas $\gtrsim 10^{24} \text{ cm}^{-2}$. This is not inconsistent with the upper limit derived from previous CO measurements ($\lesssim 2 \times 10^{24} \text{ cm}^{-2}$, assuming a covering fraction of unity; see Dermer et al. 1997 for more detail). These limits on the column density are consistent with our partial covering absorption model ($N_{\text{H}} \sim 1.6 \times 10^{24} \text{ cm}^{-2}$). From an extrapolation of the HXD/PIN observation and model, we derive an upper limit to the 50–100 keV photon flux of $6.2 \times 10^{-5} \text{ photons cm}^{-2}$ or $6.9 \times 10^{-12} \text{ ergs s}^{-1} \text{ cm}^{-2}$. This value is more stringent than the OSSE value ($1.5 \times 10^{-4} \text{ photons cm}^{-2}$) by a factor of ~ 2 .

5.6 Summary

The results of our analysis of *Suzaku* XIS (0.5–10 keV) and HXD/PIN (15–40 keV) observations of five of the brightest and best-known local ULIRGs (F05189–2524, F08572+3915, Mrk 273, PKS 1345+12, and Arp 220) have been presented and compared with earlier *Chandra* and *XMM-Newton* data. The results can be summarized as follows:

1. The XIS observations of F05189–2524 reveal a significant change in the ob-

served 2–10 keV spectrum relative to previous *Chandra* and *XMM-Newton* observations. The spectral variation in F05189–2524 suggests that the central source may have turned off, leaving behind a residual reflection component. However, an increase in column density cannot be completely ruled out. The absorption-corrected 2–10 keV luminosity to infrared luminosity ratios of F05189–2524 during its “high” state is consistent with values observed in PG quasars.

2. The XIS spectrum of Mrk 273 contains a strong Fe $K\alpha$ line and shows a change in the observed 2–10 keV spectrum relative to previous *Chandra* and *XMM-Newton* observations. Mrk 273 is marginally ($1.8\text{-}\sigma$) detected at high energies, with the HXD/PIN spectrum $\sim 5.4\%$ above the background. A change in the covering fraction of the absorber best explains the spectral variations in Mrk 273, although a drop in the intrinsic AGN luminosity cannot be formally ruled out. A column density of $\sim 10^{24} \text{ cm}^{-2}$ is derived from the *Suzaku* data. The changes in spectral shape and covering fraction on a time scale of a few years suggest that the absorbing matter is ~ 1 pc from the central source. The Mrk 273 spectrum is best modeled by a $\sim 94\%$ covering fraction model. The absorption-corrected 2–10 keV luminosity to infrared luminosity ratios of Mrk 273 is consistent with values observed in PG quasars.
3. F08572+3915 is undetected in the *Suzaku* XIS and HXD/PIN observations. The low X-ray count rate derived from unpublished *Chandra* observations, combined with mid-infrared observations, suggests that this source is highly obscured.
4. PKS 1345+12 is detected by the XIS. No apparent flux or spectral variability is detected in its 0.5–10 keV spectrum relative to previous *Chandra* observa-

tions. The net 15–40 keV HXD/PIN spectrum is only 1.1σ above the total background, not strong enough for a meaningful full-band (XIS+HXD/PIN) spectral fitting. Unlike other ULIRGs, the 0.5–2 keV spectrum of this source does not contain an obvious thermal MEKAL component. Combining this result and the fact that the absorption-corrected 2–10 keV to infrared luminosity ratio of PKS 1345+12 is in agreement with those of PG quasars, the data suggest that the X-ray luminosity of this object is dominated by an AGN.

5. Arp 220 is detected by the XIS, but not by the HXD/PIN. Its 0.5–10 keV spectrum, including the iron complex, appears unchanged since previous *Chandra* observations. The X-ray continuum emission is in agreement with the possibility that a highly obscured AGN is present. This interpretation of the data is consistent with previous CO observations. The measurements of the iron emission line at 6.7 keV can be reconciled by the ionized reflection model.
6. In all three cases where an optically thin thermal component is contributing to the soft X-ray emission detected by XIS (F05189–2524, Mrk 273, Arp 220), the temperature, $kT \sim 0.3\text{--}0.8$ keV, is consistent with previous observations of ULIRGs.
7. The variations seen in the column densities of F05189–2524 and Mrk 273 over several epochs are similar to those observed in Seyfert 2 galaxies by Risaliti et al. (2002) and in NGC 4151 by Puccetti et al. (2007). This indicates that the absorbing material is clumpy rather than a homogeneous obscuring torus.

Chapter 6

Quasar/ULIRG Evolution Study (QUEST): an X-ray survey of ULIRGs and PG QSOs

6.1 Introduction

Recent simulations support the scenario that quasars can be formed through gas-rich galaxy mergers (e.g., Hopkins et al. 2005). Past surveys include ground-based optical and near-infrared photometry (e.g., Kim et al. 2002; Surace et al. 2001; Veilleux et al. 2002), mid-infrared spectroscopy (e.g., Armus et al. 2007; Farrah et al. 2007), radio observations (e.g., Condon et al. 1991; Evans et al. 2001; Nagar et al. 2003), and X-ray snapshot studies (e.g., Franceschini et al. 2003; Ptak et al. 2003; Teng et al. 2005). Though these studies at different wavelengths have been extensive, each consists of different objects making systematic comparisons difficult. In order to form a more complete picture of the possible evolution from U/LIRGs to quasars, we are conducting a comprehensive, multi-wavelength imaging and spectroscopic survey of

local ULIRG and QSO mergers called QUEST — Quasar/ULIRG Evolution Study. The sample consists of $z < 0.3$ 1-Jy ULIRGs and Palomar Green (PG) quasars. Veilleux et al. (2009b) and references therein provide a detailed description of the QUEST sample selection criteria and it is thus not repeated here. Below are the main results from the QUEST to date:

- Galaxy Structure: Veilleux et al. (2009a, 2006) presented an *HST* NICMOS imaging study of 26 ULIRGs and 35 PG QSOs. All but one ULIRG show signs of interaction, indicating that they are mergers. AGN-like objects, including the QSOs, are generally of early morphological type and have less pronounced merger-induced morphological anomalies than systems with LINER-like or HII region-like spectral types.
- Host Stellar Dynamics: This study is based on near-infrared VLT spectra of 62 ULIRGs that cover the full range of merger states and AGN/starburst fractions seen in ULIRGs. Dasyra et al. (2006a,b) demonstrated that ULIRGs resemble intermediate mass ellipticals/lenticulars with moderate rotation in their velocity dispersion distributions and their location in the fundamental plane. The black hole masses of these ULIRGs are estimated to be of the order $10^7 - 10^8 M_{\odot}$. The black hole masses derived from similar data on a dozen PG QSOs agree with those of coalesced ULIRGs (Dasyra et al. 2007), suggesting that the bulk of the black hole growth takes place in the ULIRG phase of the merger.
- Energy Production Mechanisms: *Spitzer* IRS observations of PG QSOs have shown that starbursts are responsible for at least $\sim 30\%$, but likely most, of the far-infrared luminosity of the quasars (Schweitzer et al. 2006). Netzer et al. (2007) classified the QSO spectra into weak- and strong- far-infrared

emitting sources. The underlying AGN spectral energy distributions (SEDs) of these two categories of objects are the same or very similar. IRS spectra for 76 ULIRGs were analyzed by Veilleux et al. (2009b) and combined with the QSO data to show that, on average, AGN contribute to $\sim 40\%$ of the bolometric luminosity in the QUEST ULIRGs. Most of the ULIRGs do not show any obvious signatures of nuclear activity in the mid-infrared. In contrast, almost all of the QSOs show clear signs of nuclear activity. A significant number of AGN-dominated systems are in binaries. The *Spitzer* results suggest the statistical probability of powerful nuclear activity increases along the merger sequence, but AGNs may occur at any time along this sequence due to stochastic accretion events.

In the present chapter, we focus on the X-ray properties of the QUEST ULIRGs and PG QSOs. The sample consists of 40 ULIRGs and 26 PG QSOs from the QUEST sample that have available X-ray data from *Chandra* and *XMM-Newton*. Table 6.1 lists the QUEST objects with X-ray data.

The organization of this chapter is as follows. A discussion of data taking and reduction techniques is in §6.2. The spectral fitting analysis for both ULIRGs and PG QSOs are described in §6.3. We attempt to address the origin of the soft excess seen in PG QSOs in §6.4. In §6.5, we comment on the possible evolutionary link between ULIRGs and quasars, combining the X-ray data with recent *Spitzer* and *HST* observations. The results are summarized in §6.6. Throughout this chapter, we adopt $H_0 = 70 \text{ km s}^{-1} \text{ Mpc}^{-1}$, $\Omega_M = 0.3$, and $\Omega_\Lambda = 0.7$.

Table 6.1. The X-ray QUEST Sample

Galaxy (1)	z (2)	$\log(\frac{L_{bol}}{L_{\odot}})$ (3)	Type (4)	IC (5)	NS (6)	$N_{H, Gal}$ (7)	Ref (8)
ULIRGs							
F00091–0738	0.118	12.36	HII	IIIb	2.31	3.23	1
F00188–0856	0.128	12.43	L	V	< 0.34	3.21	2
F00456–2904:SW	0.110	12.29	HII	IIIa	22.80	1.68	1
F01004–2237	0.118	12.36	HII	V	< 0.32	1.58	2
F01166–0844:SE	0.118	12.15	HII	IIIb	10.78	4.67	1
PG0157+001	0.163	12.69	S1	IVb	< 0.42	2.56	2, 3, 4
F02021–2103	0.116	12.13	none	IVa	< 0.32	1.55	1
IRAS03521+0028	0.152	12.62	L	IIIb	3.86	12.5	2
F04103–2838	0.117	12.30	L	IVb	< 0.32	2.45	2, 5
F05024–1941	0.192	12.43	S2	IIIb	3.29	3.78	...
F05189–2524	0.043	12.22	S2	IVb	< 0.13	1.92	6, 7, 8
F07598+6508	0.148	12.58	S1	IVb	< 0.39	4.32	7
F08572+3915	0.058	12.22	L	IIIb	5.65	2.60	8
F09039+0503	0.125	12.16	L	IVa	< 0.34	3.94	1
UGC 5101	0.039	12.05	L	...	< 0.12	2.67	6
F09539+0857	0.128	12.13	L	V	< 0.34	3.08	...
F10190+1322:W	0.077	12.09	HII	IIIb	5.97	3.78	2
F10190+1322:E	0.076	12.09	L	IIIb	5.92	3.78	2
F10565+2448	0.043	12.11	HII	...	6.80	1.54	...
F11095–0238	0.107	12.32	L	IIIb	1.03	4.52	1
F11119+3257	0.189	12.67	S1	IVb	< 3.16	2.15	...
F11223–1244:W	0.199	12.64	S2	IIIa	97.85	4.98	...
F12072–0444	0.128	12.45	S2	IIIb	2.25	3.32	2
F12112+0305	0.073	12.38	L	IIIb	4.18	1.75	2, 10
3C 273	0.158	12.76	S1	IVb	< 0.41	1.79	3
Mrk 231	0.042	12.60	S1	IVb	< 0.12	1.26	6, 9
F13218+0552	0.205	12.68	S1	V	< 0.50	2.26	...
Mrk 273	0.038	12.24	S2	IVb	0.75	1.09	6, 8, 9
F13451+1232	0.122	12.36	S2	IIIb	6.57	1.90	7, 8
F14348–1447	0.083	12.42	L	IIIb	5.45	7.83	9, 10
F15130–1958	0.109	12.23	S2	IVb	< 0.30	8.60	2
F15250+3608	0.055	12.12	L	...	< 0.16	1.56	2, 9
Arp 220	0.018	12.26	L	IIIb	0.33	4.27	6, 8
F15462–0450	0.100	12.28	S1	IVb	< 0.28	9.91	1
F16090–0139	0.134	12.61	L	IVa	< 2.37	9.25	2
NGC 6240	0.024	11.91	L	...	0.74	5.78	6
F17208–0014	0.043	12.50	HII	...	< 0.13	9.96	2, 6, 9
F21208–0519:N	0.130	12.12	HII	IIIa	15.53	5.13	1
F21329–2346	0.125	12.21	L	IIIb	2.62	3.75	1
F22491–1808	0.078	12.25	HII	IIIb	2.36	2.69	9, 10
F23234+0946	0.128	12.21	L	IIIb	8.14	2.76	1
PG QSOs							
PG0050+124	0.061	12.07	QSO	IVb	< 0.18	4.99	3, 4
PG0804+761	0.100	12.08	QSO	2.98	3
PG0838+770	0.131	11.76	QSO	IVb	< 0.35	2.09	11
PG0844+349	0.064	11.44	QSO	IVb	< 0.18	3.29	3, 4
PG0953+414	0.234	12.52	QSO	1.14	3, 4
PG1001+054	0.161	11.86	QSO	V	< 0.41	2.39	3
PG1004+130	0.240	12.68	QSO	3.70	...
PG1116+215	0.176	12.54	QSO	V	< 0.45	1.28	3, 4
PG1126–041	0.060	11.52	QSO	V	< 0.17	4.30	...
PG1211+143	0.081	11.96	QSO	2.75	3, 4
PG1229+204	0.063	11.56	QSO	V	< 0.18	2.21	...
PG1244+026	0.048	11.02	QSO	1.75	3, 4
PG1307+085	0.155	12.34	QSO	V	< 0.40	2.11	3, 4

Table 6.1

Galaxy	z	$\log(\frac{L_{bol}}{L_{\odot}})$	Type	IC	NS	$N_{H, Gal}$	Ref
(1)	(2)	(3)	(4)	(5)	(6)	(7)	(8)
PG1309+355	0.184	12.31	QSO	V	< 0.46	1.03	3, 4
PG1351+640	0.088	12.04	QSO	2.15	...
PG1411+442	0.090	11.78	QSO	IVb	< 0.25	1.15	3
PG1426+015	0.086	11.92	QSO	IVb	< 0.24	2.83	...
PG1435-067	0.126	11.91	QSO	V	< 0.34	5.34	11
PG1440+356	0.079	11.80	QSO	V	< 0.22	1.03	3, 4
PG1448+273	0.065	11.43	QSO	2.44	...
PG1501+106	0.036	11.33	QSO	2.34	3, 4
PG1613+658	0.129	12.29	QSO	IVb	< 0.35	2.87	3
PG1626+554	0.133	11.83	QSO	V	< 0.35	1.91	3
PG2130+099	0.063	11.77	QSO	IVb	< 0.18	4.64	...
B2 2201+31A	0.295	13.27	QSO	V	< 0.66	11.8	11
PG2214+139	0.066	11.77	QSO	V	< 0.19	4.96	3

References. — 1 = *Chandra* AO 10 object; 2 = Teng et al. 2005; 3 = Piconcelli et al. 2005; 4 = Crummy et al. 2006; 5 = Teng et al. 2008; 6 = Ptak et al. 2003; 7 = Imanishi 2004; 8 = Teng et al. 2009; 9 = Franceschini et al. 2003; 10 = Sanders et al. (2003); 11 = *XMM-Newton* AO 7 object

Note. — Col.(1): Galaxy name. Coordinate-based names beginning with "F" are sources in the IRAS Faint Source Catalog. Col.(2): Redshift. Col.(3): Bolometric luminosity. For ULIRGs, we assume $L(bol) = 1.15L(IR)$. For PG QSOs, we assume $L(bol) = 7L(5100 \text{ \AA})$ (Netzer et al. 2007). Col.(4): Optical spectral type, from Veilleux et al. (1995, 1999a) and Rupke et al. (2005a). Col.(5): Interaction class, from Veilleux et al. 2002, Veilleux et al. 2006, or Veilleux et al. 2009 (in order of preference). Col.(6): Nuclear separation, in kpc. Col.(7): Galactic column density from Dickey and Lockman (1990) in units of 10^{20} cm^{-2} . Col.(8): References for X-ray data.

6.2 Observations and Data Reduction

The observations of ULIRGs and PG QSOs presented in this paper are selected from the *Chandra* and *XMM-Newton* archives as well as our own (PI: Veilleux) guest observer (GO) programs (*Chandra* cycle 10 and *XMM-Newton* cycle 7). Only ACIS-S data are considered for the *Chandra* analysis. Similarly, only EPIC data are considered for the *XMM-Newton* observations. Table 6.2 lists details on the available observations.

Table 6.2. Journal of Observations

Galaxy (1)	Date (2)	Telescope (3)	Obs ID (4)	PI (5)	Exposure (6)
ULIRGs					
F00091–0738	2008 November 1	CXO	70188510342	Veilleux	15.2
F00188–0856	2003 September 4	CXO	7007814102	Wilson	9.8
	2004 December 20	XMM	0200630201	Imanishi	38.0
F00456–2904:SW	2009 May 22	CXO	70188610343	Veilleux	15.1
F01004–2237	2003 August 3	CXO	7007824103	Wilson	9.4
F01166–0844:SE	2008 October 31	CXO	70188710344	Veilleux	15.8
PG0157+001	2000 July 29	XMM	0101640201	Aschenbach	4.5
	2003 August 23	CXO	7007834104	Wilson	10.6
F02021–2103	2009 July 16	CXO	70188810345	Veilleux	15.1
IRAS03521+0028	2002 December 25	CXO	7007844105	Wilson	7.2
F04103–2838	2003 April 28	CXO	7007854106	Wilson	10.0
	2006 February 13	XMM	0301330401	Wilson	17.5
F05024–1941	2007 February 8	XMM	0405950401	Terashima	20.1
F05189–2524	2001 March 17	XMM	0085640101	Heckman	6.3
	2001 October 30	CXO	6001682034	Heckman	19.3
	2002 January 30	CXO	6001683432	Heckman	14.7
F07598+6508	2000 March 21	CXO	700121816	Green	1.5
	2001 October 25	XMM	0094400301	Sanders	12.7
F08572+3915	2004 April 13	XMM	0200630101	Imanishi	13.3
	2006 January 26	CXO	7012806862	Komossa	14.3
F09039+0503	2008 December 31	CXO	70188910346	Veilleux	16.2
UGC 5101	2001 May 28	CXO	6001672033	Heckman	48.7
	2001 November 12	XMM	0085640201	Heckman	24.0
F09539+0857	2004 January 6	CXO	7008894806	Vignali	5.2
F10190+1322	2003 January 31	CXO	7007864107	Wilson	9.4
	2003 May 5	XMM	0146990101	Risaliti	16.3
F10565+2448	2003 October 23	CXO	6003263952	Martin	29.2
	2003 June 17	XMM	0150320201	Martin	22.9
F11095–0238	2009 April 9	CXO	70189010347	Veilleux	15.5
F11119+3257	2002 June 30	CXO	7005763137	Anabuki	15.2
F11223–1244	2006 June 8	XMM	0405950101	Terashima	0.0
F12072–0444	2003 February 1	CXO	7007884109	Wilson	9.2
F12112+0305	2001 December 30	XMM	0081340801	Franceschini	16.0
	2003 April 15	CXO	7007894110	Wilson	10.0
3C 273 ^a	2000 June 14	XMM	0126700301	Jansen	44.7
	2000 June 17	XMM	0126700801	Jansen	36.0
	2001 June 13	XMM	0136550101	Jansen	62.0
	2003 July 7	XMM	0159960101	Pollock	40.6
	2004 June 30	XMM	0136550801	Jansen	11.7
	2007 January 12	XMM	0414190101	Parmar	47.9
Mrk 231	2000 October 19	CXO	7003891031	Garmire	36.0
	2001 June 7	XMM	0081340201	Franceschini	17.2
Mrk 231 (cont.)	2003 February 3	CXO	7007074028	Gallagher	41.0
	2003 February 11	CXO	7007084029	Gallagher	49.5
	2003 February 20	CXO	7007094030	Gallagher	32.2
F13218+0552	2004 July 11	XMM	0200660301	Matt	5.1
Mrk 273	2000 April 19	CXO	700114809	Xia	41.0
	2002 May 7	XMM	0101640401	Aschenbach	18.0
F13451+1232	2000 February 24	CXO	700141836	Ward	19.7
F14348–1447	2002 July 29	XMM	0081341401	Franceschini	6.8
	2006 March 12	CXO	7012796861	Komossa	14.8
F15130–1958	2003 June 2	CXO	7007904111	Wilson	9.8
F15250+3608	2002 February 22	XMM	0081341101	Franceschini	15.0
	2003 August 27	CXO	7007914112	Wilson	9.2
Arp 220	2000 June 24	CXO	700174869	Clements	56.1
	2002 August 11	XMM	0101640801	Aschenbach	10.5
	2003 January 15	XMM	0101640901	Aschenbach	8.3
	2005 January 14	XMM	0205510201	Sanders	5.8
	2005 February 20	XMM	0205510401	Sanders	4.8
	2005 February 27	XMM	0205510501	Sanders	0.0

Table 6.2

Galaxy (1)	Date (2)	Telescope (3)	Obs ID (4)	PI (5)	Exposure (6)
F15462–0450	2009 April 23	CXO	70189110348	Veilleux	15.2
F16090–0139	2003 February 10	CXO	7007924113	Wilson	9.8
NGC 6240	2000 September 22	XMM	0101640101	Aschenbach	11.3
	2001 July 29	CXO	7002061590	Predehl	37.1
	2002 March 12	XMM	0101640601	Aschenbach	5.8
	2003 March 14	XMM	0147420201	Netzer	3.4
	2003 March 18	XMM	0147420301	Netzer	0.0
	2003 August 13	XMM	0147420401	Netzer	7.8
	2003 August 21	XMM	0147420501	Netzer	3.4
	2003 August 29	XMM	0147420601	Netzer	1.6
	F17208–0014	2001 October 25	CXO	6001692035	Heckman
2002 February 19		XMM	0081340601	Franceschini	9.8
2003 May 7		CXO	7007934114	Wilson	8.6
F21208–0519	2009 March 31	CXO	70189210349	Veilleux	15.1
F21329–2346	2009 June 21	CXO	70189310350	Veilleux	15.2
F22491–1808	2001 May 24	XMM	0081340901	Franceschini	17.9
	2007 July 13	CXO	7014857821	Sanders	14.4
F23234+0946	2009 August 15	CXO	70189410351	Veilleux	15.1
PG QSOs					
PG0050+124	2002 June 22	XMM	0110890301	Watson	18.3
	2005 July 18	XMM	0300470101	Gallo	57.8
PG0838+770	2009 March 2	XMM	0550870401	Veilleux	12.5
PG0844+349	2000 November 5	XMM	0103660201	Aschenbach	8.5
PG0953+414	2001 November 22	XMM	0111290201	Watson	10.9
PG1001+054	2003 May 4	XMM	0150610101	Schartel	8.7
PG1004+130	2003 May 4	XMM	0140550601	Brandt	18.0
	2005 January 5	CXO	7010295606	Garmire	41.3
PG1116+215	2001 December 2	XMM	0111290401	Watson	5.5
	2004 December 17	XMM	0201940101	Steenbrugge	5.6
	2004 December 19	XMM	0201940201	Steenbrugge	5.0
PG1126–041	2004 December 21	XMM	0202060201	Schartel	28.7
PG1211+143	2001 June 15	XMM	0112610101	Turner	48.9
	2004 June 21	XMM	0208020101	Reeves	34.4
PG1229+204	2005 July 9	XMM	0301450201	Matt	17.2
PG1244+026	2001 June 17	XMM	0051760101	Fabian	4.3
PG1307+085	2002 June 13	XMM	0110950401	Watson	10.2
PG1309+355	2002 June 10	XMM	0109080201	Mason	23.9
PG1351+640	2004 June 23	XMM	0205390301	O'Brien	43.3
PG1411+442	2002 July 10	XMM	0103660101	Aschenbach	21.9
PG1426+015	2000 July 28	XMM	0102040501	Jansen	0.5
PG1435–067	2009 February 2	XMM	05508070201	Veilleux	0.4
PG1440+356	2001 December 23	XMM	0107660201	Mushotzky	15.3
	2003 January 1	XMM	0005010101	Guainazzi	17.2
	2003 January 4	XMM	0005010201	Guainazzi	10.4
	2003 January 7	XMM	0005010301	Guainazzi	18.1
	2003 February 8	XMM	0152660101	Kawaguchi	18.1
PG1448+273	2003 February 8	XMM	0152660101	Kawaguchi	18.1
PG1501+106	2001 January 13	XMM	0112910201	Turner	5.9
	2001 January 13	XMM	0070740101	Petrucci	7.6
	2001 January 14	XMM	0070740301	Petrucci	9.0
	2005 January 16	XMM	0205340201	Petrucci	29.7
	2005 July 17	XMM	0205340401	Petrucci	16.3
PG1613+658	2001 April 13	XMM	0102040601	Jansen	1.8
	2001 August 29	XMM	0102041301	Jansen	2.1
PG1626+554	2002 May 5	XMM	0109081101	Mason	0.4
PG2130+099	2003 May 16	XMM	0150470701	Santos-Lleo	25.4
B2 2201+31A	2008 December 1	XMM	0550871001	Veilleux	9.3

Table 6.2

Galaxy (1)	Date (2)	Telescope (3)	Obs ID (4)	PI (5)	Exposure (6)
PG2214+139	2002 May 12	XMM	0103660301	Aschenbach	6.6

Note. — Col.(1): Galaxy name. Coordinate-based names beginning with "F" are sources in the IRAS Faint Source Catalog. Col.(2): Observation start date. Col.(3): Telescope used (CXO = *Chandra*; XMM = *XMM-Newton*). Col.(4): Observation identification number. Col.(5): Principal investigator of the observation. Col.(6): Net exposure time in ks after selection of good time interval.

^a3C 273 is often observed by *XMM-Newton* for calibration purposes. We selected the six observations that have the longest integration times and also maximize the period of elapsed time between the first and final observations.

6.2.1 Data Calibration and Extraction

Chandra Observations

The reduction of the archived *Chandra* data was performed using CIAO version 4.1.1 and CALDB version 4.1. The cycle 10 GO data were reduced using CIAO version 4.1.2 and CALDB version 4.1.3. The Science Analysis Threads for ACIS data¹ outline the procedure used to process and reduce the data. Table 6.2 lists the total exposure for each observation after the selection of good time intervals where the data are not affected by background flares.

The source spectra were extracted with circular regions centered on the source. For most observations, background spectra were selected from an annular source-free region that surrounds the nuclear extraction area. However, in particularly crowded fields, a nearby circular, source-free region was used.

¹<http://cxc.harvard.edu/ciao4.1/index.html>

XMM-Newton Observations

The archived *XMM-Newton* data were processed using the *XMM-Newton* Science Analysis System (SAS), version 7.1.0, released on 2007 July 8. The event lists were re-calibrated with the latest available calibration files as of 2008 July. The Cycle 7 GO data on PG 0838+770, PG 1435–067, and B2 2201+31A were reduced using SAS version 8.0.1. The standard processing procedures outlined in § 4.13 of the *XMM-Newton* SAS User’s Guide (Issue 5.0) were followed for both archived and GO data. Times of high background flares were flagged and the total good time interval for each observation is listed in Table 6.2. The standard method of background screening involves discarding time intervals affected by background flares where the background count rates at energies above 10 keV are above the recommended thresholds of 0.35 counts s⁻¹ and 1 counts s⁻¹ for EPIC-MOS and EPIC-pn data, respectively. While the MaxSNR method introduced by Piconcelli et al. (2004) would maximize the total net exposure times of the data, this method is only appropriate to use for data of high-flux sources. X-ray observations of U/LIRGs (e.g., Franceschini et al. 2003; Ptak et al. 2003; Teng et al. 2005) have shown that these data have low signal-to-noise ratios (SNRs). Therefore, we have conservatively chosen to use the standard method of background screening for a consistent treatment of ULIRG and PG QSO data.

The cross-calibration between the EPIC-MOS and the EPIC-pn cameras has some time and energy dependencies². Complications to the fits may result if spectra from both detectors are modeled simultaneously. Therefore, we chose to model the spectra from only the EPIC-pn camera due to its high quantum efficiency and the inability to extract background spectra when the small window mode was used in

²*XMM-Newton* Calibration Documentation: <http://xmm2.esac.esa.int/docs/documents/CAL-TN-0052-5-0.ps.gz>.

many of the EPIC-MOS observations. The EPIC-MOS data were used only in the few cases where the EPIC-pn data were unavailable or have much lower SNRs than the EPIC-MOS data: PG 0838+770 has very low SNRs, PG 1244+026 has very few detected counts above ~ 5 keV, PG 1613+658 and PG 1626+554 have data highly affected by background flares.

The SAS task EPATPLOT was used to determine whether the observations on the PG QSOs were affected by pile up. Only three sets of observations were found to be piled-up: PG 0844+349, the 17 December 2004 observation of PG 1116+215, and PG 1426+015. In these cases, the observations were re-extracted using annular regions to exclude the central part of the source which is the most susceptible to pile-up, as recommended by the SAS User's Guide. This pile-up correction method is reliable and does not affect the shape of the output source spectrum³.

The *XMM-Newton* source spectra were also extracted with circular regions centered on the source. For EPIC-pn data, the pointing center falls near a CCD gap. Thus, the background was selected from a nearby circular region in which no obvious background source resides. The background regions for EPIC-MOS data were selected in a similar fashion.

Where there are multiple observations of the same source with the same instrument and filters, an average spectrum is created using the FTOOLS task MATHPHA giving each input spectrum equal weight. The sources where this was performed are the EPIC-pn observations of PG 0050+124, PG 1116+215, PG 1440+356, and PG 1501+106.

³*XMM-Newton* Calibration Documentation: <http://xmm2.esac.esa.int/docs/documents/CAL-TN-0036-1-0.ps.gz>.

6.3 Spectral Analysis

The spectral analysis was performed using XSPEC v12.5.0. All quoted errors are 90% limits on one parameter ($\Delta\chi^2$ or $\Delta\text{c-stat} = 2.706$). The errors of the derived values in the rest of this paper are assumed to be at the 90% confidence level. Because of the differences in calibration, the effective energy range is 0.3–10.0 keV for EPIC-pn, 0.6–10.0 keV for EPIC-MOS, and 0.5–8.0 keV for ACIS. For consistency between the different detectors and with the literature, the soft X-ray band measurements are made between 0.5–2.0 keV while the hard X-ray band measurements are made between 2.0–10.0 keV where the best-fit models are used to extrapolate the 0.5–0.6 keV and 8.0–10.0 keV measurements from the EPIC-MOS and ACIS observations, respectively.

6.3.1 Results: PG QSOs

Depending on the number of detected counts, the extracted spectra of the PG QSOs are binned differently for spectral modeling. Their source spectra were binned to at least 50 counts per bin with the exception of those from fainter sources with relatively short integration times (PG 0838+770, PG 1001+054, PG 1004+130, PG 1126–041, PG 1244+026, PG 1309+355, PG 1411+442, PG 1426+015, PG 1435–067, PG 1613+658, PG 1626+554, and PG 2214+139) which were binned to at least 15 counts per bin so that χ^2 statistics would be applicable.

In modeling the spectra, we take the same basic approach as in Teng et al. (2009): first, we assume a simple power-law distribution absorbed only by the Galactic column. If the model is not a satisfactory fit to the data, then we consider adding a MEKAL component to describe the starburst, absorption by intervening material near the central source, and emission lines to model Fe $K\alpha$ and lines of other

Table 6.3. PG QSOs: PL Model Best-fit Values

Galaxy (1)	Obs. Date (2)	kT (3)	Γ (4)	N_H (5)	E_{line} (6)	σ_{line} (7)	EW (8)	χ^2_{ν} (d.o.f.) (9)	$F_{0.5-2}$ (10)	F_{2-10} (11)	$L_{0.5-2}$ (12)	L_{2-10} (13)
PG0050+124	2002 Jun 22 ^a	...	$2.31^{+0.02}_{-0.02}$	$0.04^{+0.01}_{-0.03}$	1.22 (630)	$8.38^{+9.31}_{-0.07}$	$8.25^{+7.57}_{-0.07}$	0.96	0.74
	2005 Jul 18 ^a	...	$2.34^{+0.009}_{-0.007}$	$56.86^{+18.15}_{-14.59}$	1.09 (812)	$5.16^{+0.03}_{-0.03}$	$4.93^{+0.11}_{-0.17}$	0.93	0.68
PG0838+770	2009 March 2	...	$1.49^{+0.48}_{-0.08}$	1.06 (138)	$0.29^{+0.03}_{-0.04}$	$0.78^{+0.08}_{-0.08}$	0.14	0.35
PG0844+349	2000 Nov 5	$0.15^{+0.05}_{-0.06}$	$2.66^{+0.05}_{-0.06}$	$6.13^{+3.03}_{-1.39}$	6.4(f)	0.0(f)	$0.11^{+0.19}_{-0.11}$	0.86 (264)	$6.55^{+0.13}_{-0.21}$	$5.13^{+0.31}_{-0.36}$	1.42	0.63
					6.7(f)	0.0(f)	$0.18^{+0.21}_{-0.17}$					
PG0953+414	2001 Nov 22	$0.16^{+0.03}_{-0.07}$	$2.44^{+0.03}_{-0.03}$	$18.52^{+9.84}_{-5.66}$	1.04 (324)	$3.39^{+0.05}_{-0.07}$	$2.93^{+0.17}_{-0.19}$	10.89	6.51
PG1001+054	2003 May 4	$0.09^{+0.01}_{-0.01}$	$2.01^{+0.67}_{-0.01}$	$8.09^{+5.47}_{-3.57}$	0.96 (19)	$0.02^{+0.01}_{-0.01}$	$0.12^{+0.05}_{-0.05}$	0.10	0.12
PG1004+130	2003 May 4	...	$1.67^{+0.20}_{-0.11}$	$2.99^{+2.57}_{-1.37}$	1.04 (111)	$0.09^{+0.01}_{-0.01}$	$0.31^{+0.06}_{-0.08}$	0.30	0.57
	2005 Jan 5	...	$1.52^{+0.17}_{-0.26}$	$1.44^{+0.64}_{-0.69}$	1.06 (95)	$0.10^{+0.01}_{-0.03}$	$0.43^{+0.07}_{-0.17}$	0.32	0.77
PG1116+215	2001 Dec 2	$0.08^{+0.041}_{-0.006}$	$2.53^{+0.03}_{-0.01}$	$27.21^{+16.01}_{-4.13}$	1.00 (255)	$4.34^{+0.22}_{-0.06}$	$3.27^{+0.23}_{-0.29}$	8.45	4.44
	2004 Dec 17	$0.09^{+0.007}_{-0.006}$	$2.49^{+0.01}_{-0.01}$	$31.61^{+5.14}_{-2.34}$	1.15 (664)	$3.70^{+0.03}_{-0.03}$	$3.11^{+0.07}_{-0.09}$	8.35	4.65
	2004 Dec 19	$0.12^{+0.13}_{-0.04}$	$2.51^{+0.04}_{-0.04}$	$20.21^{+5.94}_{-5.10}$	0.98 (238)	$4.00^{+0.09}_{-0.10}$	$3.51^{+0.23}_{-0.26}$	8.51	4.63
PG1126-041	2004 Dec 21	$0.11^{+0.01}_{-0.01}$	$1.95^{+0.10}_{-0.10}$	$4.66^{+0.42}_{-0.39}$	1.13 (309)	$0.09^{+0.01}_{-0.01}$	$1.14^{+0.14}_{-0.28}$	0.11	0.13
PG1211+143	2001 Jun 15 ^a	$0.19^{+0.01}_{-0.02}$	$2.83^{+0.01}_{-0.01}$	$12.98^{+0.94}_{-2.34}$	1.41 (489)	$2.69^{+0.03}_{-0.04}$	$2.90^{+0.08}_{-0.08}$	2.13	0.87
	2004 Jun 21 ^a	$0.21^{+0.02}_{-0.01}$	$2.63^{+0.02}_{-0.02}$	$12.40^{+0.90}_{-1.49}$	6.4(f)	0.2(f)	$0.18^{+0.12}_{-0.12}$	1.21 (533)	$3.23^{+0.04}_{-0.04}$	$3.07^{+0.09}_{-0.10}$	1.59	0.78
PG1229+204	2005 Jul 9	$0.09^{+0.01}_{-0.01}$	$2.38^{+0.03}_{-0.03}$	$13.52^{+5.77}_{-3.36}$	6.4(f)	0.0(f)	$0.06^{+0.08}_{-0.06}$	1.13 (402)	$3.17^{+0.05}_{-0.06}$	$3.16^{+0.16}_{-0.17}$	0.61	0.41
					6.7(f)	0.0(f)	$0.11^{+0.11}_{-0.09}$					
PG1244+026	2001 Jun 17	$0.62^{+0.06}_{-0.07}$	$2.72^{+0.07}_{-0.07}$	0.89 (240)	$6.58^{+0.21}_{-0.20}$	$2.55^{+0.13}_{-0.13}$	0.38	0.14
PG1307+085	2002 Jun 13	$0.11^{+0.01}_{-0.01}$	$1.89^{+0.11}_{-0.10}$	$5.64^{+2.62}_{-1.84}$	1.13 (145)	$0.77^{+0.04}_{-0.04}$	$1.89^{+0.23}_{-0.27}$	1.05	1.43
PG1309+355	2002 Jun 10 ^a	...	$2.19^{+0.07}_{-0.06}$	$6.02^{+3.68}_{-1.84}$	6.4(f)	0.0(f)	$0.12^{+0.17}_{-0.12}$	1.03 (264)	$0.40^{+0.02}_{-0.01}$	$0.69^{+0.07}_{-0.08}$	0.74	0.76
PG1351+640	2004 Jun 23 ^a	$0.16^{+0.07}_{-0.05}$	$2.42^{+0.04}_{-0.04}$	$14.61^{+5.72}_{-3.81}$	1.06 (281)	$0.59^{+0.01}_{-0.03}$	$0.62^{+0.05}_{-0.06}$	0.25	0.17
PG1411+442	2002 Jul 10	$0.12^{+0.18}_{-0.02}$	$2.41^{+0.18}_{-0.15}$	$26.29^{+6.24}_{-4.08}$	6.4(f)	0.0(f)	$0.17^{+0.32}_{-0.17}$	1.01 (139)	$0.08^{+0.07}_{-0.11}$	$0.50^{+0.07}_{-0.17}$	0.40	0.26
PG1426+015	2000 Jul 28	...	$2.38^{+0.06}_{-0.11}$	1.01 (148)	$8.14^{+0.35}_{-0.38}$	$5.92^{+0.60}_{-0.57}$	1.65	1.09
PG1435-067	2009 Feb 2	...	$2.36^{+0.10}_{-0.10}$	1.25 (60)	$2.60^{+0.23}_{-0.25}$	$2.10^{+0.37}_{-0.35}$	1.30	0.88
PG1440+356	2001 Dec 23	...	$3.02^{+0.04}_{-0.04}$	$8.92^{+8.66}_{-3.51}$	1.17 (164)	$5.12^{+0.16}_{-0.14}$	$2.41^{+0.28}_{-0.31}$	2.12	0.55
	2003 Jan 1 ^a	...	$2.86^{+0.01}_{-0.02}$	$14.40^{+2.88}_{-2.77}$	1.34 (433)	$5.49^{+0.06}_{-0.07}$	$3.12^{+0.10}_{-0.10}$	2.37	0.79
	2003 Jan 4	...	$2.98^{+0.02}_{-0.02}$	$8.25^{+2.03}_{-1.49}$	0.96 (344)	$4.86^{+0.07}_{-0.07}$	$2.46^{+0.16}_{-0.15}$	1.99	0.55
	2003 Jan 7	...	$2.86^{+0.02}_{-0.02}$	$12.67^{+3.45}_{-2.70}$	1.45 (340)	$2.90^{+0.05}_{-0.05}$	$1.74^{+0.09}_{-0.10}$	1.34	0.44
PG1448+273	2003 Feb 8	$0.23^{+0.01}_{-0.02}$	$2.80^{+0.02}_{-0.01}$	$16.72^{+6.24}_{-4.39}$	1.22 (381)	$3.91^{+0.05}_{-0.06}$	$1.97^{+0.10}_{-0.11}$	0.89	0.31
PG1501+106	2001 Jan 13 ^a	$0.08^{+0.01}_{-0.00}$	$2.46^{+0.02}_{-0.02}$	$23.12^{+6.40}_{-4.56}$	1.23 (481)	$14.14^{+0.18}_{-0.07}$	$13.24^{+0.25}_{-0.25}$	1.12	0.68
	2001 Jan 13 ^a	$0.09^{+0.01}_{-0.01}$	$2.50^{+0.02}_{-0.02}$	$18.66^{+3.60}_{-2.77}$	6.4(f)	0.0(f)	$0.04^{+0.06}_{-0.04}$	1.09 (566)	$16.08^{+0.08}_{-0.17}$	$14.76^{+0.26}_{-0.23}$	1.23	0.70
	2001 Jan 14 ^a	$0.09^{+0.01}_{-0.01}$	$2.45^{+0.02}_{-0.02}$	$15.88^{+2.42}_{-2.07}$	1.14 (624)	$16.02^{+0.09}_{-0.13}$	$15.63^{+0.27}_{-0.22}$	1.17	0.71
	2005 Jan 16 ^a	$0.09^{+0.001}_{-0.001}$	$2.26^{+0.01}_{-0.01}$	$13.01^{+0.57}_{-0.50}$	6.7(f)	0.2(f)	$0.14^{+0.07}_{-0.06}$	1.56 (821)	$4.93^{+0.04}_{-0.05}$	$9.78^{+0.13}_{-0.14}$	0.55	0.47
PG1613+658	2005 Jul 17 ^a	$0.11^{+0.01}_{-0.01}$	$2.11^{+0.02}_{-0.02}$	$11.48^{+1.69}_{-1.56}$	6.7(f)	0.15(f)	$0.11^{+0.06}_{-0.07}$	1.24 (691)	$6.80^{+0.06}_{-0.09}$	$11.51^{+0.27}_{-0.29}$	0.42	0.45
PG1613+658	2001 Apr 13	...	$1.95^{+0.10}_{-0.10}$	$28.24^{+10.778}_{-20.67}$	0.99 (135)	$2.58^{+0.38}_{-0.19}$	$4.22^{+0.73}_{-0.82}$	1.90	2.38
	2001 Aug 29	...	$2.12^{+0.08}_{-0.08}$	$10.45^{+10.78}_{-4.77}$	0.98 (246)	$4.00^{+0.27}_{-0.16}$	$5.29^{+0.60}_{-0.73}$	2.74	2.67
PG1626+554	2002 May 5	...	$2.04^{+0.15}_{-0.14}$	0.95 (33)	$2.99^{+0.57}_{-0.48}$	$3.45^{+0.65}_{-0.53}$	1.49	1.62
PG2130+099	2003 May 16 ^a	$0.08^{+0.004}_{-0.000}$	$2.29^{+0.05}_{-0.05}$	$5.91^{+0.73}_{-0.52}$	6.4(f)	0.1(f)	$0.15^{+0.11}_{-0.10}$	1.31 (481)	$1.88^{+0.05}_{-0.04}$	$3.43^{+0.18}_{-0.19}$	0.51	0.42
B2 2201+31A	2008 Dec 1	$0.19^{+0.03}_{-0.05}$	$2.11^{+0.04}_{-0.06}$	$40.42^{+28.98}_{-16.91}$	1.04 (212)	$2.55^{+0.07}_{-0.08}$	$4.61^{+0.33}_{-0.43}$	20.18	19.57
PG2214+139	2002 May 12	$0.17^{+0.02}_{-0.02}$	$1.80^{+0.16}_{-0.16}$	$4.48^{+0.68}_{-0.68}$	1.14 (207)	$0.28^{+0.03}_{-0.04}$	$3.19^{+0.41}_{-1.04}$	0.29	0.44

^aThe spectrum requires additional components for redshifted absorption edges originating from O VII or O VIII. See notes on individual sources for details.

Note. — (f) denotes a fixed value. Col.(1): Galaxy name. Col.(2): Observation start date. Col.(3): Gas temperature from the MEKAL component in units of keV. Col.(4): Photon index of the direct and indirect power-law components. Col.(5): Hydrogen column density within the source in units of 10^{22} cm^{-2} . Col.(6): Rest-frame energy of the iron emission line(s) in units of keV. Col.(7): Width of the iron line(s) in units of keV. Col.(8): The equivalent width of the iron line(s) in units of keV. Col.(9): Reduced χ^2 of the best-fit model followed by the number of degrees of freedom in (). Col.(10): Observed 0.5–2 keV flux in units of $10^{-12} \text{ erg s}^{-1} \text{ cm}^{-2}$. Col.(11): Observed 2–10 keV flux in units of $10^{-12} \text{ erg s}^{-1} \text{ cm}^{-2}$. Col.(12): Nominal absorption corrected 0.5–2 keV luminosity in units of $10^{44} \text{ erg s}^{-1}$. Col.(13): Nominal absorption corrected 2–10 keV luminosity in units of $10^{44} \text{ erg s}^{-1}$.

elements, if applicable. The F-test is used to determine whether the additional components to the basic model are significant⁴. We assume $P_{F-test} < 0.001$ for significant additions. Hereafter, we refer to these models as the Power-Law (PL) models. Table 6.3 lists the best-fit parameters of the PL models to the PG QSOs. More complex models involving reflection and scattering such as those presented in Piconcelli et al. (2005) (hereafter P05 models) and the blurred ionized reflection model presented in Crummy et al. (2006) (C06) were also considered. The details of these models are discussed below. Tables 6.4 and 6.5 list the best-fit parameters to the P05 and C06 models to the PG QSO data, respectively. Figure 6.1 displays the quasar spectra with the best-fit PL, P05, and C06 models. The PL models appear to be as good as, or better than, the P05 and C06 models in fitting the data.

Figure 6.2 shows comparisons of the reduced χ^2 values between the PL models and the P05 and C06 models. The C06 models are modified versions of that presented in Crummy et al. (2006). The models presented in the original paper require extreme values for the accretion disc that are unphysical. For example, the disc emissivity index (ϵ , the power law dependence of the emissivity, $r^{-\epsilon}$) ranges from 1.3 to 10.0, the upper limit of allowable values. In our modified version, the emissivity index of the disc in the KDBLUR model component is fixed at the more commonly accepted value of 3.0. Since the iron abundance is less reliable, we conservatively fix the abundance of the REFLION component at solar. For the majority of objects, the inclination of the disc is also fixed at the default value of 30 degrees in order for the fit to converge so that $\chi^2_{\nu} < 2.0$ (see Table 6.5). As the figures show, with the exception of a handful of sources, none of the above models is statistically favored.

⁴Under certain conditions, such as testing for a spectral line, it is inappropriate to use the F-test for model selection. See Protassov et al. (2002) for caveats and details.

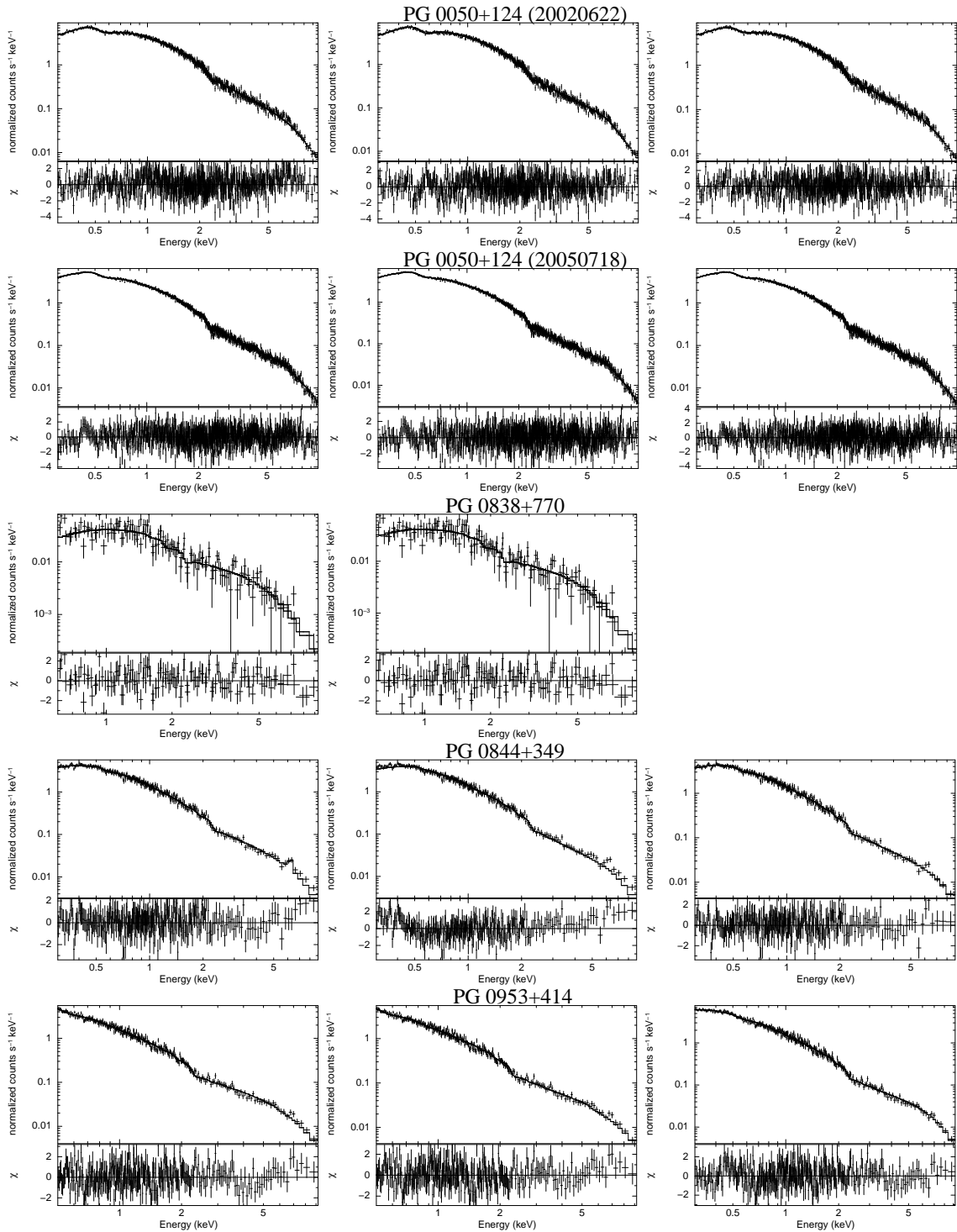


Figure 6.1: *XMM-Newton* spectra of PG QSOs and the best-fit power-law (left column), C06 (middle column), and P05 (right column) models. See text for more details (§ 6.3.1).

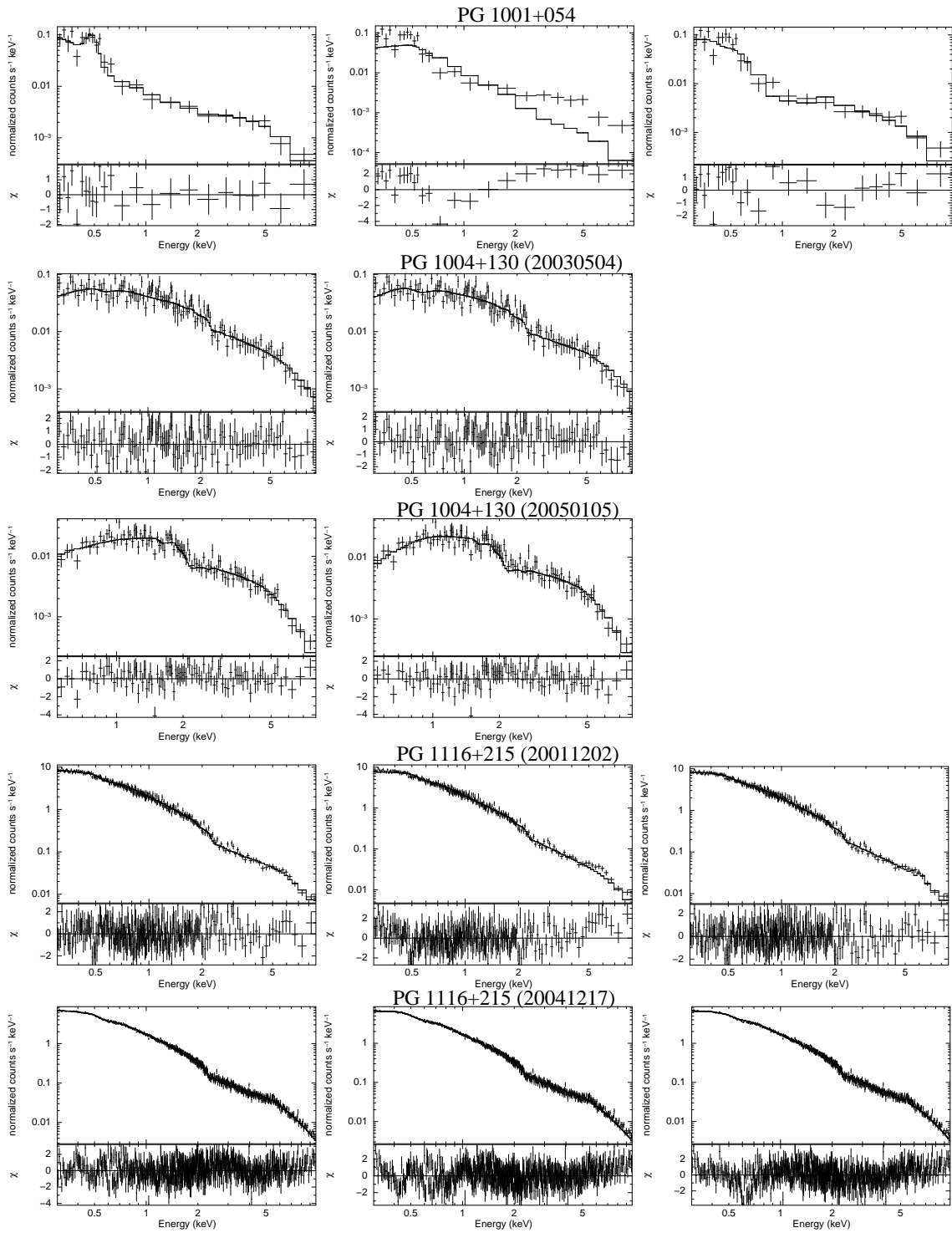


Figure 6.1: Cont.

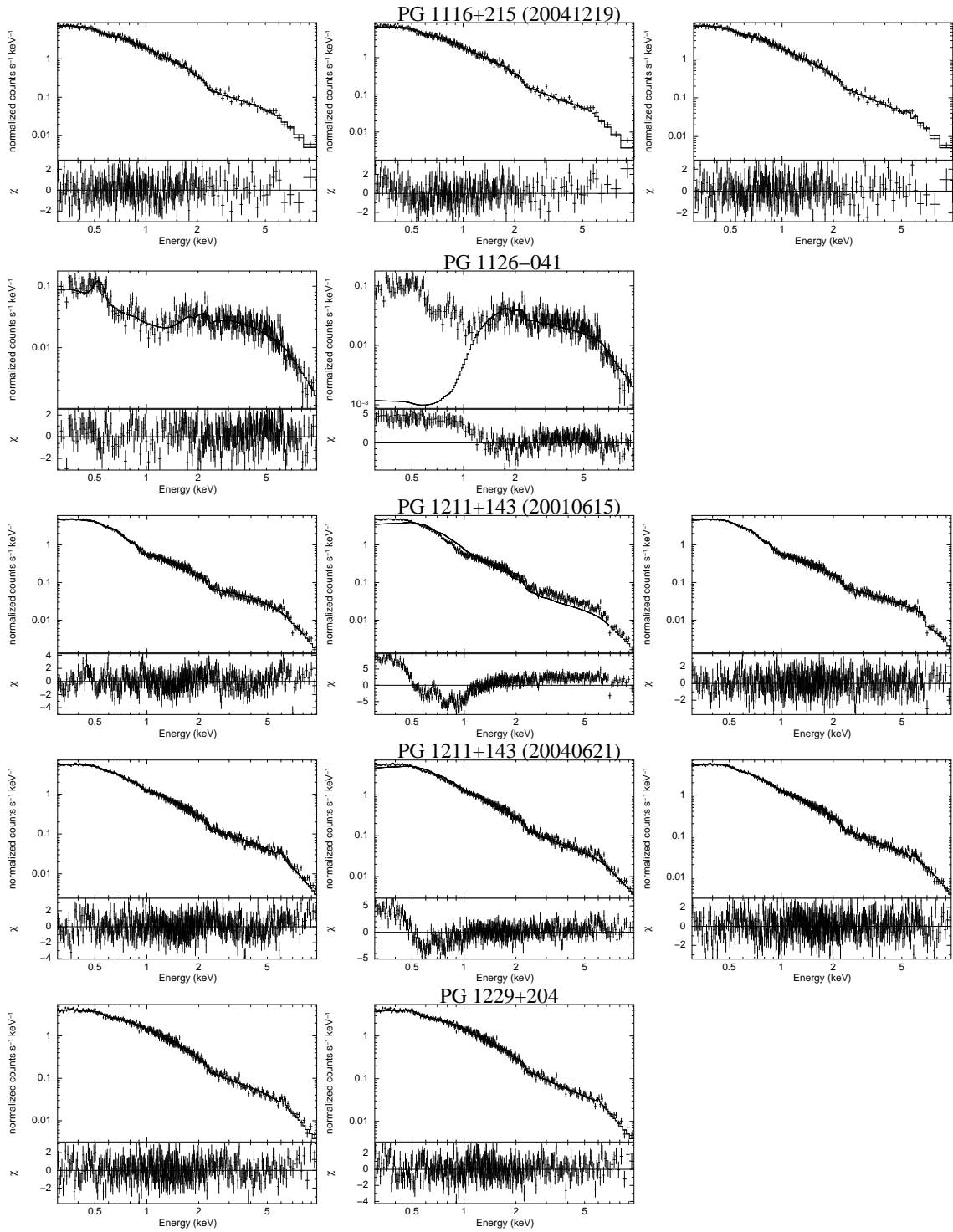


Figure 6.1: Cont.

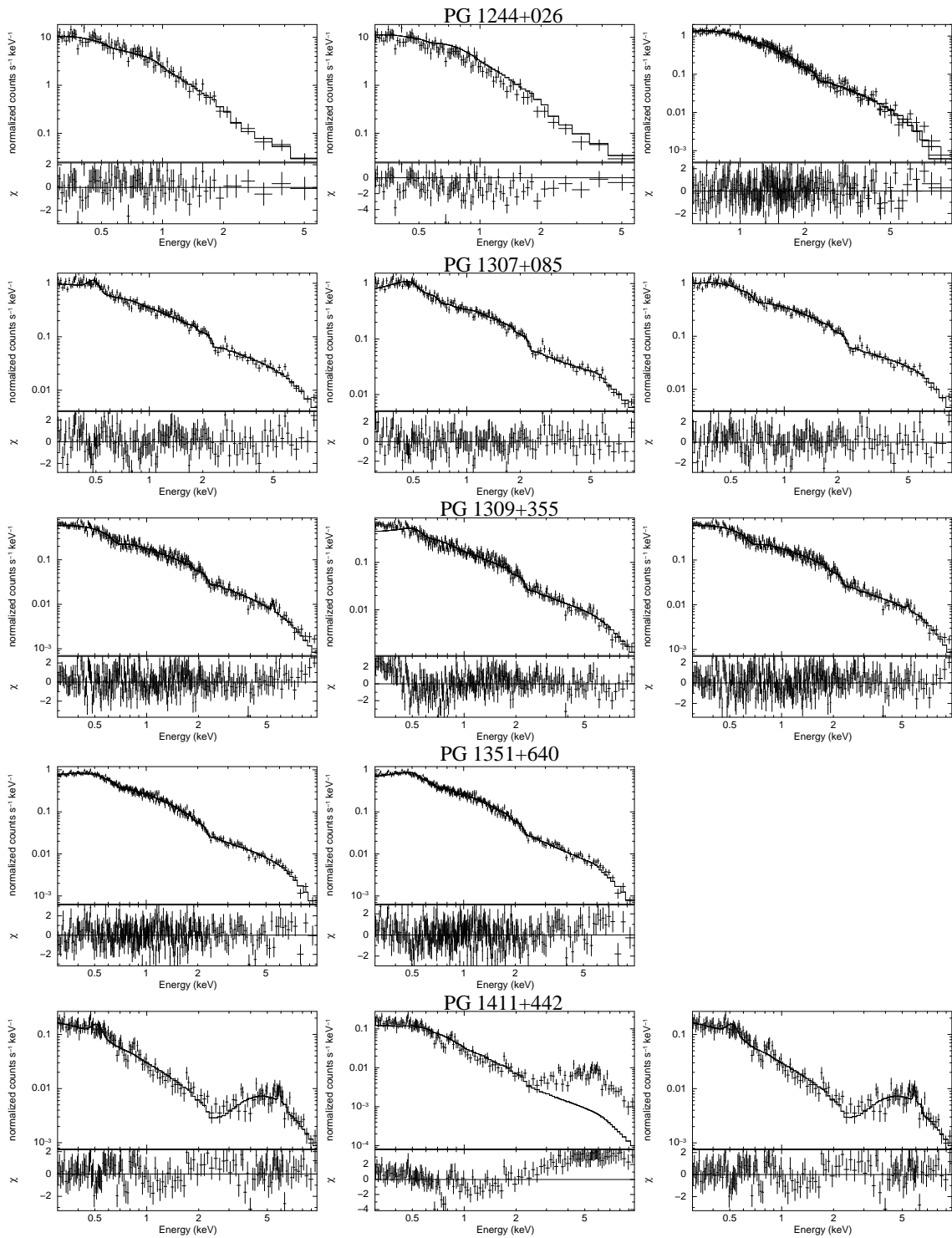


Figure 6.1: Cont.

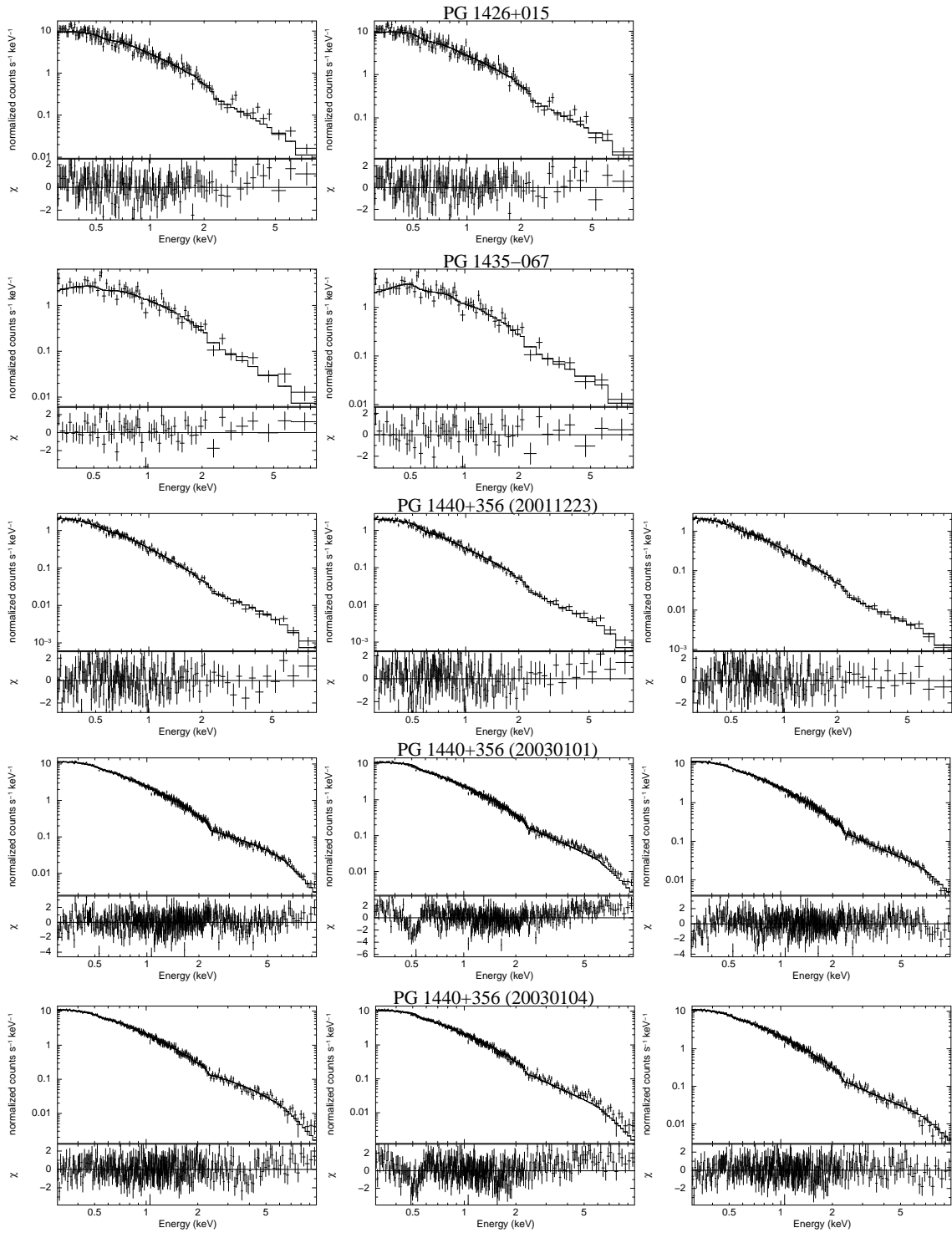


Figure 6.1: Cont.

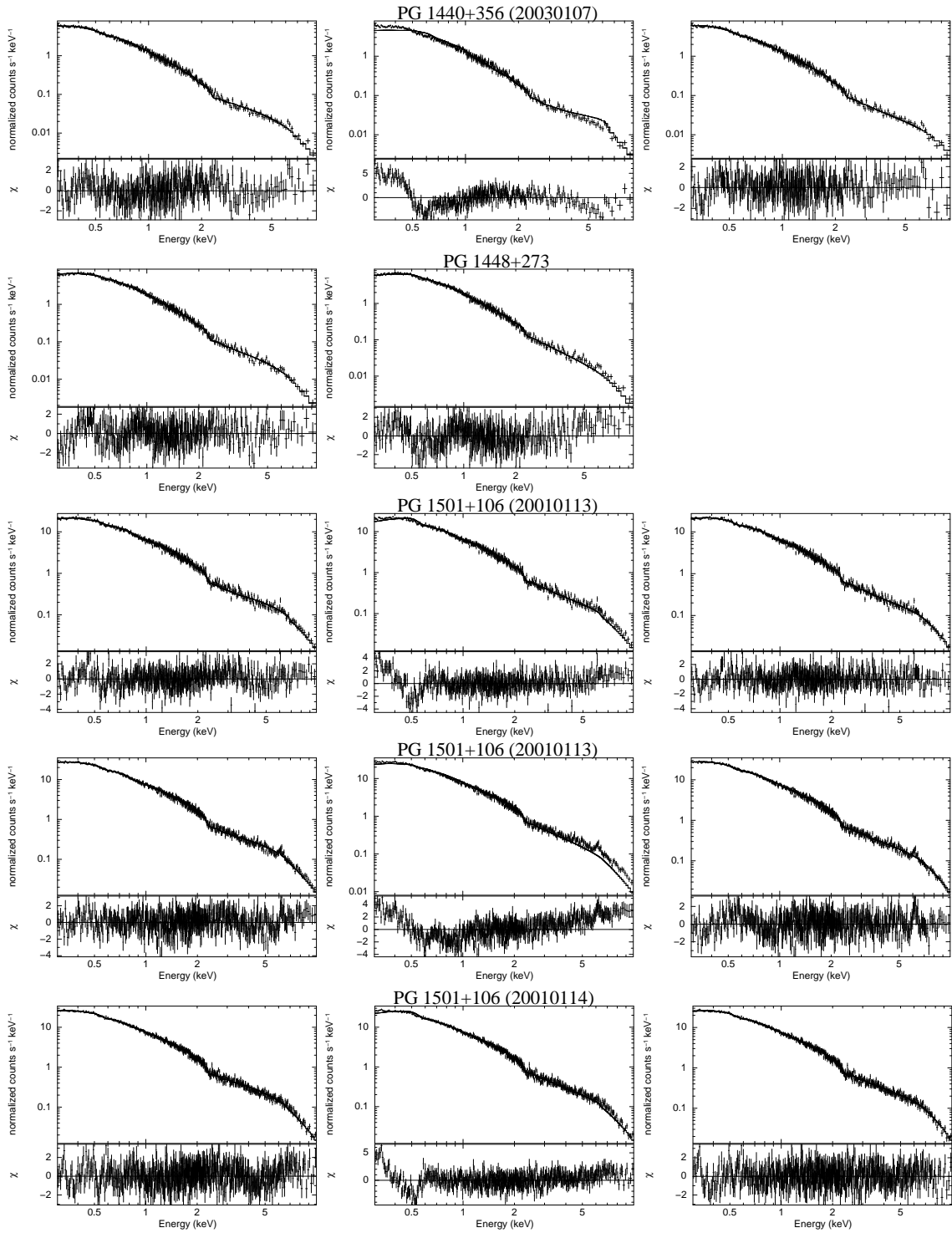


Figure 6.1: Cont.

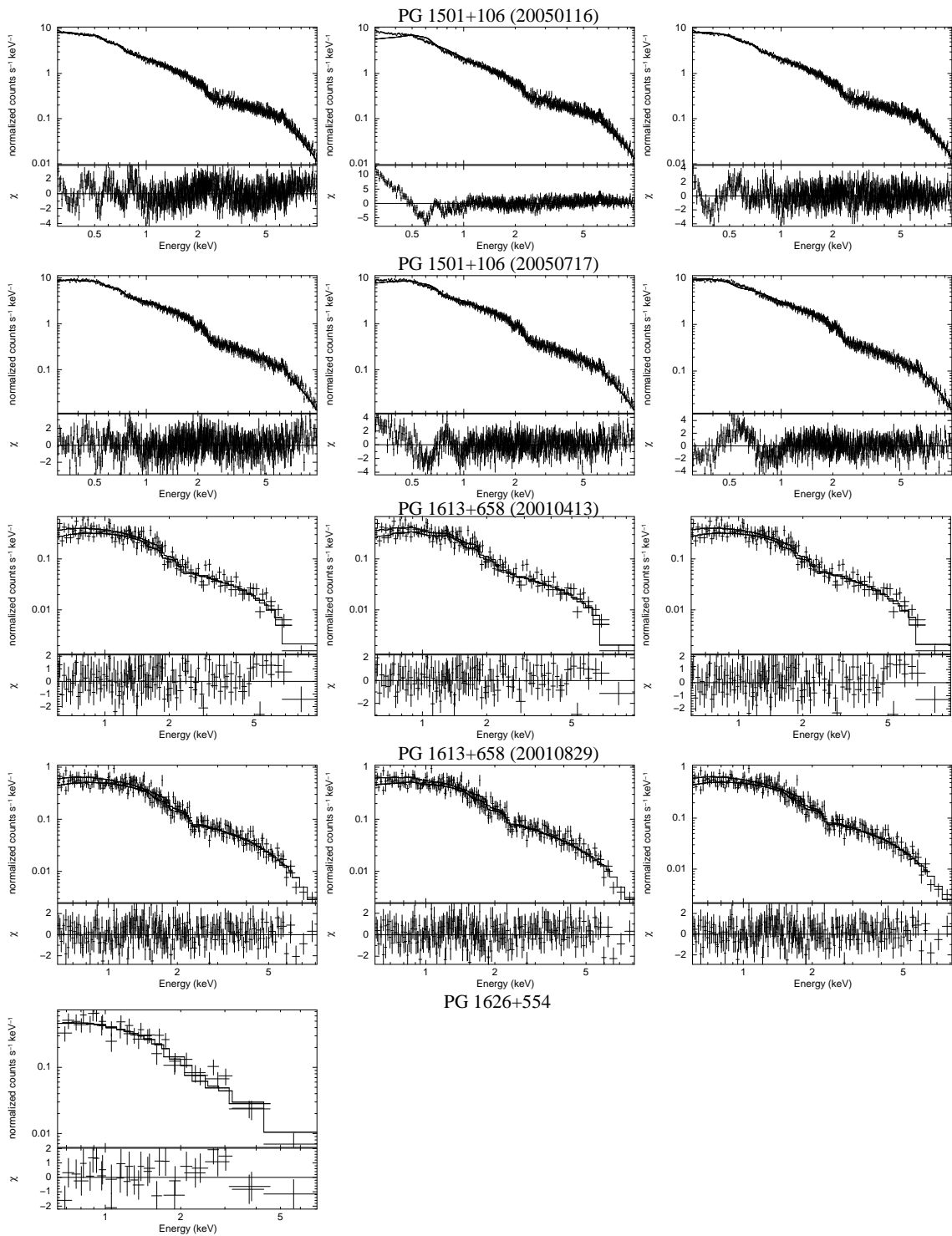


Figure 6.1: Cont.

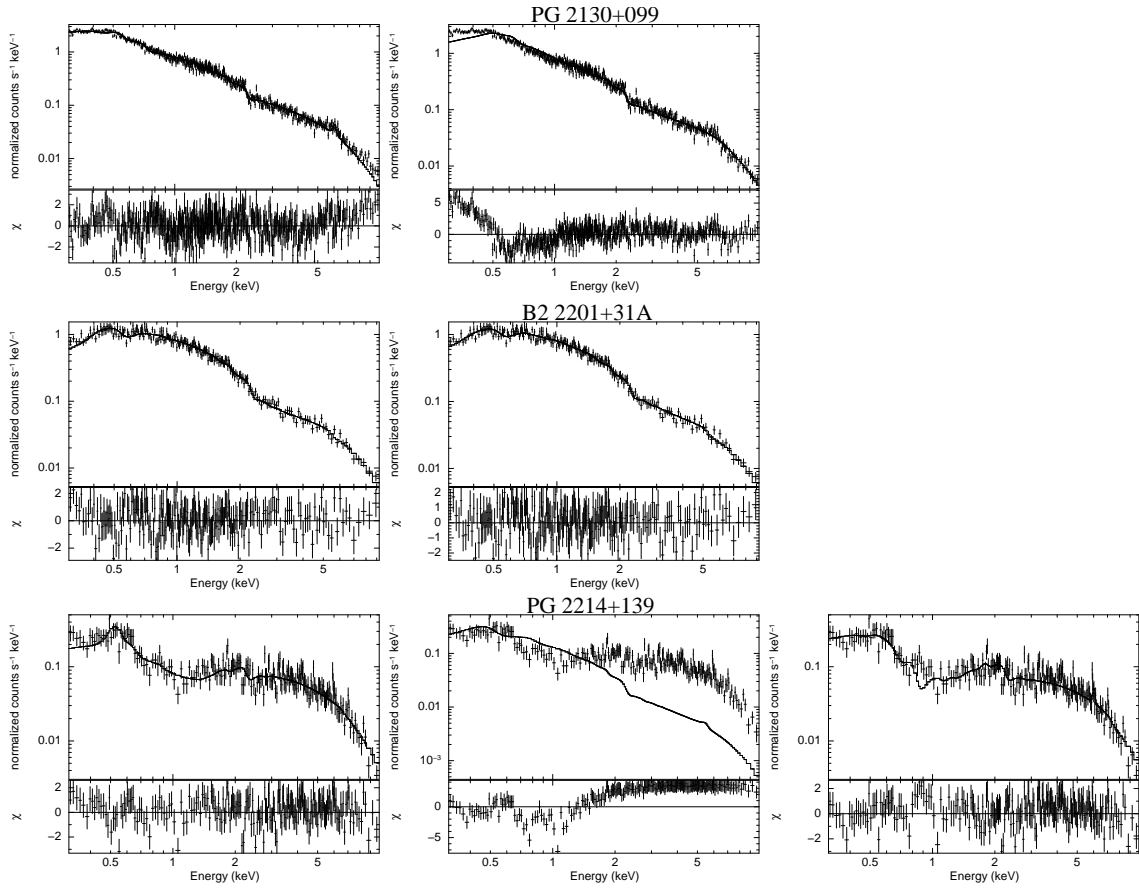


Figure 6.1: Cont.

In terms of the basic spectral properties, the PL models seem to be equally good in determining the photon index as both P05 and C06. Figure 6.3 is a comparison of the photon index as determined by the three methods. The P05 and PL models appear to be consistent with each other; however, the PL model requires softer spectra than the C06 models. Nevertheless, the photon indices as determined by all three methods are within the range previously measured in the PG QSOs by other authors (e.g., Porquet et al. 2004).

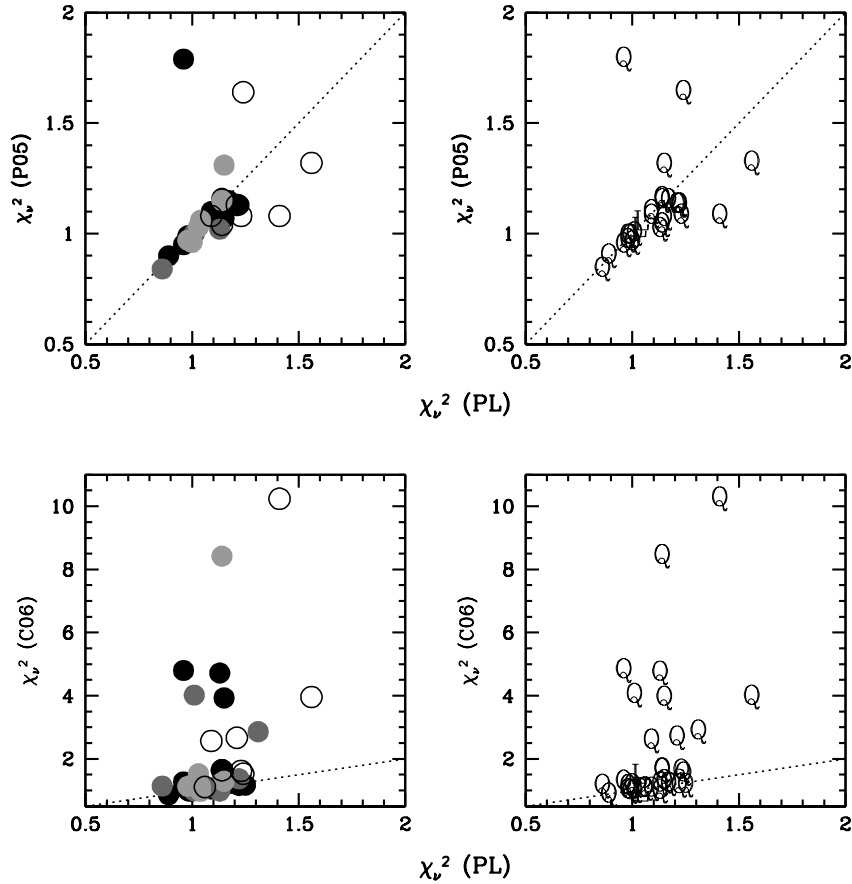


Figure 6.2: Comparison of the reduced χ^2 values from the power-law models with those of Piconcelli et al. (2005) (P05; top) and our modified Crummy et al. (2006) model (C06; bottom) for all PG QSOs. In the left panels, the symbol represents the Netzer et al. (2007) far-infrared SED classification of each source where black circles represent strong FIR emitters, dark gray circles weak FIR emitters, light gray circles undetected FIR emitters, and open circles sources with unknown SED classifications. In the right panels, the symbols represent radio loudness. With the exception of two sources (PG 1211+143 and PG 1501+106), the statistics suggest that the power-law models are as good, or better, descriptions of the quasar spectra as the P06 and C06 models.

Table 6.4. PG QSOs: P05 Model^aBest-fit Values

Galaxy (1)	Obs. Date (2)	kT (3)	Γ (4)	NH (5)	E_{line} (6)	σ_{line} (7)	EW (8)	χ^2_{ν} (d.o.f.) (9)	$F_{0.5-2}$ (10)	F_{2-10} (11)	$L_{0.5-2}$ (12)	L_{2-10} (13)
PG0050+124	2002 Jun 22 ^b	$0.07^{+0.007}_{-0.007}$; $0.21^{+0.007}_{-0.011}$	$2.25^{+0.05}_{-0.03}$	$0.09^{+0.08}_{-0.02}$	6.4(f)	0.0(f)	$0.04^{+0.06}_{-0.03}$	1.13 (626)	$8.38^{+1.07}_{-0.36}$	$8.33^{+0.11}_{-0.15}$	1.09	0.76
2005 Jul 18	0.08	$0.002^{+0.002}_{-0.001}$; $0.25^{+0.01}_{-0.01}$	$2.09^{+0.03}_{-0.03}$	$0.04^{+0.02}_{-0.02}$	6.4(f)	0.0(f)	$0.02^{+0.03}_{-0.02}$	1.10 (812)	$5.16^{+1.24}_{-0.32}$	$4.89^{+0.44}_{-0.44}$	0.60	0.44
PG0844+349	2000 Nov 5	$0.08^{+0.01}_{-0.01}$; $0.19^{+0.03}_{-0.03}$	$2.06^{+0.07}_{-0.09}$	0.84 (266)	$6.51^{+0.32}_{-0.57}$	$5.37^{+0.31}_{-0.39}$	0.73	0.53
PG0953+414	2001 Nov 22 ^c	$2.11^{+0.32}_{-0.14}$	$2.57^{+0.02}_{-0.15}$	1.06 (326)	$3.40^{+0.06}_{-0.06}$	$2.98^{+0.20}_{-0.20}$	5.81	4.87
PG1001+054	2003 May 4	...	$2.06^{+0.16}_{-0.16}$	$8.05^{+4.34d}_{-1.48}$	1.79 (21)	$0.02^{+0.004}_{-0.004}$	$0.10^{+0.03}_{-0.04}$	0.08	0.09
PG1116+215	2001 Dec 2 ^b	$0.34^{+0.05}_{-0.05}$	$2.18^{+0.04}_{-0.04}$...	$6.4(f)$; $7.17(f)$	$0.0(f)$; $0.0(f)$	$0.05^{+0.15}_{-0.05}$; $0.18^{+0.32}_{-0.18}$	0.96 (253)	$4.35^{+0.24}_{-0.15}$	$3.29^{+0.17}_{-0.28}$	3.37	2.70
2004 Dec 17	...	$0.34^{+0.018}_{-0.008}$	$2.05^{+0.03}_{-0.03}$...	$6.4(f)$	$0.0(f)$	$0.07^{+0.05}_{-0.05}$	1.31 (665)	$3.71^{+0.03}_{-0.03}$	$3.12^{+0.46}_{-0.39}$	3.35	2.68
PG1211+143	2001 Jun 15 ^b	$2.04^{+0.16}_{-0.16}$; $0.11^{+0.003}_{-0.001}$	$2.02^{+0.09}_{-0.06}$...	$6.4(f)$; $7.17(f)$	$0.0(f)$; $0.0(f)$	$0.12^{+0.19}_{-0.12}$; $0.08^{+0.17}_{-0.08}$	0.97 (238)	$4.01^{+0.30}_{-0.04}$	$3.56^{+0.67}_{-0.23}$	3.73	3.09
2004 Jun 21	$2.06^{+0.23}_{-0.13}$; $0.11^{+0.001}_{-0.001}$	$2.43^{+0.11}_{-0.05}$	$2.20^{+0.04}_{-0.05}$...	$6.4(f)$	$0.1(f)$	$0.06^{+0.06}_{-0.09}$	1.08 (486)	$2.66^{+0.05}_{-0.05}$	$2.99^{+0.30}_{-0.23}$	0.49	0.49
PG1244+026	2001 Jun 17	$0.16^{+0.01}_{-0.01}$	$2.49^{+0.12}_{-0.07}$	1.13 (537)	$3.19^{+0.04}_{-0.03}$	$3.20^{+0.24}_{-0.23}$	0.58	0.52
PG1307+085	2002 Jun 13 ^b	$1.97^{+0.25}_{-0.19}$	$2.23^{+0.07}_{-0.07}$	1.02 (145)	$0.80^{+0.04}_{-0.04}$	$1.88^{+0.24}_{-0.24}$	0.56	1.04
PG1309+355	2002 Jun 10 ^b	$2.06^{+0.54}_{-0.63}$	$2.20^{+0.05}_{-0.08}$...	$6.4(f)$	$0.0(f)$	$0.09^{+0.09}_{-0.08}$	1.03 (264)	$0.40^{+0.02}_{-0.01}$	$0.69^{+0.08}_{-0.08}$	0.40	0.66
PG1411+442	2002 Jul 10	$0.12^{+0.02}_{-0.02}$	$2.35^{+0.08}_{-0.18}$	$25.17^{+3.65e}_{-3.03}$	$6.4(f)$	$0.0(f)$	$0.17^{+0.12}_{-0.11}$	1.00 (139)	$0.08^{+0.01}_{-0.01}$	$0.43^{+0.08}_{-0.20}$	0.44	0.26
PG1440+356	2001 Dec 23	...	$1.13^{+0.45}_{-0.56}$; $3.10^{+0.09}_{-0.07}$	1.15 (164)	$5.12^{+0.31}_{-0.19}$	$2.70^{+0.47}_{-0.49}$	0.82	0.42
2003 Jan 1	$1.35^{+0.15}_{-0.15}$; $3.04^{+0.04}_{-0.04}$	1.16 (435)	$5.46^{+0.10}_{-0.10}$	$3.31^{+0.32}_{-0.32}$	0.88	0.51
2003 Jan 4	$1.18^{+0.24}_{-0.24}$; $3.08^{+0.05}_{-0.04}$	0.95 (344)	$4.86^{+0.09}_{-0.09}$	$2.75^{+0.37}_{-0.40}$	0.78	0.42
2003 Jan 7	$1.36^{+0.21}_{-0.21}$; $3.03^{+0.06}_{-0.06}$	1.07 (340)	$2.88^{+0.05}_{-0.05}$	$1.86^{+0.40}_{-0.40}$	0.46	0.29
PG1501+106	2001 Jan 13	$2.30^{+0.27}_{-0.18}$; $0.63^{+0.08}_{-0.06}$	$2.81^{+0.04}_{-0.03}$	1.08 (483)	$13.88^{+0.22}_{-0.24}$	$13.77^{+0.94}_{-1.03}$	0.45	0.41
2001 Jan 13	$2.25^{+0.25}_{-0.16}$; $0.68^{+0.12}_{-0.03}$	$2.73^{+0.03}_{-0.04}$	$2.39^{+0.04}_{-0.04}$	1.08 (569)	$15.85^{+0.21}_{-0.18}$	$15.22^{+0.98}_{-0.70}$	0.52	0.46
2001 Jan 14	$2.18^{+0.14}_{-0.14}$; $0.10^{+0.004}_{-0.004}$	$2.60^{+0.02}_{-0.03}$	$2.67^{+0.03}_{-0.03}$	1.04 (626)	$15.87^{+0.14}_{-0.14}$	$16.09^{+0.73}_{-0.70}$	0.52	0.48
2005 Jan 16 ^b	$1.21^{+0.70}_{-0.23}$; $2.55^{+2.69}_{-0.28}$	$2.60^{+0.02}_{-0.03}$	$2.67^{+0.03}_{-0.03}$...	$6.7(f)$	$0.0(f)$	$0.07^{+0.03}_{-0.04}$	1.32 (821)	$4.83^{+0.17}_{-0.20}$	$10.24^{+2.60}_{-0.58}$	0.07	0.31
2005 Jul 17	$2.31^{+0.13}_{-0.13}$; $0.69^{+0.28}_{-0.04}$	$2.02^{+0.14}_{-0.14}$	$2.02^{+0.14}_{-0.14}$	1.64 (694)	$6.61^{+0.14}_{-0.14}$	$11.89^{+0.60}_{-0.60}$	0.21	0.36
PG1613+658	2001 Apr 13	$2.27^{+2.19}_{-0.71}$	$2.20^{+0.14}_{-0.14}$	0.99 (135)	$2.59^{+0.37}_{-0.18}$	$4.17^{+0.91}_{-1.31}$	1.24	1.83
2001 Aug 29	...	$1.56^{+0.72}_{-0.25}$	$2.20^{+0.16}_{-0.13}$	0.99 (246)	$4.01^{+0.72}_{-0.62}$	$5.08^{+0.66}_{-0.62}$	1.93	2.24
PG2214+139	2002 May 12 ^f	...	$1.56^{+0.11}_{-0.11}$	$6.72^{+1.73}_{-1.31}$; $0.55^{+0.21}_{-0.20}$; $0.11^{+0.20}_{-0.11}$	1.15 (205)	$0.28^{+0.02}_{-0.11}$	$3.22^{+0.42}_{-0.88}$	0.19	0.42

^aThe best-fit models presented in Table 10 of Piconcelli et al. (2005) are used as the basis for the modeling of each spectrum.

^bThe spectrum requires additional components for redshifted absorption edges originating from O VII or O VIII. See notes on individual sources for details.

^cAlthough Piconcelli et al. (2005) found that the double blackbody plus power law model best describes the spectrum, we found that a single blackbody plus power law model is a better fit.

^dThe absorber here is an ionized absorber with ionization parameter at 237^{+62}_{-67} erg cm⁻².

^eThe absorber here is a partial-covering absorber with the covering fraction at $0.96^{+0.01}_{-0.01}$.

^fPiconcelli et al. (2005) suggests the best-fit model is a two-phase warm absorber with a power-law component. The column density parameters are listed in order for the respective phases at 1.5×10^5 and 3×10^4 K. These two phases have ionization parameters of 99^{+21}_{-17} and 6^{+12}_{-3} erg cm⁻², respectively.

Note. — (f) denotes a fixed value. Col.(1): Galaxy name. Col.(2): Observation start date. Col.(3): Temperature(s) of the blackbody, bremsstrahlung, or Raymond-Smith component(s) in units of keV. Col.(4): Photon index of the power-law component(s). Col.(5): Hydrogen column density within the source in units of 10^{22} cm⁻². Col.(6): Rest-frame energy of the iron emission line(s) in units of keV. Col.(7): Width of the iron line(s) in units of keV. Col.(8): The equivalent width of the iron line(s) in units of keV. Col.(9): Reduced χ^2 of the best-fit model followed by the number of degrees of freedom in (). Col.(10): Observed 0.5–2 keV flux in units of 10^{-12} erg s⁻¹ cm⁻². Col.(11): Observed 2–10 keV flux in units of 10^{-12} erg s⁻¹ cm⁻². Col.(12): Nominal absorption corrected 0.5–2 keV luminosity in units of 10^{44} erg s⁻¹. Col.(13): Nominal absorption corrected 2–10 keV luminosity in units of 10^{44} erg s⁻¹.

Table 6.5. PG QSOs: C06 Model^aBest-fit Values

Galaxy (1)	Obs. Date (2)	Γ (3)	N_H (4)	R_{in} (5)	i (6)	ξ (7)	χ^2_{ν} (d.o.f.) (8)	$F_{0.5-2}$ (9)	F_{2-10} (10)	$L_{0.5-2}$ (11)	L_{2-10} (12)
PG0050+124	2002 Jun 22 ^b	$2.26^{+0.02}_{-0.02}$	$0.04^{+0.002}_{-0.003}$	4.5(f)	30.0(f)	10000(f)	1.16 (633)	$8.37^{+0.34}_{-0.23}$	$8.27^{+0.24}_{-0.13}$	0.98	0.75
	2005 Jul 18 ^b	$2.16^{+0.01}_{-0.01}$...	$1.93^{+0.29}_{-0.22}$	$87.7^{+1.8}_{-0.6}$	2870^{+720}_{-801}	1.05 (810)	$5.16^{+0.61}_{-2.34}$	$4.87^{+0.56}_{-1.91}$	0.55	0.44
PG0838+770	2009 March 2	$1.49^{+0.09}_{-0.09}$...	4.5(f)	30.0(f)	30(f)	1.06 (137)	$0.29^{+0.05}_{-0.03}$	$0.77^{+0.17}_{-0.05}$	0.14	0.35
PG0844+349	2000 Nov 5	$2.32^{+0.04}_{-0.04}$...	$1.72^{+0.62}_{-0.49}$	30.0(f)	999^{+45}_{-387}	1.15 (267)	$6.76^{+2.55}_{-3.32}$	$4.58^{+2.23}_{-0.23}$	0.76	0.45
PG0953+414	2001 Nov 22	$2.30^{+0.02}_{-0.02}$...	$1.90^{+0.87}_{-0.67}$	30.0(f)	48^{+16}_{-12}	1.04 (324)	$3.39^{+1.02}_{-0.71}$	$2.93^{+0.82}_{-0.75}$	5.79	4.79
PG1001+054	2003 May 4	2.0(f)	...	1.24	30.0(f)	297	4.80 (21)
PG1004+130	2003 May 4	$1.40^{+0.05}_{-0.05}$...	4.5(f)	30.0(f)	30^{+299}_{-0}	1.08 (111)	$0.10^{+0.04}_{-0.02}$	$0.33^{+0.34}_{-0.09}$	0.18	0.57
	2005 Jan 5	$1.24^{+0.09}_{-0.10}$	$0.14^{+0.08}_{-0.07}$	4.5(f)	30.0(f)	30(f)	1.10 (96)	$0.09^{+0.01}_{-0.02}$	$0.43^{+0.04}_{-0.06}$	0.19	0.74
PG1116+215	2001 Dec 2	$2.33^{+0.04}_{-0.04}$...	$1.78^{+0.79}_{-0.55}$	30.0(f)	999^{+107}_{-410}	1.16 (256)	$4.43^{+1.91}_{-2.56}$	$2.97^{+1.64}_{-1.35}$	4.03	2.57
	2004 Dec 17 ^b	$2.17^{+0.01}_{-0.01}$...	$4.07^{+0.84}_{-0.58}$	30.0(f)	402^{+32}_{-24}	1.29 (663)	$3.69^{+0.14}_{-0.34}$	$3.09^{+0.10}_{-0.20}$	3.35	2.68
	2004 Dec 19	$2.14^{+0.04}_{-0.05}$...	$1.64^{+0.36}_{-0.41}$	30.0(f)	1433^{+500}_{-829}	1.13 (239)	$4.20^{+1.90}_{-2.59}$	$3.25^{+1.70}_{-1.93}$	3.82	2.81
PG1126-041	2004 Dec 21	1.65	2.33	4.5(f)	30.0(f)	300	4.72 (310)
PG1211+143	2001 Jun 15	1.99	...	1.33	30.0(f)	298	10.24 (494)
	2004 Jun 21	2.02	...	1.52	30.0(f)	300	2.67 (539)
PG1229+204	2005 Jul 9 ^{b,c}	$2.05^{+0.04}_{-0.04}$...	4.5(f)	30.0(f)	391^{+31}_{-59}	1.21 (403)	$3.15^{+0.23}_{-0.39}$	$3.15^{+0.23}_{-0.37}$	0.33	0.30
PG1244+026	2001 Jun 17	$2.53^{+0.04}_{-0.09}$...	$1.38^{+0.29}_{-0.15}$	$87.3^{+1.7}_{-0.6}$	299^{+4}_{-144}	0.86 (238)	$6.61^{+4.04}_{-3.86}$	$2.98^{+0.01}_{-1.23}$	0.39	0.16
PG1307+085	2002 Jun 13 ^b	$1.70^{+0.02}_{-0.02}$...	4.5(f)	30.0(f)	31^{+2}_{-2}	0.98 (145)	$0.81^{+0.13}_{-0.08}$	$1.98^{+0.25}_{-0.23}$	0.55	1.29
PG1309+355	2002 Jun 10	$1.61^{+0.02}_{-0.02}$...	4.5(f)	30.0(f)	$303^{+0.29}_{-0.93}$	1.53 (267)	$0.41^{+0.11}_{-0.07}$	$0.75^{+0.17}_{-0.19}$	0.04	0.72
PG1351+640	2004 Jun 23 ^b	$2.22^{+0.03}_{-0.02}$...	4.5(f)	30.0(f)	30^{+2}_{-0}	1.11 (283)	$0.59^{+0.06}_{-0.03}$	$0.60^{+0.06}_{-0.04}$	0.12	0.12
PG1411+442	2002 Jul 10	2.0(f)	...	4.5(f)	30.0(f)	285	4.02 (143)
PG1426+015	2000 Jul 28	$2.31^{+0.07}_{-0.07}$...	$1.82^{+2.92}_{-0.59}$	30.0(f)	30^{+28}_{-0}	0.99 (145)	$8.01^{+17.77}_{-8.01}$	$6.67^{+14.77}_{-6.67}$	1.63	1.23
PG1435-067	2009 Feb 2	$2.20^{+0.13}_{-0.13}$...	4.5(f)	30.0(f)	67^{+110}_{-37}	1.17 (58)	$2.55^{+0.61}_{-1.16}$	$2.60^{+0.80}_{-1.06}$	1.29	1.09
PG1440+356	2001 Dec 23	$2.76^{+0.04}_{-0.04}$...	$1.74^{+1.47}_{-0.51}$	30.0(f)	30^{+20}_{-0}	1.21 (163)	$5.19^{+10.88}_{-5.19}$	$2.21^{+4.12}_{-2.21}$	0.83	0.34
	2003 Jan 1	$2.63^{+0.02}_{-0.02}$...	$1.65^{+0.55}_{-0.42}$	30.0(f)	30^{+1}_{-0}	1.67 (434)	$5.55^{+2.29}_{-1.66}$	$2.80^{+1.26}_{-0.90}$	0.89	0.43
	2003 Jan 4	$2.74^{+0.02}_{-0.02}$...	$1.63^{+0.75}_{-0.40}$	30.0(f)	30^{+3}_{-0}	1.27 (343)	$4.94^{+5.18}_{-4.94}$	$2.13^{+2.25}_{-2.13}$	0.79	0.33
	2003 Jan 7	2.0(f)	...	1.24	30.0(f)	622	3.93 (340)
PG1448+273	2003 Feb 8	$2.56^{+0.04}_{-0.05}$...	$1.70^{+0.56}_{-0.47}$	30.0(f)	1407^{+73}_{-69}	1.37 (382)	$3.97^{+2.50}_{-1.95}$	$1.81^{+1.13}_{-0.83}$	0.45	0.19
PG1501+106	2001 Jan 13	$2.29^{+0.01}_{-0.01}$...	$1.78^{+0.29}_{-0.55}$	30.0(f)	30^{+1}_{-0}	1.62 (484)	$14.23^{+2.28}_{-0.29}$	$12.62^{+1.73}_{-0.75}$	0.47	0.38
	2001 Jan 13	2.27	...	1.73	30.0(f)	958	2.57 (570)
	2001 Jan 14	$2.26^{+0.01}_{-0.01}$...	$1.78^{+0.25}_{-0.55}$	30.0(f)	30^{+1}_{-0}	1.44 (627)	$16.18^{+1.63}_{-0.01}$	$14.82^{+1.57}_{-0.36}$	0.53	0.45
PG1613+658	2005 Jan 16	1.51	...	1.67	30.0(f)	289	3.96 (825)
	2005 Jul 17 ^b	$1.63^{+0.02}_{-0.04}$...	$1.59^{+0.37}_{-0.36}$	30.0(f)	488^{+88}_{-35}	1.53 (693)	$6.88^{+0.65}_{-0.87}$	$11.46^{+1.10}_{-1.02}$	0.57	0.35
	2001 Apr 13	$1.99^{+0.14}_{-0.14}$	$0.23^{+0.10}_{-0.20}$	$1.24^{+53.63}_{-0.00}$	$50.6^{+6.7}_{-8.2}$	110^{+169}_{-76}	0.97 (132)	$2.49^{+2.45}_{-1.41}$	$4.19^{+5.64}_{-2.10}$	2.22	1.87
PG2130+099	2001 Aug 29	$1.99^{+0.15}_{-0.08}$	$0.01^{+0.13}_{-0.01}$	4.5(f)	$47.3^{+7.0}_{-47.3}$	30^{+1089}_{-0}	1.00 (244)	$4.08^{+1.45}_{-1.19}$	$5.26^{+1.41}_{-0.90}$	1.97	2.31
	2003 May 16	1.59	...	1.56	30.0(f)	300	2.86 (485)
B2 2201+31A	2008 Dec 1	$2.08^{+0.03}_{-0.07}$...	$2.15^{+3.99}_{-0.92}$	30.0(f)	31^{+9}_{-1}	0.97 (213)	$2.51^{+0.77}_{-0.72}$	$4.65^{+1.17}_{-1.88}$	10.08	13.02
PG2214+139	2002 May 12	2.0(f)	...	4.5(f)	30.0(f)	30	8.42 (210)

^aThe accretion disk emissivity index of the kdblur component and the iron abundance of the reflion component are fixed at 3.0 and Solar, respectively. The error estimates of individual parameters, fluxes, and luminosities for poor fits (i.e. $\chi^2_{\nu} > 2.0$) are not calculated.

^bThe spectrum requires additional components for redshifted absorption edges originating from O VII or O VIII. See notes on individual sources for details.

^cThe inclusion of a Gaussian for the emission line at 6.4 keV is required. See notes on individual sources for details.

Note. — (f) denotes a fixed value. Col.(1): Galaxy name. Col.(2): Observation start date. Col.(3): Photon index of the direct and indirect power-law components. Col.(4): Hydrogen column density within the source in units of 10^{22} cm⁻². Col.(5): Inner radius of the accretion disk in gravitational radii with the outer radius fixed at the default value (100 gravitational radii). Col.(6): Inclination of the accretion disk to the line of sight in degrees. Col.(7): Ionization parameter of the gas. Col.(8): Reduced χ^2 of the best-fit model followed by the number of degrees of freedom in (). Col.(9): Observed 0.5–2 keV flux in units of 10^{-12} erg s⁻¹ cm⁻². Col.(10): Observed 2–10 keV flux in units of 10^{-12} erg s⁻¹ cm⁻². Col.(11): Nominal absorption corrected 0.5–2 keV luminosity in units of 10^{44} erg s⁻¹. Col.(12): Nominal absorption corrected 2–10 keV luminosity in units of 10^{44} erg s⁻¹.

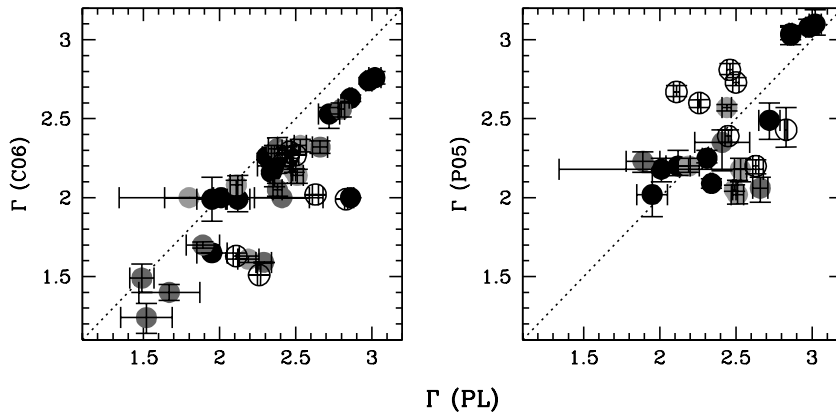


Figure 6.3: Comparison of the spectral index for the power-law models with those from the C06 (left panels) and P05 (right panels) models. The meaning of the symbols is the same as that in Figure 6.2 for the SED classifications. The dotted lines are one-to-one ratios to help guide the eye. The indices based on the power-law and the P05 models tend to be steeper than those from the C06 model. Almost all of the indices are softer than the canonical value of 1.8 for AGNs but are still within the upper end of the range observed in other AGNs. Because the P05 model is not universal for the PG QSOs, the P05 figure is missing data from sources in their sample that do not overlap with our sample.

6.3.2 Results: ULIRGs

As with previous U/LIRG surveys (e.g., Franceschini et al. 2003; Ptak et al. 2003; Teng et al. 2005), a majority of the ULIRGs in this survey were detected, but with relatively few counts and are much fainter than the average PG QSO. We separate into three “brightness” categories: weak, moderate, and strong.

The “weak” sources are those with count rates $\lesssim 0.01$ and 0.05 counts per second when observed by *Chandra* and *XMM-Newton*, respectively. With the time allocated, these sources do not have enough counts for traditional spectral fitting and their spectral properties and fluxes are measured using the HR method (see Appendix A and Teng et al. 2005, for details). The spectral properties derived using the HR method for the weak ULIRGs are listed in Table 6.6.

Table 6.6: Hardness Ratio Estimates of Weak ULIRGs

Galaxy (1)	Date (2)	Extended? (3)	Total (4)	Hard (5)	Soft (6)	HR (7)	Γ (8)	N_H (9)	$F_{0.5-2 \text{ keV}}$ (10)	$F_{2-10 \text{ keV}}$ (11)	$L_{0.5-2 \text{ keV}}$ (12)	$L_{2-10 \text{ keV}}$ (13)
F00091-0738	2008 November 1	No	7	$3^{+3.6}_{-3.6}$	$4^{+3.2}_{-1.9}$	$-0.14^{+0.59}_{-0.33}$	$1.03^{+0.66}_{-1.13}$	$0.44^{+1.47}_{-0.40}$	0.11	0.56	0.04	0.20
F00188-0856	2003 September 4	No	16	$6^{+3.6}_{-2.4}$	$10^{+3.1}_{-3.1}$	$-0.25^{+0.25}_{-0.25}$	$1.1^{+0.6}_{-0.6}$	$0.36^{+0.31}_{-0.31}$	0.42	1.69	0.20	0.71
	2004 December 20	...	164	$52^{+8.8}_{-7.7}$	$112^{+10.7}_{-9.7}$	$-0.37^{+0.09}_{-0.08}$	$1.45^{+0.16}_{-0.17}$	$0.14^{+0.09}_{-0.02}$	0.42	1.12	0.20	0.47
F00456-2904: SW	2009 May 22	Yes	43	$9^{+4.1}_{-2.9}$	$34^{+6.9}_{-5.8}$	$-0.21^{+0.22}_{-0.17}$	$1.15^{+0.31}_{-0.41}$	$0.35^{+0.35}_{-0.21}$	0.74	3.11	0.22	0.94
F01004-2237	2003 August 3	No	20	$6^{+3.6}_{-2.4}$	$14^{+4.8}_{-3.7}$	$-0.40^{+0.32}_{-0.24}$	$1.4^{+0.6}_{-0.6}$	$0.16^{+0.47}_{-0.36}$	0.26	3.64	0.09	1.29
F02021-2103	2009 October 12	No	39	$18^{+4.2}_{-4.2}$	$21^{+4.6}_{-4.6}$	$-0.08^{+0.16}_{-0.16}$	$0.89^{+0.36}_{-0.36}$	$0.55^{+0.23}_{-0.23}$	0.56	3.56	0.19	1.21
IRAS03521+0028	2002 December 25	No	3	$1^{+2.3}_{-1.3}$	$2^{+2.6}_{-1.3}$	$-0.33^{+1.23}_{-0.54}$	$1.5^{+1.9}_{-3.4}$	$0.25^{+5.64}_{-0.00}$	0.14	0.33	0.09	0.20
F04103-2838	2003 April 28	No	30	$12^{+4.6}_{-3.4}$	$18^{+5.3}_{-4.2}$	$-0.20^{+0.24}_{-0.18}$	$1.05^{+0.35}_{-0.45}$	$0.43^{+0.40}_{-0.24}$	0.74	3.37	0.26	1.17
	2006 February 13	No	184	$79^{+9.9}_{-8.9}$	$105^{+11.3}_{-10.2}$	$-0.14^{+0.08}_{-0.07}$	$1.06^{+0.11}_{-0.12}$	$0.38^{+0.10}_{-0.10}$	0.80	4.10	0.28	1.42
	2007 February 8	...	129	$57^{+7.5}_{-8.5}$	$72^{+8.5}_{-8.5}$	$-0.12^{+0.09}_{-0.09}$	$1.05^{+0.14}_{-0.14}$	$0.40^{+0.14}_{-0.14}$	0.79	3.91	0.81	4.02
F05024-1941	2001 October 25	...	240	$50^{+8.1}_{-7.0}$	$190^{+14.9}_{-13.8}$	$-0.70^{+0.08}_{-0.07}$	$2.26^{+0.24}_{-0.23}$...	2.45	1.93	1.42	1.12
F07598+6508: E	2006 January 26	No	9	$7^{+3.8}_{-2.6}$	$2^{+2.6}_{-1.3}$	$0.56^{+0.49}_{-0.26}$	$-0.43^{+0.67}_{-0.00}$	$2.40^{+0.10}_{-0.10}$	0.06	3.01	0.01	0.24
F08572+3915: NW	2008 December 31	Yes	34	$7^{+3.8}_{-2.6}$	$27^{+6.3}_{-5.2}$	$-0.59^{+0.25}_{-0.20}$	$2.00^{+0.70}_{-0.57}$	<0.18	0.58	0.68	0.23	0.27
F09039+0503	2001 May 28	Yes	512	$194^{+13.0}_{-12.8}$	$318^{+15.8}_{-15.8}$	$-0.24^{+0.05}_{-0.05}$	$1.10^{+0.10}_{-0.10}$	$0.36^{+0.09}_{-0.07}$	1.61	7.36	0.06	0.25
UGC 5101	2001 November 12	...	698	$318^{+18.9}_{-17.8}$	$380^{+20.5}_{-19.5}$	$-0.09^{+0.04}_{-0.04}$	$0.97^{+0.07}_{-0.07}$	$0.45^{+0.05}_{-0.07}$	2.67	14.93	0.09	0.51
F10190+1322	2003 January 31	No	16	$6^{+3.6}_{-2.4}$	$10^{+4.3}_{-3.1}$	$-0.25^{+0.36}_{-0.25}$	$1.18^{+0.50}_{-0.68}$	$0.35^{+0.65}_{-0.30}$	0.46	1.70	0.07	0.24
	2003 May 5	...	131	$45^{+7.8}_{-6.7}$	$86^{+10.3}_{-9.3}$	$-0.31^{+0.10}_{-0.09}$	$1.36^{+0.19}_{-0.16}$	$0.19^{+0.10}_{-0.08}$	0.97	2.99	0.14	0.42
F10565+2448	2003 October 23	Yes	346	$91^{+10.6}_{-9.6}$	$255^{+17.0}_{-16.8}$	$-0.47^{+0.06}_{-0.05}$	$1.62^{+0.14}_{-0.13}$	$0.05^{+0.07}_{-0.04}$	2.43	5.00	0.10	0.21
	2003 June 17	...	691	$166^{+13.9}_{-12.9}$	$525^{+23.9}_{-23.9}$	$-0.52^{+0.04}_{-0.04}$	$1.71^{+0.09}_{-0.09}$	<0.56	3.83	6.87	0.16	0.29
F11095-0238	2009 April 9	No	48	$15^{+5.0}_{-3.9}$	$33^{+6.8}_{-5.7}$	$-0.38^{+0.15}_{-0.15}$	$1.53^{+0.34}_{-0.39}$	$0.13^{+0.24}_{-0.00}$	0.77	1.81	0.22	0.52
F12072-0444	2003 February 1	No	16	$2^{+2.6}_{-1.3}$	$14^{+4.8}_{-3.7}$	$-0.75^{+0.43}_{-0.25}$	$2.5^{+4.6}_{-1.1}$...	0.66	0.36	0.28	0.15
F12112+0305	2001 December 30	...	227	$77^{+9.8}_{-8.8}$	$150^{+13.3}_{-12.3}$	$-0.32^{+0.08}_{-0.07}$	$1.33^{+0.12}_{-0.14}$	$0.18^{+0.09}_{-0.06}$	1.34	4.31	0.17	0.55
	2003 April 15	No	51	$14^{+3.7}_{-3.7}$	$37^{+6.1}_{-6.1}$	$-0.45^{+0.15}_{-0.15}$	$1.5^{+0.4}_{-0.4}$	$0.11^{+0.24}_{-0.24}$	1.50	3.26	0.19	0.41
F13218+0552	2004 July 11	...	41	$15^{+5.0}_{-3.9}$	$26^{+6.2}_{-5.1}$	$-0.27^{+0.20}_{-0.16}$	$1.39^{+0.29}_{-0.33}$	$0.17^{+0.21}_{-0.05}$	1.29	3.77	1.54	4.49
F14348-1447	2002 July 29	...	117	$31^{+6.6}_{-5.5}$	$86^{+10.3}_{-9.3}$	$-0.47^{+0.12}_{-0.10}$	$1.77^{+0.22}_{-0.24}$	<0.15	2.73	4.17	0.45	0.74
F14348-1447: NE	2006 March 12	Yes	24	$6^{+3.6}_{-2.4}$	$18^{+5.3}_{-4.2}$	$-0.50^{+0.25}_{-0.17}$	$1.83^{+0.62}_{-0.69}$	<0.32	0.78	1.17	0.13	0.19
F14348-1447: SW	2006 March 12	No	33	$13^{+3.6}_{-3.6}$	$20^{+4.4}_{-4.4}$	$-0.21^{+0.17}_{-0.17}$	$1.20^{+0.52}_{-0.52}$	$0.37^{+0.31}_{-0.21}$	0.77	3.02	0.13	0.50
F15130-1958	2003 June 2	No	38	$7^{+2.6}_{-2.6}$	$31^{+6.6}_{-5.5}$	$-0.63^{+0.24}_{-0.19}$	$2.15^{+0.75}_{-0.65}$	<0.17	1.59	1.33	0.47	0.40
F15250+3608	2002 February 22	...	215	$38^{+6.2}_{-6.2}$	$177^{+14.3}_{-13.3}$	$-0.65^{+0.09}_{-0.08}$	$2.02^{+0.24}_{-0.23}$...	1.76	1.98	0.12	0.14
	2003 August 27	No	37	$5^{+3.4}_{-2.2}$	$32^{+6.7}_{-5.6}$	$-0.73^{+0.25}_{-0.20}$	$2.27^{+1.24}_{-0.77}$	<0.07	1.43	0.96	0.10	0.07
F15462-0450	2009 April 23	No	496	$260^{+16.1}_{-15.4}$	$236^{+15.4}_{-15.4}$	$0.05^{+0.04}_{-0.04}$	$0.78^{+0.09}_{-0.09}$	$0.79^{+0.10}_{-0.09}$	7.02	52.70	1.74	13.05
F16090-0139	2003 February 10	Yes	27	$10^{+4.3}_{-3.1}$	$17^{+4.2}_{-4.1}$	$-0.41^{+0.23}_{-0.20}$	$1.57^{+0.53}_{-0.45}$	$0.15^{+0.33}_{-0.00}$	0.82	2.34	0.38	1.09

Continued on Next Page...

Table 6.6 – Continued

Galaxy (1)	Date (2)	Extended? [†] (3)	Total (4)	Hard (5)	Soft (6)	HR (7)	Γ (8)	NH (9)	$F_{0.5-2 \text{ keV}}$ (10)	$F_{2-10 \text{ keV}}$ (11)	$L_{0.5-2 \text{ keV}}$ (12)	$L_{2-10 \text{ keV}}$ (13)
F17208-0014	2001 October 25	Yes	478	$155^{+13.5}_{-12.4}$	$323^{+19.0}_{-18.0}$	$-0.35^{+0.05}_{-0.05}$	$1.49^{+0.10}_{-0.11}$	$0.21^{+0.06}_{-0.06}$	2.12	5.31	0.09	0.22
	2002 February 19	...	245	$82^{+10.1}_{-9.6}$	$163^{+13.8}_{-13.8}$	$-0.33^{+0.07}_{-0.07}$	$1.55^{+0.13}_{-0.13}$	$0.17^{+0.06}_{-0.06}$	3.18	7.29	0.13	0.31
	2003 May 7	Yes	92	$30^{+5.5}_{-5.5}$	$62^{+8.9}_{-7.9}$	$-0.35^{+0.11}_{-0.11}$	$1.43^{+0.27}_{-0.27}$	$0.23^{+0.18}_{-0.18}$	3.52	8.49	0.15	0.36
F21208-0519: N	2009 March 31	No	14	$3^{+2.9}_{-1.6}$	$11^{+4.4}_{-3.3}$	$-0.57^{+0.43}_{-0.30}$	$2.00^{+1.20}_{-0.95}$	<0.45	0.33	0.38	0.14	0.17
F21208-0519: S	2009 March 31	No	6	$1^{+2.3}_{-0.8}$	$5^{+3.4}_{-2.2}$	$-0.67^{+0.82}_{-0.47}$	$2.3^{+\infty}_{-1.8}$	<1.00	0.17	0.12	0.07	0.05
F21329-2346	2009 June 21	No	27	$9^{+4.1}_{-4.9}$	$18^{+5.3}_{-4.2}$	$-0.33^{+0.26}_{-0.26}$	$1.40^{+0.44}_{-0.44}$	$0.20^{+0.36}_{-0.16}$	0.51	1.47	0.20	0.59
F22491-1808	2001 May 24	...	174	$34^{+6.9}_{-5.8}$	$140^{+12.9}_{-11.8}$	$-0.61^{+0.10}_{-0.09}$	$1.96^{+0.23}_{-0.23}$...	1.16	1.43	0.17	0.21
	2007 July 13	Yes	41	$5^{+3.4}_{-2.2}$	$36^{+7.1}_{-6.0}$	$-0.76^{+0.15}_{-0.10}$	$2.50^{+0.60}_{-0.61}$...	1.13	0.62	0.17	0.09
F23234+0946	2009 Aug 15	Yes	39	$1^{+2.3}_{-0.8}$	$38^{+7.2}_{-6.1}$	$-0.95^{+0.27}_{-0.05}$	$4.0^{+\infty}_{-2.0}$...	1.09	0.08	0.46	0.03

Note. — [†] We arbitrarily consider a source “weak” when its count rate is $\lesssim 0.01$ and 0.05 counts per second when observed with *Chandra* and *XMM-Newton*, respectively. Col.(1): Galaxy name. Coordinate-based names beginning with “F” are sources in the IRAS Faint Source Catalog. Col.(2): Observation start date. Col.(3): Whether the source is extended when compared with the telescope PSF. The symbol “...” denotes *XMM-Newton* observations where radial profiles were not created; all these observations are assumed to be unresolved due to the large PSF of the telescope relative to *Chandra*. Col.(4): Total counts in the 0.5–8.0 keV band. Col.(5): Total counts in the 0.5–2.0 keV band. Col.(6): Total counts in the 2.0–8.0 keV band. Col.(7): The hardness ratio. Col.(8): The estimated Γ based on the hardness ratio and assuming Galactic absorption. Col.(9): The estimated total absorption assuming $\Gamma = 1.7$ in units of 10^{22} cm^{-2} . Col.(10): The estimated observed 0.5–2.0 keV flux assuming the estimated Γ and Galactic absorption in units of $10^{-14} \text{ erg s}^{-1} \text{ cm}^{-2}$. Col.(11): The estimated observed 2.0–10.0 keV flux assuming the estimated Γ and Galactic absorption in units of $10^{-14} \text{ erg s}^{-1} \text{ cm}^{-2}$. Col.(12): Derived 0.5–2 keV luminosity from Col. (10) in units of $10^{42} \text{ erg s}^{-1}$. Col. (13): Derived 2–10 keV luminosity from Col. (11) in units of $10^{42} \text{ erg s}^{-1}$.

The “moderate” sources are those with relatively low count rates, but the exposure times are long enough to obtain low signal-to-noise spectra with more than 100, but less than 1000, counts. For these sources, their spectral properties are modeled using both the HR method and traditional spectral fitting. The traditional spectral fits were performed using the Cash Statistics (c-stat) option in XSPEC on unbinned spectra. The details of the fitting procedure are the same as those in Teng et al. (2008). Only the PL models are applied to these low signal-to-noise spectra. The best-fit properties are presented in Table 6.7.

Finally, the “strong” sources are those with relatively high count rates and relatively high signal-to-noise spectra having more than 1000 counts. The spectral modeling was performed using the χ^2 statistics option in XSPEC as the spectra were binned to at least 15 counts per bin, with the exception of 3C 273, which was binned to at least 100 counts per bin. Again, only the PL models were applied to the moderate signal-to-noise ULIRG spectra. The spectral properties of these sources are also listed in Table 6.7.

Table 6.7: Best-fit Parameters for ULIRG Spectra with > 100 Counts

Galaxy (1)	Date (2)	Model (3)	kT (4)	Γ (5)	$N_{\text{H,source1}}$ (6)	f_{cover1} (7)	$N_{\text{H,source2}}$ (8)	f_{cover2} (9)	E_{line} (10)	σ (11)	EW (12)	Stat (13)	d.o.f (14)	$F_{0.5-2\text{keV}}$ (15)	$F_{2-10\text{keV}}$ (16)	$L_{0.5-2\text{keV}}^{\text{corr}}$ (17)	$L_{2-10\text{keV}}^{\text{corr}}$ (18)
Cash Statistics (unbinned spectra with < 1000 counts)																	
F00188-0856	2004 Dec 20	A	...	$1.76^{+0.33}_{-0.27}$	716.0	1940	$0.42^{+0.16}_{-0.14}$	$0.77^{+0.53}_{-0.33}$	0.20	0.33
F04103-2838*2006	Feb 13	C	$0.10^{+0.03}_{-0.08}$	$1.36^{+0.44}_{-0.44}$	$0.19^{+0.33}_{-0.19}$	$6.43^{+0.26}_{-0.26}$	$0.26^{+0.24}_{-0.26}$	$1.62^{+1.58}_{-1.12}$	848.1	1953	$2.17^{+0.87}_{-0.87}$	$4.56^{+2.04}_{-0.97}$	0.64	1.35
F05024-1941	2007 Feb 8	D	...	$1.94^{+0.56}_{-0.47}$	$32.9^{+243.9}_{-29.5}$	$0.86^{+0.09}_{-0.40}$	646.5	1938	$0.50^{+0.38}_{-0.50}$	$2.28^{+2.10}_{-2.28}$	4.45	5.62
F07598+6508	2001 Oct 25	D	...	$2.95^{+0.27}_{-0.23}$	$52.2^{+44.8}_{-19.6}$	$0.95^{+0.05}_{-0.15}$	655.6	1938	$2.02^{+6.61}_{-2.02}$	$2.50^{+2.98}_{-2.50}$	29.17	8.40
F10190+1322	2003 May 5	A	...	$1.78^{+0.62}_{-0.66}$	661.5	1940	$0.62^{+0.30}_{-0.30}$	$1.11^{+1.20}_{-1.14}$	0.10	0.16
F10565+2448	2003 Oct 23	C	$0.68^{+0.17}_{-0.12}$	$2.14^{+0.66}_{-0.53}$	$0.30^{+0.57}_{-0.21}$	352.3	507	$3.19^{+1.00}_{-2.06}$	$3.72^{+2.07}_{-4.18}$	0.23	0.17
2003 Jun 17	C	$0.68^{+0.14}_{-0.07}$	$1.41^{+0.25}_{-0.23}$	$0.03^{+0.04}_{-0.03}$	1118.9	1937	$3.49^{+0.67}_{-0.73}$	$6.72^{+1.69}_{-2.78}$	0.17	0.37
F12112+0305	2001 Dec 30	B	$0.11^{+0.07}_{-0.03}$	581.9	1940	$0.10^{+0.20}_{-0.10}$	$0.00^{+1.19}_{-0.10}$	0.01	0.00
F14348-1447	2002 Jul 29	A	...	$1.97^{+0.45}_{-0.45}$	521.2	1940	$1.62^{+0.78}_{-0.82}$	$2.48^{+2.30}_{-1.72}$	0.35	0.43
F15250+3608	2002 Feb 22	D ^b	$0.53^{+0.12}_{-0.18}$	$2.56^{+0.85}_{-0.43}$	$132.3^{+202.0}_{-76.8}$	613.2	1936	$1.54^{+3.62}_{-0.48}$	$3.54^{+3.77}_{-3.38}$	11.31	5.65
Apr 20	2000 Jun 24	C	$0.65^{+0.05}_{-0.05}$	$1.82^{+0.19}_{-0.19}$	$125.2^{+25.2}_{-29.5}$	$0.98^{+0.01}_{-0.04}$	1.83(f)	0.0(f)	$0.05^{+0.22}_{-0.05}$	605.4	505	$6.31^{+1.59}_{-3.99}$	$22.83^{+10.32}_{-22.83}$	1.69	2.55
2002 Aug 11	C	$0.65^{+0.12}_{-0.15}$	$1.65^{+0.17}_{-0.15}$	6.70(f)	0.0(f)	$1.21^{+1.40}_{-1.21}$	1213.6	1937	$7.24^{+1.09}_{-1.04}$	$11.58^{+3.50}_{-3.46}$	0.06	0.08
2003 Jan 15	C	$0.63^{+0.08}_{-0.18}$	$1.25^{+0.19}_{-0.23}$	6.70(f)	0.0(f)	$0.81^{+1.26}_{-0.81}$	1019.7	1937	$6.51^{+1.16}_{-1.23}$	$21.18^{+4.57}_{-4.03}$	0.05	0.12
2005 Jan 14	C	$0.62^{+0.12}_{-0.12}$	$1.45^{+0.50}_{-0.54}$	$78.1^{+136.5}_{-63.0}$	$0.88^{+0.10}_{-0.36}$	849.7	1936	$6.16^{+3.46}_{-3.46}$	$15.76^{+15.74}_{-15.74}$	0.22	0.50
2005 Feb 20	C	$0.59^{+0.11}_{-0.24}$	$1.24^{+0.36}_{-0.36}$	585.7	1248	$7.72^{+2.21}_{-2.21}$	$17.03^{+10.89}_{-17.03}$	0.06	0.12
F15462-0450	2009 Apr 23	D	...	$1.55^{+0.38}_{-0.37}$	$1.30^{+0.78}_{-0.66}$	$0.79^{+0.10}_{-0.20}$	479.6	508	$6.19^{+1.42}_{-6.19}$	$41.06^{+9.55}_{-41.28}$	4.92	11.17
F17208-0014	2001 Oct 25	C	$0.74^{+0.14}_{-0.16}$	$2.44^{+1.63}_{-0.88}$	$0.43^{+0.83}_{-0.30}$	1.83(f)	0.0(f)	$0.07^{+0.35}_{-0.07}$	484.5	506	$1.53^{+0.77}_{-1.40}$	$1.59^{+1.73}_{-1.59}$	0.16	0.07
2002 Feb 19	C	$0.67^{+0.13}_{-0.13}$	$0.60^{+0.53}_{-0.53}$	863.1	1938	$1.82^{+0.73}_{-0.73}$	$7.98^{+7.63}_{-7.63}$	0.11	0.35
F22491-1808	2001 May 24	C	$0.71^{+0.17}_{-0.16}$	$2.20^{+0.42}_{-0.38}$	633.4	1938	$1.17^{+0.35}_{-0.33}$	$0.69^{+1.23}_{-0.69}$	0.19	0.10
χ^2 Statistics (spectra binned to at least 15 counts bin ⁻¹)																	
PG0157+001	2000 Jul 29	E	$2.66^{+1.02}_{-0.66}$	$2.54^{+0.09}_{-0.09}$	136.4	148	$101.69^{+8.81}_{-8.09}$	$96.74^{+27.06}_{-42.53}$	83.20	67.00
2003 Aug 23	C	$0.3^{+0.1}_{-0.1}$	$2.1^{+0.1}_{-0.1}$	138.2	130	$150.16^{+14.24}_{-25.06}$	$134.76^{+12.14}_{-21.96}$	99.99	72.99
F05189-2524	2001 Mar 17	D	$0.08^{+0.01}_{-0.01}$	$2.23^{+0.07}_{-0.06}$	$7.83^{+0.53}_{-0.51}$	$0.98^{+0.01}_{-0.00}$	164.1	165	$12.19^{+2.65}_{-2.65}$	$302.82^{+86.72}_{-86.72}$	28.06	23.04
2001 Oct 30	D	$0.20^{+0.04}_{-0.02}$	$1.49^{+0.10}_{-0.22}$	$6.67^{+0.70}_{-0.75}$	$0.96^{+0.30}_{-0.33}$	131.8	118	$9.46^{+2.02}_{-2.63}$	$256.44^{+66.96}_{-109.44}$	6.41	15.85
2002 Jan 30	D	$0.21^{+0.04}_{-0.03}$	$1.41^{+0.14}_{-0.22}$	$5.81^{+0.68}_{-0.88}$	$0.97^{+0.01}_{-0.01}$	114.6	108	$9.49^{+1.67}_{-4.30}$	$336.91^{+46.49}_{-277.88}$	7.23	19.96
UGC 5101	2001 May 28	D	$0.70^{+0.15}_{-0.12}$	$1.27^{+0.58}_{-0.35}$	$0.17^{+0.59}_{-0.15}$	1.00 (f)	$137.65^{+46.41}_{-37.51}$	$0.96^{+0.01}_{-0.10}$	28.6	24	$2.04^{+4.95}_{-0.74}$	$16.78^{+27.97}_{-16.77}$	1.85	6.45
2001 Nov 12	D	$0.85^{+0.39}_{-0.21}$	$1.81^{+0.40}_{-0.40}$	$0.19^{+0.18}_{-0.32}$	1.00 (f)	$78.23^{+33.67}_{-23.67}$	$0.97^{+0.02}_{-0.06}$	d	38.2	45	$2.28^{+1.99}_{-1.99}$	$19.45^{+19.43}_{-19.43}$	3.06	4.75
F11119+3257	2002 Jun 30	D ^b	...	$1.97^{+0.17}_{-0.16}$	$1.71^{+0.20}_{-0.19}$	97.1	106	$26.41^{+7.99}_{-7.99}$	$155.91^{+17.49}_{-39.71}$	143.92	173.32

Continued on Next Page...

Table 6.7 – Continued

Galaxy (1)	Date (2)	Model (3)	kT (4)	Γ (5)	$N_{\text{H,source1}}$ (6)	f_{cover1} (7)	$N_{\text{H,source2}}$ (8)	f_{cover2} (9)	E_{line} (10)	σ (11)	EW (12)	Stat (13)	d.o.f (14)	$F_{0.5-2\text{keV}}$ (15)	$F_{2-10\text{keV}}$ (16)	$L_{0.5-2\text{keV}}^{\text{corr}}$ (17)	$L_{2-10\text{keV}}^{\text{corr}}$ (18)
3C 273	2000 Jun 14	E ^d	$0.94^{+0.05}_{-0.05}$ $2.94^{+0.15}_{-0.15}$	$2.07^{+0.01}_{-0.01}$	1587.5	1571	$4.30^{+0.02}_{-0.02} \times 10^3$	$8.08^{+0.15}_{-0.14} \times 10^3$	3.10×10^3	5.52×10^3
	2000 Jun 17	E	$0.08^{+0.002}_{-0.002}$ $2.65^{+0.11}_{-0.10}$	$1.81^{+0.01}_{-0.01}$	1600.6	1481	$1.00^{+0.01}_{-0.01} \times 10^3$	$7.72^{+0.09}_{-0.10} \times 10^3$	2.89×10^3	5.27×10^3
	2001 Jun 13	E ^d	$0.89^{+0.02}_{-0.01}$ $2.93^{+0.05}_{-0.04}$	$2.28^{+0.01}_{-0.01}$	1922.4	1725	$5.39^{+0.02}_{-0.02} \times 10^3$	$9.66^{+0.10}_{-0.12} \times 10^3$	3.90×10^3	6.60×10^3
	2003 Jul 7	E	$0.79^{+0.04}_{-0.03}$ $2.91^{+0.13}_{-0.11}$	$2.08^{+0.01}_{-0.01}$	1701.2	1589	$6.38^{+0.03}_{-0.02} \times 10^3$	$9.79^{+0.13}_{-0.13} \times 10^3$	4.60×10^3	6.69×10^3
	2004 Jun 30	E	$0.82^{+0.07}_{-0.06}$ $2.84^{+0.18}_{-0.18}$	$2.13^{+0.02}_{-0.02}$	978.7	943	$4.01^{+0.03}_{-0.04} \times 10^3$	$6.80^{+0.21}_{-0.24} \times 10^3$	2.89×10^3	4.65×10^3
	2007 Jan 12	E ^d	$0.93^{+0.18}_{-0.04}$ $3.32^{+0.01}_{-0.01}$	$1.96^{+0.02}_{-0.01}$	1843.7	1708	$4.87^{+0.03}_{-0.03} \times 10^3$	$1.27^{+0.03}_{-0.02} \times 10^4$	3.50×10^3	8.73×10^3
Mrk 231	2000 Oct 19	D	$0.69^{+0.20}_{-0.11}$	$1.78^{+0.46}_{-0.23}$	$3.03^{+1.61}_{-0.99}$	$0.76^{+0.12}_{-0.17}$	$45.10^{+60.34}_{-21.31}$	$0.77^{+0.11}_{-0.15}$	87.7	89	$8.74^{+1.25}_{-7.67}$	$68.17^{+26.19}_{-67.14}$	4.95	7.88
	2001 Jun 7	D	$0.49^{+0.11}_{-0.08}$	$1.44^{+0.07}_{-0.04}$	$8.34^{+1.89}_{-1.71}$	$0.76^{+0.03}_{-0.04}$	$6.43^{+0.14}_{-0.13}$	$0.21^{+0.14}_{-0.10}$	$0.40^{+1.15}_{-0.40}$	139.4	133	$10.22^{+1.09}_{-3.57}$	$63.50^{+19.07}_{-33.93}$	1.39	3.54
	2003 Feb 3	D	$0.80^{+0.09}_{-0.09}$	$1.87^{+0.20}_{-0.20}$	$3.75^{+1.17}_{-1.17}$	$0.80^{+0.10}_{-0.11}$	$30.87^{+35.77}_{-12.45}$	$0.70^{+0.10}_{-0.12}$	82.1	91	$9.08^{+6.86}_{-6.86}$	$61.54^{+61.45}_{-61.45}$	4.25	5.82
	2003 Feb 11	D	$0.65^{+0.05}_{-0.05}$	$1.16^{+0.19}_{-0.16}$	$8.03^{+3.14}_{-2.32}$	$0.75^{+0.12}_{-0.14}$	101.3	95	$8.62^{+1.05}_{-4.38}$	$66.15^{+23.75}_{-66.04}$	1.00	3.56
	2003 Feb 20	B	$0.66^{+0.05}_{-0.05}$	$0.25^{+0.07}_{-0.09}$	76.31	79	$8.15^{+1.07}_{-1.07}$	$80.22^{+10.34}_{-13.06}$	0.35	3.31
Mrk 273	2000 Apr 19	D	$0.86^{+0.11}_{-0.07}$	$1.63^{+0.16}_{-0.18}$	$41.29^{+6.03}_{-5.37}$	$6.31^{+0.03}_{-0.03}$	$0.00^{+0.06}_{-0.00}$	$0.23^{+0.62}_{-0.00}$	67.3	85	$7.08^{+0.76}_{-0.77}$	$82.12^{+18.78}_{-50.32}$	5.28	10.73
	2002 May 7	D	$0.70^{+0.07}_{-0.06}$	$1.86^{+0.13}_{-0.13}$	$59.32^{+13.54}_{-13.54}$	$6.49^{+0.19}_{-0.16}$	$0.25^{+0.20}_{-0.11}$	$0.67^{+4.44}_{-0.67}$	115.4	89	$9.07^{+1.02}_{-0.77}$	$37.20^{+29.53}_{-29.53}$	4.29	6.44
F13451+1232	2000 Feb 24	D	...	$1.55^{+0.12}_{-0.12}$	$3.95^{+0.53}_{-0.49}$	$0.97^{+0.01}_{-0.01}$	53.4	60	$4.06^{+0.99}_{-3.25}$	$102.40^{+17.80}_{-72.00}$	21.56	49.05
NGC 6240	2000 Sep 22	D	$0.76^{+0.04}_{-0.12}$	$2.14^{+0.13}_{-0.12}$	$0.19^{+0.03}_{-0.03}$	$1.00^{(f)}$	$160.66^{+14.32}_{-12.71}$	$0.98^{+0.01}_{-0.01}$	$1.83^{(f)}$	$0.00^{(f)}$	$0.06^{+0.05}_{-0.04}$	365.8	333	$62.64^{+11.70}_{-5.98}$	$188.90^{+11.70}_{-36.30}$	60.70	59.78
	2001 Jul 29	D	$0.86^{+0.03}_{-0.03}$	$2.03^{+0.15}_{-0.13}$	$0.25^{+0.04}_{-0.04}$	$1.00^{(f)}$	$66.49^{+33.78}_{-29.56}$	$0.81^{+0.06}_{-0.06}$	$1.83^{(f)}$	$0.00^{(f)}$	$0.04^{+0.24}_{-0.04}$	250.9	203	$54.98^{+3.55}_{-36.31}$	$165.81^{+21.39}_{-147.68}$	5.69	6.95
	2002 Mar 12	D	$0.62^{+0.06}_{-0.04}$	$2.04^{+0.18}_{-0.17}$	$0.20^{+0.05}_{-0.05}$	$1.00^{(f)}$	$142.69^{+19.21}_{-17.13}$	$0.98^{+0.01}_{-0.01}$	$1.06^{(f)}$	$0.00^{(f)}$	$0.05^{+0.05}_{-0.02}$	219.5	171	$56.02^{+4.20}_{-8.18}$	$199.13^{+15.17}_{-46.33}$	41.04	46.02

Continued on Next Page...

Table 6.7 – Continued

Galaxy (1)	Date (2)	Model (3)	kT (4)	Γ (5)	$N_{\text{H,source1}}$ (6)	f_{cover1} (7)	$N_{\text{H,source2}}$ (8)	f_{cover2} (9)	E_{line} (10)	σ (11)	EW (12)	Stat (13)	d.o.f (14)	$F_{0.5-2\text{keV}}$ (15)	$F_{2-10\text{keV}}$ (16)	$L_{0.5-2\text{keV}}^{\text{corr}}$ (17)	$L_{2-10\text{keV}}^{\text{corr}}$ (18)
	2003 Mar 14	D	$0.82^{+0.07}_{-0.06}$	$2.00^{+0.25}_{-0.21}$	$0.21^{+0.07}_{-0.06}$	1.00(f)	$109.25^{+34.12}_{-22.24}$	$0.94^{+0.03}_{-0.05}$	1.83(f) 6.40(f)	0.00(f) 0.00(f)	$0.08^{+0.42}_{-0.08}$ $0.22^{+0.39}_{-0.39}$	102.6	102	$55.38^{+27.34}_{-35.85}$	$190.13^{+64.47}_{-167.14}$	17.70	21.50
	2003 Aug 13	D	$0.82^{+0.05}_{-0.05}$	$1.82^{+0.16}_{-0.15}$	$0.14^{+0.04}_{-0.03}$	1.00(f)	$146.43^{+21.24}_{-18.38}$	$0.96^{+0.02}_{-0.03}$	7.01(f) 1.83(f) 6.40(f)	0.00(f) 0.00(f) 0.00(f)	$0.09^{+0.96}_{-0.09}$ $0.04^{+0.05}_{-0.04}$ $0.25^{+0.21}_{-0.25}$	264.1	237	$56.34^{+120.16}_{-6.58}$	$205.86^{+269.44}_{-25.26}$	23.07	37.10
	2003 Aug 21	D	$0.82^{+0.08}_{-0.09}$	$1.90^{+0.22}_{-0.20}$	$0.16^{+0.05}_{-0.05}$	1.00(f)	$201.58^{+29.52}_{-25.81}$	$0.99^{+0.01}_{-0.02}$	6.67(f) 7.01(f) 1.83(f) 6.40(f)	0.00(f) 0.00(f) 0.00(f) 0.00(f)	$0.14^{+0.24}_{-0.14}$ $0.09^{+0.24}_{-0.03}$ $0.03^{+0.19}_{-0.03}$ $0.52^{+0.38}_{-0.32}$	120.8	111	$56.91^{+5.30}_{-41.70}$	$211.91^{+25.69}_{-96.51}$	67.26	97.67
	2003 Aug 29	D	$0.85^{+0.15}_{-0.09}$	$1.41^{+0.32}_{-0.31}$	$0.07^{+0.09}_{-0.07}$	1.00(f)	$155.52^{+48.72}_{-27.96}$	$0.96^{+0.01}_{-0.05}$	6.67(f) 1.38(f) 1.83(f) 6.40(f)	0.00(f) 0.00(f) 0.00(f) 0.00(f)	$0.07^{+0.07}_{-0.07}$ $0.08^{+0.63}_{-0.08}$ $0.12^{+1.14}_{-0.12}$ $0.20^{+1367.42}_{-0.20}$	36.1	51	$58.15^{+108.45}_{-36.92}$	$227.68^{+342.72}_{-226.37}$	13.50	37.89

Note. — Col.(1): Galaxy name. Coordinate-based names beginning with "F" are sources in the IRAS Faint Source Catalog. Col.(2): Observation start date. Col.(3): Best-fit continuum model, all modified by Galactic absorption: A = single power law, B = MEKAL only, C = MEKAL plus power law, D = scattering model or partial covering model, E = blackbody plus power law. Col.(4): MEKAL temperature, if applicable, in units of keV. Col.(5): Spectral index of the power law (or reflection) model. Col. (6)–(9): Absorption within the source and corresponding covering fraction for the covering fraction absorber model. The absorption values are in units of 10^{22} cm^{-2} . Col.(10): Rest energy of the emission line(s) in units of keV. Col. (11): Line width(s) of the emission line(s) in units of keV. Col. (12): Equivalent width(s) of the emission line(s) in units of keV. Col. (13)–(14): Fitting statistics and degrees of freedom, respectively. Col. (15)–(16): Observed flux after background subtraction in units of $10^{-14} \text{ erg s}^{-1} \text{ cm}^{-2}$. Col. (17)–(18): Nominal absorption corrected luminosities in units of $10^{42} \text{ erg s}^{-1}$.

^aValues taken from Teng et al. (2008). The energy bands in that paper are 0.2–2 keV and 2–10 keV.

^bThe ratio of the normalization parameters between the scattered component to the direct component is 249 for F1119+3257, 24 for F15250+3508, 62 for F1119+3257, 24 for the 2000 observation of Mrk 273, and 18 for the 2002 observation of Mrk 273.

^cThe addition of an emission line at 6.4 keV does improve the fit, but not statistically significant.

^dThe addition of a red-shifted oxygen edge improves the fit significantly. See notes on individual sources for details.

^eThe addition of this absorption component does improve the fit, but not significantly.

In general, the 2–10 keV band is less likely to be affected by obscuration and this is where AGN emission dominates. Figure 6.4 is a comparison of the 2–10 keV and infrared luminosities of the U/LIRGs and PG QSOs. The U/LIRGs include the 26 RBGS objects from the *Chandra* archive for a total of 66 objects. For AGN-dominated objects like the PG QSOs, the 2–10 keV luminosity is consistently about 3% of the infrared luminosity. The 2–10 keV luminosity of the U/LIRGs, however, vary between 0.0001 to 3% of the infrared luminosity. Comparison with the effective optical depth found by Veilleux et al. (2009b) suggest AGN-dominated objects also have the smallest τ_{eff} . A majority of the ULIRGs fall between $\log(L_{2-10keV}/L_{IR})$ of $(-4.5, -1.5)$. The importance of nuclear activity relative to that of the starburst increases with the infrared luminosity of the ULIRG.

We also compared the 2–10 keV luminosity with the bolometric luminosity of the U/LIRGs and PG QSOs; the 2–10 keV to bolometric luminosity ratio is our proxy for AGN dominance. The bolometric luminosity is defined as $L_{bol} = 1.15L_{IR}$ for the U/LIRGs and $L_{bol} = 7L_{5100\text{\AA}} + L_{IR}$ for the PG QSOs. The left panel in Figure 6.5 plots this ratio against the total bolometric luminosity of our sample. For the U/LIRGs there is simply a small shift in both axes from Figure 6.4. Again, we observed the three orders of magnitude spread in the 2–10 keV to bolometric luminosity for the U/LIRGs. The right-hand panel is the same ratio plotted against only the AGN-contributions to the bolometric luminosity as derived by Veilleux et al. (2009b). Again, the less obscured objects are more likely to be AGN-dominated.

Applying the photometric black hole mass estimates from Veilleux et al. (2009a) to our X-ray observations, we derived the 2–10 keV-to-Eddington luminosity ratio, our proxy for the Eddington ratio. Figure 6.6 compares the Eddington ratio derived from the X-ray methods with that from the mid-infrared methods presented in Veilleux et al. (2009b). Since the X-ray values are only the 2–10 keV luminosity and

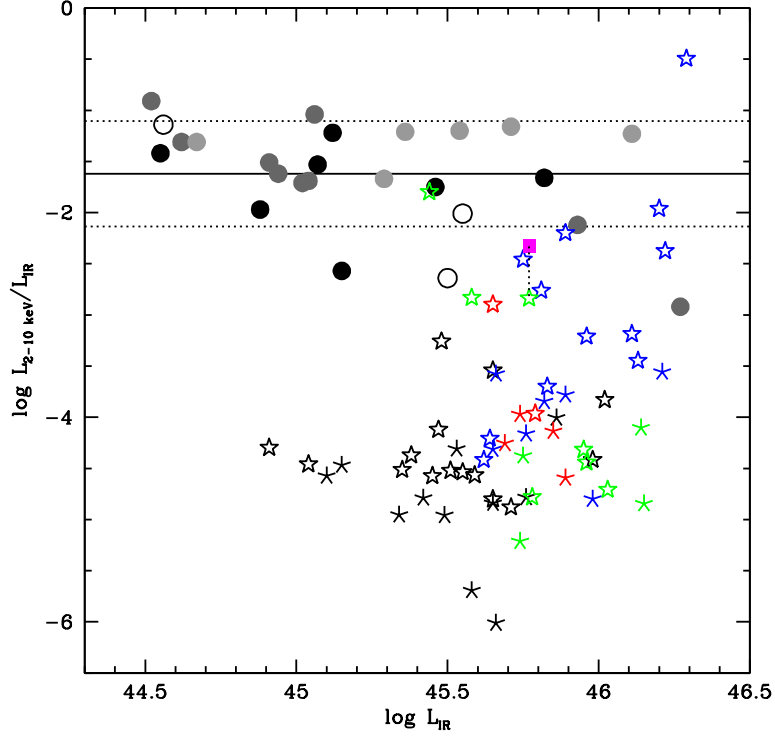


Figure 6.4: Comparison of 2–10 keV luminosity and the IR luminosity for the PG QSOs and the U/LIRGs. The x-axis is the IR luminosity and the y-axis is the absorption-corrected 2–10 keV luminosity divided by the IR luminosity. The symbols for the PG QSOs are the same as those in Figure 6.2 for the SED and the values are from the global modeling in § 6.4.2. For the U/LIRGs, the open stars represent the values derived from spectral fitting and the skeletal stars represent the values derived from the HR method. The colors of the stars symbolize the effective optical depth (τ_{eff}) taken from Veilleux et al. (2009b) where red represents objects with the highest τ_{eff} , green intermediate τ_{eff} , and blue the lowest τ_{eff} . The black stars are values from the RBGS archive sample (median $L_{IR} = 10^{11.98} L_{\odot}$), where τ_{eff} is unavailable. The magenta square is the absorption-corrected value for Mrk 273 derived from *Suzaku* data (Teng et al. 2009) linked with the value derived from only the *Chandra/XMM-Newton* data to demonstrate the affects of poor absorption correction. The solid line is the average $\log(L_{2-10keV}/L_{IR})$ for the PG QSOs (~ -1.6) and the dotted lines represent $1-\sigma$. The \log hard X-ray-to-IR luminosity ratio of a majority of the U/LIRGs appear to be ~ -4.5 , approximately where the archive sample is clustered. The ratios between the quasars and the U/LIRGs span about three orders of magnitude.

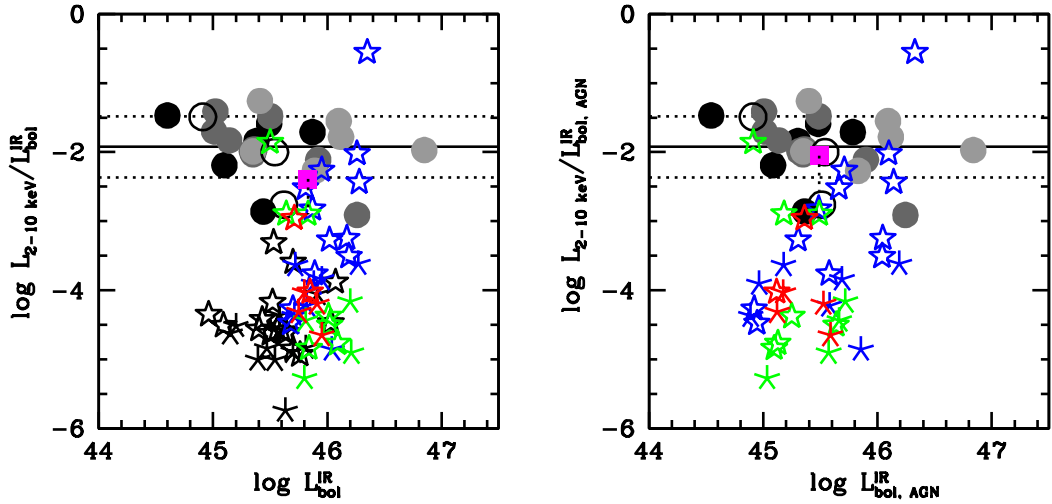


Figure 6.5: Comparison of the bolometric luminosity with the absorption-corrected 2–10 keV luminosity. The symbols for the PG QSOs are the same as those in Figure 6.2 and the symbols for the U/LIRGs are the same as those in Figure 6.4. In the left figure, the X-axis is the total bolometric luminosity. There is a clear trend between the 2–10 keV luminosity and the bolometric luminosity for the PG QSOs: the brighter the AGN is in the X-ray, the more it contributes to the total bolometric luminosity. The solid line is the average 2–10 keV to bolometric luminosity ratio for the PG QSOs and the dotted lines represent $1\text{-}\sigma$ from that average. The total 0.5–10 keV luminosity of the PG QSOs are $\sim 0.5 - 11\%$ of the bolometric luminosity. Nearly all of the U/LIRG values fall off this trend. The right panel plots the same 2–10 keV luminosity as a function of the AGN contribution to the bolometric luminosity ($L_{\text{bol,AGN}} = f_{\text{AGN}} L_{\text{bol}}$) from *Spitzer* Veilleux et al. (2009b). The lines are the same as those in the left panel. The PG QSO values still follow the same trend as well as some of the U/LIRGs.

not the bolometric luminosity of the AGN, there is a correction factor of about 1.5–2 for the X-ray values. The two methods are linearly correlated for the PG QSOs, but a discrepancy between the X-ray and mid-infrared AGN diagnostic methods is observed for the U/LIRGs. The cause of this discrepancy is explored further in § 6.5.1.

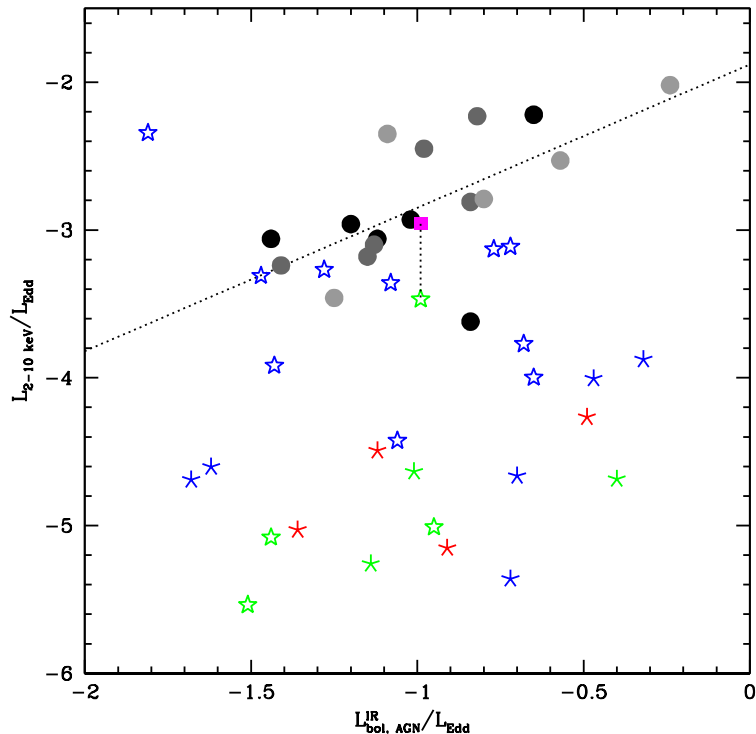


Figure 6.6: We compare the X-ray and infrared-determined log Eddington ratios for the U/LIRGs (same symbols as Figure 6.4) and the PG QSOs (same symbols as Figure 6.2). The black hole masses are taken from Veilleux et al. (2009a). The PG QSO values determined by the two methods are linearly related. The dotted line represents this linear relationship where $\log ER_X = (0.97 \pm 0.52) \log ER_{IR} - (1.88 \pm 0.51)$ with $R^2 = 0.43$. This correlation is significant at the 99.97% confidence level. Unlike the quasars, a majority of the (U)LIRG values are not correlated. Again, this may be due to the difference in estimating the AGN contributions by the two methods.

6.4 PG QSOs: the Origin of the Soft Excess

PG QSOs have been very well studied in the X-ray and at other wavelengths. However, many X-ray studies on PG QSOs in the literature have focused on only a handful of objects. Most studies have found that the X-ray spectra of PG QSOs tend to be more or less featureless, with sometimes small emission features near the iron K complex arising from neutral or ionized iron. Often, these iron emission

lines have relatively small equivalent widths (~ 100 eV) and are generally narrow. The continua of the X-ray spectra can be fit by a power law with $\Gamma \sim 1.8$ for the AGN, but the X-ray spectra of some PG QSOs (as well as some Seyfert galaxies) also contain what is termed the “soft excess” where there is emission in excess of the power-law at below ~ 2 keV. Bianchi et al. (2009) uses a model-independent method of comparing the 0.5–2 keV and 2–10 keV flux ratios as an independent measure of the soft excess strength. The authors confirm that the soft excess is a common feature in active galaxies.

The current leading models for the soft excess are:

- Porquet et al. (2004) at first thought that the soft excess originates from the inner accretion disc. The advantage of this model is that the smooth rise of the soft excess seems to connect with the UV accretion disc spectrum. However, the inferred blackbody temperatures from the modeling are too hot to come directly from emission of a thin accretion disc. Thus, they prefer their alternate model, the Compton up-scattering of the extreme ultraviolet photons from the accretion disc to form the soft excess.
- Instead of a universal model for the soft excess, Piconcelli et al. (2005) found in their survey of 42 PG QSOs that the X-ray continua of these quasars are well fit by a combination of four different models. The four models are blackbody, multicolor blackbody, bremsstrahlung, and power law.
- Crummy et al. (2006) presented a blurred reflection model as a universal model for the PG QSO spectra. Blurred reflection, caused by the relativistic motion in the accretion disc, is invoked due to the lack of broad iron lines observed in these objects. While this model fits the spectra well, it also requires extreme values for some of the model parameters.

- Sobolewska & Done (2007) favor a complex absorption model based on their spectral modeling of two AGNs (PG 1211+143 and 1H0707–495) with large observed soft excesses.

6.4.1 Modeling PG QSOs as a Class

The soft excess is an ubiquitous feature in AGN spectra. If this attribute is common to all the objects in this class and if there is an universal model, then each observed spectrum should be a small variation of the global model. Each of the models tested describes individual objects almost equally well. If a universal model exists, then modeling all the objects with a single universal model may help select a preferred model. For this multi-source fitting, we chose to use only *XMM-Newton* EPIC-pn observations to minimize cross-calibration issues. This includes 22 objects except PG 0804+761 (undetected), PG 1244+026 (few counts above ~ 5 keV), PG 1613+658, and PG1626+554 (no pn data). Average spectra for objects with multiple observations are created using the FTOOLS task MATHPHA and used for the multi-source fitting.

For most of the models we tested using this global fitting method, we treated the continuum model as having two components and all of these components are modified by Galactic absorption. Since most of the PG QSO spectra do not show strong iron lines (see Figure 6.1), we only applied the global model to the continuum. The first of these components is AGN emission which includes the standard power law for an AGN spectrum and when applicable, a reflected or scattered portion. The second is the soft-excess component. This can be a MEKAL model (for starburst), blackbody, or a Comptonization model. For all the objects, we linked the photon index, soft-excess temperature, and the normalizations for each component to be the same for all objects. However, we allow model parameters that describe char-

acteristics that may vary in individual sources, such as disc inclination, ionization parameter, and intrinsic source absorption, to be free. Since each source also has different brightnesses, a multiplicative factor is included for each of the components to adjust for the differences in intensity amongst the sources as well as the relative contributions between the different model components. Simply, the global model can be described in equation form: $\text{Model}_i = \text{Abs}_{\text{Gal},i} \times \text{Abs}_{\text{int},i} \times [\text{X}_i \times \text{AGN} + \text{Y}_i \times \text{SE}]$, where X_i is the multiplicative factor for the AGN component that varies depending on the source i and Y_i is a similar factor for the soft excess component.

6.4.2 The Favored Model

We first tested a simple power law model for the global QSO fit. It is a very poor fit to the data, giving a reduced $\chi^2 \sim 8.0$. We then tested the absorption-based models for the origin of the soft excess. A scattering model, see Teng et al. (2009) for a description, provided a better fit ($\chi^2_{\nu} \sim 3.0$) but the model offered a poor description of the data at higher energies. A single partial covering absorption model also gave a very poor fit ($\chi^2_{\nu} \sim 3.4$). An additional partial covering absorber provided a much better fit ($\chi^2_{\nu} \sim 1.8$); however, the model severely underestimated the spectral flux above ~ 5 keV. In this model, the nominal photon index of the spectrum was ~ 2.8 , much steeper than the generally observed range for AGNs (1.6–2.2). By adding a MEKAL component for the soft excess to the double-partial-covering model, we derived an even better model to the data ($\chi^2_{\nu} \sim 1.5$), but the model still underestimated the flux above ~ 5 keV as shown in Figure 6.7.

We then considered the Comptonization model of Porquet et al. (2004) for the soft excess. This model gives $\chi^2_{\nu} \sim 2.1$. While this is a much better fit to the data than the simple power law models large residuals remain, providing a poor fit both at low ($\lesssim 0.5$ keV) and at high ($\gtrsim 4$ keV) energies.

Finally, we tested the reflection-based models for the soft excess. The reflection-based models are XSPEC models PEXRAV (a neutral reflector), PEXRIV (an ionized reflector), and a blurred reflection model (the C06 model), the same modified version discussed in § 6.3.1. REFLION is a more complex model than PEXRIV. PEXRIV considers only bound-free transitions in the reflected spectrum; REFLION also includes the ionization states and transitions for O and Fe ions. We first modeled each reflection-based model without a soft-excess component. These attempts produced very poor fits to the data ($\chi^2_{\nu} \gtrsim 4.0$). We then added a redshifted blackbody component to each of the reflection models for the soft excess. The reduced χ^2 value for the PEXRAV model is ~ 1.3 , a great improvement over the previous models. This model describes well the spectra above ~ 1 keV, but is a poor model below this energy (see Figure 6.7). The PEXRIV plus blackbody model appeared to be a good fit to the data ($\chi^2_{\nu} \sim 1.2$; Figure 6.7), except for an absorption feature around 0.7 keV (the atomic transition of N VII or O VII). Lastly, for the C06 model, we again fixed the disc emissivity index at 3.0 and the abundance at solar. The inner and outer accretion disc radii were both fixed at the default values, 4.5 and 100 gravitational radii, respectively. Surprisingly, the more complex model for an ionized reflector gives a worse fit than the simpler PEXRIV model ($\chi^2_{\nu} \sim 1.4$; Figure 6.7). In particular, this model is a very poor description of the spectra above ~ 4 keV.

Based on the statistics and the residuals of the models, the multi-source fitting method indicates that a reflection-based model is favored as the universal model. However, there is still a requirement for a blackbody component in order to model the soft excess. One reason why the PEXRIV model offers a better fit than the REFLION model may be because many of the spectra do not require an ionized reflection component. Only 10/22 objects (45%) require the ionization parameter to

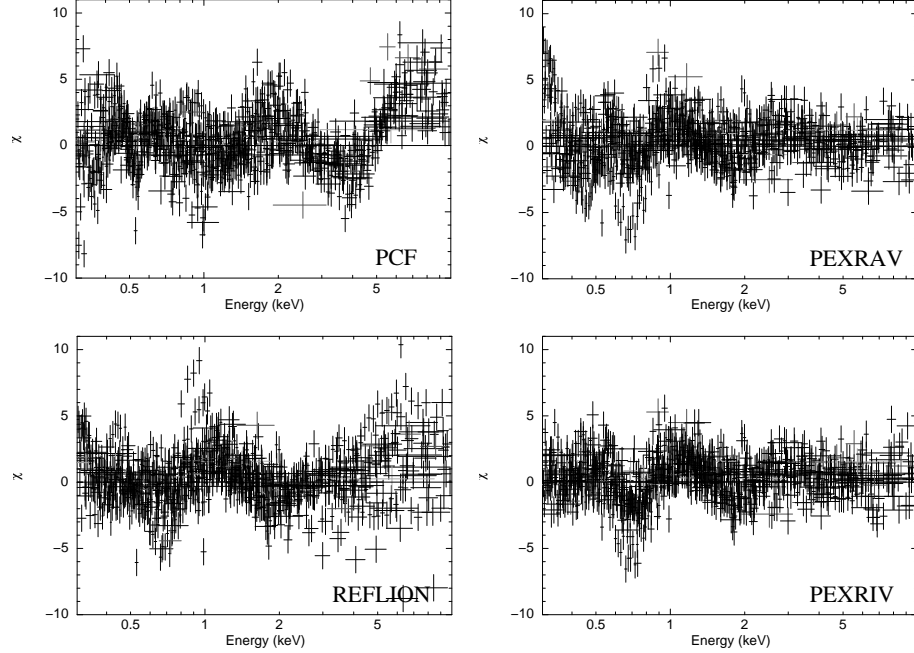


Figure 6.7: Comparison of the goodness of fit between the different models for the PG QSOs as a class. The x-axis is energy in the observer’s frame and the y-axis is the residuals in terms of sigmas. Four different models are compared for the *continuum* of the X-ray spectrum. The residuals are binned to at least 10-sigmas for display only. Clockwise from the top left, the models presented are (1) MEKAL plus two partial covering absorbers ($\chi^2_\nu \sim 1.47$), (2) a redshifted blackbody plus a neutral reflection model (PEXRAV; $\chi^2_\nu \sim 1.29$), (3) a redshifted blackbody plus an ionized reflection model (PEXRIV; $\chi^2_\nu \sim 1.18$), and (4) a redshifted blackbody plus a more complex ionized reflection model (REFLION; $\chi^2_\nu \sim 1.42$). All of the above models include absorption by the Galaxy and an underlying power-law model for the AGN component. The PEXRIV model is the preferred model based on the fitting statistics and the residuals.

be above 30 erg cm s^{-1} , the minimum value for the REFLION model. The PEXRIV model allows a full range of ionization parameters, starting with a minimum value of 0 erg cm s^{-1} . It should be noted that the PEXRIV model requires a steeper photon index (2.37) than the REFLION model (2.02). While a photon index of ~ 2.4 is steeper than the generally accepted value, it is the median value seen in PG QSOs (see Figure 6.3). When a redshifted absorption edge centered at around $\sim 0.68 \text{ keV}$ was added to PEXRIV model described above, the statistics greatly improved ($\chi^2_\nu \sim 1.1$; Figure 6.8). For the three objects with EPIC-MOS data that

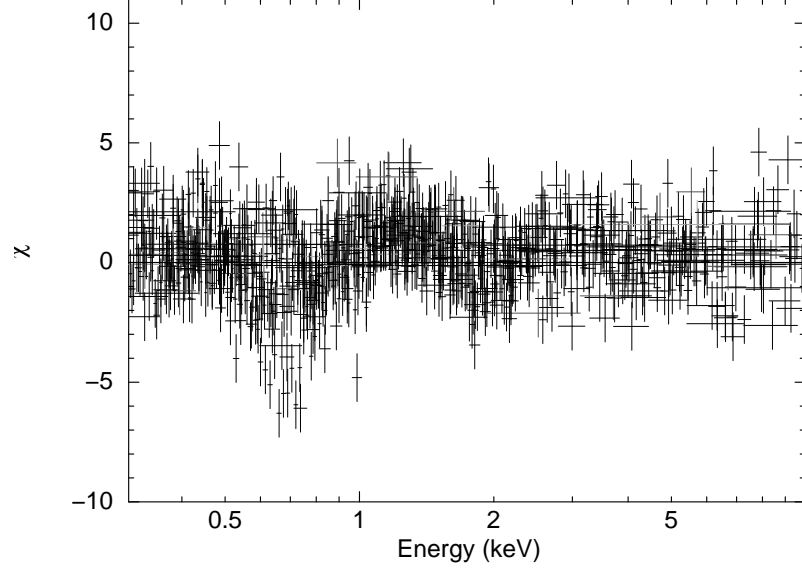


Figure 6.8: The rebinned residuals of the blackbody plus PEXRIV model with a redshifted absorption edge at $0.68^{+0.006}_{-0.003}$ keV with $\tau \sim 0.31^{+0.02}_{-0.03}$ ($\chi^2_{\nu} \sim 1.13$). The absorption feature is consistent with the atomic transitions of O VII or O VIII. The addition of the absorption edge component improves the fit significantly, with $\Delta\chi^2 \sim 338$ for a change in two degrees of freedom. The large absorption feature still seen near 0.7 keV in the residuals is due to one source, PG 0050+124.

were not included in the multi-source fitting, we applied the best-fit global model with the AGN and soft excess components fixed to individually model the MOS spectra. The best global fit implies that $\Gamma = 2.37 \pm 0.02$ and $kT = 0.127 \pm 0.001$ keV with an absorption edge at 0.68 ± 0.01 keV and optical depth of $0.31^{+0.02}_{-0.03}$. The nominal energy of the absorption edge is consistent with the atomic transitions of O VII and O VIII. The reflected portion of the AGN contribution is $\sim 6\text{--}37\%$ of the power law luminosity for all 25 objects. Some of the other parameters derived from the PEXRIV model for the PG QSOs are listed in Table 6.8.

Table 6.8. PG QSOs: Derived Parameters from the Global PEXRIV Model

Galaxy (1)	N_H (2)	ξ (3)	Soft-Excess		Power Law				Refelction			
			$F_{0.5-2}$ (4)	$L_{0.5-2}$ (5)	$F_{0.5-2}$ (6)	F_{2-10} (7)	$L_{0.5-2}$ (8)	L_{2-10} (9)	$F_{0.5-2}$ (10)	F_{2-10} (11)	$L_{0.5-2}$ (12)	L_{2-10} (13)
PG0050+124	0.02	0.0	0.81	0.07	7.92	5.74	0.71	0.51	0.05	1.05	0.005	0.09
PG0838+770	0.78	103.9	16.32	7.39	0.74	0.50	0.34	0.22	0.01	0.11	0.006	0.05
PG0844+349	0.00	0.0	128.93	12.75	6.15	4.12	0.61	0.41	0.07	1.29	0.007	0.13
PG0953+414	0.00	0.0	25.62	41.88	3.25	2.17	5.32	3.55	0.05	0.86	0.08	1.41
PG1001+054	3.03	155.2	1.39	0.99	0.08	0.05	0.06	0.04	0.01	0.07	0.006	0.05
PG1004+130	0.56	12.0	1.62	2.81	0.19	0.13	0.33	0.22	0.01	0.17	0.02	0.30
PG1116+215	0.00	0.1	43.18	37.38	3.80	2.54	3.29	2.20	0.05	0.87	0.04	0.75
PG1126-041	4.16	1.3	3.71	0.32	1.40	0.94	0.12	0.08	0.03	0.49	0.002	0.04
PG1211+143	0.27	137.9	179.59	29.19	3.21	2.15	0.52	0.35	0.15	1.08	0.02	0.18
PG1229+204	0.00	0.0	1.81	1.73	3.20	2.14	0.31	0.21	0.06	1.11	0.005	0.11
PG1244+026	0.00	0.0	156.25	8.48	3.68	2.46	0.20	0.13	0.02	0.35	0.001	0.02
PG1307+085	0.60	0.0	30.92	20.21	1.46	0.98	0.96	0.64	0.05	0.93	0.03	0.61
PG1309+355	0.52	78.3	12.54	11.94	0.65	0.44	0.62	0.42	0.03	0.28	0.03	0.27
PG1351+640	0.00	88.3	3.87	0.75	0.56	0.38	0.11	0.07	0.03	0.26	0.005	0.05
PG1411+442	610.01	1.8	4.29	0.87	1.83	1.23	0.37	0.25	0.03	0.44	0.005	0.09
PG1426+015	0.03	413.5	40.22	7.40	8.58	5.74	1.58	1.06	0.35	1.34	0.06	0.25
PG1435-067	0.00	171.2	9.81	4.09	2.82	1.89	1.17	0.79	0.11	0.76	0.05	0.32
PG1440+356	0.00	552.6	107.79	16.61	3.39	2.27	0.52	0.35	0.17	0.53	0.03	0.08
PG1448+273	0.00	0.0	129.83	13.28	2.97	1.99	0.30	0.20	0.02	0.30	0.002	0.03
PG1501+106	0.27	130.5	483.37	14.54	13.10	8.76	0.39	0.26	0.63	4.65	0.02	0.14
PG1613+658	0.29	4.7	103.88	45.59	4.98	3.01	2.18	1.46	0.11	1.79	0.05	0.79
PG1626+554	0.29	0.0	80.88	37.89	4.49	3.01	2.10	1.41	0.03	0.58	0.01	0.27
PG2130+099	0.56	103.5	99.01	9.47	3.28	2.20	0.31	0.21	0.17	1.42	0.02	0.14
B2 2201+31A	0.25	0.2	90.30	250.63	4.07	2.72	11.30	7.55	0.12	1.96	0.33	5.44
PG2214+139	3.80	9.2	10.07	1.06	3.25	2.17	0.34	0.23	0.10	1.59	0.01	0.17

Note. — Col.(1): Galaxy name. Col.(2): Intrinsic column density in units of 10^{22} cm^{-2} . Col.(3): Ionization parameter from the PEXRIV component in erg cm s^{-1} . Col.(4): Absorption-corrected 0.5–2 keV flux for the soft-excess component (blackbody) in units of 10^{-14} $\text{erg s}^{-1} \text{cm}^{-2}$. The 2–10 keV flux of this component is $\sim 10^3$ smaller, and so is insignificant. Col.(5): 0.5–2 keV luminosity in units of 10^{42} erg s^{-1} for the soft-excess. Col.(6)–(7): Absorption-corrected 0.5–2 keV and 2–10 keV flux for the power law component in units of 10^{-12} $\text{erg s}^{-1} \text{cm}^{-2}$. Col.(8)–(9): Absorption corrected 0.5–2 keV and 2–10 keV luminosity of the power law component in units of 10^{44} erg s^{-1} . Col.(10)–(11): Absorption-corrected 0.5–2 keV and 2–10 keV flux in units of 10^{-12} $\text{erg s}^{-1} \text{cm}^{-2}$ for the reflected component. Col.(12)–(13): Absorption-corrected 0.5–2 keV and 2–10 keV luminosity of the reflected component in units of 10^{44} erg s^{-1} .

Disc Inclination

Crummy et al. (2006) suggested that the *XMM-Newton* data are sufficient to robustly measure the inclination angle of the accretion disc. As noted previously, their model requires extreme values for some of the parameters. When these parameters are fixed at more commonly accepted values (*i.e.* emissivity index = 3.0, $Z = Z_\odot$), the fit often requires the disc inclination angle to be fixed at the default value of 30 degrees in order for the fits to converge when the spectra are modeled individ-

ually (Table 6.5). Figure 6.9 shows distributions of the inclination angles from the global PEXRIV and the modified C06 models from the 22 EPIC-pn spectra; neither of these matches a random distribution. The distribution determined by Crummy et al. (2006) also does not reproduce the random distribution. The inclination measurements are highly dependent on the model, which may indicate that the data cannot adequately assess the inclination values. This may also be a result of the small number of quasars in the sample. In any case, we caution against relying too heavily on the inclination measurements derived from the models whether fitted to individual or multiple sources. Since the subsequent analyses are based mainly on good X-ray flux measurements, we choose the PEXRIV model as the best-fit model despite its shortcomings.

Source of the Soft Excess

The global modeling of the quasar spectra suggest that the soft excess is not well-described by an absorption model (§ 6.4.2). Figure 6.10 clearly shows that the soft excess flux based on the global PEXRIV model is correlated with the total X-ray (0.5–10 keV) flux from the model. Linear regression analysis suggests that the two properties are linearly correlated: $\log L_{\text{bbody}} = (1.04 \pm 0.28) \log L_{\text{pl}} - (2.69 \pm 12.28)$. The correlation is very strong with $R^2 = 0.65$ and a significance of $> 99.99\%$. The outlier, PG 0050+124, is removed from the regression analysis; recall that this is the only source that retains an absorption feature in the residuals after the inclusion of the 0.7 keV absorption edge (see Figure 6.8). This linear correlation is much stronger than that found in a sample of *Swift*/BAT AGNs with soft excess ($R^2 = 0.48$; Winter et al. 2009). The soft excess in AGNs and PG QSOs seem to arise from the same process. The linear relationship between the blackbody and power law luminosities precludes absorption as the origin of the soft excess, in

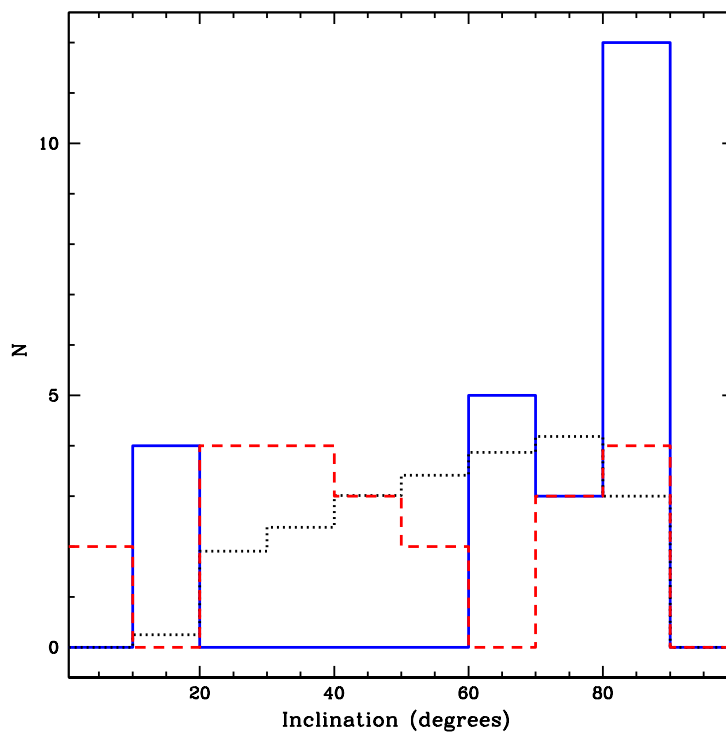


Figure 6.9: The solid blue line represents the histogram of the inclination angles of the 22 PG QSOs with EPIC-pn data measured using the PEXRIV model. The red dashed line is the histogram of inclinations using the modified blurred reflection model of Crummy et al. (2006). Both of these distributions are markedly different from the inclination measurements presented in Crummy et al. (2006) which peaks between 60–70 degrees (not shown). The black dotted line is a random distribution of $\cos(i)$ values selected between 0.05 and 0.95 (the limits of the model) simulated for 10000 objects then normalized to 22 to compare with the objects observed. Unlike Crummy et al. (2006) who found a deficit of sources at high and low inclinations when compared with the random distribution, here we see a deficit between 20–60 degrees and excess at the highest and lowest inclination bins. This implies the inclination angles are highly model dependent and we caution against heavy reliance on their accuracy.

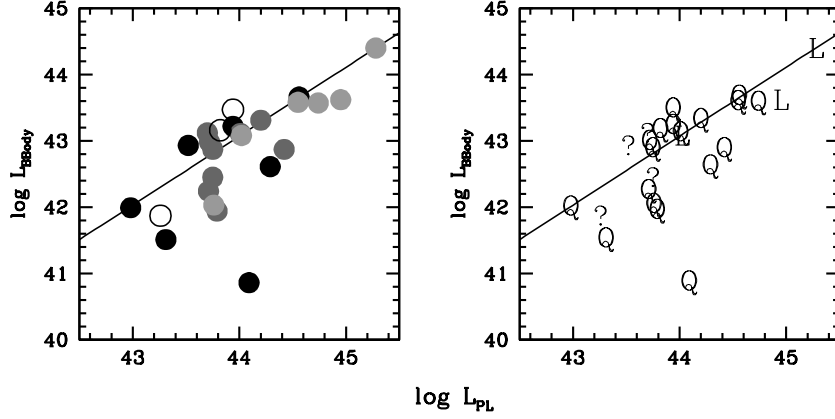


Figure 6.10: A plot of the absorption-corrected blackbody (or the soft excess) luminosity versus power law luminosity from the best-fit PEXRIV model to the PG QSOs. The meaning of the symbols is the same as that in Figure 6.2. The solid line is the linear regression fit to the data except for PG 0050+124, the outlier near (44, 41). The correlation is significant (>99.99%) with $R^2 = 0.65$ for $\log L_{\text{bbbody}} = (1.04 \pm 0.28) \log L_{\text{pl}} - (2.69 \pm 12.28)$. The slope of the line implies that $L_{\text{pl}} \propto L_{\text{bbbody}}$.

agreement with Winter et al. (2009). Figure 6.11 compares the soft excess luminosity with starburst contribution to the bolometric luminosity found in PG QSOs from Veilleux et al. (2009b). No correlation is seen between these two quantities and the soft excess luminosities are much higher than the expected starburst luminosity based on far-infrared measurements of star forming galaxies (Persic et al. 2004). Since the global model fits the AGN and the soft excess components independent of each other, it does not require the AGN components to be correlated with the soft excess. Therefore, the linear relationship between the input power law and the soft excess luminosities is real and implies a link between the source of the power law and the soft excess. We also compared the soft excess luminosity with black hole mass and ionization state of the reflector. Neither of these quantities seems to be correlated with the soft excess.

Many authors (e.g., Gierliński & Done 2004; Winter et al. 2009) have argued that if the soft excess were due to thermal emission arising from the accretion disc, then

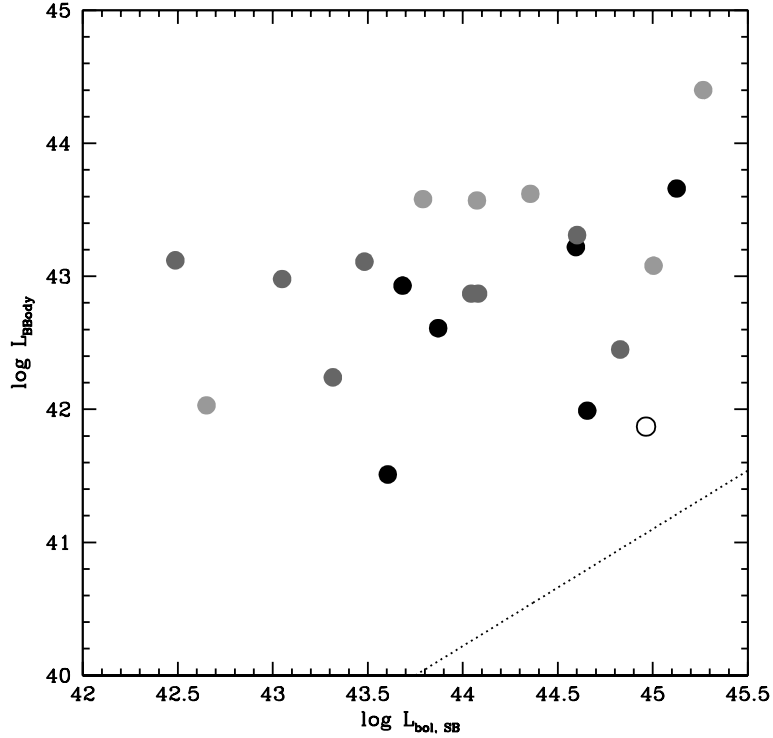


Figure 6.11: A comparison of the soft excess luminosity (represented by the blackbody model) and the starburst contribution to the bolometric luminosity calculated from the mid-infrared values presented in Veilleux et al. (2009b). The meaning of the symbols is the same as that in Figure 6.2. The dotted line represents the 2–10 keV to far-infrared luminosities of star forming galaxies in Persic et al. (2004). The luminosity derived from the blackbody model is much higher than expected from star formation. There is no correlation between the two quantities, implying that the soft excess is not related to the starburst.

the blackbody temperature should correlate with the mass of the black hole or the Eddington ratio. Contrary to this, previous studies and § 6.3.1 have found that the thermal temperature of the soft excess is consistently ~ 0.1 keV. The constancy of the temperature seems unexpected since the thermal temperature depends on both the black hole mass and the Eddington ratio: $T \propto M^{-1/4}(L/L_{Edd})^{1/4}$. However, the masses of both Seyferts (Winter et al. 2009) and PG QSOs (Veilleux et al. 2009a) span two orders of magnitude ($\sim 10^7 - 10^9 M_\odot$). Using the absorption corrected 2–10 keV to Eddington luminosity ratio as a proxy for the Eddington ratio, we also

find the 2–10 keV to Eddington luminosity ratio spans two orders of magnitude for both PG QSOs and Seyferts (Figure 6.4 and Winter et al. 2009). This implies that the thermal temperature should be nearly constant based on the equation above. Figure 6.12 is a histogram of the estimated PG QSO disc temperatures calculated using the photometric black hole mass estimates of Veilleux et al. (2009a) and the 2–10 keV luminosities. These are only estimates because the hard X-ray to bolometric luminosity correction for AGNs is uncertain. As the figure shows, the disc temperature is fairly constant for all objects, with a mean of ~ 1 eV and a standard deviation of ~ 0.4 eV. Of course, this may be an effect of small number statistics. However, the measured soft excess temperature of 0.1 keV is still too high to be explained by the thermal emission from the disc.

The mechanism producing the soft excess must be mass independent. Compton up scattering is one such mechanism since the Compton temperature scales as $\sqrt{M/R}$. Therefore, coronal effects could be a cause for the soft excess. However, the virial temperatures corresponding to broad line region velocities (a few $\times 10^3$ km s $^{-1}$) are much too high (a few keV) to form the soft excess.

6.5 The Multi-wavelength Properties of QUEST ULIRGs and PG QSOs

Netzer et al. (2007) found that PG QSOs can be separated into two different types of far-infrared sources: strong- and weak- far-infrared emitters. The authors found that both types of far-infrared emitters have similar underlying AGN SEDs. When comparing the far-infrared SEDs with the X-ray spectral index, the P05 models show no correlation between the photon index and the FIR strength of the PG QSO. On the other hand, the stronger FIR-emitters have softer spectra than the weaker FIR-

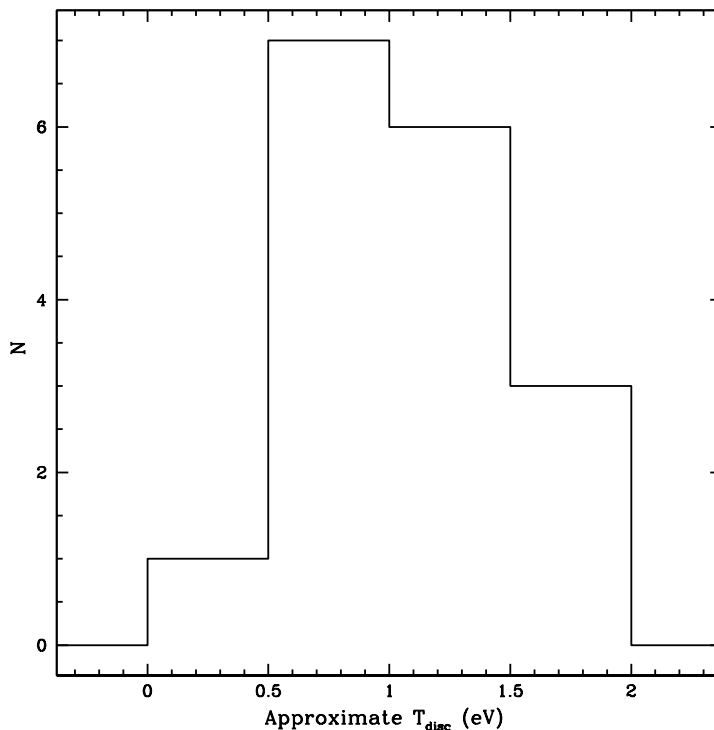


Figure 6.12: A histogram of the thermal temperature of the accretion disc as derived from the photometric black hole mass of Veilleux et al. (2009a) and the 2–10 keV luminosity. The scatter is small and the histogram peaks near 1 eV with a standard deviation of 0.4 eV. These are only estimates of the temperature because the 2–10 keV to bolometric correction for AGNs is uncertain.

emitters in the reflection-based C06 models. This may imply that some of the softer spectra have contributions from the starburst that is thought to be responsible for the FIR emission (Netzer et al. 2007).

6.5.1 AGN Contributions to Bolometric Luminosity

Veilleux et al. (2009b) presented six independent methods of determining the AGN contribution to the overall luminosity of ULIRGs and QSOs as part of the *Spitzer*-QUEST study. The details of the methods are presented in the Appendix of Veilleux et al. (2009b). Since the hard X-ray is dominated by the AGN, here we compare the 2–10 keV luminosity results on the PG QSOs with the mid-infrared AGN diagnostic

methods to examine how well each method can determine the contribution of the AGN to the overall energetics of these sources.

We only have available data for the PG QSOs to test three of the methods: flux ratio of the fine structure lines [Ne V] and [Ne II], flux ratio of [O IV] and [Ne II], and the *Spitzer* 30-to-15 micron flux ratio. The other methods involve measurements of the polycyclic aromatic hydrocarbon (PAH) features, which are often not measured in individual PG QSOs. Figure 6.13 plots the derived AGN contribution from these methods, and the average of these values, against the absorption-corrected 2–10 keV to bolometric luminosity ratio. The figures show a trend where the sources with higher X-ray contributions have high mid-infrared AGN percentages, but sources with lower X-ray contributions show a large range in their mid-infrared AGN percentages. We have identified two possible causes for the discrepancy between the X-ray and the mid-infrared results.

Zero-point Calibrations

Another source of error may be the definitions of the zero-points for the mid-infrared methods in Veilleux et al. (2009b). The AGN zero points were derived from the FIR-undetected PG QSOs. The lack of far-infrared detection implies that there are no starburst contributions to the infrared measurements. Thus, the AGN zero points are accurate. On the other hand, the starburst zero points are derived from HII ULIRGs which are known to be different than the pure starbursts in terms of gas density and radiation fields. Brandl et al. (2006) derived the f_{30}/f_{15} micron flux ratio and the 7.7 micron PAH equivalent widths for a sample of starburst nuclei. The values derived from these sources are lower than those found in the HII ULIRGs, but the two different methods are hard to compare. If we were to assume the Brandl et al. (2006) values as the starburst zero points, then the estimated AGN

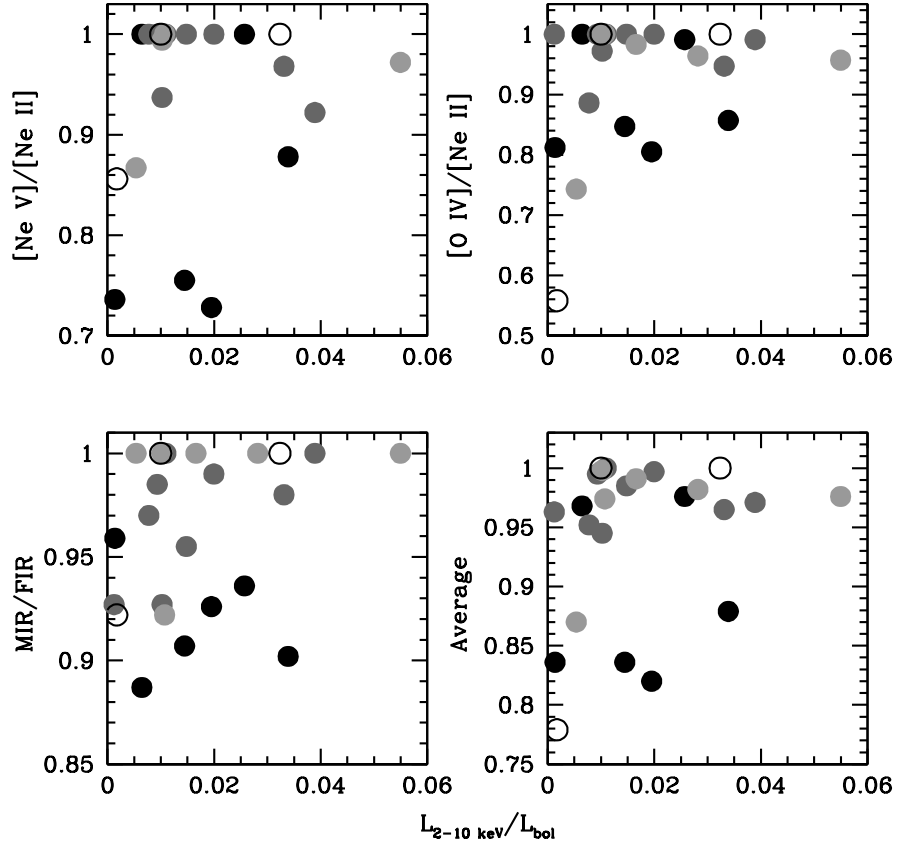


Figure 6.13: Comparison of absorption-corrected $L_{2-10 \text{ keV}}/L_{\text{bol}}$ and the AGN contribution determined by Veilleux et al. (2009b) for the PG QSOs. The meaning of the symbols is the same as those in Figure 6.2. The y-axis of the top panels show the fractions as found using the fine structure line ratios $[\text{Ne V}]/[\text{Ne II}]$ and $[\text{O IV}]/[\text{Ne II}]$. The bottom left are the fractions derived from the mid-infrared to far-infrared flux ratios while the bottom right panel shows the AGN fraction from the average of the three methods with available data for the quasars. Note the difference in range between the mid-infrared and the X-ray methods. Veilleux et al. (2009b) estimates the errors in the AGN fraction derived from the *Spitzer* data is approximately 15%. The scatter in the X-ray data may be in part due to variation in the 2–10 keV to total AGN luminosity conversion for individual sources. The obscuration in X-ray can have a large effect. Other causes for the discrepancy between the estimates from the two different wavelength are explored in § 6.5.1.

contributions from the mid-infrared data would be lower.

A Matter of Obscuration

A possible source for the discrepancy is that the X-ray and the mid-infrared observations probe different regions of the AGN. The X-ray is the direct (or reflected) emission from the accretion disc of the black hole. Its source occupies a small volume, on the scale of less than a parsec. In contrast, the mid-infrared diagnostic method of measuring AGN emission relies on the detection of fine structure lines which come from the narrow line region. The narrow line region covers a much larger volume, on the order of hundreds of parsecs. Thus, the mid-infrared emitting region is less likely to be affected by obscuration than the central X-ray emitting region.

The lower than expected hard X-ray to bolometric luminosity ratio may be due to the poor absorption correction. Despite being less susceptible to obscuration by dust than the optical or infrared wavelengths, the X-ray results may still be affected. Both *Chandra* and *XMM-Newton* operate at 0.5–10 keV, below the peak of the Compton reflection hump, the detection of which can better constrain the absorbing column. Teng et al. (2009) had a marginal detection of Mrk 273 at above 10 keV with *Suzaku*. The simultaneous modeling of the *Suzaku*, *Chandra*, and *XMM-Newton* spectra found that the source is highly obscured. The absorption corrected 2–10 keV luminosity with the *Suzaku* data is ~ 3.2 times that derived from *Chandra* or *XMM-Newton* data alone. Mrk 273 is also one of the sources that exhibits moderate extinction from the mid-infrared data ($\tau_{eff} \sim 6.4$). This is a change of about half an order of magnitude or $\sim 30\%$ in AGN percentage (Figure 6.4). Therefore, the absolute hard X-ray to bolometric luminosity ratio is uncertain.

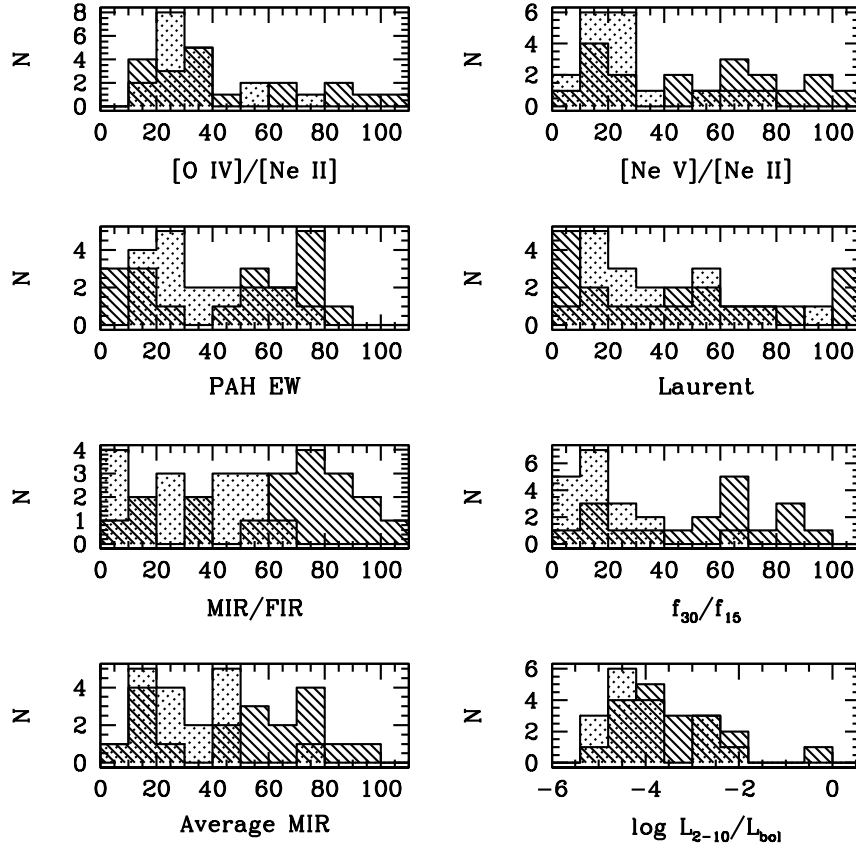


Figure 6.14: Histograms showing the distribution of percent of AGN contribution to the bolometric luminosity of the QUEST ULIRGs derived from the six mid-infrared methods presented in Veilleux et al. (2009b), the average of the six methods, and the 2–10 keV luminosity. The solid line hashes are the less obscured sources with $\tau_{eff} \lesssim 3.3$ derived by Veilleux et al. (2009b), the objects with blue symbols Figure 6.4. The dotted hashes are the more obscured ULIRGs with $\tau_{eff} > 3.3$, the red and green symbols in Figure 6.4. Note that the x-axis of the X-ray plot is in a log scale. For the mid-infrared methods, the less obscured objects span a larger range in the fractional AGN contribution than the more obscured objects. The more obscured objects tend to have low to moderate AGN fractions. These correspond to mixed starburst-AGN systems that are still largely dominated by the starburst. The less obscured objects can be separated into two groups — either early-merger starburst-dominated systems or late-merger AGN-dominated ULIRGs. This implies that extinction peaks in the intermediate stages of the interaction, but AGN dominance peaks at later merger stages. This does not appear to be the case for the X-ray distribution; a K-S test suggest that the two populations do not differ significantly.

The uncertainty in the X-ray AGN contributions is demonstrated in Figure 6.14. In terms of the mid-infrared methods, the distribution in AGN contributions can be separated into two different populations based on the effective optical depth (Veilleux et al. 2009b). The less obscured objects ($\tau_{eff} < 3.3$) clearly span a larger range of AGN contributions. These objects correspond to the AGN-dominated sources (high AGN contributions) and the starburst-dominated sources (low AGN contributions) in Veilleux et al. (2009b). On the other hand, the objects with higher τ_{eff} represent objects with a mixture of the starburst and AGN (low AGN contributions). This is not seen in the distribution from the X-ray method. There is no distinction between the objects with high or low τ_{eff} , as supported by the K-S test, indicating that the infrared and X-ray methods are probing regions of different size scales. The distribution should span a larger range since the values derived from the HR method are likely upper limits and the values derived from spectral fitting may be lower limits, depending on the amount of intrinsic absorption.

6.5.2 Trends with Merger Phase

The standard evolutionary scenario from Sanders et al. (1988a) states that starburst-dominated “cool” U/LIRGs evolve into AGN-dominated “warm” ULIRGs and then eventually optically selected quasars. In this scenario, the AGNs turn on only near the end of the merging process. Figure 6.15 demonstrates that the agreement between the AGN fractional contribution and the properties of U/LIRGs and PG QSOs observed at other wavelengths is again seen in the X-ray data. Here we use the hard X-ray to bolometric luminosity ratio as a proxy for fractional AGN contribution, assuming that the conversion factor between 2–10 keV luminosity and the bolometric luminosity is the same for all sources. The top panel of the figure supports previous arguments that “warm” objects are more likely to be AGN-dominated.

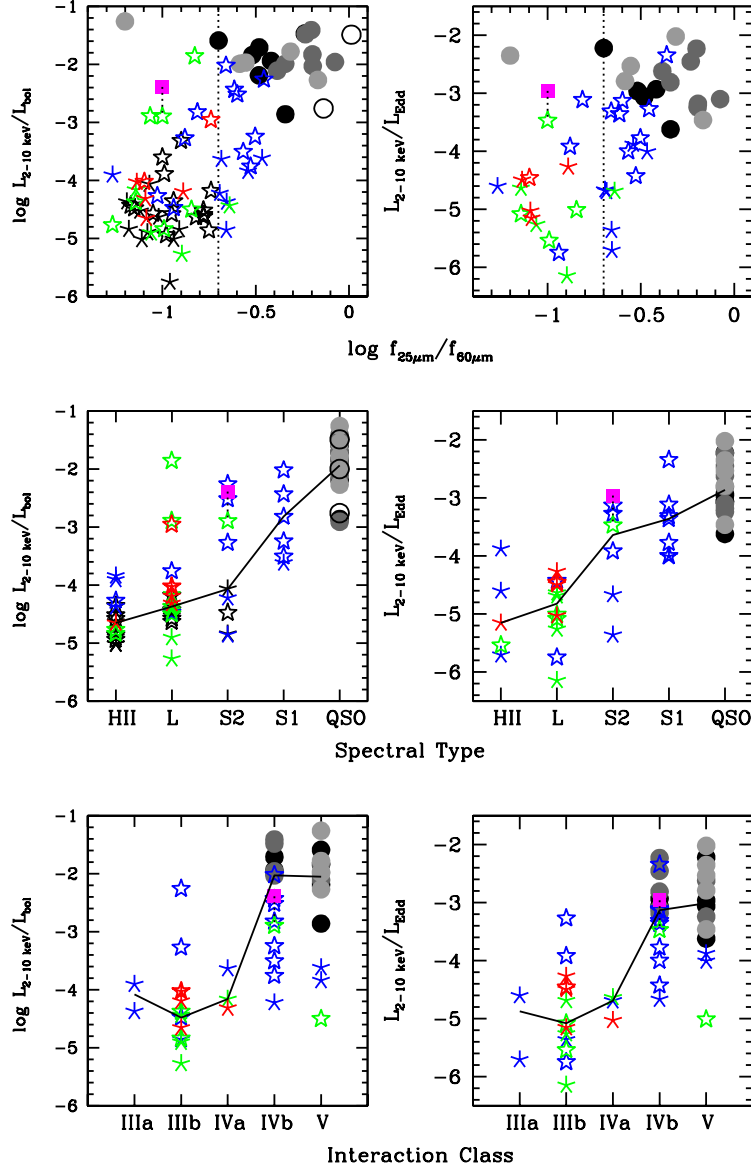


Figure 6.15: A comparison of the 2–10 keV to bolometric luminosity ratio (our proxy for AGN dominance; left) and the X-ray determined $\log(L_{2-10\text{keV}}/L_{\text{Edd}})$ (right) with some of the physical properties of the U/LIRGs and PG QSOs: dust temperature (top), optical spectral type (middle), and interaction class (bottom). The symbols for the PG QSOs are the same as those in Figure 6.2 for the SED and the symbols for the U/LIRGs are the same as those in Figure 6.4. In the bottom two rows, the line connects the median values for each type/class of objects. The infrared-warmer objects appear to have higher hard X-ray to bolometric luminosity ratios. The more Seyfert-like objects and the more advanced mergers also tend to have a greater AGN component with the PG QSOs extending these trends. These qualitative correlations are the same as those observed in a similar analysis of the *Spitzer* data (Veilleux et al. 2009b).

There is a clear clustering of PG QSOs in the top right and ULIRGs in the bottom left of the figures. There are transitional objects with both warm and cool colors, all of which have small to moderate values of τ_{eff} . This supports the idea that the cool, starburst-dominated, and obscured objects evolve to become warm, AGN-dominated, “naked” quasars.

The middle panels of Figure 6.15 demonstrate that the more powerful the AGN, the more likely the source is optically classified as either a QSO or a Seyfert type galaxy. The HII galaxies have the lowest hard X-ray to bolometric luminosity ratios as expected. The LINERs have a large range of 2–10 keV to bolometric luminosity ratios which may be due to the energy source of LINERs being a mixture of AGN and starburst (Sturm et al. 2006). Some of the objects with lower $L_{2-10keV}/L_{bol}$ in the Seyfert-2 and LINER classifications may be due to poor absorption corrections.

In terms of interaction classes (as defined by Veilleux et al. 2002), the bottom panels of Figure 6.15 show that AGN activity is the most dominant in the remnants with the latest interaction classes – IVb and V. These objects are either near the final stages of the merger (very close binary system) or have merged (single nucleus system). The steep increase of AGN dominance between classes IVa and IVb suggests that the majority of black hole growth occurs in the post-merger phase of the interaction. As seen in the figures, powerful AGNs can even occur in systems in the early stages of the merger (class IIIb). This is contrary to the established evolutionary scenario where the AGN turns on during the final stages of merging. However, the AGNs may pre-date the mergers or have been turned on due to stochastic accretion events.

While the absolute fractional AGN contribution to the overall power of U/LIRGs and PG QSOs based on the X-ray data are uncertain, the relative trends observed are likely real. These trends are also seen in the *Spitzer* data of Veilleux et al.

(2009b). This further suggests that a modification to the standard evolutionary scenario is needed. Nuclear activity can occur at any time in the evolution from mergers to quasars as nuclear activity can be triggered by random accretion events. However, the likelihood of finding AGN-dominated U/LIRGs increases along the merger sequence and in objects with warmer color temperatures.

It is interesting to compare these results with the predictions of numerical simulations (e.g., Hopkins et al. 2008, and references therein). These models suggest that the starburst dominates the total luminosity prior to and during the merger (phase D of Hopkins et al. 2008). After coalescence, the central black hole grows rapidly before the “blowout” phase (phase E) where an AGN driven wind expels the remaining dust and gas, removing material for both accretion and star formation. The result is a luminous, blue quasar with little star formation (phase F). The accretion rate of the active nucleus peaks between phases D and E. Then the luminosity of the quasar fades during the post-blowout quasar stage. For comparison, Figure 6.16 shows the evolution of the AGN luminosity along the final stages of the merger sequence derived from the mid-infrared and X-ray data. The data indicate that star formation peaks prior to the coalescence of the nuclei. The accretion rate increases rapidly and peaks at final coalescence. There is no significant change in the quasar luminosity after the blowout has occurred. The fading of the quasar must happen well after the quasar has become “naked”.

6.6 Summary

We have performed an uniform analysis of X-ray data on 40 ULIRGs and 26 PG QSOs from the QUEST sample. These data were archival and new observations obtained using *Chandra* and *XMM-Newton*. The X-ray results were compared with those

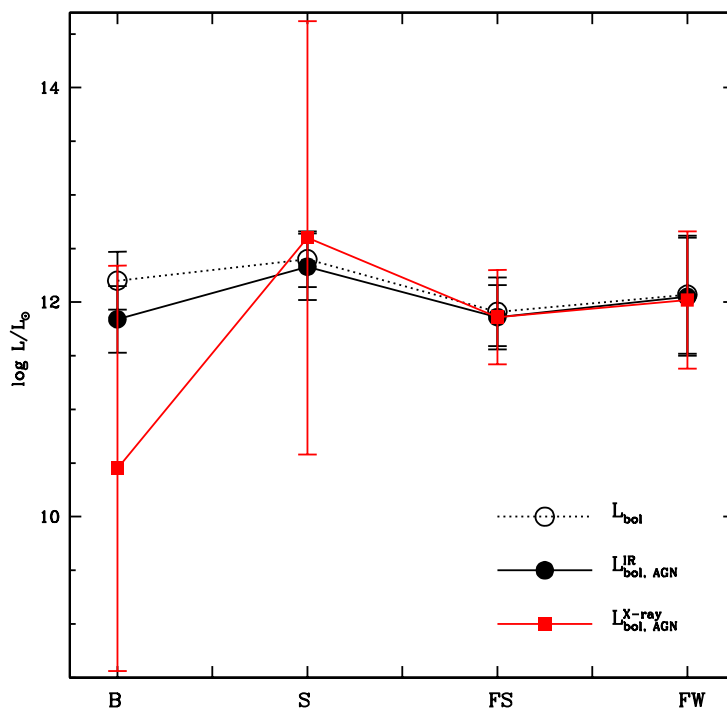


Figure 6.16: The evolution of the AGN bolometric luminosity as a function of merger stage is plotted. In the x-axis, B represents binary U/LIRGs (interaction classes IIIab–IVa, phase D of Hopkins et al. 2008), S represents single nucleus U/LIRGs (interaction classes IVb–V, phase D), FS are far-infrared strong PG QSOs where there are still ongoing star formation but the black hole dominates the feedback process (the “blowout” stage, phase E), and FW represents far-infrared weak PG QSOs where star formation has stopped (phase F). The open circles trace the mean total bolometric luminosity of the objects from both the QUEST and RBGS samples, the filled circles show the mean infrared-derived AGN bolometric luminosity from Veilleux et al. (2009b) for the QUEST sample only, and the filled squares represent the mean absorption-corrected 2–10 keV luminosity for both the QUEST and RBGS samples normalized to the $L_{\text{bol,AGN}}^{\text{IR}}$ value for the FS sources. Each error bar represents one standard deviation in each category of objects. The large error bars in the X-ray may be attributed to poor absorption correction or a large inherent distribution in nuclear activity. Though not statistically significant, several conclusions can be drawn from this figure: 1) the contribution of the starburst to the total bolometric luminosity decreases as the merger advances, 2) the 2–10 keV to bolometric luminosity correction for these AGNs is ~ 50 , the normalization factor between the infrared and X-ray values, 3) there is essentially no difference in AGN power between the far-infrared strong and weak PG QSOs, in agreement with Netzer et al. (2007), and 4) the growth of the AGN occurs most rapidly at final coalescence.

from QUEST studies at other wavelengths and the major conclusions are as follows:

1. By fitting the PG QSO spectra simultaneously, we have found an universal model for the quasars. The origin of the ubiquitous soft excess in PG QSOs and AGNs is still uncertain, but we can now rule out complex absorption as the cause. The best-fit universal model indicates that the soft excess luminosity is linearly related to the 0.5–10 keV absorption-corrected power law luminosity. This implies that the source of the soft excess must be related to the central black hole, rather than an external factor such as absorption or starburst.
2. There does not appear to be any correlation between the far-infrared emission strength and any of the X-ray properties tested in this paper. This supports the Netzer et al. (2007) conclusion that there is no obvious difference in the underlying AGN power between the strong or weak far-infrared emitting PG QSOs.
3. The X-ray QUEST results generally agree qualitatively with those from Veilleux et al. (2009b). While the absolute contribution from the AGN is uncertain due to poor absorption corrections, the trends seen in the data are real. The likelihood of powerful nuclear activity increases along the merger sequence and in objects with warmer dust temperatures. The presence of nuclear activity in binary U/LIRGs requires modifications to the standard Sanders et al. (1988a) evolutionary scenario. The AGNs in these sources may be pre-existing or caused by random accretion events in the lifetime of the mergers.
4. The luminosity of the AGN in U/LIRGs and PG QSOs evolve with merger stage. The starburst dominates the total power in these sources prior to the merger. Then the black hole grows rapidly during coalescence at which point the AGN dominates the bolometric luminosity. This AGN likely is the

main driver of galactic scale winds, quenching star formation (e.g., Murray et al. 2005). As a result, a luminous quasar remains. The predictions from theoretical simulations are largely consistent with these results.

Chapter 7

Summary and Conclusions

7.1 Overview

Systematic ground- and space-based observations at multiple wavelengths have shown that nearly all U/LIRGs with infrared luminosity above $10^{11.5} L_{\odot}$ are involved in strong tidal interactions or mergers of gas-rich disk galaxies. U/LIRGs have heightened star formation rates relative to normal galaxies, and the fraction of AGNs and the number of single-nucleus sources increases with increasing infrared luminosity. These sources also have large molecular gas concentrations in their central kpc regions, making it difficult to probe the central energy source. Thus, in these systems, hard X-ray observations are arguably one of the best methods to quantify the dominant energetic process.

This dissertation focused on X-ray observations of U/LIRGs in order to determine the evolution of the energy source in these objects. New and archived observations from *Chandra*, *XMM-Newton*, and *Suzaku* were used to characterize the X-ray properties of these sources and explore their possible connections to quasars. A goal of the thesis was to determine whether there is an evolutionary trend, as predicted by Sanders et al. (1988), where the starburst-to-AGN ratio and the intrinsic col-

umn density of a U/LIRG decreases as the merger proceeds and the optical quasar emerges from its dusty cocoon.

Chapters 2, 3, and 4 use *Chandra* and *XMM-Newton* observations for a statistical study of the presence of AGNs in U/LIRGs. In Chapter 2, we performed a snapshot survey on 14 1-Jy ULIRGs and found that a majority of these objects are too faint for traditional model fitting of the X-ray spectra to disentangle the starburst/AGN contributions. As a solution to this problem, we developed a method of estimating the X-ray spectral shapes, and thus the X-ray luminosity, of these low-count sources based on their hardness ratios. *XMM-Newton* follow-up presented in Chapter 3 shows that the hardness ratio method works. We applied the hardness ratio method to an additional 34 sources from the *Chandra* archive in Chapter 4. The spectral fitting of sources with moderate count rates further supports the hardness ratio method as an excellent way to approximate the X-ray properties of low-count sources compared with the traditional method of spectral fitting given that the internal absorptions are not too high – $N_H \lesssim 10^{22} \text{ cm}^{-2}$.

Chapter 5 relies on deep observations of five well-known local U/LIRGs with *Suzaku* to determine whether the weak X-ray detections of U/LIRGs are attributed to intrinsically weak X-ray sources or highly obscured AGNs. The results are varied for each of the five sources, but only one, Mrk 273, was marginally detected at $>10 \text{ keV}$. Reflection contributes significantly to the overall X-ray spectrum of some of these sources, suggesting high obscuration ($N_H \sim 10^{22-24} \text{ cm}^{-2}$).

Chapter 6 compared the X-ray properties of 40 U/LIRGs with those of 26 PG quasars using new and archived *Chandra* and *XMM-Newton* data. This is part of a multi-wavelength imaging and spectroscopic survey of local U/LIRGs and PG quasars. The main goal of the campaign is to determine whether there is a fundamental link between U/LIRGs, infrared-excess quasars, and optical quasars.

The X-ray results are compared with those from *Hubble*, *Spitzer*, and VLT to acquire a full picture of U/LIRG-quasar evolution.

7.2 Key Results

In this thesis, we performed an X-ray study of the largest sample of luminous and ultraluminous infrared galaxies to date. Here are some of the key results:

1. U/LIRGs are generally X-ray faint. We developed a method using the X-ray hardness ratio to approximate the starburst-to-AGN ratio in these sources. The method is an excellent way to estimate the 2–10 keV luminosity as long as the objects are not too highly obscured ($N_H \lesssim 10^{22} \text{ cm}^{-2}$).
2. The X-ray spectra of U/LIRGs can be generally described by a combination of a power law for the AGN and a MEKAL component for circumnuclear star formation. The hard X-ray to infrared luminosity ratios of U/LIRGs ($\log[L_{2-10\text{keV}}/L_{IR}] \sim [-4, -1]$) overlap with those of radio quiet quasars ($\sim [-2, -1]$). This suggests that the U/LIRGs at the upper-end of the luminosity range are dominated by AGNs.
3. The X-ray faintness of U/LIRGs is likely due to high intrinsic obscuration. Only one of the five nearest, brightest U/LIRGs was detected by *Suzaku* at above 10 keV. Modeling of the *Suzaku* data with earlier epochs of *Chandra* and *XMM-Newton* data found that these sources are Compton-thick.
4. The origin of the soft excess seen in PG QSOs and many Seyfert galaxies is still uncertain. However, by modeling all the PG QSO spectra simultaneously with an universal model, we can now rule out circumnuclear star formation or complex absorption as the cause. The soft excess luminosity is linearly

correlated with the power law luminosity, implying that the source of the soft excess must be related to the central black hole, rather than an external factor.

5. While the absolute AGN contribution to the bolometric luminosity in U/LIRGs is uncertain due to possible poor absorption corrections, the trend of increasingly dominant nuclear activity with increasing infrared luminosity is most likely real. The X-ray observations agree with previous optical and infrared studies in that the likelihood of powerful nuclear activity increases along the merger sequence and in objects with warmer dust temperatures. The presence of nuclear activity in binary U/LIRGs requires modifications to the standard evolutionary scenario. The AGNs in these sources may be pre-existing or due to stochastic accretion events in the lifetime of the mergers.
6. The luminosity of the AGN in U/LIRGs and PG QSOs evolve with merger stage. The starburst dominates the total power in these sources prior to the merger. Then the black hole grows rapidly during coalescence at which point the AGN dominates the bolometric luminosity. This AGN likely is the main driver of galactic scale winds, quenching star formation (e.g., Murray et al. 2005). As a result, a luminous quasar remains. The predictions from theoretical simulations are largely consistent with these results.

7.3 Future Work

A natural progression of this thesis is to continue X-ray surveys of U/LIRGs. While U/LIRGs are faint in the X-ray, likely due to heavy obscuration, our hardness ratio method provides good estimates of the spectral properties of these sources even with very few counts. The inverted spectra sources ($\Gamma < 1$) identified by the hardness ratio method are likely heavily obscured sources. Longer follow-up observations on

these objects may discover Compton-thick U/LIRGs by spectral fitting.

Since the literature is biased against faint objects, we can sort through the X-ray archives and use the hardness ratio method to identify not only obscured U/LIRGs, but also other types of obscured AGNs. Obscured AGNs are responsible for a large fraction of the cosmic X-ray background, but the true distribution of these objects is unknown. Data from recent large-area X-ray surveys can be combined with those at other wavelengths to conduct a complete census of the obscured AGN population.

An outstanding issue with the X-ray study of U/LIRGs is proper absorption correction. Modern X-ray instruments are not sensitive enough to detect these objects at above 10 keV. Two current and future missions have the potential to contribute greatly to this area of research.

The more immediate solution to the obscuration problem is the *Herschel* Space Observatory. *Herschel* was launched in May, 2009 by the European Space Agency. The instruments onboard the telescope operates in the far-infrared to sub-millimeter wavelength range of 55 to 672 μm . This is the energy range in which dust emission peaks. Instead of measuring the direct AGN emission from U/LIRGs, *Herschel* observations could constrain the amount of obscuring material in these objects which can be translated into estimates of the column density.

The other telescope is NuSTAR, poised to launch in 2011. NuSTAR will be the first focusing hard X-ray telescope, operating at between 6 to 80 keV. The detector onboard NuSTAR will be an imaging detector with spatial resolution of $46''$; it will not have the source confusion problem that plagues *Suzaku*-HXD. At its operating energy range, NuSTAR will be able to measure the Compton hump component of AGN spectra if the source is highly obscured. The modeling of these high energy spectra would allow for proper absorption correction of Compton-thick U/LIRGs as well as other types of obscured AGNs.

Appendix A

The Reliability of the Hardness Ratio Method

As discussed in the § 6.3.2, U/LIRGs are notoriously difficult to observe in the X-ray. Most of these objects are faint, either due to the lack of an AGN or the presence of heavy obscuration. Traditional spectral fitting cannot be used to model the complex spectra of these sources when counts are limited. The hardness ratio method developed in Teng et al. (2005) has proven to be effective in finding obscured AGNs in at least one case. *IRAS* F04103–2838 was found to contain both a starburst and an AGN with only 30 detected counts in a 10 ksec *Chandra* observation. A deeper (~ 20 ksec) *XMM-Newton* follow-up revealed an Fe K α line at rest-frame energy of ~ 6.5 keV, consistent with cold neutral iron (Teng et al. 2008). The hard X-ray emission is dominated by a nearly Compton-thick AGN with intrinsic 0.2–10 keV luminosity $\sim 10^{43-44}$ ergs s $^{-1}$.

Since the detected counts of the majority of objects in the U/LIRG surveys are low, the errors associated with the HR method are inherently large. To further test the reliability of the HR method in recovering the input spectrum, we have

performed a set of simulations. In these simulations, we set the input model of an unabsorbed AGN at $z \sim 0.1$ as a redshifted power law with Γ at 1.8 (the canonical value for AGNs) absorbed by a Galactic column of $2 \times 10^{20} \text{ cm}^{-2}$. The normalization of the input power law model was such that the model 0.5–10 keV flux is $\sim 5 \times 10^{-14} \text{ ergs s}^{-1} \text{ cm}^{-2}$, the mean value observed in faint U/LIRGs.

We first tested the dependence of the HR method on the number of detected counts by varying the exposure times in the simulations. For each exposure time tested, the average of 1000 simulations showed that the nominal Γ and the 0.5–2 keV and 2–10 keV flux values are remarkably stable even when the “detected” counts were reduced to as low as 30 (a 5 ksec exposure). On average, the output Γ determined from the HR method remained the same as the input, but the error bars increased as the number of detected counts decreased. The nominal 0.5–2 and 2–10 keV fluxes are within 1% of those from the input model. The top portion of Table A.1 summarizes these results.

In the HR method, we assumed that the only absorption is from the Galaxy, but this is not the case for the U/LIRGs we observe. The internal absorption in these objects are often high. Therefore, we also tested the dependence of the HR method on the intrinsic absorption of the source. To this end, we added intrinsic source absorption to the input spectrum. For 15 ksec exposures, we varied the intrinsic source absorption between $10^{20-22} \text{ cm}^{-2}$ by steps of $5 \times 10^{20} \text{ cm}^{-2}$ to see how the measured spectral parameters using the HR method are affected. Figure A.1 shows the results of these simulations. As the internal column increases, the photon index becomes flatter and then inverted ($\Gamma < 1$). Γ begins to become inverted when the column is $\gtrsim 5 \times 10^{21} \text{ cm}^{-2}$ as seen in the bottom portion of Table A.1. Since the 0.5–2 keV flux is more readily affected by absorption, it deviates from the input spectrum by more than 10% when the absorption is at only $1 \times 10^{21} \text{ cm}^{-2}$. On the

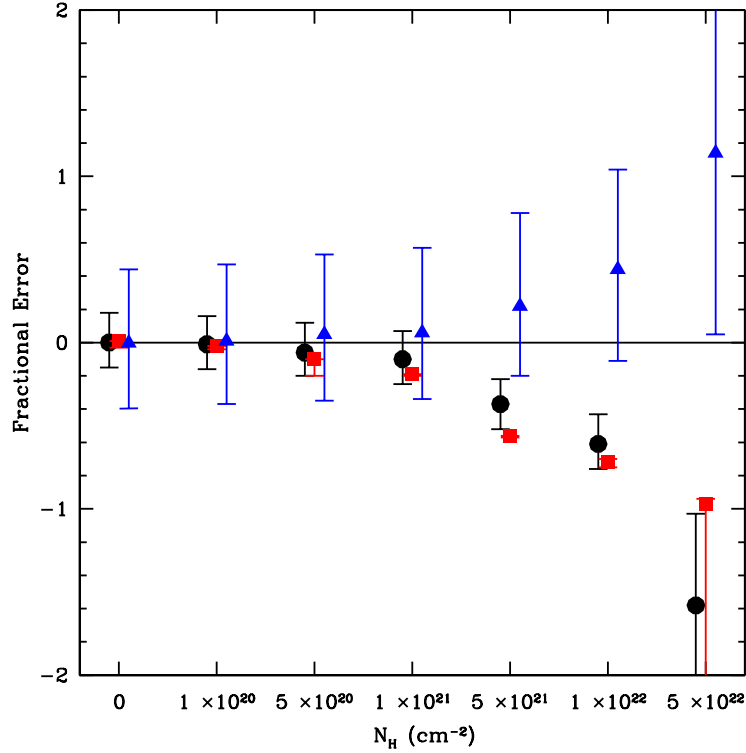


Figure A.1: The fractional errors of the HR method from the average of 1000 simulations. The output photon index (black circles), 0.5–2 keV flux (red squares) and 2–10 keV flux (blue triangles), both corrected for Galactic absorption from the simulated *Chandra* spectra, are plotted against the input intrinsic column density. It is clear from the plot that the photon index derived from a single power law model deviates from the input value of 1.8 when the source column density is $\gtrsim 10^{21} \text{ cm}^{-2}$, becoming more inverted ($\Gamma_{\text{HR}} \sim 0.71$ at N_H of $1 \times 10^{22} \text{ cm}^{-2}$). The 0.5–2 keV flux, more readily affected by absorption than the 2–10 keV flux, follows the same trend as the photon index. On the other hand, the hard-band flux is stable up to $N_H \sim 5 \times 10^{21} \text{ cm}^{-2}$. These results of the simulations demonstrate that an inverted spectrum source from the HR method is an indication of obscuration in the source.

Table A.1. Quantifying the Errors in the Hardness Ratio Method

Exposure (1)	Hard (2)	Soft (3)	HR (4)	Γ (5)	N_H (6)	$F_{0.5-2}$ (7)	Error $_{0.5-2}$ (8)	F_{2-10} (9)	Error $_{2-10}$ (10)
Input	1.8	...	1.77	...	2.95	...
100	139.6±11.7	453.2±21.2	-0.53±0.05	1.80 ^{+0.13} _{-0.12}	...	1.77	0.0	2.94	-0.3
75	104.7±10.6	339.3±18.3	-0.53±0.05	1.80 ^{+0.14} _{-0.13}	...	1.77	0.0	2.94	-0.3
50	70.1±8.1	225.6±15.3	-0.53±0.07	1.80 ^{+0.17} _{-0.15}	...	1.76	-0.6	2.93	-0.7
25	35.0±5.9	113.3±10.6	-0.53±0.09	1.80 ^{+0.21} _{-0.21}	...	1.77	0.0	2.94	-0.3
20	27.9±5.1	90.1±9.5	-0.53±0.10	1.80 ^{+0.28} _{-0.24}	...	1.76	-0.6	2.92	-1.0
15	21.0±4.6	67.8±8.3	-0.53±0.12	1.80 ^{+0.33} _{-0.27}	...	1.77	0.0	2.93	-0.7
10	14.0±3.8	45.2±6.6	-0.53±0.15	1.80 ^{+0.41} _{-0.32}	...	1.77	0.0	2.93	-0.7
5	6.9±2.8	22.7±4.9	-0.53±0.21	1.80 ^{+0.65} _{-0.47}	...	1.77	0.0	2.94	-0.3
15	21.0±4.6	66.4±7.8	-0.52±0.12	1.78 ^{+0.31} _{-0.26}	1.0×10^{20}	1.73	-2.3	2.96	0.3
15	21.1±4.5	61.5±7.7	-0.49±0.12	1.70 ^{+0.31} _{-0.26}	5.0×10^{20}	1.59	-10.2	3.08	4.4
15	20.8±4.7	55.6±7.6	-0.45±0.13	1.62 ^{+0.31} _{-0.27}	1.0×10^{21}	1.43	-19.2	3.12	5.8
15	19.9±4.4	30.4±5.5	-0.21±0.14	1.13 ^{+0.27} _{-0.26}	5.0×10^{21}	0.79	-55.4	3.60	22.0
15	18.5±4.3	18.2±4.4	0.01±0.17	0.71 ^{+0.32} _{-0.28}	1.0×10^{22}	0.49	-72.3	4.24	43.7
15	12.2±3.6	1.68±1.28	0.76±0.34	-1.04 ^{+0.99} _{-∞}	5.0×10^{22}	0.05	-97.2	6.30	114.6
15	8.3±3.0	0.2±0.45	0.94±0.49	...	1.0×10^{23}
15	1.7±1.3	0.01±0.06	1.00±1.13	...	5.0×10^{23}
15	0.5±0.7	0.001±0.03	1.00±1.93	...	1.0×10^{24}

Note. — Col.(1): Simulated exposure time in ksec. Col.(2): Average counts in the hard band from 1000 simulations. Col.(3): Average counts in the soft band from 1000 simulations. Col.(4): The hardness ratio. Col.(5): Spectral index derived from the hardness ratio method. Col.(6): Input column density from within the source in units of cm^{-2} . Col.(7): Observed 0.5–2 keV flux in units of $10^{-14} \text{ erg s}^{-1} \text{ cm}^{-2}$ assuming only Galactic absorption. Col.(8): The percent error of the simulated 0.5–2 keV flux relative to that of the input model. Col.(9): Same as (7), but for the 2–10 keV band. Col.(10): Same as (8), but for the 2–10 keV band.

other hand, the 2–10 keV flux is more stable, but begins to deviate from the input spectrum when the absorption is high enough that Γ becomes inverted. Of course, if the source has a softer spectrum (e.g., containing a commonly seen soft-excess component), then it would require a higher column for the spectrum to become inverted.

One of the important usages of the HR method is to estimate the photon index of the X-ray spectrum which in turn gives estimates of the 0.5–2 and 2–10 keV fluxes of our targets. The spectral index is the parameter that is the basis for the flux estimates. As shown by the simulations, the accuracy of Γ based on the HR method depends on the intrinsic absorption of the source. Figure A.2 compares the Γ derived from the HR method and the traditional method for the moderately bright

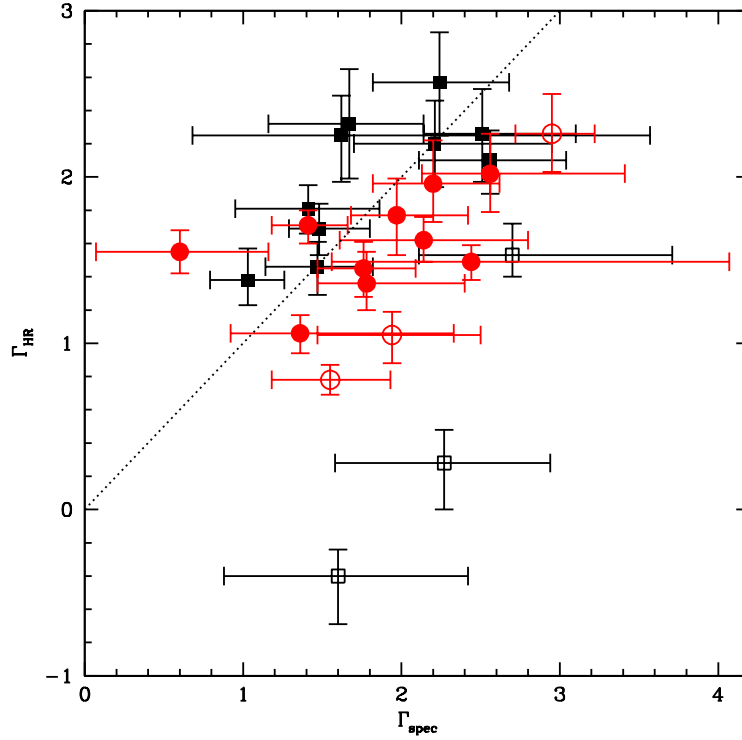


Figure A.2: A comparison of the values of Γ derived from the traditional spectral fitting method (x-axis) and the HR method (y-axis). Included are the 13 objects from the QUEST sample (circles) that have enough counts for spectral fitting and also have been determined to have a power-law component in their spectra. We add to these 13 more nuclei from the RBGS sample (squares). The error bars are at 90% confidence level. The dotted line is the line of equality to help guide the eye. For most of the objects (filled symbols), the values of Γ derived from both methods are consistent with each other to within the errors. For the six sources with open symbols, the hardness ratio method severely underestimates Γ . All six objects have $N_H > 10^{22} \text{ cm}^{-2}$. This plot demonstrates that the hardness ratio method is a good estimator of the spectral properties of these faint sources as long as the column densities are $\lesssim 10^{22} \text{ cm}^{-2}$, consistent with our simulation results.

U/LIRGs in § 6.3.2 and in the archived *Chandra* sample discussed in Appendix B. The figure shows that our measurements from the two methods are consistent with each other unless the intrinsic column densities are $\gtrsim 10^{22} \text{ cm}^{-2}$, in agreement with the simulations. The next consideration is to see how well the estimated fluxes from the HR method match those of the traditional method. We have plotted in Figure A.3 the 0.5–2 keV and 2–10 keV fluxes derived from both the HR and the traditional fitting method with more complex spectral models for the moderately bright U/LIRGs in § 6.3.2. As the figure shows, the majority of the HR flux values from a simple unabsorbed power law model are within 50% of the spectral fitting values of more complex models. The HR method is more likely to overestimate the fluxes in both the soft and hard bands. The median values for F_{HR}/F_{fits} are approximately 1.2 and 1.3 for the soft and hard bands, respectively.

As Teng et al. (2009) and other authors have demonstrated, the X-ray spectra of U/LIRGs are often more complex than a simple power law model can characterize. We further tested the HR method by assuming that the input model contains a reflection component or that the intrinsic absorption is due to a partial covering absorber. The addition of a reflection or a partial covering component flattens the AGN power law spectrum, mimicking the effects of high intrinsic absorption. For an intrinsic absorption of $1 \times 10^{22} \text{ cm}^{-2}$, the HR method recovers the input flux very well for both the reflection and partial covering models¹. In fact, for both models, the recovered 0.5–2 keV fluxes are within 2% of the input model flux. On the other

¹The reflection model assumes a power law plus a PEXRAV component. The normalization of the reflected component is set to 2% of the intrinsic power law component as measured in the complex *Suzaku* spectrum of *IRAS* F05189–2524 (Teng et al. 2009). The photon index of the power law spectrum is fixed at 1.8 and the recovered Γ is $0.70_{-0.30}^{+0.32}$. For the partial covering model, the covering factor is assumed to be 90%, similar to that found in Mrk 273 (Teng et al. 2009). In this case, the input Γ is again fixed at 1.8 and the HR estimate of Γ is $0.91_{-0.28}^{+0.30}$.

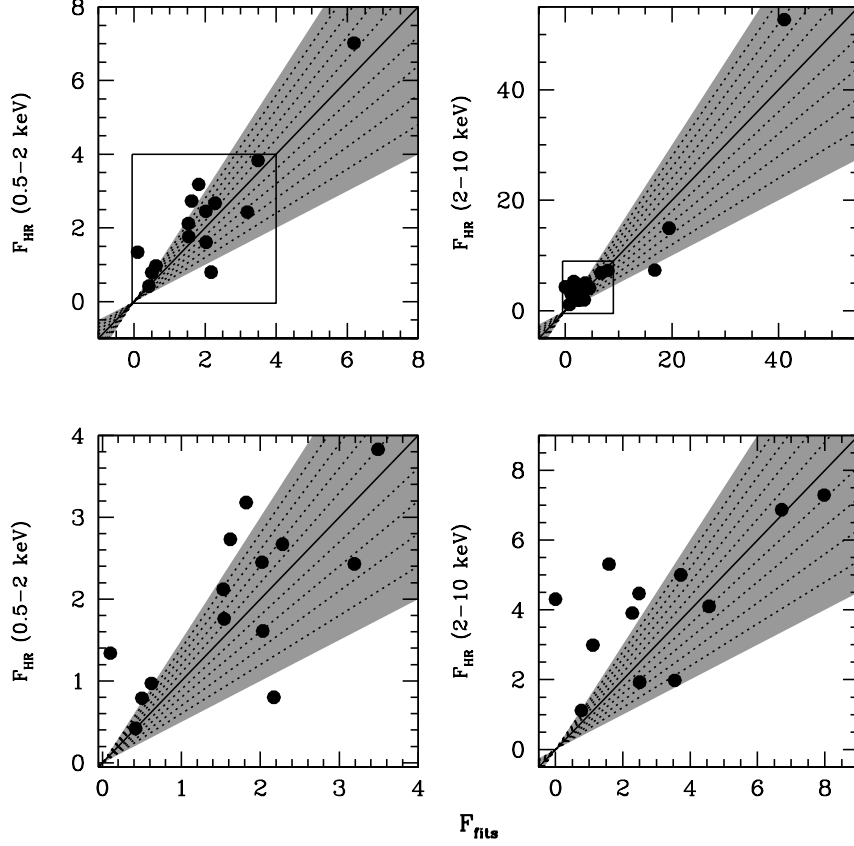


Figure A.3: A comparison of the 0.5–2 keV (left) and 2–10 keV (right) flux values of the U/LIRGs derived from spectral fitting (x-axis) and the HR method (y-axis) for objects with enough counts for spectral fitting using c-stat. The flux values are in units of 10^{-14} erg s $^{-1}$ cm $^{-2}$. The bottom figures are close-up views of the boxed regions in the top panels. The solid line is a line of equality with each dotted line representing a 10% deviation from the spectral fitting values. Most of the HR values are within 50% (the shaded regions) from the fitted values. The HR method tends to overestimate the fluxes, especially at 2–10 keV, when obscuration is high. The median values for F_{HR}/F_{fits} are ~ 1.2 and 1.3 for the soft and hard bands, respectively. This is an indication that many of these objects are obscured (see Figure A.1).

hand, the HR estimates of the 2–10 keV fluxes are above the input values by 56.4 and 35.3% for the reflection and partial covering models, respectively. These errors are comparable to or better than the estimates obtained for the simple power law model at the same column density (Table A.1). Therefore, even for objects with complex spectra, the HR method is able to provide fair approximations of their spectral properties.

Appendix B

Notes on Individual RBGS

Sources

- IRAS F01364–1042: This is an unresolved source detected by *Chandra*. Its optical centroid position is consistent with the peak X-ray emission. No emission is detected between 6–8 keV.
- III Zw 035: Both nuclei are detected. The northeastern nucleus exhibits unresolved hard X-ray emission.
- IRAS 03359+1523: Both nuclei of this source are detected, but the western nucleus is only at two counts. Only the eastern nucleus is the *IRAS*-detected U/LIRG. The soft X-ray emission of the eastern nucleus is extended. A quick comparison of the X-ray data with archived *HST* ACS images suggests that some of the soft X-ray emission of the eastern nucleus extends perpendicular to the disk of the galaxy. This X-ray emission may be due to winds from a starburst in the disk.
- ESO 203–IG001: The northeastern nucleus is detected by *Chandra*. Only

emission from 0.5–2 keV is detected and thus the HR method cannot be used to constrain the X-ray spectrum.

- VII Zw 031: This source has extended X-ray emission. Spectrum shows two emission lines at 0.83 and 1.38 keV, both arising from Fe XVII. There is also a suggestion of an emission line at 1.86 keV (Si XIII) which is statistically insignificant. From the modeling of its X-ray spectrum, the unabsorbed MEKAL to full *Chandra* band flux ratio suggest that this source is dominated by a starburst ($\sim 71\%$).
- ESO 255–IG007: All three nuclei in this interacting system are detected by *Chandra*. Nucleus A is the U/LIRG detected by *IRAS*. It consists of mostly extended emission in the 0.5–6 keV range. The peak of the X-ray emission corresponds to the optical centroid position. The spectrum of this source is best-fit by two MEKAL models with temperatures of ~ 0.68 and 2.72 keV. There does not appear to be any contribution from an AGN source. Nucleus B also consists of mostly extended emission in the 0.5–6 keV range. To within the errors, the optical centroid position is consistent with both X-ray emission peaks in this galaxy, one of which contains unresolved 2–6 keV emission. Nucleus C is only detected at 20 counts.
- IRAS 07251–0248: This source is only detected at 5 counts. All of its emission is in the 0.5–2 keV band and thus the HR method cannot be used to constrain its X-ray spectral shape.
- ESO 060–IG016: Only the eastern nucleus, the U/LIRG, is detected. The nucleus exhibits unresolved hard X-ray emission and extended soft X-ray emission. The spectrum of the eastern nucleus is best-fit by the scattering model where $\sim 2\%$ of the emission is scattered. The absorbing column has a density

of $\sim 1.7 \times 10^{23} \text{ cm}^{-2}$. The high column density explains why the source appears so “blue” in the false-color images and estimated to have an inverted spectrum ($\Gamma < 1$) from the HR since most of the red, soft X-ray emission is suppressed.

- F08572+3915: Optically classified as a LINER, this is a highly obscured source (Teng et al. 2009, and references therein). NED also classifies this source as a Seyfert 2. The HR analysis suggest this source has an inverted spectrum, very similar to ESO 060–IG016E and ESO 069–IG006S.

- IRAS 09022–3615: This object has extended X-ray emission. The optical centroid is in between the two peaks in the X-ray emission. The primary X-ray peak is mostly 0.5–6 keV emission while the secondary X-ray peak is mostly 2–8 keV emission. The spectrum of this source has a power law index of ~ 1.0 . This suggests that the spectrum is produced either by X-ray binaries which generally have spectral indices of 1.1–1.4 (Persic et al. 2004) or reflection has flattened an AGN spectrum with a spectral index of ~ 1.8 . The latter scenario is unlikely since Fe K lines with large equivalent widths would be detected. An emission line is seen at 1.06 keV, consistent with emission arising from Fe XVIII–XXII.

- IRAS F09111–1007: The hard X-ray emission of this source is unresolved while the soft X-ray emission is extended, consistent with the Seyfert 2 classification in the optical.

- UGC 04881: Both nuclei of this source are detected with the bulk of the emission between 0.5–2 keV. The soft X-ray emission appears to be extended.

- IRAS F10038–3338: Mis-identified as IC 2545 in Sanders et al. (2003). Both

nuclei are treated as one object for the purposes of this paper due to the uncertainties in the DSS centroid positions. The bulk of the X-ray emission is between 0.5 and 2 keV.

- IRAS F10173+0828: This source is only detected at 11 counts, the bulk of which are in the 0.5–2 keV band.
- IRAS 13120–5453: This object exhibits extended emission in the 0.5–6 keV energy range. There appears to be an X-ray core that coincides with the optical nucleus. The spectrum of this source is best-fit by a moderately absorbed power law with an index of ~ 1.5 . The X-ray spectral properties of this source is consistent with that of a Seyfert 2 galaxy. An emission line is identified at 1.83 keV, which is due to Si XIII.
- VV 250B: This source was mis-identified as VV 250A in Sanders et al. (2003). The spectrum of this source is well-fit by an absorbed power law plus a MEKAL model. The contribution of the MEKAL component to the overall unabsorbed X-ray spectrum is only $\sim 8\%$. There is an emission line at 3.86 keV, likely due to Ca XIX. VV 250A is the designation of the northwestern galaxy in this interacting pair which is also detected in the X-ray with ~ 10 counts.
- UGC 08387: There is soft X-ray emission perpendicular to the disk. Its X-ray morphology suggests that it contains an unresolved hard X-ray core at the center, implying the presence of an AGN. The spectrum of this source is well-fit by a MEKAL plus a power law model. The MEKAL contribution to the unabsorbed X-ray spectrum is $\sim 19\%$ which hints that the X-ray spectrum of this source is dominated by the AGN. There is an emission line at 1.86 keV, consistent with emission arising from Si XIII.

- IRAS 14378–3651: This source is unresolved. The location of the X-ray emission peak is consistent with the optical centroid. The HR analysis suggests that this source has an inverted power law spectrum. Given that this source is optically classified as a Seyfert 2 galaxy, it is unsurprising that the observed soft X-ray counts are affected by a large column similar to those seen in ESO 060–IG016E and ESO 069–IG06S.

- VV 340A: This is the northern member of an interacting pair of galaxies. There is unresolved hard X-ray emission corresponding to the optical centroid from this nucleus. The 0.5–2 keV emission is extended. The best-fit model to the X-ray spectrum is a MEKAL model plus a power law model. There is an Si XIII emission line at 1.86 keV and an Fe K α emission line at 6.4 keV. The equivalent width of the iron line is extraordinarily high (~ 24 keV). This may be due to a weak continuum at above 6 keV, a blend of several lines, reflection/scattering, or a combination of any of these. The MEKAL contribution to the overall unabsorbed X-ray spectrum is only $\sim 27\%$. VV 340B is also detected in the X-ray with ~ 55 counts.

- I Zw 107: Both nuclei in this galaxy are detected in the X-ray. The northern nucleus has extended soft X-ray emission. The peak of the X-ray emission is consistent with the optical centroid. The X-ray spectrum of this source is a moderately absorbed power law plus a MEKAL component. The MEKAL to the full *Chandra* band flux ratio is $\sim 83\%$, consistent with the optical spectral identification of being HII-like. There appears to be a line at 1.86 keV, but it is statistically insignificant. The southern nucleus is detected at only 16 counts, most of which are in the 0.5–2 keV energy range.

- NGC 6090: Both nuclei in this galaxy are detected. The northeastern nu-

cleus is the *IRAS*-detected U/LIRG and has extended soft X-ray emission. Although the optical centroid corresponds with some X-ray emission, its location is not consistent with the X-ray peak in this nucleus. The X-ray peak contains unresolved 2–6 keV emission. The X-ray spectrum, however, is well-fit by a double MEKAL model, with temperatures of ~ 0.8 and 3.1 keV. An emission line arising from Mg XI is prominent at 1.38 keV. The southwestern nucleus consists of extended emission in the 0.5–6 keV energy range.

- ESO 069–IG006: Both nuclei of this interacting pair are detected. Although the peak X-ray emission from the northern nucleus does not correspond with the optical centroid, the optical centroid does correspond to the secondary X-ray emission peak. The spectrum of the northern nucleus is well-fit by a double MEKAL model at temperatures of ~ 0.6 and 1.8 keV. There is an emission line at 1.8 keV, likely due to Fe XXIII–XXV. The southern nucleus exhibits unresolved hard X-ray emission and is best-fit by an absorbed power law model with a spectral index consistent with the canonical index of an AGN. The optical classification of this source is unknown, but the southern nucleus likely contains an AGN component.
- IRAS F17132+5313: Both nuclei of this galaxy are detected. The peak X-ray emission from the northeastern nucleus does not correspond to the optical centroid. The bulk of the emission from the northeastern nucleus is between 0.5–2 keV. The southwestern nucleus is only detected at four counts in the soft band only. The HR method cannot be used to estimate its spectral properties.
- IRAS F18293–3413: This source consists of mostly extended X-ray emission in the 0.5–6 keV energy range. The optical centroid corresponds with the X-ray peak, which contains unresolved 2–6 keV emission. The X-ray spectrum of

this source is best-fit by a MEKAL plus an absorbed power law model. The MEKAL flux is $\sim 24\%$ of the unabsorbed full-band emission. Two emission lines are seen at 1.36 and 1.86 keV, arising from Mg XI and Si XIII respectively.

- ESO 593–IG008: Both nuclei are treated as one object due to the uncertainties in the DSS centroid positions of the nuclei. The X-ray emission peak corresponds to the optical centroid position. The soft X-ray emission of this source is extended.
- IRAS 19297–0406: Source is not detected by *Chandra*.
- IRAS 19542+1110: Source is not detected by *Chandra*.
- CGCG 448–020: Both nuclei are detected by *Chandra*, but only the southeastern nucleus is U/LIRG as observed by *IRAS*. The optical centroid of the southeastern nucleus corresponds to the peak X-ray emission. The spectrum of the southeastern nucleus is best-fit by a moderately absorbed power law and a MEKAL model. The MEKAL component contributes $\sim 19\%$ to the overall unabsorbed X-ray spectrum. There is also extended 2–6 keV emission which corresponds to a tidal tail in the DSS image. The northwestern nucleus is detected at only 5 counts between 0.5–2 keV and the HR is ineffective in constraining its X-ray spectrum.
- IRAS 21101+5810: Source is not detected by *Chandra*.
- ESO 239–IG002: There is extended soft X-ray emission along with unresolved 2–6 keV emission at the center. The spectrum of this source is best-fit by a combination of the a MEKAL model and a power law model. The unabsorbed MEKAL flux is $\sim 18\%$ that of the full *Chandra* band flux. No emission lines are detected.

- NGC 7592: Both nuclei in this galaxy are detected. The eastern nucleus is dominated by extended soft X-ray emission. The spectrum of this nucleus is best described by a double MEKAL model with temperatures ~ 0.6 and 4.1 keV. The western nucleus also has extended soft X-ray emission, but also contains an unresolved hard X-ray ($2\text{--}8$ keV) core. The spectrum of this nucleus is best-fit by a MEKAL plus power law model. The value of the power law Γ and the unresolved hard X-ray nucleus is consistent with the optical spectral type of this galaxy being Seyfert 2. The MEKAL to the unabsorbed $0.5\text{--}8$ keV flux is $\sim 26\%$ for the western nucleus.
- ESO 077-IG014: Both nuclei in this object are detected and have extended soft X-ray emission. In both nuclei, the peaks of the X-ray emission corresponds to the optical centroid positions.

Appendix C

Ultraluminous X-ray Sources (ULXs) in the RBGS Sample

Several galaxies in the RBGS sample have discrete, point-like X-ray sources that are ULX candidates (Table C.1). These sources are generally located in the disk (spiral arms) of the galaxy. A quick look at the archived *HST* images of these galaxies show that many of these candidates appear to have optical counterparts. However, further analysis of the *HST* and *Chandra* astrometric uncertainties is required to confirm the correlation between the two wavelengths. Many of these candidates have X-ray photons only in the 0.5–2 keV band and are similar to the super-soft X-ray sources in NGC 300 and NGC 4631 (e.g., Kong & Di Stefano 2003; Winter et al. 2006). Super-soft X-ray sources appear to be best described by an absorbed blackbody model with $kT \sim 60$ eV (Winter et al. 2006). Thus, for ULX candidates with no hard counts, we assume only Galactic absorption and a 60 eV blackbody model to estimate the X-ray luminosity based on the source count rates. For objects with hard counts, a power-law model (with Γ fixed at 1.8) modified by only Galactic absorption is assumed. The estimated luminosities are above 10^{39} erg s $^{-1}$. The X-

ray properties of these isolated sources are also very similar to the discrete X-ray sources seen in the LIRG Arp 299 and other starburst galaxies (Zezas et al. 2003, and references therein).

Table C.1. Properties of ULX Candidates

ULX ID	RA (2)	Dec (3)	D_{centrd} (4)	Total Counts (5)	Soft Counts (6)	Hard Counts (7)	Count Rate (8)	Estimated $F_{0.5-2 \text{ keV}}$ (9)	Estimated $F_{2-10 \text{ keV}}$ (10)	Estimated $L_{0.5-2 \text{ keV}}$ (11)	Estimated $L_{2-10 \text{ keV}}$ (12)	Estimated $L_{0.5-10 \text{ keV}}$ (13)	Location (14)
III Zw 035SW X1	01 44 30.34	+17 06 01.60	0.8	3	3	0	2.0	1.3	—	1.9	—	1.9	merger interface
III Zw 035NE X1	01 44 30.74	+17 06 12.20	4.2	4	4	0	2.7	1.8	—	2.5	—	2.5	disk
VII Zw 031 X1	05 16 45.27	+79 40 14.70	3.4	3	2	1	2.0	0.7	1.0	3.9	6.2	10.1	disk
VII Zw 031 X2	05 16 46.13	+79 40 16.50	3.4	3	3	0	2.0	1.6	—	9.6	—	9.6	disk
VII Zw 031 X3	05 16 46.75	+79 40 14.60	1.7	5	3	0	3.3	2.7	—	16.0	—	16.0	disk
VII Zw 031 X4	05 16 46.86	+79 40 15.60	2.7	3	3	0	2.0	1.6	—	9.6	—	9.6	disk
VII Zw 031 X5	05 16 46.90	+79 40 12.50	1.5	5	5	0	3.3	2.7	—	16.0	—	16.0	disk
ESO 255-IG007A X1	06 27 21.24	-47 10 37.10	4.9	3	1	2	2.2	0.7	1.1	2.1	3.3	5.4	disk
ESO 255-IG007B X1	06 27 22.49	-47 10 45.20	1.4	3	3	0	2.2	1.4	—	4.4	—	4.4	disk
ESO 255-IG007B X2	06 27 22.49	-47 10 48.60	2.5	5	3	2	3.7	1.1	1.8	3.5	5.5	8.9	disk
IRAS 09022-3615 X1	09 04 12.53	-36 27 02.33	2.1	3	2	1	2.0	0.9	1.4	6.9	10.8	17.6	disk
IRAS F09111-1007 X1	09 13 38.69	-10 19 19.30	1.8	3	3	0	2.0	1.3	—	7.9	—	7.9	disk
VV 250B X1	13 15 34.66	+62 07 27.40	2.1	3	3	0	2.1	1.7	—	3.2	—	3.2	disk
VV 250B X2	13 15 34.77	+62 07 26.10	2.3	3	2	1	2.1	0.6	0.9	1.1	1.8	2.9	disk
VV 250B X3	13 15 35.06	+62 07 30.60	2.6	3	2	1	2.1	0.6	0.9	1.1	1.8	2.9	disk
VV 250B X4	13 15 35.49	+62 07 32.20	5.7	3	3	0	2.1	1.7	—	3.2	—	3.2	disk
UGC 08387 X1	13 20 35.15	+34 08 18.70	4.6	3	3	0	2.1	1.0	—	1.1	—	1.1	disk
UGC 08387 X2	13 20 35.79	+34 08 14.30	10.1	6	5	1	4.2	1.2	1.9	1.3	2.0	3.3	disk/tidal tail
VV 340A X1	14 57 00.74	+24 37 01.70	1.2	4	3	1	2.6	0.7	1.2	1.6	2.5	4.1	disk
VV 340A X2	14 57 00.82	+24 37 03.70	3.1	4	4	0	2.6	1.5	—	3.3	—	3.2	disk
VV 340A X3	14 57 00.91	+24 37 07.90	7.3	3	3	0	2.0	1.1	—	2.5	—	2.5	disk
VV 340A X4	14 57 01.04	+24 37 09.10	9.1	3	3	0	2.0	1.1	—	2.5	—	2.5	disk
NGC 6090NE X1	16 11 40.59	+52 27 28.50	1.4	10	8	2	6.8	1.9	3.0	3.2	5.1	8.3	disk
NGC 6090NE X2	16 11 40.75	+52 27 26.10	2.8	8	6	2	5.4	1.5	2.4	2.6	4.1	6.7	disk
NGC 6090NE X3	16 11 40.81	+52 27 29.10	3.4	6	5	1	4.1	1.2	1.8	2.0	3.0	5.0	disk
NGC 6090NE X4	16 11 40.97	+52 27 24.60	5.3	3	3	0	2.0	1.0	—	1.7	—	1.7	disk
IRAS F18293-3413 X1	18 32 41.20	-34 11 28.70	3.0	6	3	3	4.4	1.5	2.4	1.0	1.5	2.5	disk
CGCG 448-020SE X1	20 57 24.12	+17 07 40.30	4.4	4	4	0	2.7	2.7	—	6.9	—	6.9	merger interface
CGCG 448-020SE X2	20 57 24.20	+17 07 37.90	2.7	3	3	0	2.1	2.0	—	5.2	—	5.2	disk
CGCG 448-020NW X1	20 57 23.55	+17 07 47.90	3.2	3	3	0	2.1	2.0	—	5.2	—	5.2	disk
CGCG 448-020NW X2	20 57 23.59	+17 07 46.50	2.5	2	2	0	1.4	1.3	—	3.5	—	3.5	disk
NGC 7592E X1	23 18 22.49	-04 24 58.60	1.0	4	4	0	2.9	1.8	—	2.0	—	2.0	disk
NGC 7592E X2	23 18 22.53	-04 24 56.20	2.7	3	3	0	2.2	1.3	—	1.5	—	1.5	disk

Note. — Col. (1): ULX candidate identification. Col (2-3): the coordinates of the ULX position given in J2000.0 coordinates. Col (4): the distance from the DSS optical centroid positions in arcseconds. Col (5): number of detected 0.5–8 keV counts. Col. (6–7): number of detected counts in the soft band (0.5–2 keV) and in the hard band (2–8 keV), respectively. Col. (8) total count rate in 10^{-4} counts per second. Col. (9–10): estimated X-ray fluxes in 10^{-15} ergs $\text{s}^{-1} \text{cm}^{-2}$. For sources with only soft counts, a blackbody model with $kT = 60$ eV for super-soft X-ray sources is assumed; otherwise, a power law model with $\Gamma = 1.8$ is assumed. Col. (11–13): estimated X-ray luminosities in 10^{39} ergs s^{-1} . Col. (14): location of the ULX in the host galaxy.

Bibliography

- Armus, L., Charmandaris, V., Bernard-Salas, J., Spoon, H. W. W., Marshall, J. A., Higdon, S. J. U., Desai, V., Teplitz, H. I., Hao, L., Devost, D., Brandl, B. R., Wu, Y., Sloan, G. C., Soifer, B. T., Houck, J. R., & Herter, T. L. 2007, *ApJ*, 656, 148
- Arnaud, K. A. 1996, in *Astronomical Society of the Pacific Conference Series*, Vol. 101, *Astronomical Data Analysis Software and Systems V*, ed. G. H. Jacoby & J. Barnes, 17–+
- Balestra, I., Boller, T., Gallo, L., Lutz, D., & Hess, S. 2005, *A&A*, 442, 469
- Bianchi, S., Guainazzi, M., Matt, G., Fonseca Bonilla, N., & Ponti, G. 2009, *A&A*, 495, 421
- Boller, T., & Bertoldi, F. 1996, in *Astronomical Society of the Pacific Conference Series*, Vol. 103, *The Physics of Liners in View of Recent Observations*, ed. M. Eracleous, A. Koratkar, C. Leitherer, & L. Ho, 159–+
- Boller, T., Gallo, L. C., Lutz, D., & Sturm, E. 2002, *MNRAS*, 336, 1143
- Boller, T., Keil, R., Hasinger, G., Costantini, E., Fujimoto, R., Anabuki, N., Lehmann, I., & Gallo, L. 2003, *A&A*, 411, 63
- Braitto, V., Della Ceca, R., Piconcelli, E., Severgnini, P., Bassani, L., Cappi, M., Franceschini, A., Iwasawa, K., Malaguti, G., Marziani, P., Palumbo, G. G. C., Persic, M., Risaliti, G., & Salvati, M. 2004, *A&A*, 420, 79
- Braitto, V., Franceschini, A., Della Ceca, R., Severgnini, P., Bassani, L., Cappi, M.,

- Malaguti, G., Palumbo, G. G. C., Persic, M., Risaliti, G., & Salvati, M. 2003, *A&A*, 398, 107
- Brandl, B. R., Bernard-Salas, J., Spoon, H. W. W., Devost, D., Sloan, G. C., Guilles, S., Wu, Y., Houck, J. R., Weedman, D. W., Armus, L., Appleton, P. N., Soifer, B. T., Charmandaris, V., Hao, L., Higdon, J. A., Marshall, S. J., & Herter, T. L. 2006, *ApJ*, 653, 1129
- Bryant, P. M., & Scoville, N. Z. 1999, *AJ*, 117, 2632
- Cash, W. 1979, *ApJ*, 228, 939
- Clements, D. L., McDowell, J. C., Shaked, S., Baker, A. C., Borne, K., Colina, L., Lamb, S. A., & Mundell, C. 2002, *ApJ*, 581, 974
- Colbert, E. J. M., Heckman, T. M., Ptak, A. F., Strickland, D. K., & Weaver, K. A. 2004, *ApJ*, 602, 231
- Condon, J. J., Huang, Z., Yin, Q. F., & Thuan, T. X. 1991, *ApJ*, 378, 65
- Costantini, E., Gallo, L. C., Brandt, W. N., Fabian, A. C., & Boller, T. 2007, *MNRAS*, 378, 873
- Crummy, J., Fabian, A. C., Gallo, L., & Ross, R. R. 2006, *MNRAS*, 365, 1067
- Dasyra, K. M., Tacconi, L. J., Davies, R. I., Genzel, R., Lutz, D., Naab, T., Burkert, A., Veilleux, S., & Sanders, D. B. 2006a, *ApJ*, 638, 745
- Dasyra, K. M., Tacconi, L. J., Davies, R. I., Genzel, R., Lutz, D., Peterson, B. M., Veilleux, S., Baker, A. J., Schweitzer, M., & Sturm, E. 2007, *ApJ*, 657, 102
- Dasyra, K. M., Tacconi, L. J., Davies, R. I., Naab, T., Genzel, R., Lutz, D., Sturm, E., Baker, A. J., Veilleux, S., Sanders, D. B., & Burkert, A. 2006b, *ApJ*, 651, 835
- Dermer, C. D., Bland-Hawthorn, J., Chiang, J., & McNaron-Brown, K. 1997, *ApJ*, 484, L121+
- Desai, V., Armus, L., Spoon, H. W. W., Charmandaris, V., Bernard-Salas, J., Brandl, B. R., Farrah, D., Soifer, B. T., Teplitz, H. I., Ogle, P. M., Devost, D.,

- Higdon, S. J. U., Marshall, J. A., & Houck, J. R. 2007, *ApJ*, 669, 810
- Dickey, J. M., & Lockman, F. J. 1990, *ARA&A*, 28, 215
- Downes, D., & Eckart, A. 2007, *A&A*, 468, L57
- Downes, D., & Solomon, P. M. 1998, *ApJ*, 507, 615
- Elvis, M., Wilkes, B. J., McDowell, J. C., Green, R. F., Bechtold, J., Willner, S. P., Oey, M. S., Polomski, E., & Cutri, R. 1994, *ApJS*, 95, 1
- Evans, A. S., Frayer, D. T., Surace, J. A., & Sanders, D. B. 2001, *AJ*, 121, 1893
- Evans, A. S., Kim, D. C., Mazzarella, J. M., Scoville, N. Z., & Sanders, D. B. 1999, *ApJ*, 521, L107
- Evans, A. S., Mazzarella, J. M., Surace, J. A., & Sanders, D. B. 2002, *ApJ*, 580, 749
- Fabian, A. C. 2006, in *ESA Special Publication*, Vol. 604, *The X-ray Universe 2005*, ed. A. Wilson, 463–+
- Farrah, D., Bernard-Salas, J., Spoon, H. W. W., Soifer, B. T., Armus, L., Brandl, B., Charmandaris, V., Desai, V., Higdon, S., Devost, D., & Houck, J. 2007, *ApJ*, 667, 149
- Franceschini, A., Braito, V., Persic, M., Della Ceca, R., Bassani, L., Cappi, M., Malaguti, P., Palumbo, G. G. C., Risaliti, G., Salvati, M., & Severgnini, P. 2003, *MNRAS*, 343, 1181
- Gallo, L. C., Boller, T., Tanaka, Y., Fabian, A. C., Brandt, W. N., Welsh, W. F., Anabuki, N., & Haba, Y. 2004, *MNRAS*, 347, 269
- Gehrels, N. 1986, *ApJ*, 303, 336
- Genzel, R., Lutz, D., Sturm, E., Egami, E., Kunze, D., Moorwood, A. F. M., Rigopoulou, D., Spoon, H. W. W., Sternberg, A., Tacconi-Garman, L. E., Tacconi, L., & Thatte, N. 1998, *ApJ*, 498, 579
- Genzel, R., Tacconi, L. J., Rigopoulou, D., Lutz, D., & Tecza, M. 2001, *ApJ*, 563, 527

- George, I. M., Turner, T. J., Netzer, H., Nandra, K., Mushotzky, R. F., & Yaqoob, T. 1998, *ApJS*, 114, 73
- Ghisellini, G., Haardt, F., & Matt, G. 1994, *MNRAS*, 267, 743
- Gierliński, M., & Done, C. 2004, *MNRAS*, 349, L7
- González-Martín, O., Masegosa, J., Márquez, I., Guerrero, M. A., & Dultzin-Hacyan, D. 2006, *A&A*, 460, 45
- Griffiths, R. E., Ptak, A., Feigelson, E. D., Garmire, G., Townsley, L., Brandt, W. N., Sambruna, R., & Bregman, J. N. 2000, *Science*, 290, 1325
- Grimes, J. P., Heckman, T., Strickland, D., & Ptak, A. 2005, *ApJ*, 628, 187
- Grupe, D., Komossa, S., & Gallo, L. C. 2007, *ApJ*, 668, L111
- Guainazzi, M., Nicastro, F., Fiore, F., Matt, G., McHardy, I., Orr, A., Barr, P., Fruscione, A., Papadakis, I., Parmar, A. N., Uttley, P., Perola, G. C., & Piro, L. 1998, *MNRAS*, 301, L1
- Helou, G., Soifer, B. T., & Rowan-Robinson, M. 1985, *ApJ*, 298, L7
- Holczer, T., Behar, E., & Arav, N. 2010, *ApJ*, 708, 981
- Hopkins, P. F., Hernquist, L., Cox, T. J., Di Matteo, T., Martini, P., Robertson, B., & Springel, V. 2005, *ApJ*, 630, 705
- Hopkins, P. F., Hernquist, L., Cox, T. J., & Kereš, D. 2008, *ApJS*, 175, 356
- Hornschemeier, A. E., Heckman, T. M., Ptak, A. F., Tremonti, C. A., & Colbert, E. J. M. 2005, *AJ*, 129, 86
- Hughes, J. P., Rakowski, C. E., Burrows, D. N., & Slane, P. O. 2000, *ApJ*, 528, L109
- Imanishi, M., Dudley, C. C., & Maloney, P. R. 2006, *ApJ*, 637, 114
- Imanishi, M., & Terashima, Y. 2004, *AJ*, 127, 758
- Imanishi, M., Terashima, Y., Anabuki, N., & Nakagawa, T. 2003, *ApJ*, 596, L167
- Ishida, C. M. 2004, PhD thesis, AA(UNIVERSITY OF HAWAII)

Iwasawa, K. 1999, MNRAS, 302, 96

Iwasawa, K., Sanders, D. B., Evans, A. S., Trentham, N., Miniutti, G., & Spoon, H. W. W. 2005, MNRAS, 357, 565

Joseph, R. D. 1999, Ap&SS, 266, 321

Kennicutt, Jr., R. C. 1998, ApJ, 498, 541

Kim, D.-C., & Sanders, D. B. 1998, ApJS, 119, 41

Kim, D.-C., Veilleux, S., & Sanders, D. B. 2002, ApJS, 143, 277

Kinugasa, K., & Tsunemi, H. 1999, PASJ, 51, 239

Komossa, S., Burwitz, V., Hasinger, G., Predehl, P., Kaastra, J. S., & Ikebe, Y. 2003, ApJ, 582, L15

Kong, A. K. H., & Di Stefano, R. 2003, ApJ, 590, L13

Kormendy, J., & Sanders, D. B. 1992, ApJ, 390, L53

Krolik, J. H., Madau, P., & Zycki, P. T. 1994, ApJ, 420, L57

Leighly, K. M. 1999, ApJS, 125, 317

Lonsdale, C. J., Smith, H. J., & Lonsdale, C. J. 1993, ApJ, 405, L9

Lutz, D., Veilleux, S., & Genzel, R. 1999, ApJ, 517, L13

Maloney, P. R., & Reynolds, C. S. 2000, ApJ, 545, L23

Matt, G., Bianchi, S., Guainazzi, M., & Molendi, S. 2004, A&A, 414, 155

McDowell, J. C., Clements, D. L., Lamb, S. A., Shaked, S., Hearn, N. C., Colina, L., Mundell, C., Borne, K., Baker, A. C., & Arribas, S. 2003, ApJ, 591, 154

McKernan, B., Yaqoob, T., & Reynolds, C. S. 2007, MNRAS, 379, 1359

Murray, N., Quataert, E., & Thompson, T. A. 2005, ApJ, 618, 569

Nagar, N. M., Wilson, A. S., Falcke, H., Veilleux, S., & Maiolino, R. 2003, A&A, 409, 115

Netzer, H., Lemze, D., Kaspi, S., George, I. M., Turner, T. J., Lutz, D., Boller, T., & Chelouche, D. 2005, ApJ, 629, 739

- Netzer, H., Lutz, D., Schweitzer, M., Contursi, A., Sturm, E., Tacconi, L. J.,
Veilleux, S., Kim, D., Rupke, D., Baker, A. J., Dasyra, K., Mazzarella, J., &
Lord, S. 2007, *ApJ*, 666, 806
- Persic, M., & Rephaeli, Y. 2002, *A&A*, 382, 843
- Persic, M., Rephaeli, Y., Braito, V., Cappi, M., Della Ceca, R., Franceschini, A., &
Gruber, D. E. 2004, *A&A*, 419, 849
- Piconcelli, E., Jimenez-Bailón, E., Guainazzi, M., Schartel, N., Rodríguez-Pascual,
P. M., & Santos-Lleó, M. 2004, *MNRAS*, 351, 161
- . 2005, *A&A*, 432, 15
- Polletta, M., Bassani, L., Malaguti, G., Palumbo, G. G. C., & Caroli, E. 1996,
ApJS, 106, 399
- Porquet, D., Reeves, J. N., O'Brien, P., & Brinkmann, W. 2004, *A&A*, 422, 85
- Protassov, R., van Dyk, D. A., Connors, A., Kashyap, V. L., & Siemiginowska, A.
2002, *ApJ*, 571, 545
- Ptak, A., Heckman, T., Levenson, N. A., Weaver, K., & Strickland, D. 2003, *ApJ*,
592, 782
- Ptak, A., Serlemitsos, P., Yaqoob, T., & Mushotzky, R. 1999, *ApJS*, 120, 179
- Puccetti, S., Fiore, F., Risaliti, G., Capalbi, M., Elvis, M., & Nicastro, F. 2007,
MNRAS, 377, 607
- Ranalli, P., Comastri, A., & Setti, G. 2003, *A&A*, 399, 39
- Reynolds, C. S. 1997, *MNRAS*, 286, 513
- Risaliti, G., Elvis, M., Fabbiano, G., Baldi, A., & Zezas, A. 2005, *ApJ*, 623, L93
- Risaliti, G., Elvis, M., & Nicastro, F. 2002, *ApJ*, 571, 234
- Risaliti, G., Gilli, R., Maiolino, R., & Salvati, M. 2000, *A&A*, 357, 13
- Ross, R. R., & Fabian, A. C. 2005, *MNRAS*, 358, 211
- Rupke, D. S., Veilleux, S., & Sanders, D. B. 2002, *ApJ*, 570, 588

- . 2005a, *ApJ*, 632, 751
- . 2005b, *ApJS*, 160, 87
- . 2005c, *ApJS*, 160, 115
- Rybicki, G. B., & Lightman, A. P. 1979, *Radiative processes in astrophysics* (New York, Wiley-Interscience, 1979. 393 p.)
- Sanders, D. B. 1999, *Ap&SS*, 266, 331
- Sanders, D. B., Mazzarella, J. M., Kim, D.-C., Surace, J. A., & Soifer, B. T. 2003, *AJ*, 126, 1607
- Sanders, D. B., & Mirabel, I. F. 1996, *ARA&A*, 34, 749
- Sanders, D. B., Phinney, E. S., Neugebauer, G., Soifer, B. T., & Matthews, K. 1989, *ApJ*, 347, 29
- Sanders, D. B., Soifer, B. T., Elias, J. H., Madore, B. F., Matthews, K., Neugebauer, G., & Scoville, N. Z. 1988a, *ApJ*, 325, 74
- . 1988b, *ApJ*, 325, 74
- Schweitzer, M., Lutz, D., Sturm, E., Contursi, A., Tacconi, L. J., Lehnert, M. D., Dasyra, K. M., Genzel, R., Veilleux, S., Rupke, D., Kim, D., Baker, A. J., Netzer, H., Sternberg, A., Mazzarella, J., & Lord, S. 2006, *ApJ*, 649, 79
- Scoville, N. Z., Evans, A. S., Thompson, R., Rieke, M., Hines, D. C., Low, F. J., Dinshaw, N., Surace, J. A., & Armus, L. 2000, *AJ*, 119, 991
- Severgnini, P., Risaliti, G., Marconi, A., Maiolino, R., & Salvati, M. 2001, *A&A*, 368, 44
- Sobolewska, M. A., & Done, C. 2007, *MNRAS*, 374, 150
- Soifer, B. T., Neugebauer, G., Matthews, K., Egami, E., Becklin, E. E., Weinberger, A. J., Ressler, M., Werner, M. W., Evans, A. S., Scoville, N. Z., Surace, J. A., & Condon, J. J. 2000, *AJ*, 119, 509
- Spoon, H. W. W., Marshall, J. A., Houck, J. R., Elitzur, M., Hao, L., Armus, L.,

- Brandl, B. R., & Charmandaris, V. 2007, *ApJ*, 654, L49
- Strickland, D. K., & Stevens, I. R. 2000, *MNRAS*, 314, 511
- Sturm, E., Rupke, D., Contursi, A., Kim, D., Lutz, D., Netzer, H., Veilleux, S., Genzel, R., Lehnert, M., Tacconi, L. J., Maoz, D., Mazzarella, J., Lord, S., Sanders, D., & Sternberg, A. 2006, *ApJ*, 653, L13
- Surace, J. A., Sanders, D. B., & Evans, A. S. 2000, *ApJ*, 529, 170
- . 2001, *AJ*, 122, 2791
- Taniguchi, Y., Yoshino, A., Ohyama, Y., & Nishiura, S. 1999, *ApJ*, 514, 660
- Teng, S. H., Veilleux, S., Anabuki, N., Dermer, C. D., Gallo, L. C., Nakagawa, T., Reynolds, C. S., Sanders, D. B., Terashima, Y., & Wilson, A. S. 2009, *ApJ*, 691, 261
- Teng, S. H., Veilleux, S., Wilson, A. S., Young, A. J., Sanders, D. B., & Nagar, N. M. 2008, *ApJ*, 674, 133
- Teng, S. H., Wilson, A. S., Veilleux, S., Young, A. J., Sanders, D. B., & Nagar, N. M. 2005, *ApJ*, 633, 664
- Terashima, Y., Iyomoto, N., Ho, L. C., & Ptak, A. F. 2002, *ApJS*, 139, 1
- Terashima, Y., & Wilson, A. S. 2003, *ApJ*, 583, 145
- Tran, Q. D., Lutz, D., Genzel, R., Rigopoulou, D., Spoon, H. W. W., Sturm, E., Gerin, M., Hines, D. C., Moorwood, A. F. M., Sanders, D. B., Scoville, N., Taniguchi, Y., & Ward, M. 2001, *ApJ*, 552, 527
- Vaughan, S., Reeves, J., Warwick, R., & Edelson, R. 1999, *MNRAS*, 309, 113
- Veilleux, S., Cecil, G., & Bland-Hawthorn, J. 2005, *ARA&A*, 43, 769
- Veilleux, S., Kim, D., Rupke, D. S. N., Peng, C. Y., Tacconi, L. J., Genzel, R., Lutz, D., Sturm, E., Contursi, A., Schweitzer, M., Dasyra, K. M., Ho, L. C., Sanders, D. B., & Burkert, A. 2009a, *ApJ*, 701, 587
- Veilleux, S., Kim, D.-C., Peng, C. Y., Ho, L. C., Tacconi, L. J., Dasyra, K. M.,

- Genzel, R., Lutz, D., & Sanders, D. B. 2006, *ApJ*, 643, 707
- Veilleux, S., Kim, D.-C., & Sanders, D. B. 1999a, *ApJ*, 522, 113
- . 2002, *ApJS*, 143, 315
- Veilleux, S., Kim, D.-C., Sanders, D. B., Mazzarella, J. M., & Soifer, B. T. 1995, *ApJS*, 98, 171
- Veilleux, S., Rupke, D. S. N., Kim, D., Genzel, R., Sturm, E., Lutz, D., Contursi, A., Schweitzer, M., Tacconi, L. J., Netzer, H., Sternberg, A., Mihos, J. C., Baker, A. J., Mazzarella, J. M., Lord, S., Sanders, D. B., Stockton, A., Joseph, R. D., & Barnes, J. E. 2009b, *ApJS*, 182, 628
- Veilleux, S., Sanders, D. B., & Kim, D.-C. 1997, *ApJ*, 484, 92
- . 1999b, *ApJ*, 522, 139
- Vignati, P., Molendi, S., Matt, G., Guainazzi, M., Antonelli, L. A., Bassani, L., Brandt, W. N., Fabian, A. C., Iwasawa, K., Maiolino, R., Malaguti, G., Marconi, A., & Perola, G. C. 1999, *A&A*, 349, L57
- Warren, J. S., Hughes, J. P., Badenes, C., Ghavamian, P., McKee, C. F., Moffett, D., Plucinsky, P. P., Rakowski, C., Reynoso, E., & Slane, P. 2005, *ApJ*, 634, 376
- Winter, L. M., Mushotzky, R. F., & Reynolds, C. S. 2006, *ApJ*, 649, 730
- Winter, L. M., Mushotzky, R. F., Reynolds, C. S., & Tueller, J. 2009, *ApJ*, 690, 1322
- Xia, X.-Y., Boller, T., Wu, H., Deng, Z.-G., Gao, Y., Zou, Z.-L., Mao, S., & Boerner, G. 1998, *ApJ*, 496, L9+
- Xia, X. Y., Xue, S. J., Mao, S., Boller, T., Deng, Z. G., & Wu, H. 2002, *ApJ*, 564, 196
- Zezas, A., Ward, M. J., & Murray, S. S. 2003, *ApJ*, 594, L31